

PHOTO-ELECTROSWITCHABLE
ARYLAMINOAZOBENZENES

by

KATIE STRICKLAND KEANE

SILAS C. BLACKSTOCK, COMMITTEE CHAIR
MARCO BONIZZONI
KEVIN H. SHAUGHNESSY
SHANLIN PAN
CLAUDIA K.A. MEWES

A DISSERTATION

Submitted in partial fulfillment of the requirements
for the degree of Doctor of Philosophy
in the Department of Chemistry & Biochemistry
in the Graduate School of
The University of Alabama

TUSCALOOSA, ALABAMA

2021

Copyright Katie Strickland Keane 2021
ALL RIGHTS RESERVED

ABSTRACT

Azobenzenes consist of two phenyl rings linked by an azo unit (N=N), existing in *E* or *Z* isomeric forms. Their ability to reversibly transform between 'extended' thermodynamically favored *E* and higher energy 'contracted' *Z* isomeric forms upon photo-stimulation make them useful molecular 'flexors.' *E*→*Z* switching is rapidly achieved using light, which has popularized the use of azobenzenes in a variety of chemical systems to gain nano mechanical photoswitchable characteristics. In most cases, *Z*→*E* isomerization occurs slowly thermally or, when possible by photoisomerization, though slower than photo *E*→*Z* conversion and typically incomplete.

To address the *Z*→*E* isomerization limits (slow or incomplete), we have developed using electron removal as a new azobenzene switching mechanism for amino-substituted azobenzenes and investigated the prospect of switching multiple azo linkages with a single electron loss event. Blackstock and coworkers have covalently attached a redox aryl amine to the azobenzene moiety allowing for rapid, catalytic, and complete *Z*→*E* isomerization upon oxidation. The oxidized redox auxiliary dramatically reduces the *Z*→*E* isomerization energy barrier by factors of at least 10⁵. Once initiated, the aryl amine radical cation is chemically stable and persistent enough to exchange electrons with a neutral *Z* isomer amine, generating an efficient electron-transfer chain reaction for *Z*→*E* isomerization.

The synthesis, photo- and thermoisomerization, and lifetime effects of linking multiple azobenzenes to a single arylamine redox center are investigated for four tertiary amine derivatives: 4-methoxy-4'-(*N,N*-dianisyl)-aminoazobenzene (**11**), *N,N*-bis(azobenzene)-*p*-anisidine (**20**), *N,N*-bis(2,2',6,6'-tetrafluoroazobenzene)-*p*-anisidine (**21**), and *N,N,N*-tris(azobenzene)amine (**29**). Blue

light irradiation of these azobenzene systems yields an equilibrium of *Z*-enriched isomers as a photostationary state (PSS). Dynamic UV-vis and NMR spectroscopy are used to measure PSS compositions and thermal dynamics of these mixtures. *Ortho*-fluorination is employed to increase *Z* isomer lifetime from hours (**20**) to weeks (**21**), resulting in an extended switching time domain for the dual-flexor system. Electron loss from a single arylamine efficiently catalyzes the *Z*→*E* isomerization of up to three connected azobenzene units, resulting in rapid, large geometry changes for these conglomerate structures. Stimulated, reversible flexing is thus demonstrated using electronic excitation and electron transfer. Incorporating a photosensitizer (methylene blue) allows for a dual photo, photo-electron transfer *Z,E* switching mechanism, which can be easily cycled with light. Red light excites methylene blue, which in turn oxidizes the redox amine to achieve rapid, complete *Z*→*E* conversion. Thus, blue and red light irradiation in tandem is shown to generate an *E*→*Z*→*E* switching cycle for three of the systems (**11**, **20**, and **29**).

DEDICATION

To my wonderful mother, Veronica Martin, for always being one phone call away with encouraging words and guidance.

LIST OF ABBREVIATIONS AND SYMBOLS

°C	degree Celsius
μL	microliter(s)
Å	angstrom (1 Å = 10 ⁻¹⁰ m)
AcOH	acetic acid
Anhydr	anhydrous
Aq	aqueous
B3LYP	Becke, 3-parameter, Lee-Yang-Parr
BINAP	2,2'-bis(diphenylphosphino)-1,1'-binaphthyl
br	broad
CAN	ceric ammonium nitrate
CDCl ₃	deuterated chloroform
COSY	homonuclear correlation spectroscopy
CV	cyclic voltammetry
d	doublet (NMR)
DA	donor-acceptor
DCM	dichloromethane
dd	doublet of doublets
DDQ	2,3-dichloro-5,6-dicyano-1,4-benzoquinone
DI H ₂ O	deionized water

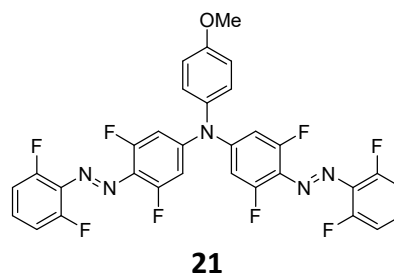
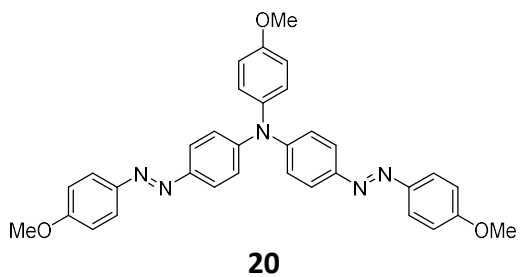
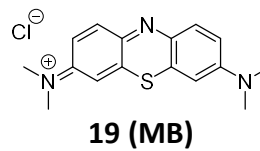
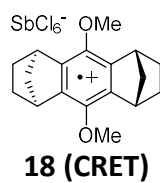
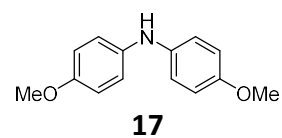
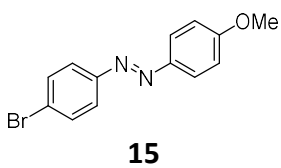
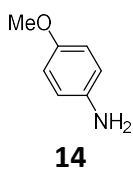
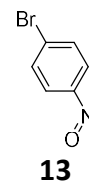
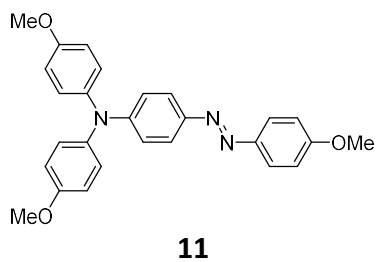
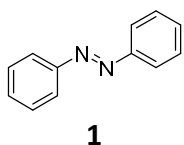
DMSO	dimethyl sulfoxide
dppf	1,1'-bis(diphenylphosphino)ferrocene
<i>E</i> -	entgegen (trans)
E°	redox potential
EI	electron ionization
EI-MS	electron impact mass spectroscopy
EPR	electron paramagnetic resonance
ET	electron transfer
Et ₂ O	diethyl ether
EtOAc	ethyl acetate
EtOH	ethanol
G	Gauss
g	gram
h	hour(s)
HMBC	heteronuclear multi-bond coherence spectroscopy
HOMO	highest occupied molecular orbital
HRMS	high resolution mass spectroscopy
HSQC	heteronuclear single quantum coherence spectroscopy
Hz	hertz, s ⁻¹
ITO	indium tin oxide
J	coupling constant
K	kelvin
kcal	kilocalorie

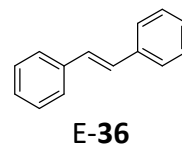
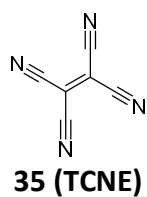
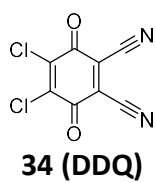
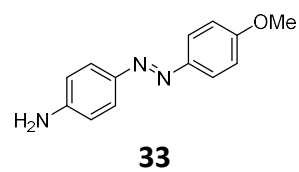
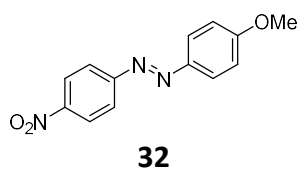
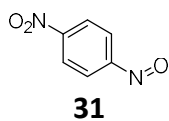
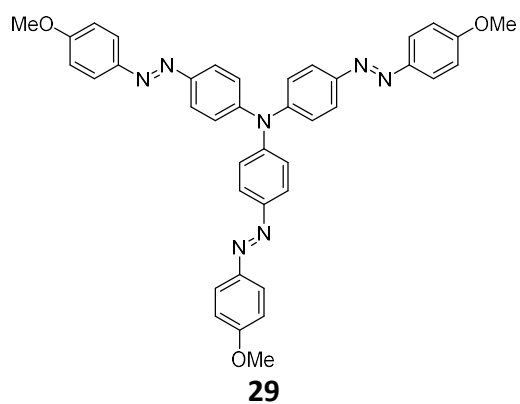
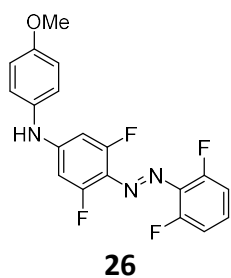
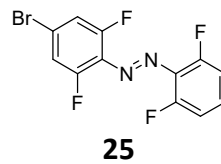
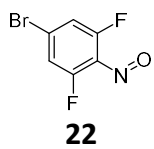
kJ	kilojoule
L	liter(s)
LED	light-emitting diode
Ln	natural logarithm
LUMO	lowest unoccupied molecular orbital
M	molar / molarity
m	multiplet (NMR)
MB	methylene blue
MeOH	methanol
MHz	megahertz
min	minute(s)
mL	milliliter(s)
mM	millimolar
mmol	millimole
mol	mole
mp	melting point
N ₂	nitrogen gas
-NAn ₂	<i>p</i> -dianisylamino
NMR	nuclear magnetic resonance spectroscopy
NOE	nuclear overhauser effect spectroscopy
P(<i>t</i> Bu) ₃	tri- <i>tert</i> -butylphosphine
Pd(dba) ₂	bis(dibenzylideneacetone)palladium(0)
Pd(OAc) ₂	palladium(II) acetate

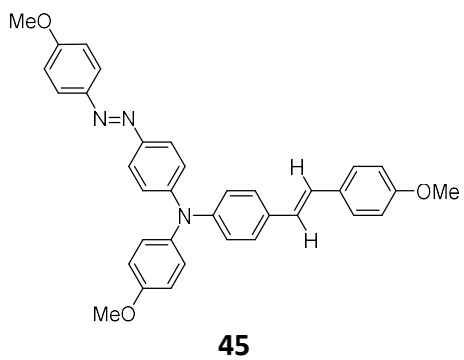
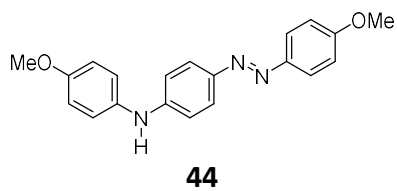
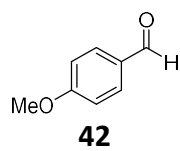
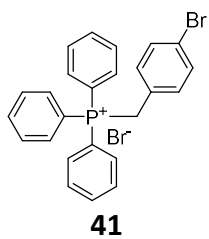
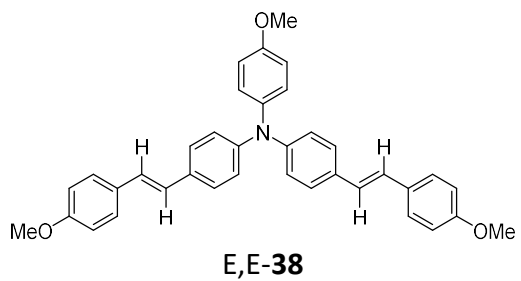
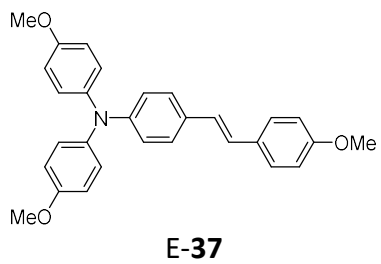
PED	photo-electrochemical device
ppm	parts per million
PSS	photostationary state
q	quartet (NMR)
ra	redox auxiliary
ra-azo	redox auxiliary-appended azobenzene
RBF	round bottom flask
rt	room temperature
s	second(s) or singlet (NMR)
SCE	saturated calomel electrode
t	triplet (NMR)
$t_{1/2}$	half-life
TBABF ₄	tetrabutylammonium tetrafluoroborate
TFA	trifluoroacetic acid
THF	tetrahydrofuran
TLC	thin layer chromatography
UV-vis	ultraviolet-visible spectroscopy
V	volt(s)
W	watt(s)
XRD	X-ray diffraction
Z-	zusammen (cis)
ΔG	change in free energy of reaction
ΔG^\ddagger	Gibbs free energy of activation

ϵ molar extinction coefficient
 δ chemical shift

COMPOUND STRUCTURE LEGEND







ACKNOWLEDGMENTS

I would like to first express my gratitude to my professors during my time in the program, especially my committee members for their extra guidance and commitment.

I am truly grateful and appreciative for my advisor, Dr. Silas Blackstock, who has made a huge impact on my personal and professional development as a chemist. I appreciate all the encouragement, contributions, and support from the Blackstock group members (Ariel, David, Izzy, and Cory) and from fellow chemistry graduate students that came into my life during every stage of the journey.

Lastly, I would like to thank my husband, parents, siblings, and friends that became like family, for their unlimited love and encouragement. Each played an integral role to support me as I accomplished my goals, along with filling my time at UA with wonderful experiences and memories.

CONTENTS

ABSTRACT.....	ii
DEDICATION.....	iv
LIST OF ABBREVIATIONS AND SYMBOLS	v
COMPOUND STRUCTURE LEGEND	x
ACKNOWLEDGMENTS	xiii
CONTENTS.....	xiv
LIST OF TABLES.....	xix
LIST OF FIGURES	xx
LIST OF SCHEMES.....	xxv
CHAPTER 1 INTRODUCTORY OVERVIEW OF AZOBENZENES.....	1
1.1. Introduction	1
1.2. Electronic Structure of Azobenzene.....	2
1.3. Photochemistry of Azobenzene.....	4
1.4. Thermal Isomerization of Azobenzene	6
1.5. Substitution Effects on the Absorption Spectra of Azobenzenes.....	7
1.6. Multi-Azobenzene Systems.....	8
1.7. Research Goals.....	15

CHAPTER 2 PHOTO-ELECTRO-TRANSFER CATALYSIS OF REDOX AUXILIARY-MEDIATED AZOBENZENE	16
2.1. Introduction	16
2.2. Theoretical Explanation of Redox Auxiliary-Mediated Azobenzene Isomerization	18
2.3. Redox $Z \rightarrow E$ Switching of Dianisylamine Appended Azobenzene.....	21
2.3.1. Synthesis of AA-AB (11).....	22
2.3.2. Photochemistry and optical absorption of AA-AB (11)	24
2.3.3. Thermal $Z \rightarrow E$ isomerization of AA-AB (11).....	28
2.3.4. Electrocatalytic switching of AA-AB (11)	30
2.3.5. Electrocatalytic switching of AA-AB (11) using a thin cell photo-electro device (PED) 34	
2.4. Photosensitizer for Photo-Electro Catalytic Switching of AA-AB.....	35
2.5. Introduction and Synthesis Of AA-AB ⁺⁺ (11 ⁺⁺).....	44
2.5.1. Optical absorption of AA-AB ⁺⁺ (11 ⁺⁺).....	44
2.5.2. Electron paramagnetic resonance (EPR) spectrum activity.....	45
2.6. Conclusion.....	46
2.7. Experimental Section	48
CHAPTER 3 PHOTO-REDOX SWITCHING OF BIS(AZOBENZENE) DERIVATIVES.....	60
3.1. Introduction	60
3.2. Synthesis of Redox Appended Bis(azobenzene)- <i>p</i> -anisidines	61
3.3. Photochemistry and Optical Absorption of Bis(azobenzene)- <i>p</i> -anisidines.....	64

3.4.	Thermal $Z \rightarrow E$ Isomerization of Bis(azobenzene)- <i>p</i> -anisidines	73
3.5.	Redox Switching of Bis(azobenzene)- <i>p</i> -anisidines.....	78
3.6.	Photosensitizer for Photo-Electro Catalytic Switching of Bis(azobenzene)- <i>p</i> -anisidines 82	
3.7.	Conclusions	84
3.8.	Experimental Section	85
CHAPTER 4 PHOTO-REDOX SWITCHING OF TRIS(AZOBENZENE)AMINE		95
4.1.	Introduction	95
4.2.	Synthesis of TA (29)	96
4.2.1.	Crystal Structure of TA (29).....	98
4.3.	Photochemistry and Optical Absorption of TA (29).....	100
4.4.	Thermal $Z \rightarrow E$ isomerization of TA (29).....	104
4.5.	Redox Switching of TA (29).....	107
4.6.	Photosensitizer for Photo, Photo-Electro catalytic switching of TA (29)	110
4.7.	Co-crystallization of TA•DDQ	112
4.7.1.	Synthesis	113
4.7.2.	Single-crystal XRD structure	115
4.8.	Conclusions	117
4.9	Experimental Section	119
CHAPTER 5 STILBENE BIS-SYSTEMS.....		126

5.1.	Introduction to the Electro-, Photo-, and Thermal Properties of Stilbenes	126
5.2.	Photo-Electro-Transfer Catalysis of Redox Auxiliary-Mediated Stilbene (37).....	127
5.3.	Photo-Redox Switching of Bis(stilbene)-p-anisidine.....	130
5.3.1.	Introduction.....	130
5.3.2.	Synthesis of <i>E,E</i> - and <i>Z,Z</i> -(38)	131
5.3.3.	Photo-instability of <i>E,E</i> → <i>Z,Z</i> -38	133
5.4.	Photo-Redox <i>Z</i> → <i>E</i> Switching of Dual Component Bis-system 45	134
5.4.1.	Photochemistry and Optical Absorption of 45.....	135
5.5.	Conclusions	139
5.6.	Experimental Section	140
SUMMARY AND FUTURE DIRECTIONS		146
REFERENCES		151
APPENDIX A: List of NMR Spectra		161
APPENDIX B: Excitation Source Spectra		189

LIST OF TABLES

Table 1. Unit Cell Parameters for the Crystal (**29**). 98

Table 2. Unit Cell Parameters for the Co-crystal (**29**•DDQ). 117

LIST OF FIGURES

Figure 1.1. The <i>E</i> and <i>Z</i> isomers of azobenzene (1) achieved photochemically or thermally.....	2
Figure 1.2. The absorption spectra of <i>E</i> - 1 (blue) and <i>Z</i> - 1 (red) from a solution of 4.7×10^{-4} M 1 in CDCl_3 using a 0.1 cm quartz cuvette. ²³	3
Figure 1.3. The frontier molecular orbital diagram of azobenzene (1) for its HOMO-1 (π), HOMO (n), and LUMO (π^*) and the $n \rightarrow \pi^*$ (purple) and $\pi \rightarrow \pi^*$ (pink) electronic transition.	4
Figure 1.4. Azobenzene (1) potential energy diagram for <i>E</i> and <i>Z</i> isomers with an <i>Z</i> → <i>E</i> activation energy barrier of $25.8 \text{ kcal mol}^{-1}$	6
Figure 1.5. Absorption spectra overlay showing the impact of substitution to shift absorption band wavelengths. The spectra of 1 (black) at 6.12×10^{-4} M, 2 (red) at 5.90×10^{-4} M, 3 (green) at 4.62×10^{-4} M, and 4 (purple) at 5.75×10^{-4} M in ethanol are measured using a 0.1 cm quartz cuvette at room temperature. ¹⁵	8
Figure 1.6. Symmetric bis- 5 , tris- 6 , and tetra- 7 azobenzophanes with dimethyl(methylene) linkers showing 5 in its all <i>Z</i> -state and 6 and 7 in their all <i>E</i> -states. ⁵⁰	9
Figure 1.7. Three isomeric states (<i>E,E,E</i> - 6 , <i>E,Z,Z</i> - 6 and <i>Z,Z,Z</i> - 6) are achieved by a combination of irradiation (365 nm or 448 nm) and heating from any of the other isomeric states. ⁵⁰	9
Figure 1.8. A pseudo-planar, C_3 -symmetric star-shaped azobenzene (8) capable of 2D crystalline self-assembly. High resolution STM images of self-assembled (a) <i>E,E,E</i> - 8 , (b) <i>E,Z,Z</i> - 8 , (c) <i>E,E,Z</i> - 8 at the solvent-surface interface (1-hepanoic acid - highly ordered pyrolytic graphite). The MM/MD simulations for each isomer are paired below in (d)-(f). The hydrogen bonded carboxylic acid dimers are indicated by yellow rectangles between <i>E</i> isomer arms and orange rectangles between <i>Z</i> isomer arms. Figure reproduced from Ref. 50.	10
Figure 1.9. (a) The palladium-bis(azobenzene) complexes 9 •Pd. (b) Suzuki-Miyaura cross-coupling using 9 •Pd (R = OAc). (c) Heck coupling using 9 •Pd (R = I). ⁵⁷	12
Figure 1.10. The tetrakis(azobenzene)methane (10a-c) structure with hydrogen (10a), methyl (10b), or tert-butyl (10c) groups at the terminal para positions.....	13
Figure 1.11. (a) The 3D tetrahedral structure of 10c . (b) The tetrahedral 10c structure stacking along the c-axis with each individual molecule differentiated by color. (c) Looking down the c-axis, the molecular piles form empty channels (yellow) extending down the c-axis. (d) A side view of an empty channel (yellow) formation without the molecules shown. Figure reproduced from Ref. 57.	14

Figure 2.1. An illustration of attaching a redox active (ra) group onto a system (A) to accelerate the conversion to the product (B) upon electron transfer (ET).	17
Figure 2.2. Proposed mechanism of the catalytic electron transfer cycle.	18
Figure 2.3. DFT calculations using B3LYP/6-31G* to model the relative energy differences between the <i>E</i> isomer, the <i>Z</i> isomer, and the inversion transition state of methyl yellow (3).	19
Figure 2.4. DFT calculations using B3LYP/6-31G* to model the relative energy differences between the <i>E</i> isomer, the <i>Z</i> isomer, the <i>N</i> -inversion transition state, and the rotation N-N twisted transition state of methyl yellow radical cation (3⁺), demonstrating a large reduction in the energy barrier upon a single electron loss at the ra moiety.	20
Figure 2.5. The nitrogen atom of the ra⁺ unit is half-filled and forms a pi-bond with the proximal singly-occupied N azo p-orbital at the N,N twisted transition state of methyl yellow radical cation (3⁺).	21
Figure 2.6. Target aryl-amino(azobenzene) compound 11 (AA-AB).	22
Figure 2.7. Optical spectra of 11 (5.7×10^{-5} M) in deaerated benzene in a 1.0 cm quartz cuvette.	25
Figure 2.8. Optical spectra of 11 (6.37×10^{-4} M) in deaerated benzene-d ₆ in a 0.1 cm quartz cuvette shown before irradiation (red) and following under 430 nm LED light irradiation until PSS _{430 nm} (blue) was achieved.	26
Figure 2.9. ¹ H-NMR spectroscopy of 11 showing the methoxy peaks between 3-4 ppm. Left shows the spectrum sample pre-irradiation. Right shows the spectrum of the sample at PSS _{430 nm} with a <i>Z</i> : <i>E</i> ratio of 77:23.	27
Figure 2.10. Optical spectra of 11 (6.4×10^{-4} M) in deaerated benzene-d ₆ in a 0.1 cm quartz cuvette starting at PSS _{430 nm} (red), following <i>Z</i> → <i>E</i> isomerization in the dark at 25°C until only <i>E</i> - 11 (purple) remains.	29
Figure 2.11. Cyclic voltammogram of 3 at 1.0 mM in purified dichloromethane and 0.10 M TBABF ₄ electrolyte gave an E _{p,a} of 1.11 V vs. SCE at 100 mV/s. Cyclic voltammogram of 1 at 1.0 mM in purified dichloromethane and 0.10 M TBABF ₄ electrolyte gave an E _{p,a} of 1.21 V vs. SCE at 50 mV/s. Cyclic voltammogram of 11 at 1.0 mM in purified dichloromethane and 0.10 M TBABF ₄ electrolyte gave an E° of 0.88 V vs. SCE at 50 mV/s. A platinum disc working electrode and platinum wire counter electrode were used.	31
Figure 2.12. Optical spectra of 11 (6.37×10^{-4} M) in deaerated benzene-d ₆ in a 0.1 cm quartz cuvette at PSS _{430 nm} (blue) is injected with 1 mole % CRET (18) (6.3×10^{-5} M in dichloromethane) at rt to return the <i>E</i> -isomer (red).	33
Figure 2.13. (a) Photo-electro device (PED) designed by Blackstock and coworkers to test the impact an applied voltage has on the redox appended azobenzene analogues. (b) Blackstock and Melody were able to show an automated photo-electrochromic cycling of the 11 system for more	

than 250 cycles by toggling between irradiation with 430 nm LED and applying a voltage of 1.5 V.⁷⁵..... 35

Figure 2.14. Proposed mechanism of electron transfer cycle upon excitation of **MB** with red light to its singlet excited state (S_{MB}^*), which relaxes to its triplet excited state (T_{MB}^*) before oxidizing the redox amine. The resulting doublet excited state (D_{MB}^\bullet) behaves as a reducing agent returning to its singlet ground state. The $E \rightarrow Z \rightarrow E$ cycle can then continue by irradiating your system with blue light for $E \rightarrow Z$ isomerization..... 37

Figure 2.15. Optical spectra of **11** (3.0 mL; 5.51×10^{-5} M) and **MB (19)** (5 mole %; 65.00 μ L; 1.28×10^{-4} M) in deaerated 2.1% methanol:toluene in a 1.0 cm quartz cuvette at 25 °C. (left) Overlay of optical spectra of **11:MB** following $E \rightarrow Z$ isomerization under blue light irradiation to achieve PSS_{430 nm}. (right) Overlay of optical spectra of **11:MB** following $Z \rightarrow E$ isomerization under red light irradiation to excite MB. 39

Figure 2.16. Optical spectra of **MB (19)** (3.0 mL; 2.77×10^{-6} M) in deaerated 2.1% methanol:toluene in a 1.0 cm quartz cuvette at 25 °C. Optical overlays following for 10 minutes of red light irradiation (left) or blue light irradiation (right)..... 40

Figure 2. 17. Optical spectra of **11** (3.0 mL; 5.51×10^{-5} M) in deaerated 2.1% methanol:toluene in a 1.0 cm quartz cuvette at 25 °C. The spectra overlay is starting at PSS_{430 nm} and following the $Z \rightarrow E$ isomerization until PSS_{660 nm} is achieved after ~ 1 hour. The pre-irradiation spectra (dashed-grey) is included for comparison..... 41

Figure 2.18. Optical spectra of **11** (3.0 mL; 5.51×10^{-5} M) and **MB (19)** (5 mole %; 65.00 μ L; 1.28×10^{-4} M) in deaerated 2.1% methanol:toluene in a 1.0 cm quartz cuvette at 25 °C. The spectra overlay is starting at PSS_{430 nm} and following the $Z \rightarrow E$ thermal isomerization after ~ 4 hours..... 42

Figure 2.19. The $E \rightarrow Z \rightarrow E$ cycling of **11** (5.51×10^{-5} M) and 5% **MB** (injection of 65.0 μ L of 1.28×10^{-4} M) in deaerated 2.1% methanol in toluene in a 1.0 cm quartz cuvette at 25 °C cycling from no light exposure, blue light exposure, no light exposure, and red light exposure to complete 10 cycles. The grey-dashed line shows the cycling of **11** in the absence of **MB** for 8 cycles. After toggling light sources, the solutions are followed while left in the dark until 60 minutes in total passed..... 43

Figure 2.20. Optical spectra of **11⁺PF₆⁻** (~ 1 mM) in deaerated dichloromethane in a 0.1 cm quartz cuvette at 25 °C..... 45

Figure 2.21 Pulsed EPR spectrum of **11⁺PF₆⁻** (1 mM) in purified and distilled dichloromethane taken on a Bruker ELEXSYS E680 EPR spectrometer at 293 K. 46

Figure 3.1. Target compounds 20 and 21..... 61

Figure 3.2. Optical spectrum of **20** in benzene (2.3×10^{-5} M) in a 1.0 quartz cuvette at room temperature. 65

Figure 3.3. Optical spectra overlay of 20 (2.3×10^{-5} M in benzene) while irradiating with 457 nm light in a 1.0 quartz cuvette at room temperature. Following from <i>E,E</i> - 20 to PSS _{457 nm} , with two isosbestic points seen at 312 and 528 nm.	66
Figure 3.4. ¹ H-NMR spectrum of 20 in benzene-d ₆	68
Figure 3.5. Methoxy region of the ¹ H-NMR spectra of 20 in benzene-d ₆ before and after irradiation to PSS _{457 nm}	68
Figure 3.6. The optical spectrum of <i>E,E</i> - 21 in deaerated benzene (6.6×10^{-5} M in a 1.0 cm quartz cuvette at room temperature).....	69
Figure 3.7. Structures of parent fluorinated azobenzene (27), ³ redox appended fluorinated azobenzene (28), ² and target bis-system (21).	70
Figure 3.8. Optical spectra overlay following the irradiation of <i>E,E</i> - 21 in deaerated benzene with 457 nm light from <i>E,E</i> - to PSS _{457 nm} using a 1.0 cm quartz cuvette at room temperature.	71
Figure 3.9. ¹ H-NMR spectrum of 21 in chloroform-d ₁	71
Figure 3.10. Methoxy region of the ¹ H-NMR spectra of 21 in benzene-d ₆ before and after irradiation to PSS _{457 nm} . The isomer peaks are identified as color coded: <i>E,E</i> -(black), <i>E,Z</i> - (red), <i>Z,Z</i> - (purple).	72
Figure 3.11. Isomer concentration versus time for 20 following from PSS _{457 nm} → <i>E,E</i> - 20 as determined using dynamic ¹ H-NMR spectroscopy at room temperature. The data is modeled using a 2-step consecutive rate law. The isomers are identified as color coded: <i>E,E</i> -(black), <i>E,Z</i> - (red), and <i>Z,Z</i> - (blue).	74
Figure 3.12. Isomer concentration versus time for 21 (9.61×10^{-3} M) in deaerated C ₇ D ₈ following from PSS _{457 nm} → <i>E,E</i> - 21 (at 59, 71, 87, and 101 °C) as determined using ¹ H-NMR spectroscopy. The data is modeled using a 2-step consecutive rate law. The isomers are identified as color coded: <i>E,E</i> -(blue), <i>E,Z</i> - (green), and <i>Z,Z</i> - (red).	77
Figure 3.13. Eyring plot of ln(k/T) vs. 1/T for 21 (9.61×10^{-3} M) in deaerated C ₇ D ₈ , where k ₁ (red) is the rate constant for <i>Z,Z</i> - 21 → <i>E,Z</i> - 21 and k ₂ (blue) is the rate constant for <i>E,Z</i> - 21 → <i>E,E</i> - 21 thermal isomerization at a given absolute temperature, T, in Kelvins. ¹ H-NMR spectroscopic measurements were taken in the dark using an NMR tube, and the temperature was controlled using a hot oil bath.	78
Figure 3.14. An overlay of the cyclic voltammograms of 20 (top) and 21 (bottom). Cyclic voltammogram of 20 at 1.0 mM in purified dichloromethane and 0.10 M TBABF ₄ electrolyte gave an E° of 0.92 V vs. SCE. The scan rate was 25 mV/s. Cyclic voltammogram of 21 at 1.1 mM in acetonitrile (LC-MS grade) and 0.10 M TBABF ₄ electrolyte gave an E° of 1.31 V vs. SCE. The scan rate was 50 mV/s. A platinum disc working electrode and platinum wire counter electrode were used.	79

Figure 3.15. Optical spectra overlay of 20 at PSS _{457 nm} in benzene (3.00 x 10 ⁻⁵ M) taken prior to irradiation, after irradiation at thje 457 nm PSS, and after the addition of 1.0 mol% oxidant CRET and shaking for 2 seconds in a 1.0 cm quartz cuvette at room temperature.	80
Figure 3.16. Optical spectra overlay of 21 at PSS _{457 nm} in benzene (6.6 x 10 ⁻⁵ M) followed by the addition of 15 % CRET to return the <i>E,E</i> -isomer in a 1.0 cm quartz cuvette at room temperature.	81
Figure 3.17. Photo,photo-electro cycling of 20 (3.58 x 10 ⁻⁵ M) and 5% MB (injection of 60.0 μL of 8.95 x 10 ⁻⁵ M) in deaerated 2% methanol in toluene in a 1.0 cm quartz cuvette at 25 °C, following alternating cycles of blue then red light irradiation to toggle between <i>E</i> → <i>Z</i> → <i>E</i> isomers with blue light exposure for 1 minute and red/no light exposure for 30 seconds for 15 cycles. ..	83
Figure 4.1. Target <i>N,N,N</i> -tris(azobenzene)amine compound 29 (TA).	96
Figure 4.2. Mounted crystal and crystal structure of 29 illustrating the three-blade propellar shape of the azobenzene units around the amine center (green dihedral angles). The twisting dihedral angles (red) between the phenyl ring of each azobenzene moiety.	99
Figure 4.3. (Top) Crystal structure illustrating the packing at the unit cell veiwing down the three axes (a,b, and c). (Bottom) Space-filling modeling the packing viewed down the b-axis.	100
Figure 4.4. Optical spectrum of 29 in benzene (3.3 x 10 ⁻⁵ M) in a 1.0 quartz cuvette at room temperature.	101
Figure 4.5. Optical spectra overlay of 29 (3.3 x 10 ⁻⁵ M in benzene) while irradiating with 457 nm light in a 1.0 quartz cuvette at room temperature. Following from <i>E,E,E</i> - 29 to PSS _{457 nm} , with three isosbestic points seen at 310, 374 and 518 nm.	102
Figure 4.6. ¹ H-NMR spectrum of <i>E,E,E</i> - 29 in benzene-d ₆	103
Figure 4.7. Methoxy region of the ¹ H-NMR spectra of 29 in benzene-d ₆ pre- and post-irradiation to PSS _{457 nm}	104
Figure 4.8. Optical spectrum of the thermal <i>Z</i> → <i>E</i> isomerization of 29 (5.15 x 10 ⁻⁵ M in benzene) at rt in the dark starting from PSS _{457 nm} in a 1.0 cm quartz UV-vis cell.	105
Figure 4.9. Isomer composition, determined by ¹ H-NMR spectroscopy in bezene-d ₆ , starting at PSS _{457 nm} to follow the thermal decay of <i>Z,Z,Z</i> → <i>E,Z,Z</i> - 29 (green); <i>E,Z,Z</i> → <i>E,E,Z</i> - 29 (purple); <i>E,E,Z</i> → <i>E,E,E</i> - 29 (red); and thermal growth of <i>E,E,E</i> - 29 (black) over time.	107
Figure 4.10. Cyclic voltammogram of 29 at 1.0 mM in purified dichloromethane and 0.10 M NBu ₄ PF ₆ electrolyte gave a redox potential of 1.04 V vs. SCE. Scan rate was 20 mV/s with a 90 mV peak separation.	108

Figure 4.11. Optical spectra overlay of **29** at PSS_{457 nm} in benzene (3.3×10^{-5} M) followed by the addition of 2.0 mole % CRET to return the *E,E*-isomer in a 1.0 cm quartz cuvette at rt. 109

Figure 4.12. Photo, Photo-Electro cycling of **29** (2.9×10^{-5} M) and 9.9% **MB** (injection of 100 μ L of 8.91×10^{-5} M **MB**) in deaerated 3% methanol in benzene in a 1.0 cm quartz cuvette at rt. The solution is irradiated with alternating cycles of blue then red light to toggle between *E*→*Z*→*E* isomers with blue/red light exposure for 1 min and no light exposure for 30 s for ten cycles..... 111

Figure 4.13. Benzene solutions of **20** (red-orange), **29** (red-orange), **TCNE** (colorless), and **DDQ** (yellow). The resulting mixed solutions of **20**+**TCNE** and **20**+**DDQ** (Top) or **29**+**TCNE** and **29**+**DDQ** (Middle) to illustrate any solution color changes with mixing. (Bottom) Dark blue-green solid formed for **DDQ** combinations, with crystals forming by slow evaporation for **29**/**DDQ**..... 115

Figure 4.14. Crystal structure of the **29**•**DDQ** complex illustrating the packing of the asymmetric unit cell. (bottom) Short contacts interactions between the **29**•**DDQ** complex..... 116

Figure 5.1. The *E* and *Z* isomer of stilbene (**36**) achieved photochemically. 127

Figure 5.2. (Left) The electronic absorption spectra of *E*-**36** (solid line) and *Z*-**36** (dashed line). Figure reproduced from Ref. ¹⁰⁴. (Right) Stilbene (**36**) potential energy diagram for *E* and *Z* isomers with a *Z*→*E* activation energy barrier of 46 kcal mol⁻¹..... 127

Figure 5.3. Optical spectra of **37** (5.7×10^{-5} M) in deaerated 2 % benzene in cyclohexane in a 1.0 cm quartz cuvette shown before irradiation (red) and following under 430 nm LED light Irradiation until PSS_{430 nm} (black-dashed) is achieved..... 129

Figure 5.4. Optical spectra of **37** (5.4×10^{-5} M) and **MB** (**19**) (5 mole %, 2.7×10^{-6} M) in deaerated 5% methanol:toluene in a 1.0 cm quartz cuvette at rt. Overlay of optical spectra of **36**:**MB** starting at PSS_{430nm} following under red light irradiation to excite **MB**..... 130

Figure 5.5 Target bis(stilbene) compounds *E,E*-**38** and *Z,Z*-**38**..... 131

Figure 5.6. Optical spectra overlay of **45** (5.2×10^{-5} M), **11** (5.5×10^{-5} M), and **37** (5.7×10^{-5} M) each in deaerated benzene in a 1.0 cm quartz cuvette at rt. 135

Figure 5.7. Optical spectra of *E,E*-**45** (5.2×10^{-5} M) in deaerated benzene in a 1.0 cm quartz cuvette shown before irradiation (red) and following under 457 nm LED light irradiation until PSS_{457 nm} (black) was achieved..... 137

Figure 5.8. ¹H-NMR spectroscopy of **45** showing the methoxy peaks between 3-3.5 ppm. Left shows the spectrum sample pre-irradiation. Right shows the spectrum of the sample at PSS_{457 nm} with a *E,Z*_{azo}-**45** to *E,E*-**45** of 68:32. 138

Figure 6.1. The chemical structure of alternate photooxidants New Methylene Blue N and Methylene Green..... 148

Figure 6.2. The envisioned model for host guest interactions using a bis-system such as **21**. A space-filling model of the *Z,Z*-isomeric state is shown to the right to highlight the electron rich cavity that can form.. 149

Figure 6.3. The envisioned photoredox $E \rightarrow Z \rightarrow E$ cycling of **45** with the stilbene flexor held in the *Z* isomeric state. 150

LIST OF SCHEMES

Scheme 2.1. Oxone oxidation of 12 to nitrosobenzene 13 , and Mills condensation of 13 and 14 to yield the azobenzene 15	23
Scheme 2.2. BHA coupling reactions to produce target AA-AB 11	23
Scheme 3.1. Synthesis of nitrosobenzene 23 using OXONE oxidation in a biphasic solution of dichloromethane and water. The Mills condensation reaction using trifluoroacetic acid (TFA) and dichloromethane (DCM) to generate the unsymmetrical azobenzene 25	62
Scheme 3.2. Buchwald-Hartwig Coupling of 14 and 15 using bis(dibenzylideneacetone)palladium (0) (Pd(dba) ₂), tri- <i>tert</i> -butylphosphine (P(<i>t</i> Bu) ₃), and sodium <i>tert</i> -butoxide at 111 °C in an oil bath under N ₂ atmosphere yielding 20	62
Scheme 3.3. Buchwald-Hartwig Coupling of 14 and 25 and using bis(dibenzylideneacetone)-palladium(0) (Pd(dba) ₂), 1,1'-bis(diphenylphosphino)-ferrocene (dppf), and cesium carbonate(Cs ₂ CO ₃) at 111 °C in an oil bath under N ₂ atmosphere yielding 26 . Followed by a second coupling of 14 and 26 under the same conditions to yield the target, 21	64
Scheme 4.1. Oxone oxidation of 30 to nitrosobenzene 31 , Mills condensation of 31 and 14 to yield the azobenzene 32 , followed by reduction to 4-amino-4'-methoxyazobenzene (33).	97
Scheme 4.2. BHA coupling of 33 and 15 to yield the target tris(azobenzene)- 29	97
Scheme 4.3. Donor-acceptor co-crystallization building blocks. The donor components left (20 and 29) and the acceptor components (TCNE and DDQ).	114
Scheme 5.1. Substitution reaction between 39 and 40 to produce target phosphonium salt 41 . Wittig reaction conditions between 41 and 42 to yield stilbene target (<i>E/Z</i>)- 43	132
Scheme 5.2. BHA coupling conditions and synthetic route to produce target compound <i>E,E</i> - 38 and <i>Z,Z</i> - 38	133
Scheme 5.3. BHA coupling conditions and synthetic route to produce target compound 44 and target compound <i>E,E</i> - 45	134

CHAPTER 1.

INTRODUCTORY OVERVIEW OF AZOBENZENES

1.1. Introduction

Azobenzene photoisomerization is a particularly useful photo-switchable system as molecular machines, with clean and efficient (high quantum yield) photoisomerization. Molecular machines contain switchable units that control the molecule's structure and function. These switchable units are typically responsive to external stimuli such as heat, cation addition, pH changes, pressure, and light.¹⁻⁴ Light is a highly efficient external stimulus, producing no byproducts, for photoactive compounds like azobenzene. Azobenzenes are one example of photoactive compounds that are known for rapid, reversible photoisomerization. This efficiency makes azobenzene ideal for switching, sensing, and optical data storage devices.

Azobenzenes consist of two phenyl rings attached by an azo linkage (-N=N-), and they were first reported in 1834 by Eilhard Mitscherlich.⁵ It was not until 1937, more than 100 years later, that Hartley first reported the existence of the two, *E* and *Z*, isomeric forms.⁶ The *E* and *Z* stereoisomers of azobenzene can be interconverted using distinct wavelength irradiation to induce *E*→*Z* or *Z*→*E* photoisomerization (Figure 1.1).⁶⁻⁹ Azobenzene systems are highly pigmented, usually orange to red, and widely used as dyes. However, these dynamic photoactive compounds have found a broad range of materials applications as photoactive devices¹⁰ in areas of organometallic catalysis,^{11,12} photomechanics,¹³ liquid-crystalline polymers,¹⁴ and biological molecular switches.¹⁵

Most of these applications take advantage of the large structural change that occurs for *E* or *Z* isomerization. The planar *E*-azobenzene (*E*-1) isomer has C_{2h} symmetry¹⁶ and is thermodynamically favored over the *Z*-azobenzene (*Z*-1) isomer by 10-13 kcal mol⁻¹.¹⁷⁻²¹ The non-planar *Z*-isomer has phenyl rings twisting 53° out of the C-N=N-C plane with C_2 symmetry,²² decreasing the distance between the *para* H of the phenyl groups from 9.1 Å (*E* form) to 6.1 Å (*Z* form) (Figure 1.1).⁹ This geometry change between the isomers mimics a hinge-like reorientation with the moving ring having an 8.5 Å net displacement measured at the *para*-phenyl proton. This geometry change also causes *E*-1, which has no net dipole, to transform to a polar *Z*-1 form having a dipole moment of 3 Debye.⁹

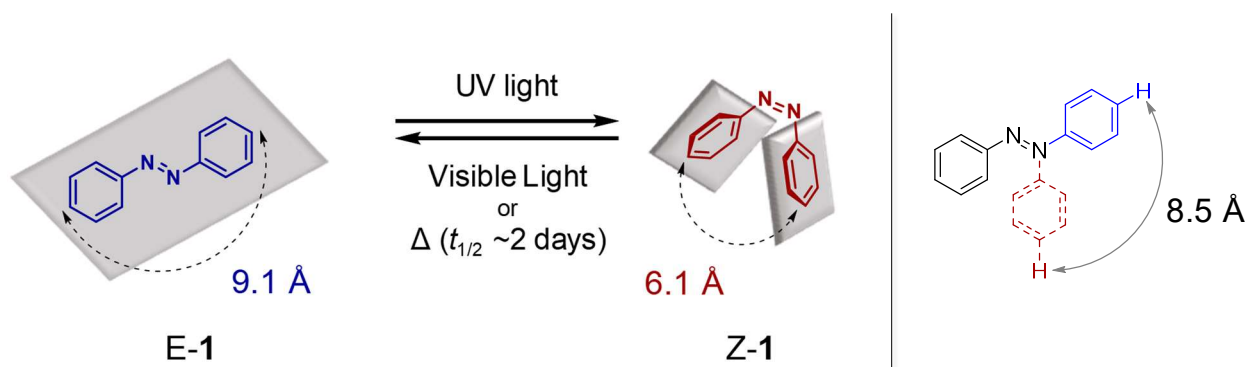


Figure 1.1. The *E* and *Z* isomers of azobenzene (**1**) achieved photochemically or thermally.

1.2. Electronic Structure of Azobenzene

Azobenzenes have two absorbance bands in the UV-visible region belonging to π - π^* and n - π^* transitions as seen in Figure 1.2 and are photochromic, as the *E* and *Z* isomeric forms have different optical spectra. The optical spectrum of *E*-1 has a strong π - π^* absorption band in the ultraviolet (UV) region (~ 320 nm, $\epsilon \sim 27,000$ L mol⁻¹ cm⁻¹) and a weaker, symmetry forbidden n - π^* absorption band in the visible region (~ 440 nm, $\epsilon \sim 950$ L mol⁻¹ cm⁻¹). In contrast, *Z*-1 has a

slightly blue shifted π - π^* band with decreased intensity (~ 280 nm, $\epsilon \sim 7,100$ L mol⁻¹ cm⁻¹) and an increased n- π^* band intensity (~ 436 nm, $\epsilon \sim 2,200$ L mol⁻¹ cm⁻¹) (Figure 1.2).²³

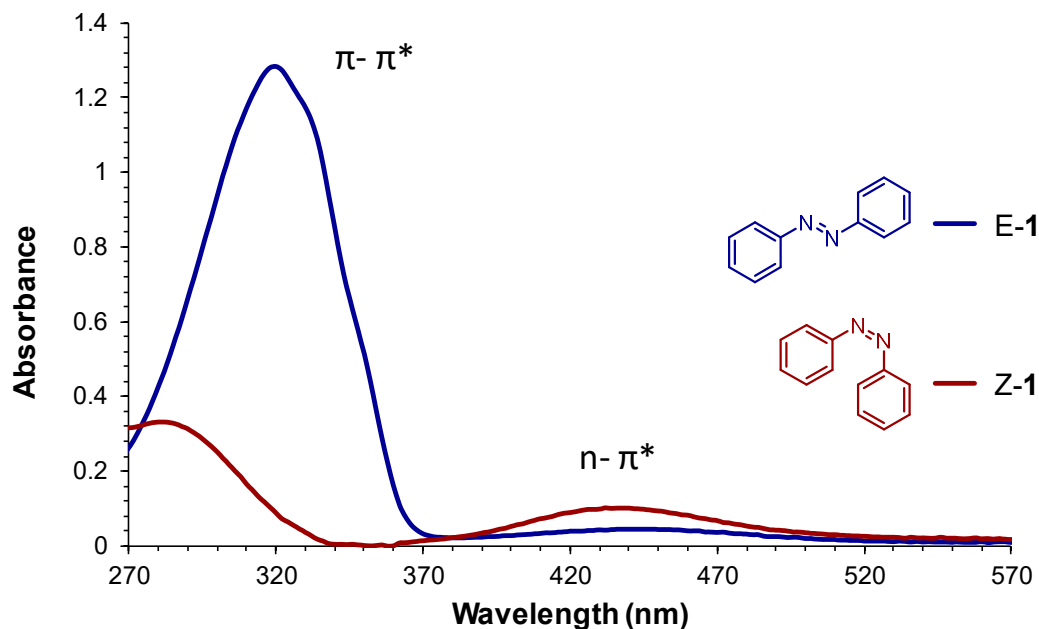


Figure 1.2. The absorption spectra of E-1 (blue) and Z-1 (red) from a solution of 4.7×10^{-4} M **1** in CDCl₃ using a 0.1 cm quartz cuvette.²³

The π - π^* and n- π^* electronic transitions for azobenzene are depicted in the molecular orbital energy diagram in Figure 1.3. The highest occupied π orbital is the HOMO-1. For E-1, absorbance around the 320 nm UV region excites an electron to the lowest unoccupied molecular orbital (LUMO, π^*), which is the second excited state, $S_2(\pi\pi^*)$. Similarly, absorbance around the 450 nm visible region excites an electron from the highest occupied molecular orbital (HOMO, n) to the π^* LUMO, generating the first excited state (S_1) of **1**. Both $S_1 \leftarrow S_0$ and $S_2 \leftarrow S_0$ excitation induce $E \rightarrow Z$ isomerization of E-1 upon relaxation to the ground state (S_0). Similarly, Z-1 undergoes $Z \rightarrow E$ isomerization upon $S_1 \leftarrow S_0$ and $S_2 \leftarrow S_0$ excitation.⁷

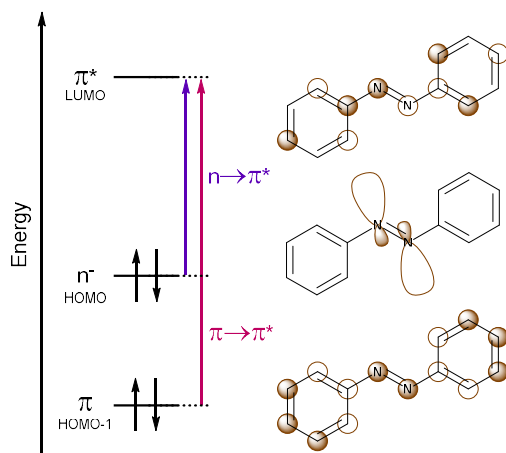


Figure 1.3. The frontier molecular orbital diagram of azobenzene (**1**) for HOMO-1 (π), HOMO (n), and LUMO (π^*) and the $n \rightarrow \pi^*$ (purple) and $\pi \rightarrow \pi^*$ (pink) electronic transition.

1.3. Photochemistry of Azobenzene

UV or visible light irradiation induces $E \rightarrow Z$ isomerization until a photostationary state (PSS) is achieved, which seldom gives complete conversion.²⁴ Instead, the PSS is a photo equilibrium point at which photoconversion of $E \rightarrow Z$ occurs at the same rate as $Z \rightarrow E$. Excitation at the stronger $\pi\text{-}\pi^*$ band of the E isomer produces a Z -rich PSS. The Z isomer has a stronger $n\text{-}\pi^*$ band than E -1, so excitation at this band converts a Z -rich mixture back to an E -rich PSS. Less band overlap between the E - and Z -isomers allows for greater conversion since band overlap means the excitation source is also irradiating the other isomer's $\pi\text{-}\pi^*$ or $n\text{-}\pi^*$ band. The $E:Z$ composition at PSS is dependent on the azobenzene substituents and reaction conditions, such as solvent, irradiation wavelength, and temperature.^{7, 25}

The respective $n\text{-}\pi^*$ and $\pi\text{-}\pi^*$ absorption bands excite azobenzene to $S_1(n\pi)$ and $S_2(\pi\pi^*)$ states. Excitation studies on the dependence of quantum yield (Φ) on solvent polarity and viscosity indicate that $Z \rightarrow E$ isomerization Φ from $n\text{-}\pi^*$ ($S_1 \leftarrow S_0$) excitation increases with solvent polarity, while $E \rightarrow Z$ isomerization Φ decreases. In contrast, polarity has no impact upon

π - π^* ($S_2 \leftarrow S_0$) excitation $E \rightarrow Z$ and $Z \rightarrow E$ conversions, and solvent viscosity did not impact these quantum yields. The temperature has a small impact on $E \rightarrow Z$ isomerization, while quantum yields for $Z \rightarrow E$ isomerization decrease with increasing temperature. The quantum yield sum for $E \rightarrow Z$ and $Z \rightarrow E$ isomerization ($\Phi_{E \rightarrow Z}$ and $\Phi_{Z \rightarrow E}$) do not equal unity, which suggests more than one mechanism path is operating. Unlike the photoisomerization of stilbene, which isomerizes only by bond rotation, the azobenzene photoisomerization mechanism is still debated with many contributing factors to consider.⁷

Four photoisomerization mechanisms have been proposed: rotation, inversion, inversion-assisted rotation, and concerted inversion. The rotation mechanism involves breaking the N=N π -bond, allowing free rotation about the remaining N-N bond while holding the N-N-C angle at $\sim 120^\circ$. The inversion mechanism involves, increasing the N=N-C angle to 180° while keeping the C-N=N-C dihedral angle at 0° , placing an azo nitrogen in an sp-hybridization state at the transition state. The concerted inversion mechanism involves a fully linear transition state with both N=N-C angles at 180° . The inversion-assisted rotation mechanism involves a large C-N=N-C dihedral angle change as the rotation mechanism with a smaller change in the N=N-C angle to assist. The transition states for each of the four mechanisms can afford both E and Z isomers, consistent with the formation of an E/Z mixture at the PSS.⁷

The isomerization mechanism varies depending on the solvent, excitation energy, and substituents. E -1 upon π - π^* excitation undergoes an inversion mechanism in hexanes (a non-viscous solvent) during $S_0 \leftarrow S_1 \leftarrow S_2$ relaxation, while n- π^* excitation proceeds by rotation during $S_0 \leftarrow S_1$ relaxation. Concerted inversion is observed during $S_0 \leftarrow S_1$ relaxation when in glycerol, carbon tetrachloride, and ethanol.⁷ Z -1 also undergoes rotation in hexanes during $S_0 \leftarrow S_1$ relaxation versus inversion during thermal relaxation. Substituents introduce steric and electronic

effects, causing concerted inversion or more than one path to dominate the isomerization mechanism.⁷

1.4. Thermal Isomerization of Azobenzene

While *Z*-1 can undergo photoisomerization to an *E*-rich state, it is not complete. The thermal activation barrier for *Z*→*E* conversion is 25.8 kcal mol⁻¹, allowing for *Z*→*E* isomerization in the absence of light at room temperature (Figure 1.4).^{26, 27} *Z*-1 has a half-life of 2-3 days under ambient conditions in the absence of oxygen.^{7, 26, 28, 29} The optimized geometries were found using DFT calculations with the B3LYP/6-31G* basis set as found to accurately reproduce the experimental geometry, activation barrier, and relative energies for *Z*- and *E*-1. The DFT results suggest an *N*-inversion mechanism.²⁸ While not a firm rule, many substituted azobenzenes favor inversion as the pathway for *Z*→*E* thermal isomerization. Rotation is more commonly seen when both electron withdrawing and electron donating groups are present on the phenyl rings.³⁰

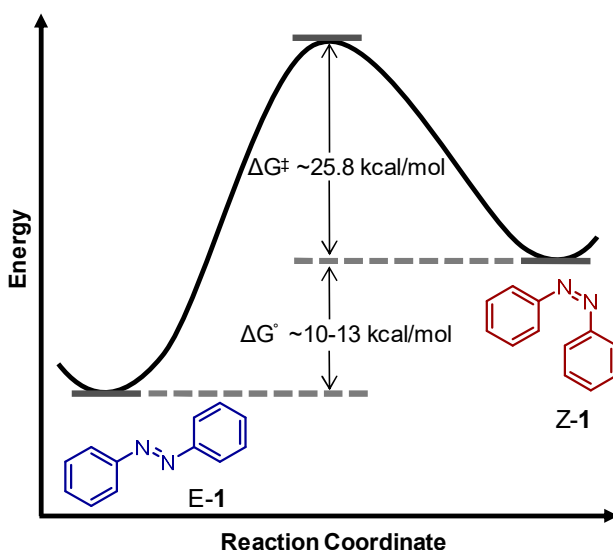


Figure 1.4. Azobenzene (1) potential energy diagram for *E* and *Z* isomers with a *Z*→*E* activation energy barrier of 25.8 kcal mol⁻¹.

Substituents have a large impact on the *Z*-isomer thermal lifetime. Tetra-*ortho*-substituted azobenzenes with MeO-, Br-, Cl-, or F- functional groups show significant impact on thermal *Z*-isomer half-lives with a half-life of up to 2 years at room temperature for 2,2',6,6'-tetrafluoroazobenzene.¹⁻⁴ Another long lived system is a xanthene based azobenzene dimer that is found to behave like a door-hinge with a *Z,Z*-isomer lifetime of 6.4 years and *Z,E*-isomer lifetime of 2.7 minutes.³¹ When the $\pi\text{-}\pi^*$ and $n\text{-}\pi^*$ absorption bands overlap, irradiation from *Z*→*E* is minimal, leaving the *Z*-isomer to relax thermally back to the *E*-isomer, which, depending on the system, can range from milliseconds to days.

1.5. Substitution Effects on the Absorption Spectra of Azobenzenes

UV light responsive azobenzenes are limited in many biological applications, since UV light damages biological components, does not deeply penetrate tissue, and causes damages to biological molecules by inducing photo oxidation or other UV stimulated side reactions. These limitations can be diminished by designing azobenzenes that are visible or near-infrared region responsive to *E*→*Z* switching, allowing for practical biological applications of azobenzenes¹⁵ like photocontrol of peptides,³²⁻³⁵ proteins,³⁶ enzymes,³⁷⁻³⁹ drug delivery,⁴⁰⁻⁴² and ion channels.⁴³⁻⁴⁶ Substituents on azobenzenes can cause a large shift in the absorption bands.^{12, 47} The addition of an electron donating group on an azobenzene red shifts the $\pi\text{-}\pi^*$ absorption band to the visible region causing it to partially overlap the $n\text{-}\pi^*$ band (Figure 1.5).^{7, 48} Having an electron donating and an electron withdrawing group on opposite phenyls has a push-pull electronic effect on azobenzene, further red shifting the $\pi\text{-}\pi^*$ absorption band to completely overlap the $n\text{-}\pi^*$ absorption band (Figure 1.5).^{47, 48} Additionally tetra-*ortho* substitution about the azo group of azobenzenes with MeO-, Br-, Cl-, or F- functional groups causes the $n\text{-}\pi^*$ absorption band of the *E* isomer to slightly red-shift and the *Z* isomer to separate the two $n\text{-}\pi^*$ absorption bands.¹⁻⁴ For

tetrafluoroazobenzene, this $n\text{-}\pi^*$ separation allows for $Z\rightarrow E$ and $E\rightarrow Z$ conversions with >500 nm and 410 nm excitation, respectively.⁴⁹

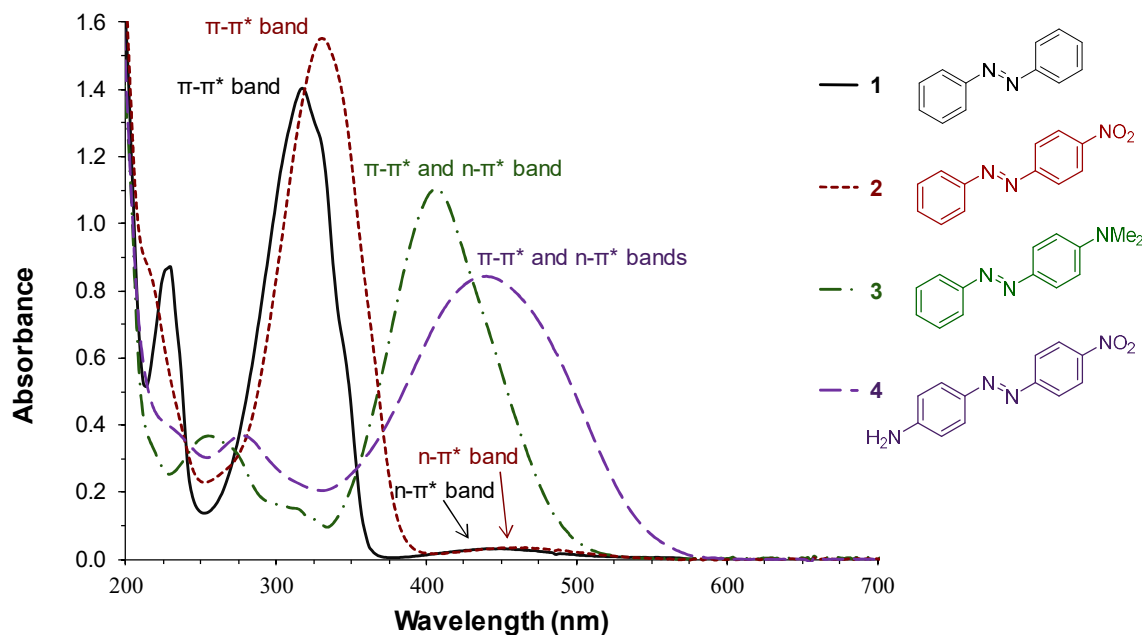


Figure 1.5. Absorption spectra overlay showing the impact of substitution to shift absorption band wavelengths. The spectra of **1** (black) at 6.12×10^{-4} M, **2** (red) at 5.90×10^{-4} M, **3** (green) at 4.62×10^{-4} M, and **4** (purple) at 5.75×10^{-4} M in ethanol are measured using a 0.1 cm quartz cuvette at room temperature.¹⁵

1.6. Multi-Azobenzene Systems

Macrocycle azobenzene systems (azobenzophanes) have shown promise in producing multi-responsive materials. A series of symmetric bis-, tris-, and tetra-azobenzophanes (**5-7**) were synthesized using dimethyl(methylene) linkers to minimize electronic coupling between azobenzene units (Figure 1.6). The isomer stability is dominated by ring strain in each azobenzophane, to the point that a reversal of thermodynamics occurs in the bis-system (**5**) making the *Z*-isomer more stable. The symmetric tris(azobenzene) macrocycle (**6**) was found to

selectively isomerize between 3 different states, showing potential for a 3-state responsive material. *E,E,E*-**6**, *E,Z,Z*-**6**, and *Z,Z,Z*-**6** isomers are achieved and reversibly generated starting from each state via a combination of irradiation (365 nm or 448 nm) or irradiation followed by heating at 80 °C (Figure 1.7). Similarly, multi-isomer states were achieved with the tetra-system (**7**), but with less persistence for the *Z*-rich states.⁵⁰

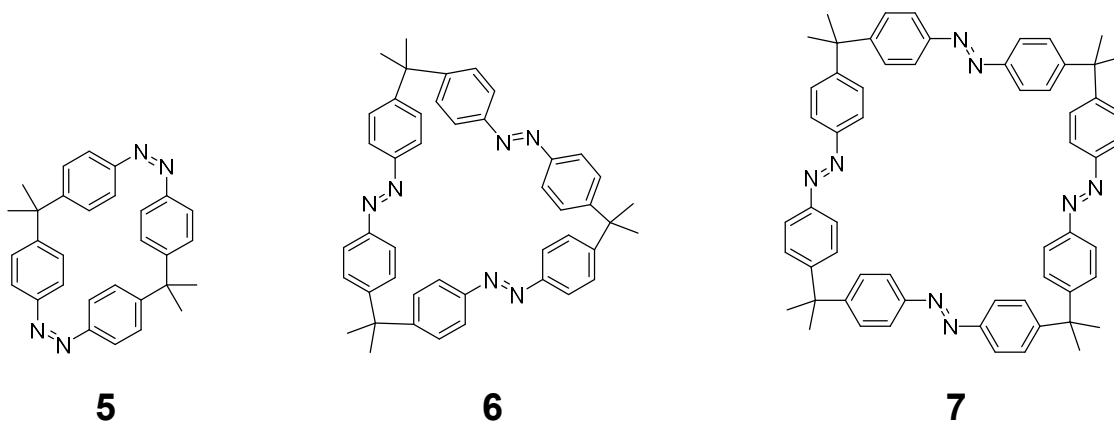


Figure 1.6. Symmetric bis-**5**, tris-**6**, and tetra-**7** azobenzophanes with dimethyl(methylene) linkers showing **5** in the all *Z*-state and **6** and **7** in the all *E*-states.⁵⁰

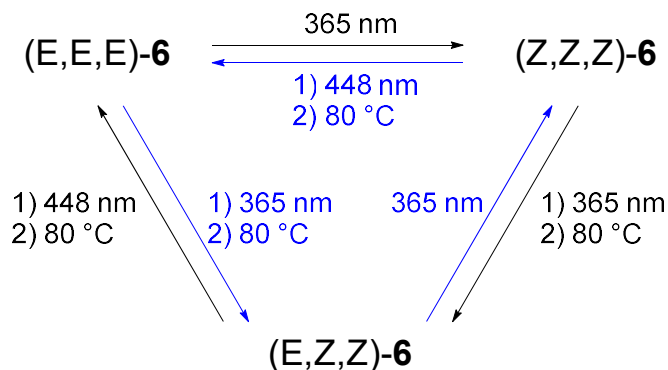


Figure 1.7. Three isomeric states (*E,E,E*-**6**, *E,Z,Z*-**6** and *Z,Z,Z*-**6**) are achieved by a combination of irradiation (365 nm or 448 nm) and heating from any of the other isomeric states.⁵⁰

Multiple azobenzene units can also be linked in a star-shaped fashion with a central linker. One such system (**8**) produced a rigid, pseudo-planar, C_3 -symmetric system via 1,3,5-substitution of a benzene core, effectively decoupling the three azobenzene units allowing for independent, simultaneous isomerization (Figure 1.8). The aim was to fabricate light responsive materials that self-assemble at a solid-liquid interface. The terminal *para* positions of the azobenzenes were substituted with carboxylic acid (COOH) groups, commonly used as organic non-covalent linkers in metal-organic and covalent-organic frameworks (MOFs and COFs). The COOH groups form strong, highly directional H-bonds, aiding in 2D and 3D self-assembly.⁵¹

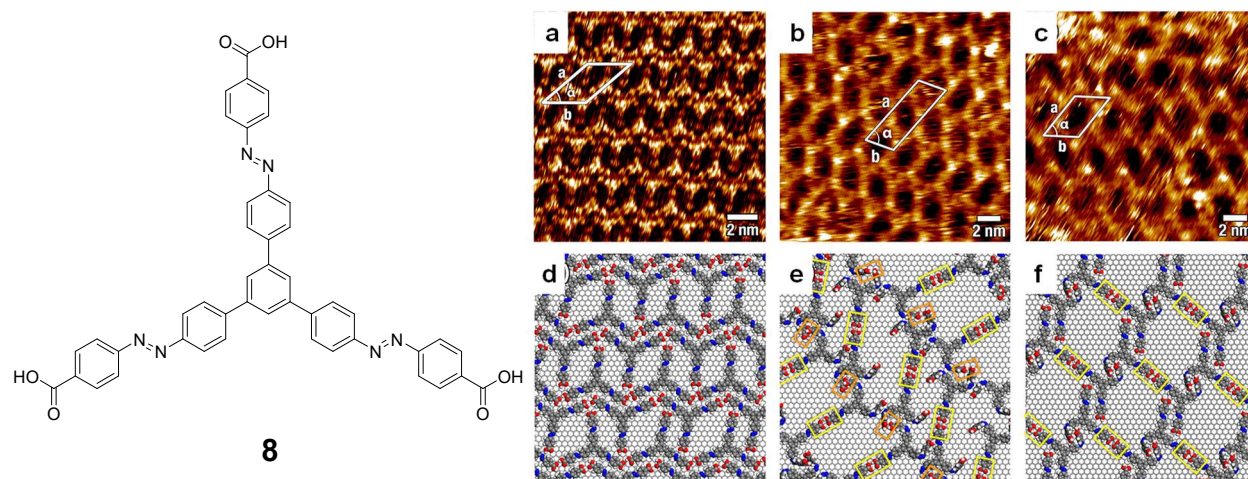


Figure 1.8. A pseudo-planar, C_3 -symmetric star-shaped azobenzene (**8**) capable of 2D crystalline self-assembly. High resolution STM images of self-assembled (a) *E,E,E*-**8**, (b) *E,Z,Z*-**8**, (c) *E,E,Z*-**8** at the solvent-surface interface (1-hepanoic acid - highly ordered pyrolytic graphite). The MM/MD simulations for each isomer are paired below in (d)-(f). The hydrogen bonded carboxylic acid dimers are indicated by yellow rectangles between *E* isomer arms and orange rectangles between *Z* isomer arms. Figure reproduced from Ref. 50.

Scanning tunneling microscopy (STM) can map the structure and dynamics of molecules on a surface at a sub-nm resolution. STM was recorded in situ at the graphite-solution interface.

The *E,E,E*-**8** isomer self-assembled into a tightly packed 2D crystalline lamellar, zigzag formation (Figure 1.8a). The tight packing favors the strong thermodynamic molecule-substrate interaction while lacking hydrogen bonding (O-H \cdots O) between the carboxylic acid groups. The variations from in situ STM upon irradiation with UV and visible light show that *E,Z,Z*-**8** and *E,E,Z*-**8** isomers have a change in geometry and unit cell parameters in the supramolecular packing. Large geometry changes upon azobenzene isomerization are observed extending from the highly rigid central linker, which allows for STM imaging. Both *E,Z,Z*-**8** and *E,E,Z*-**8** isomers form a less dense crystalline supramolecular packing stabilized by strong hydrogen bonds, balancing the less favorable molecule-substrate interactions (Figure 1.8b,c). With the *E,Z,Z*-**8** isomer, H-bonding also occurs between additional *Z* isomer arms. The PSS_(UV) has a *Z*-rich isomer composition of 63% *Z,Z,Z*-**8**, 30% *E,Z,Z*-**8**, 3% *E,E,Z*-**8**, and 4% *E,E,E*-**8**.⁵² *Z,Z,Z*→*E,E,E* thermal isomerization occurs via a step-wise process. The *Z,Z,Z*-**8** isomer could not be imaged by STM, likely because of the unfavored geometry limiting hydrogen bonding to stabilize self-assembly. STM was successful in imaging in high detail the existence of multiple isomeric states of tris(azobenzene) **8** and its surface assembly. The images were modeled by molecular mechanics/dynamics (MM/MD) simulations (Figure 1.8d-f). The varied self-assembly of **8** demonstrates the large role that non-covalent interactions and core molecular structure play in self-assembly and how the *E/Z* photoswitch can be used to trigger supramolecular structural change.^{51, 52}

Azobenzene derivatives have also been incorporated as ligands on metal-catalysts.^{11, 53-56} Bis(azobenzene) **9** can be ligated to a metal catalyst in the all *E* isomeric form (Figure 1.9). Here, the catalyst complex uses the electronics of the *E,E*-isomer, not its photoswitching property. The azobenzene moieties are N-donor ligands, which typically yield air stable, easier to synthesize,

and cheaper catalyst complexes compared to phosphine complex counterparts. The bis(azobenzene) **9** behaves as a CNN pincer ligand with a palladium(II) metal center.⁵⁷ The palladium-bis(azobenzene) complex (**9**•Pd) in Figure 1.9a is paired with one of four anionic coligands (acetato, chloro, bromo, or iodo). The **9**•Pd complex, using the iodo or acetato coligand, was successful as the catalyst in both Suzuki–Miyaura cross-coupling and Heck coupling reactions. Suzuki coupling using **9**•Pd (Figure 1.9b) gave a 93% yield with a high turnover number. Heck coupling with **9**•Pd (Figure 1.9c) produced up to an 86% yield.⁵⁷

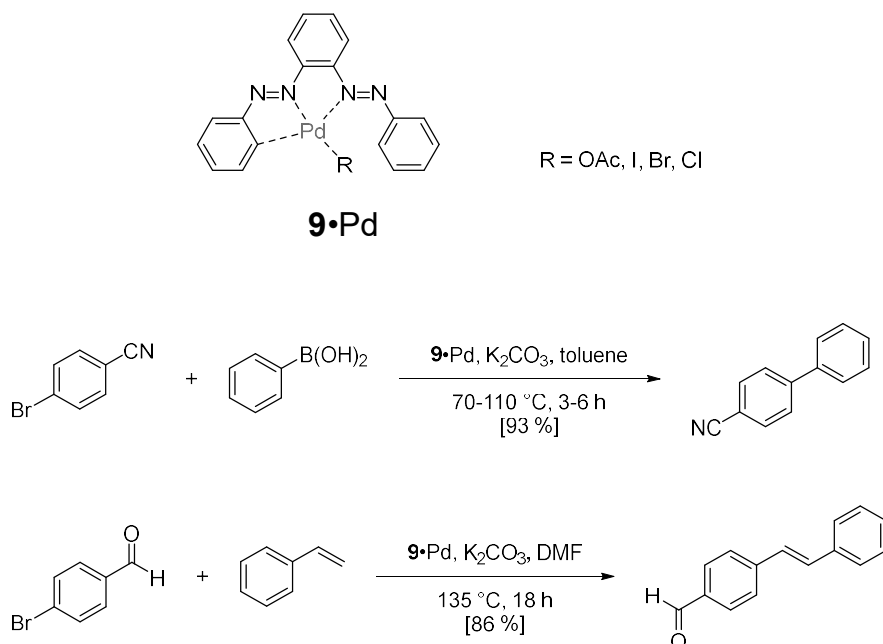


Figure 1.9. (a) The palladium-bis(azobenzene) complexes **9**•Pd. (b) Suzuki-Miyaura cross-coupling using **9**•Pd (R = OAc). (c) Heck coupling using **9**•Pd (R = I).⁵⁷

A tetrakis(azobenzene)methane star-shaped complex (**10a-c**) linked the azobenzene units in a tetrahedral fashion about a central carbon core (Figure 1.10).⁵⁸ The terminal *para* substituents were varied to observe the impact of increasingly bulky substituents on crystal packing. The Mills reaction produced each tetrahedral azobenzene system in ~70% yield from

tetrakis(4-aminophenyl)methane and an appropriately *para*-substituted nitrosobenzene. The crystals of tetrakis(azobenzene) **10a-c** had extrinsic porosity resulting only from the solid-state molecular packing, owing to the bulky azobenzene branches and molecular rigidity preventing tighter packing. The porosity allows for reversible *E*→*Z* photoisomerization in the solid state. The tetrakis(azobenzene) molecules pack along the four-fold improper rotation axes (Figure 1.11b), creating a large free volume channel from the side by side groups as modeled in Figure 1.11 (c,d). The unsubstituted terminal azobenzene system (**10a**) formed non-communicating channels with 6.7 % porosity, which is defined as the ratio of accessible volume by a 1.2 Å probe to cell volume. Methyl substituents (**10b**) produced empty channels along the c-axis with an 8.1% porosity. The bulkier *tert*-butyl functionalization (**10c**) formed the most defined empty channels with a 10.4% porosity, demonstrating that porosity increased with increasingly bulky substituents.⁵⁸

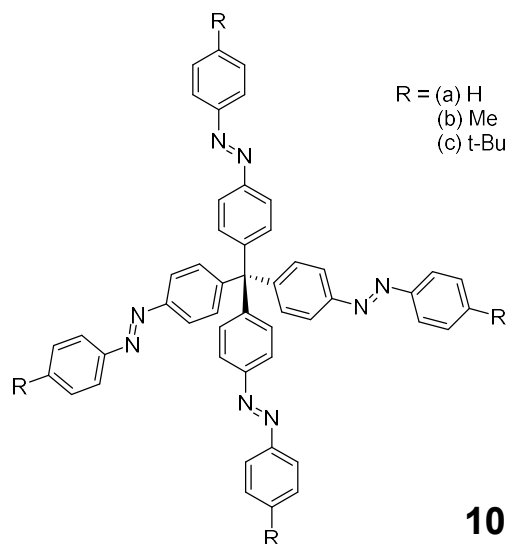


Figure 1.10. The tetrakis(azobenzene)methane (**10a-c**) structure with hydrogen (**10a**), methyl (**10b**), or *tert*-butyl (**10c**) groups at the terminal *para* positions.

A solution of **10c** in dichloromethane gave a total *Z* isomer content of 97% upon UV irradiation (365 nm). The composition at PSS₃₆₅ was 89% *Z,Z,Z,Z*-, 6% *E,Z,Z,Z*-, 3% *E,E,Z,Z*-, <1% *E,E,E,Z*-, and <1% *E,E,E,E*-**10c**. The solid-state absorption spectra and photoisomerization reactions were comparable to the solution results. The solid state photoisomerization was carried out on spin coated thin films with UV (365 nm) irradiation for 6 hours. A total 32% *Z*-isomer content is reached at the PSS_{365 nm} in the solid-state vs 97% in solution. Heating (or visible light) restored the rigid porosity and crystallinity, lost in the PSS *Z*-rich state, upon *Z*→*E* isomerization returning the *E,E,E,E*-isomeric state.⁵⁸

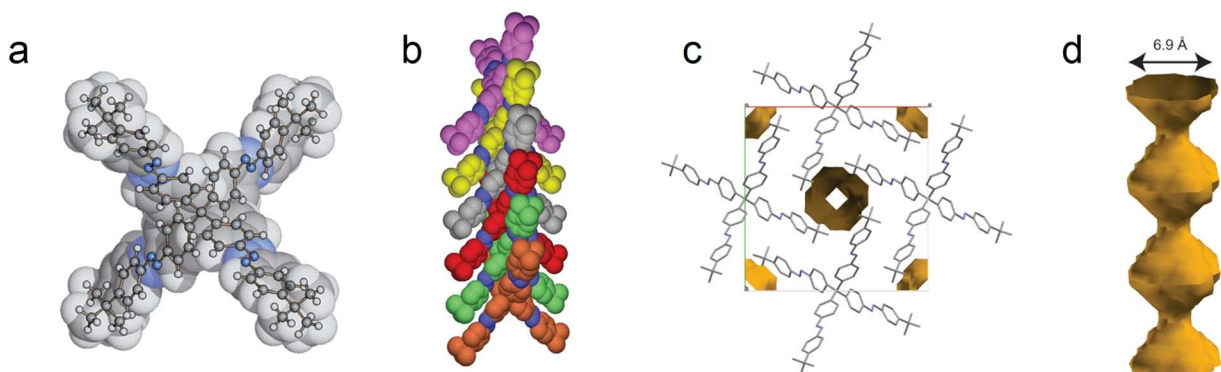


Figure 1.11. (a) The 3D tetrahedral structure of **10c**. (b) The tetrahedral **10c** structure stacking along the *c*-axis with each individual molecule differentiated by color. (c) Looking down the *c*-axis, the molecular piles form empty channels (yellow) extending down the *c*-axis. (d) A side view of an empty channel (yellow) formation without the molecules shown. Figure reproduced from Ref. 57.

The three analogues (**10a-c**) were also tested for gas adsorption ability. Negligible uptake was measured for **10a**, while both the **10b** and **10c** systems gave comparable CO₂ uptake with maximum uptake at four molecules of CO₂ per unit cell. Photoisomerization of the analogues to the *Z*-rich state gave negligible gas uptake in line with the porosity loss. Upon heating and restoration of the all *E*-state, CO₂ adsorption capacities were recovered. Reversible gas

adsorption is therefore achievable by irradiation to switch between porous and nonporous crystals. A mixed gas system of nitrogen and carbon dioxide also showed that the system has a selective affinity to adsorb CO₂.⁵⁸

1.7. Research Goals

The incorporation of azobenzene derivatives into a system creates light responsive materials, capable of achieving multiple isomeric states. The rapid and reversible photoisomerization of azobenzenes is ideal for photoregulation in biological systems, as well as, for modulating chemical reactivity and properties in materials. In our work, we have created and developed a new class of electro-active azobenzenes capable of fast, complete, and catalytic electro-stimulated $Z \rightarrow E$ conversion, along with the traditional $E \rightarrow Z$ photo conversion. The resulting derivatives, containing a linked aryl amine redox active group, are photo-electro responsive azobenzenes. My work focuses on evaluating photo-electro-transfer as a means of executing $Z \rightarrow E$ azobenzene electro catalysis of arylamino-azobenzene (Ch. 2), bis(azobenzene)-*p*-anisidine (Ch. 3), and tris(azobenzene)amine (Ch. 4), as well as, $Z \rightarrow E$ electro catalysis of stilbene incorporated bis-systems (Ch. 5).

CHAPTER 2.

PHOTO-ELECTRO-TRANSFER CATALYSIS OF REDOX AUXILIARY-MEDIATED AZOBENZENE

2.1. Introduction

The goal of this project is to control reaction rates via electron transfer (ET), specifically, by removing an electron from a redox auxiliary (**ra**) group attached to the reactive molecule. A **ra** group would ideally have minimal impact on the reaction while in the neutral state, but a large effect when an electron is removed, providing a ‘redox switch’ for reaction catalysis. Oxidation or reduction of the **ra** unit is anticipated to change the reaction energy barrier for the resulting radical cation or radical anion system. By design, the **ra** unit should be easy to oxidize (or reduce) and the radical cation (anion) state stable under ambient conditions. Aryl amines are one such robust redox active group. Figure 2.1 illustrates the concept. While the conversion of system **ra**-A to **ra**-B is a slow reaction, upon electron transfer, the conversion of the radical cation system **ra**^{•+}-A to **ra**^{•+}-B is fast, followed by reduction back to the neutral system. We are expecting this rate acceleration to derive from the stabilization of the reaction transition state by the **ra**^{•+} unit, lowering the activation energy barrier. In our case the system is azobenzene, and the reaction of interest is the slow *Z*→*E* isomerization.

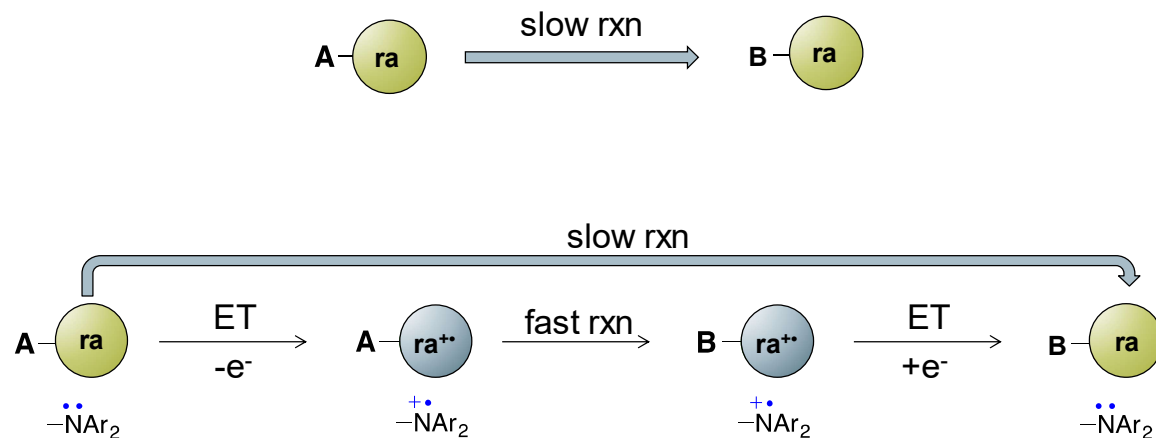


Figure 2.1. An illustration of attaching a redox active (**ra**) group onto a system (A) to accelerate the conversion to the product (B) upon electron transfer (ET).

Photoisomerization of *E*-azobenzene to the *E/Z* photostationary state (PSS) is a fast reaction occurring within seconds. While *E*→*Z* photo conversion is fast, *Z*→*E* thermal isomerization takes about 2 days in the dark in the absence of oxygen.^{7, 26, 28, 29} Blackstock and coworkers have successfully shown that attaching the electron rich redox-active dianisylamine **ra** group (An₂N-) to azobenzene allows efficient ET catalyzed *Z*→*E* isomerization.^{59, 60} The dianisylamine **ra** group is chosen because of its ease of oxidation and chemical stability in both its neutral and radical cation forms. Figure 2.2 shows the proposed ET catalyzed *Z*→*E* isomerization mechanism.

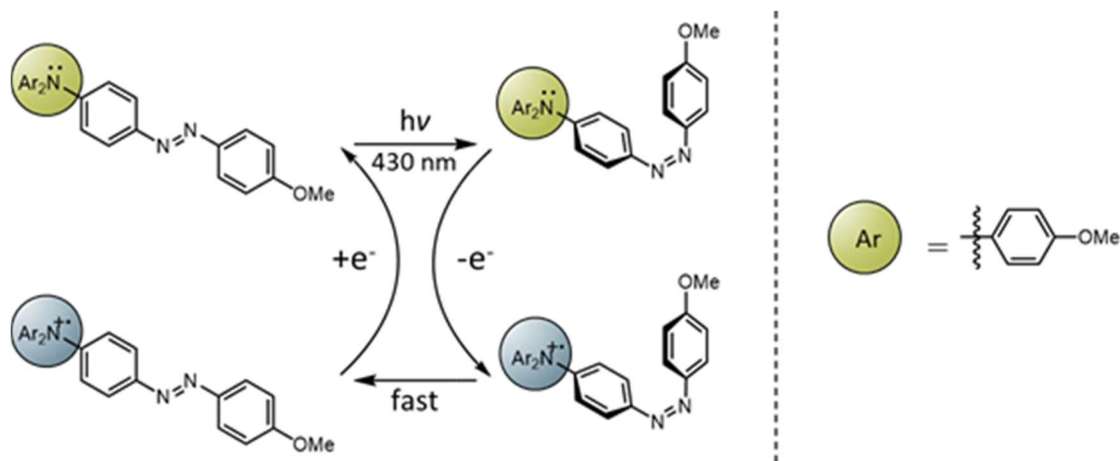


Figure 2.2. Proposed mechanism of the catalytic electron transfer cycle.

It is worth mentioning that work by Hecht and coworkers has shown that photo reduction of azobenzene in the presence of an iridium electron transfer agent effectively increases the $Z \rightarrow E$ isomerization rate via a one electron reduction mechanism.⁶¹ In this case the conversion is incomplete with at least 24% Z isomer still present in the final equilibrium mixture. The incomplete reaction results from competing photochemical reactions at the 365 nm excitation wavelength used. It is the photo-induced excited state of the iridium complex that reduces azobenzene to the radical anion. The excitation wavelength overlaps with the azobenzene chromophore, preventing complete E recovery due to competing $E \rightarrow Z$ photoisomerization. The proposed oxidative method is at an advantage with complete $Z \rightarrow E$ conversion accompanying the accelerated rate.

2.2. Theoretical Explanation of Redox Auxiliary-Mediated Azobenzene Isomerization

The **ra**-azobenzene $Z \rightarrow E$ conversion has the distinct advantage of being fast, catalytic, and complete when coupled with electron transfer. Figure 2.3 and Figure 2.4 shows the DFT calculated $Z \rightarrow E$ conversion of *N,N*-dimethyl-4-aminoazobenzene (methyl yellow, **3**) in the

neutral and radical cation state, and the significant difference in the transition state energies. The DFT calculations give a $Z \rightarrow E$ activation barrier of 23.79 kcal/mol for the neutral system **3**. The DFT theory (23.79 kcal/mol) has good agreement with the experimental energy barrier at 23.7 kcal/mol for neutral methyl yellow (**3**).⁶² The DFT calculations also give a $Z \rightarrow E$ activation barrier for the radical cation case $\mathbf{3}^{+\bullet}$ at 6.68 kcal/mol through an *N*-inversion mechanism and 1.83 kcal/mol through a rotation mechanism. The rotation mechanism experiences a 21.96 kcal/mol reduction in the $Z \rightarrow E$ activation barrier upon a single electron loss to form the radical cation $\mathbf{3}^{+\bullet}$, which translates to a rate acceleration of 1.3×10^{16} times faster than the $Z \rightarrow E$ conversion for neutral **3**. While the delocalization introduced by the **ra** unit compared to the -NMe₂ unit will likely decrease the degree of acceleration in the **ra**-azobenzene systems, this model calculation demonstrates the capability of a substantial rate enhancement in $Z \rightarrow E$ conversion upon an electron loss to form $\mathbf{ra}^{+\bullet}$ -azobenzene.

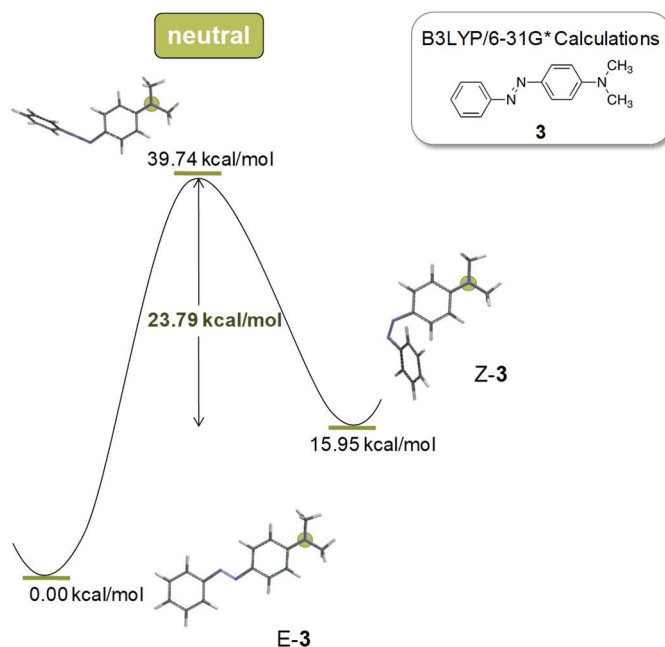


Figure 2.3. DFT calculations using B3LYP/6-31G* to model the relative energy differences between the *E* isomer, the *Z* isomer, and the inversion transition state of methyl yellow (**3**).

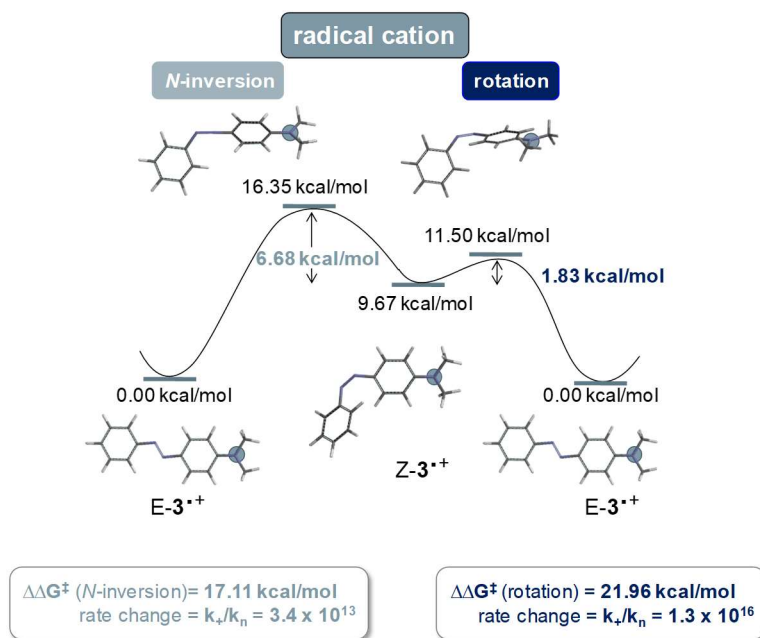


Figure 2.4. DFT calculations using B3LYP/6-31G* to model the relative energy differences between the *E* isomer, the *Z* isomer, the *N*-inversion transition state, and the rotation N-N twisted transition state of methyl yellow radical cation ($\mathbf{3}^{+\bullet}$), demonstrating a large reduction in the energy barrier upon a single electron loss at the **ra** moiety.

The predicted transition state for *Z*→*E* isomerization of neutral **3** involves inversion, while a single electron oxidation of the **ra** unit to form $\mathbf{3}^{+\bullet}$ is predicted to involve rotation. The isomerization of the neutral system **3** inverts the unsubstituted ring to avoid the higher energy cost of the filled-filled orbital overlap otherwise encountered during *N*-inversion (Figure 2.3). The accelerated *Z*→*E* isomerization for a **ra**⁺-azobenzene is hypothesized to occur from a stabilization at the azo unit (Figure 2.4) upon rotation to a N-N twisted transition state. Figure 2.5 illustrates for compound $\mathbf{3}^{+\bullet}$ a stabilizing interaction between the half-filled orbital of the **ra**⁺ nitrogen atom and the proximal singly occupied N azo p-orbital, which forms some pi-bond at the N-N twisted transition state.

Additionally, thinking of the two systems simply as a donor versus acceptor substituted azobenzene, the results agree to the quantum chemical study of $Z \rightarrow E$ isomerization of azobenzene by S. Hecht, P. Saalfrank, and coworkers.²⁹ They found that *para* or *ortho* acceptor substituents stabilize the HOMO of the transition state, while donors will have little impact. With theoretical calculations and literature supporting the hypothesis, the synthesis of amino appended azobenzene derivatives were produced and characterized.

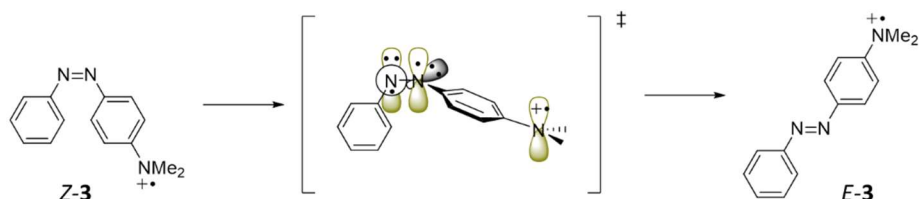


Figure 2.5. The nitrogen atom of the $ra^{+\bullet}$ unit is half-filled and forms a pi-bond with the proximal singly-occupied N azo p-orbital at the N,N twisted transition state of methyl yellow radical cation ($3^{+\bullet}$).

2.3. Redox $Z \rightarrow E$ Switching of Dianisylamine Appended Azobenzene

A variety of redox group appended azobenzene groups were synthesized and characterized by a previous group member, Carl J. Saint-Louis.⁶⁰ Substituent and ring placement alterations were made to compare the impact on radical cation stability and rate enhancement. Azobenzenes were synthesized with the dianisylamine appendage in the 2, 3, and 4 positions of the azobenzene phenyl group. In these structures, the 4' position was usually substituted with a methoxy group to aid in stabilization of the radical cation state. 4-Amino-(*N,N*-di-*p*-anisyl)-4'-methoxyazobenzene (**11**) is shown in Figure 2.6. An overview of the synthesis, $E \rightarrow Z$ characterization, $Z \rightarrow E$ characterization, and redox switching for **11** is reproduced and

summarized here in good agreement with original results by Dr. Saint-louis.⁶⁰ A novel photo, photo-electro switching system was then developed to trigger facile $E \rightarrow Z \rightarrow E$ conversion of **ra**-azobenzene systems like **11**.

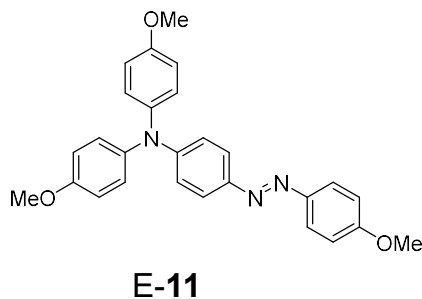
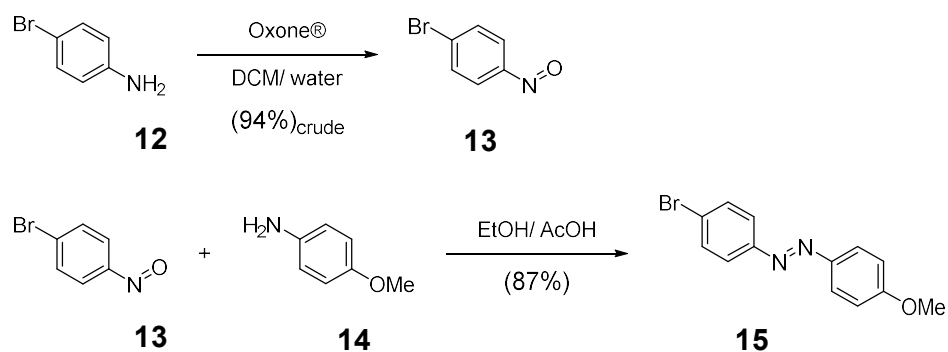


Figure 2.6. Target aryl-amino(azobenzene) compound **11** (AA-AB).

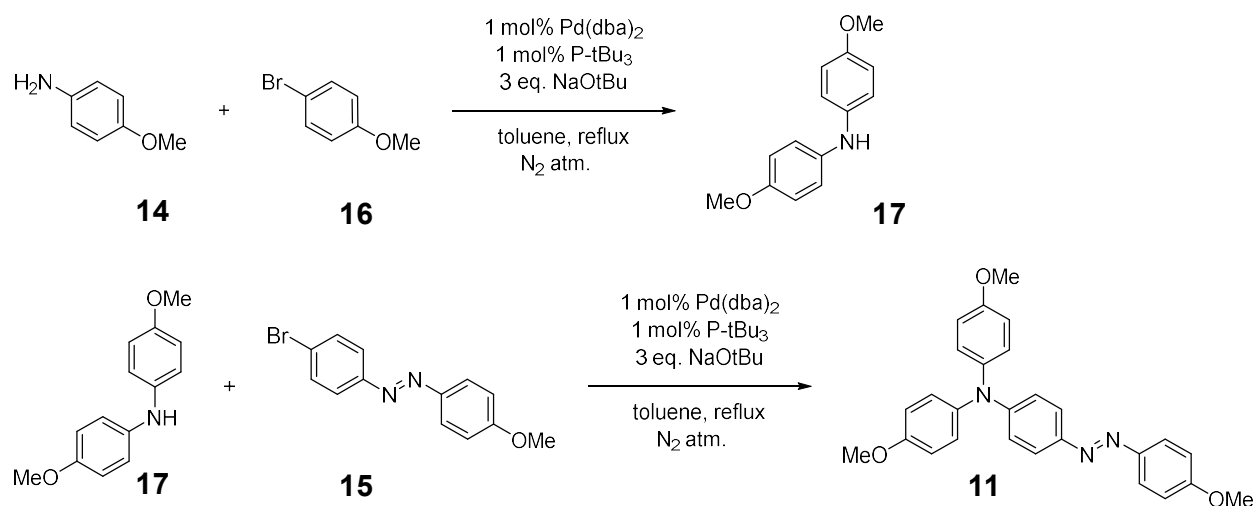
2.3.1. Synthesis of AA-AB (**11**)

Scheme 2.1 and Scheme 2.2 depict the synthetic route used to produce the target azobenzene **11**. We first generated 4-bromo-4'-methoxyazobenzene **15** via a Mills condensation^{8, 63} of *p*-bromo-nitrosobenzene **13** and *p*-anisidine **14**, the former formed by OXONE[®] (2KHSO₅•KHSO₄•K₂SO₄) oxidation⁶³ of *p*-bromoaniline **12**. The isolated crude nitrosobenzene **13** product is a beige solid (green solution) in 94 % crude yield and is used in the Mills Condensation reaction without further purification because **13** proved difficult to purify, and the two minor byproducts present (*p*-bromo-nitrobenzene^{64, 65} and 4,4'-dibromoazoxybenzene^{64, 66}) do not interfere with the subsequent step. Mills condensation reaction of **13** and **14** gave 4-bromo-4'-methoxyazobenzene **15** as a crude orange-brown solid (Scheme 2.1), which after recrystallization from 3:1 methanol-ethanol gave a pale orange-yellow solid powder in 87% yield.



Scheme 2.1. Oxone oxidation of **12** to nitrosobenzene **13**, and Mills condensation of **13** and **14** to yield the azobenzene **15**.

For introduction of the dianisylamine group, first, dianisylamine (**17**) is synthesized by Buchwald-Hartwig Amination (BHA)⁶⁷⁻⁶⁹ coupling of *p*-anisidine (**14**) and *p*-bromoanisole (**16**), which after crystallization from hexanes gave purple-grey crystalline flakes of **17** in 78% yield. Next, BHA coupling of **15** to dianisylamine (**17**) afforded, after crystallization from isopropanol, the target AA-AB (**11**) as an orange powder in 75% yield.



Scheme 2.2. BHA coupling reactions to produce target AA-AB **11**.

2.3.2. Photochemistry and optical absorption of AA-AB (**11**)

UV-vis spectroscopy is used to determine the optical properties of the azobenzene chromophore, **11**. The optical spectrum of **11** in a deaerated benzene solution (Figure 2.7) shows a π - π^* band at 436 nm, which is red-shifted in comparison to the parent azobenzene system (**1**) at 320 nm. As discussed in chapter 1, substituents in *ortho*- or *para*- positions cause red shifting, with donor groups having the greater impact. This shifting caused complete overlap of the n - π^* band, with substituents having little impact on the n - π^* orbital energies. Irradiation of the π - π^* band is known to induce $E \rightarrow Z$ switching, while the n - π^* band would induce $Z \rightarrow E$ switching. With the **11** system, the n - π^* band is overlapped and cannot be irradiated for effective $Z \rightarrow E$ isomerization, allowing for only effective $E \rightarrow Z$ photoisomerization. Irradiation of the π - π^* band is followed by dynamic UV-vis spectroscopy to monitor $E \rightarrow Z$ isomerization until an equilibrium point known as the photostationary state (PSS) is achieved. It is important to point out that the PSS is irradiation wavelength dependent and will be indicated.

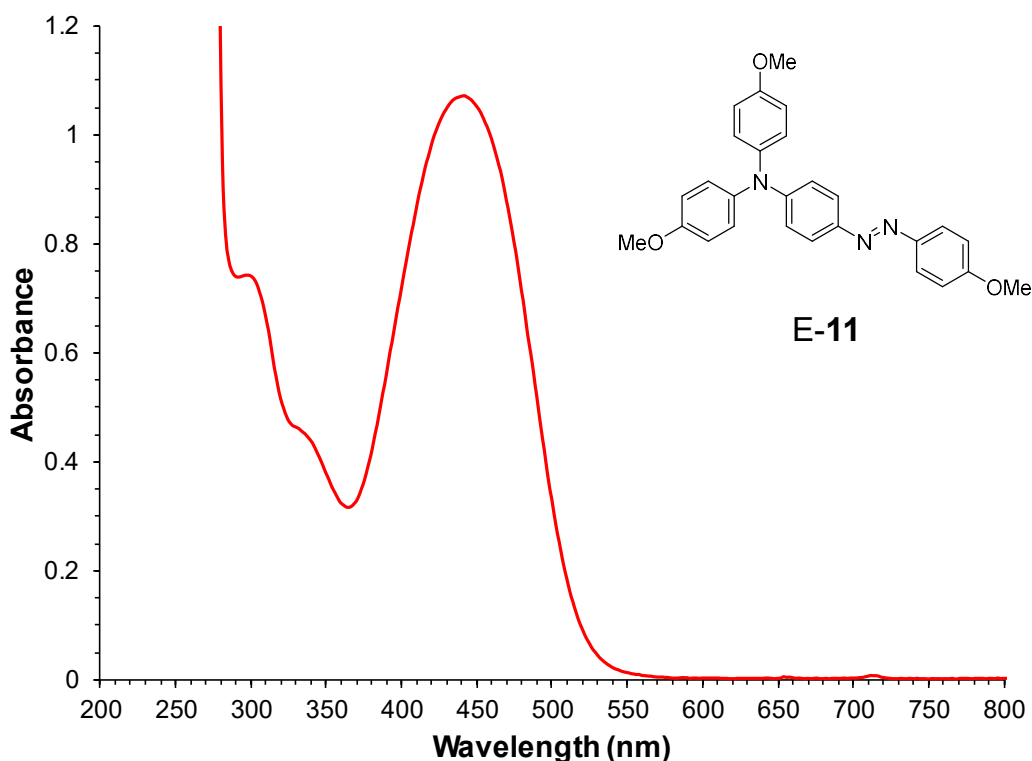


Figure 2.7. Optical spectra of **11** (5.7×10^{-5} M) in deaerated benzene in a 1.0 cm quartz cuvette.

A 430 nm LED light source is used to irradiate the 435 nm π - π^* band to photoisomerize *E*-**11** \rightarrow *Z*-**11**. The UV-vis spectra in Figure 2.8 show the change in optical properties indicating a change in species present. The spectra overlay shows the decrease in absorbance until the PSS is reached within 2 minutes in a benzene- d_6 solution. The *Z* isomer is characterized by decreased molar absorptivity relative to the *E* isomer counterpart. Four isosbestic points are observed in the spectra overlay at 318, 346, 382, and 508 nm. At these wavelengths, the total absorbance remains unchanged during photoisomerization. An isosbestic point is characteristic of two or more interconverting species without an intermediate, as is the case with *E* and *Z* isomers. At this point we have followed *E* \rightarrow *Z* isomerization in a qualitative manner to achieve PSS_{430 nm}. The actual *Z*:*E* ratio at PSS_{430 nm} is determined by $^1\text{H-NMR}$ spectroscopy.

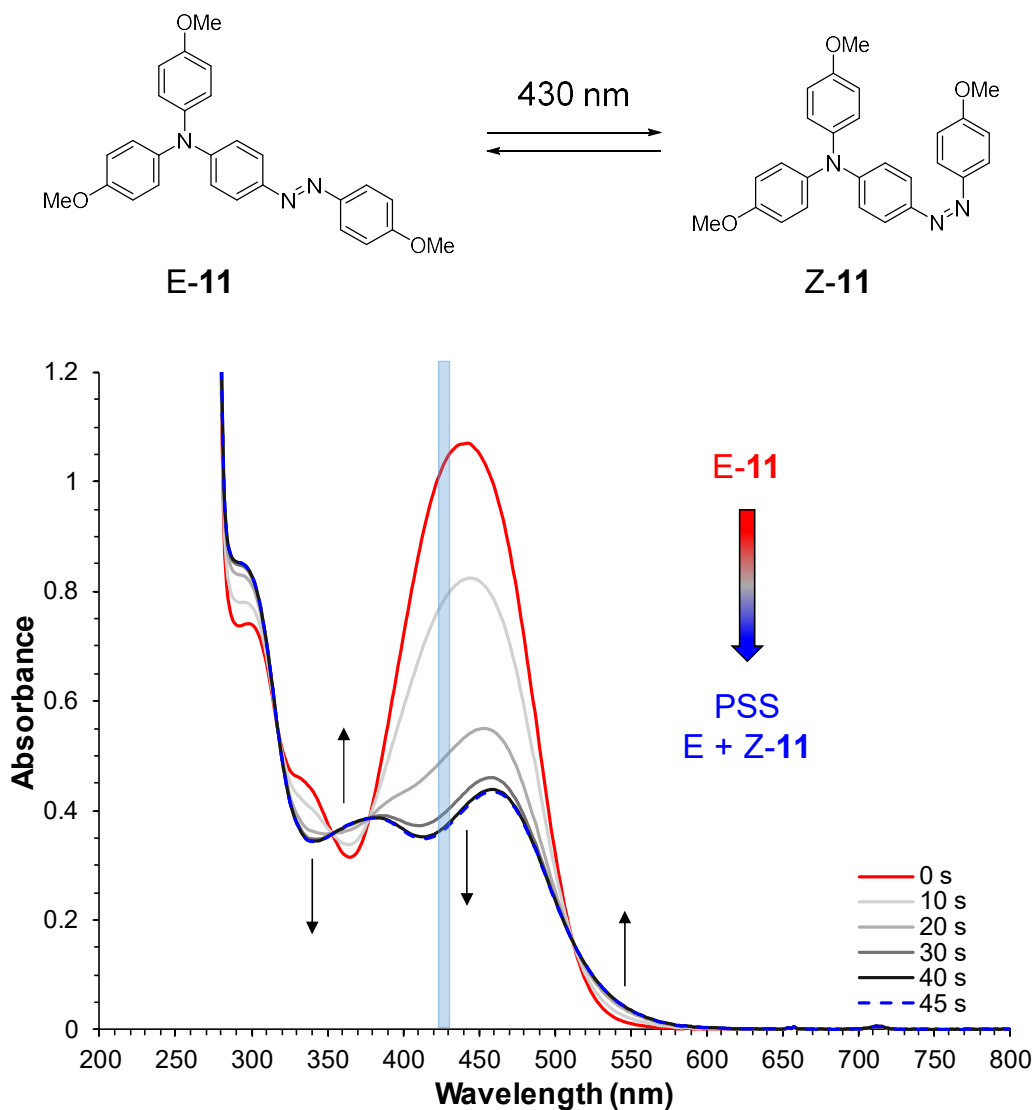


Figure 2.8. Optical spectra of **11** (6.37×10^{-4} M) in deaerated benzene- d_6 in a 0.1 cm quartz cuvette shown before irradiation (red) and following under 430 nm LED light irradiation until PSS_{430 nm} (blue) was achieved.

The $^1\text{H-NMR}$ spectrum of *E*-**11** in benzene- d_6 shows two methoxy peaks in a 2:1 ratio. The methoxy singlets at 3.2 and 3.3 ppm belong to the groups off of azobenzene and dianisylamine, respectively. The spectrum of **11** at PSS_{430 nm} contains both *E* and *Z* isomers. The *E* isomer peaks remain the same as the pre-irradiation spectrum, while the two new peaks belong to the *Z* isomer. Both *Z* isomer peaks are shielded, though to a greater extent for the methoxy

attached to the switching moiety. This effect is due to the reduced conjugation lessening the azo group's withdrawing influence. Figure 2.9 shows the $^1\text{H-NMR}$ spectra between 3 and 4 ppm before and after irradiation to PSS $_{430\text{ nm}}$. The post-irradiation spectrum still has resolved methoxy peaks, which are integrated to determine the ratio of $Z:E$ isomers as 77:23. It is now established that the UV-vis spectra in Figure 2.8 forms the ratio of 77:23 $Z:E$ -**11** in less than 2 minutes. The spectrum only contains Z - or E -**11**, with no sign of decomposition after irradiation. Effective $E \rightarrow Z$ photoisomerization has been demonstrated and characterized. The persistence of the Z rich solution is next established by dynamic UV-vis spectroscopy to follow the $Z \rightarrow E$ progression.

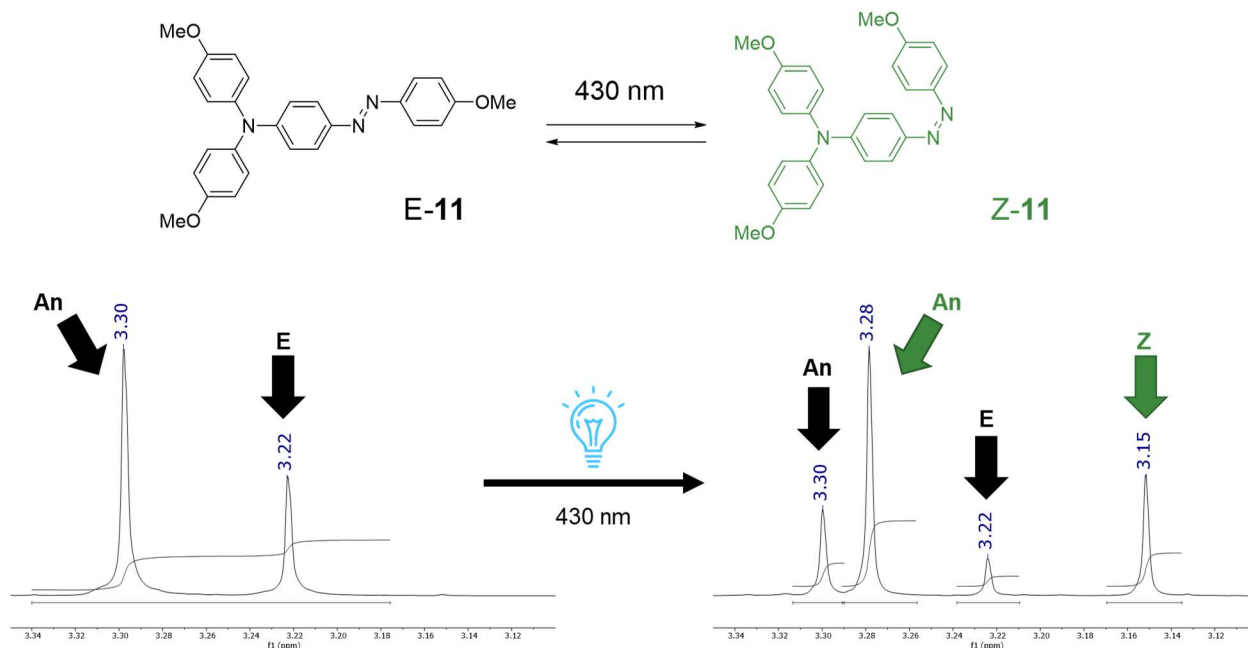


Figure 2.9. $^1\text{H-NMR}$ spectroscopy of **11** showing the methoxy peaks between 3-4 ppm. Left shows the spectrum of the sample pre-irradiation. Right shows the spectrum of the sample at PSS $_{430\text{ nm}}$ with a $Z:E$ ratio of 77:23.

2.3.3. Thermal $Z \rightarrow E$ isomerization of AA-AB (**11**)

Generally, the Z isomer is less thermally stable than the E isomer, and the Z isomer converts to the E isomer in the absence of an irradiation source. The thermal $Z \rightarrow E$ characterization, as the PSS_{430 nm} mixture of **11** in benzene relaxes to E -**11** in the dark, is followed using UV-vis spectroscopy. The absorption increases as the concentration of E -**11** increases, returning to the pre-irradiation character (Figure 2.10). The spectra overlay contains the same four isosbestic points seen in $E \rightarrow Z$ photoisomerization, showing the same interconversion between isomers. The rate constant and half-life for $Z \rightarrow E$ isomerization can now be calculated.

The concentrations of E and Z isomers are known for the pre-irradiation and PSS_{430 nm} spectra. The extinction coefficient (ϵ) for E -**11** is found by applying the Beer-Lambert law (2.1) to the pre-irradiation spectrum. The ϵ' for Z -**11** is then found by applying equation (2.2) to the PSS_{430 nm} mixture with the known E and Z isomer concentrations and E isomer ϵ value. The concentration (c') of Z -**11** can now be determined at a given time. Plotting the Z -**11** concentration versus time gives an exponential decay, while the natural log of the concentration gives a linear decay. The slope of the trend line yields the rate constant (k). The rate constant is then applied to equation (2.3) to find the half-life ($t_{1/2}$). The exponential decay of Z -**11** yields a rate constant at 298 K of $2.6 \cdot 10^{-4} \pm 2.8 \times 10^{-6} \text{ s}^{-1}$, which translates to a thermal half-life of approximately 45 minutes (2,700 seconds). The Gibbs free energy of activation (ΔG^\ddagger) is found by applying the Eyring Equation from transition state theory given in equation (2.4), where K_B is the Boltzmann constant, T is temperature in kelvin, h is the Planck constant, k is the rate constant, R is the gas constant, and κ is the transmission coefficient assumed to be 1. A comparison of $\Delta G^\ddagger_{(298 \text{ K})}$ values

for **1** (25.8 kcal/mol) versus **11** (22.3 kcal/mol) shows that $Z \rightarrow E$ isomerization energy is lower for **11** than the parent system.

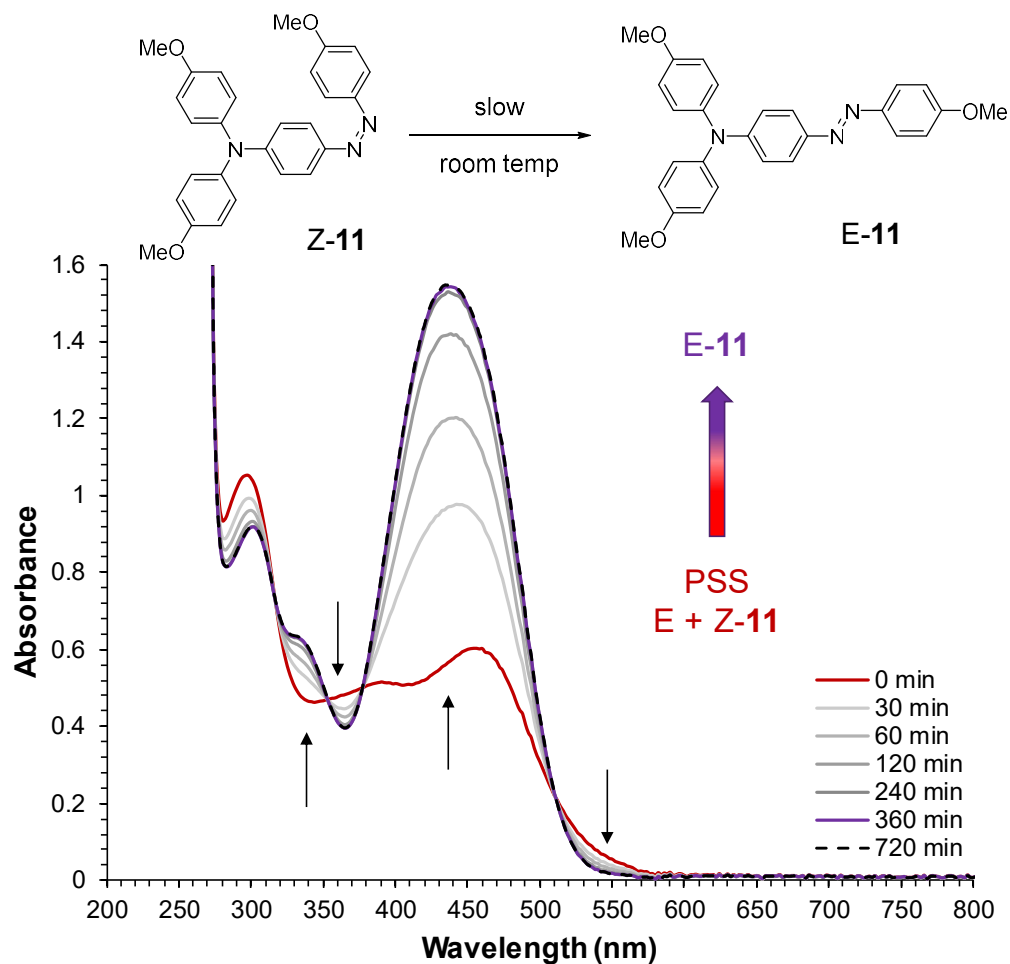


Figure 2.10. Optical spectra of **11** (6.4×10^{-4} M) in deaerated benzene- d_6 in a 0.1 cm quartz cuvette starting at PSS_{430 nm} (red), following $Z \rightarrow E$ isomerization in the dark at 25°C until only E -**11** (purple) remains.

$$A = \epsilon cl \quad (2.1)$$

$$A = (\epsilon c + \epsilon' c') l \quad (2.2)$$

$$t_{1/2} = \frac{\ln(2)}{k} \quad (2.3)$$

$$\Delta G^\ddagger = \ln\left(\frac{\kappa \cdot K_B \cdot T}{h \cdot k}\right) \cdot RT \quad \text{-or-} \quad k = \frac{\kappa \cdot K_B \cdot T}{h} \cdot e^{-\frac{\Delta G^\ddagger}{R \cdot T}} \quad (2.4)$$

The two donor substituents have reduced the thermal isomerization versus the parent **1** system half-life ~ 2 days.^{7, 26, 28, 29} However, when compared with the photochemical rate of $E \rightarrow Z$ isomerization, $Z \rightarrow E$ thermal isomerization is a slow reaction. We will now explore three methods of accelerating $Z \rightarrow E$ switching by inducing the proposed redox switching catalytic cycle. Electron transfer is induced via chemical, electrochemical, or photo-electro oxidation. Each method has pros and cons towards the $E \rightarrow Z \rightarrow E$ cycling goal.

2.3.4. Electrocatalytic switching of AA-AB (11)

The electrochemical properties for **11** were first measured by cyclic voltammetry (CV). The CV spectrum for **11** displays a single reversible oxidation wave (Figure 2.11) with the redox potential (E°) of 0.88 V vs. SCE. The reference electrode is a saturated calomel electrode (SCE), while the electrolyte is 100 mM tetrabutylammonium tetrafluoroborate (TBABF₄) in distilled dichloromethane. The spectra are calibrated to ferrocene, which is at 0.60 V vs SCE when in the same solvent, concentration, and reference electrode conditions.⁷⁰ Electrocatalytic $Z \rightarrow E$ switching is expected by applying a chemical oxidant of an appropriate E° value. The chemical oxidant, CRET (cation radical electron transfer) has a reduction potential of 1.15 V vs. SCE and is used as the single electron transfer agent.⁷¹⁻⁷³

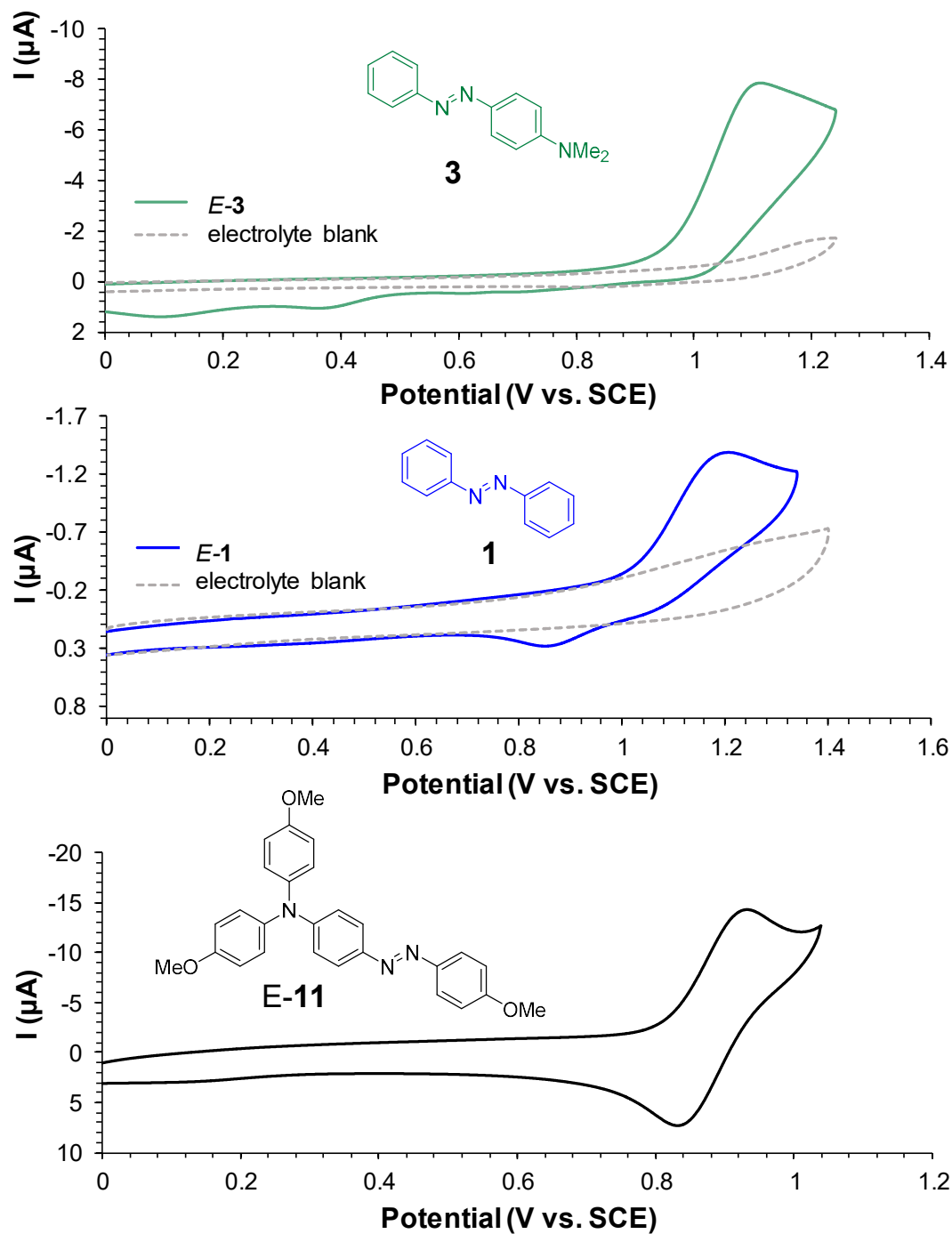


Figure 2.11. Cyclic voltammogram of **3** at 1.0 mM in purified dichloromethane and 0.10 M TBABF₄ electrolyte gave an $E_{p,a}$ of 1.11 V vs. SCE at 100 mV/s. Cyclic voltammogram of **1** at 1.0 mM in purified dichloromethane and 0.10 M TBABF₄ electrolyte gave an $E_{p,a}$ of 1.21 V vs. SCE at 50 mV/s. Cyclic voltammogram of **11** at 1.0 mM in purified dichloromethane and 0.10 M TBABF₄ electrolyte gave an E° of 0.88 V vs. SCE at 50 mV/s. A platinum disc working electrode and platinum wire counter electrode were used.

Blackstock and coworkers tested the electro- “expansion” rate for **11** with a catalytic amount of CRET (**18**) and UV-vis spectroscopy.^{60, 74} The experiment starts with irradiation of **11** in benzene to PSS_{430 nm}. The PSS_{430 nm} solution is injected with 1 mol % CRET in a methylene chloride solution. The PSS solution immediately began *Z*→*E* isomerization (Figure 2.12) to reach total *E*-**AA-AB**, reducing the thermal half-life to less than 5 milliseconds, as followed by dynamic UV-vis spectroscopy. The *Z*→*E* isomerization is both fast and complete versus a new equilibrium forming. The rate enhancement is immediately seen by comparing the thermal half-life of 2,700 seconds for the neutral system. The electron transfer cycle gained a rate acceleration of 5,400x, or an extrapolated minimum rate acceleration of 540,000x assuming 100% CRET loading. As discussed in section 2.2, the single electron oxidation of the amino center reduces the *Z*→*E* energy barrier, successfully demonstrating that oxidation of a single redox center converts a linked azobenzene moiety. While we have demonstrated that chemical oxidants are effective at *Z*→*E* switching, the oxidant does compete with the *E*→*Z* photoisomerization, preventing PSS reformation without quenching the radical cation first. Therefore, chemical oxidants give us the desired rate enhancement but not efficient *E*→*Z*→*E* cycling.

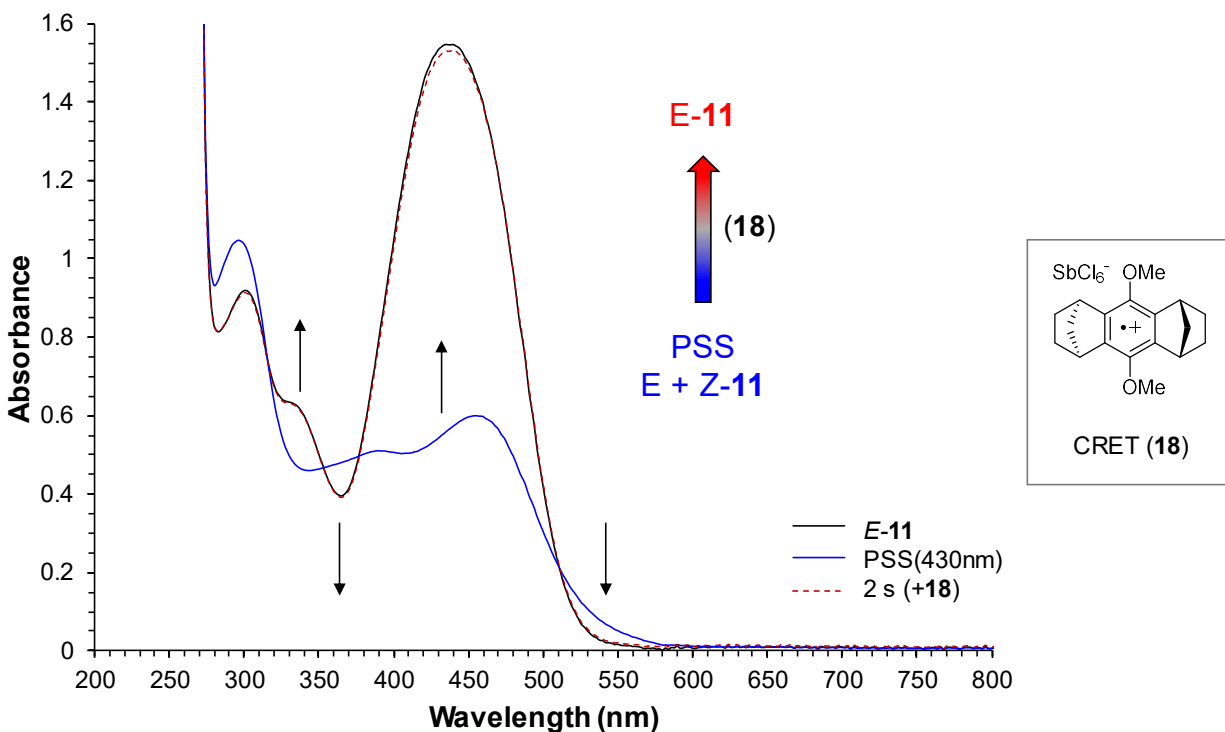
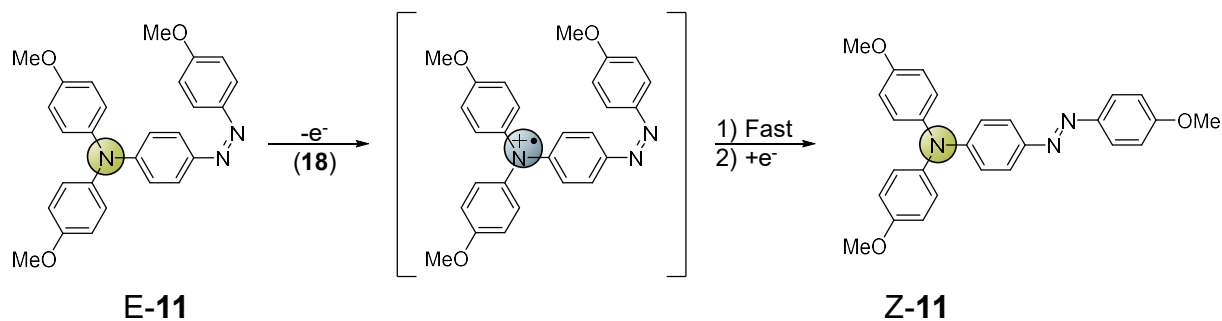


Figure 2.12—Optical spectra of **11** (6.37×10^{-4} M) in deaerated benzene- d_6 in a 0.1 cm quartz cuvette at PSS_{430 nm}(blue) is injected with 1 mole % CRET (**18**) (6.3×10^{-5} M in dichloromethane) at rt to return the *E*-isomer (red).

Hecht and coworkers demonstrate that chemical oxidants (ceric ammonium nitrate (CAN) and triarylamine radical cation salts) successfully form the azobenzene radical cation ($1^{\bullet+}$) to accelerate $Z \rightarrow E$ isomerization, but it is necessary to slowly add drop-wise with good mixing to avoid degradation of azobenzene by avoiding the destructive oxidation potential.⁷⁵ Oxidation of azobenzenes often has a destructive anodic peak, which is made even more difficult

to avoid with the *Z* isomer experiencing a higher rate of degradation than the *E* isomer. However, the addition of a redox group on azobenzene like AA-AB (**11**) gives it the ability to form a persistent radical cation within seconds upon oxidation with no signs of fatigue during repeated electrochemical switching and accelerated *Z*→*E* isomerization.

2.3.5. Electrocatalytic switching of AA-AB (11**) using a thin cell photo-electro device (PED)**

Electrochemical application of a voltage is one alternative oxidation method explored by Melody Kelley and Blackstock for turning 'on' and 'off' ET-catalysis of azo *Z*→*E* conversion.⁷⁴ A single electron transfer is achievable from an applied voltage at an electrode using a photo-electro device (PED) with **11**. The device conducts current from electrodes, while not absorbing in the UV-visible region, allowing for monitoring by UV-vis spectroscopy as well as for *E*→*Z* photoisomerization. The **11** loaded PED is irradiated for *E*→*Z* switching until PSS_{430 nm} is reached, before following up with an applied voltage (1.5 V). The PSS_{430 nm} mixture immediately begins *Z*→*E* isomerization, demonstrating that electrochemical oxidation of **11** also induces the electron transfer cycle to deliver the enhanced rate of *Z*→*E* switching. The PED set-up has the advantage of turning the oxidant on or off by controlling the voltage source, unlike adding a chemical oxidant to the solution. Both the voltage and the light source can be toggled on and off, allowing for *E*→*Z*→*E* toggling within a single device by alternating light and voltage sources. UV-vis spectroscopy monitors the change in absorbance while cycling between irradiation and oxidation. Plotting the absorbance at a single wavelength versus time (Figure 2.13) shows the robust cycling achieved using the PED cell.^{60, 74}

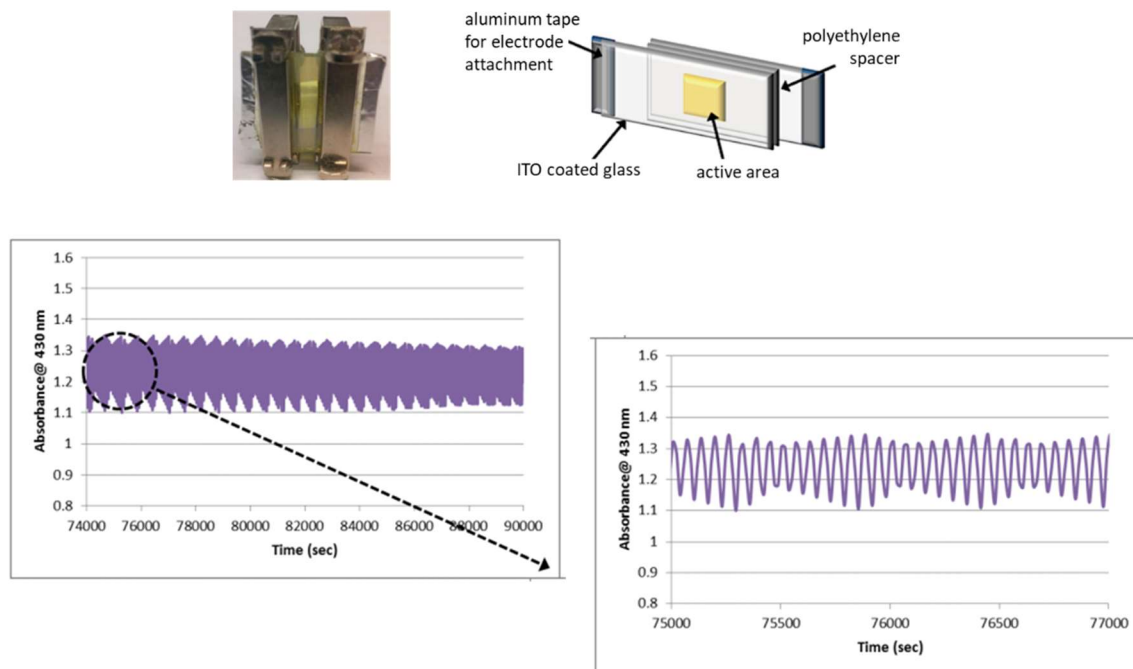


Figure 2.13. (a) Photo-electro device (PED) designed by Blackstock and coworkers to test the impact an applied voltage has on the redox appended azobenzene analogues. (b) Blackstock and Melody Kelley were able to show an automated photo-electrochromic cycling of the **11** system for more than 250 cycles by toggling between irradiation with 430 nm LED and applying a voltage of 1.5 V.⁷⁴

2.4. Photosensitizer for Photo-Electro Catalytic Switching of AA-AB

Kelley⁷⁴ and Saint-Louis⁶⁰ demonstrated that the $Z \rightarrow E$ *ra*-azobenzene catalytic redox switching can be triggered by an applied voltage at an electrode or by addition of a chemical oxidant to a solution of *ra*-azobenzene **11**. A goal of this project was to develop an alternative, simple cycling system envisioned to use two alternating wavelengths of light to achieve $E \rightarrow Z \rightarrow E$ isomerization, initiating the electron transfer cycle for the $Z \rightarrow E$ acceleration of *ra*-azobenzene systems like **11**, while retaining the advantage of turning the oxidant on or off. An organic photosensitizer would be one such solution as a temporary oxidation source having a short-lived excited state. Organic photosensitizers come in a range of absorbance wavelengths,

redox potentials, and excited state lifetimes, allowing us to choose one that minimizes absorbance overlap or interference with the photochromic system. The ideal system design would combine a redox appended azobenzene with a catalytic amount of photosensitizer, having resolved absorbance bands. Light irradiation of the azobenzene π - π^* band would still trigger photoisomerization to the PSS with minimal impact to the photosensitizer. Likewise, irradiation of the photosensitizer would have minimal impact on the azobenzene state.

Methylene blue (\mathbf{MB}^+) is a photosensitizer that absorbs in the 660 nm region. Azobenzene systems typically absorb around 400 nm, affording little overlap between the systems. Irradiation of the \mathbf{MB}^+ band at 660 nm generates a triplet excited state. The triplet excited state, $^3\mathbf{MB}^+/\mathbf{MB}^*$, has a redox potential of 0.97 V vs. SCE and a thermal lifetime of 32 microseconds in acetonitrile:nitromethane solution.⁷⁶ Therefore, the oxidizing agent, \mathbf{MB}^+ can be turned on and off, much like applying a voltage to the PED cell.

Irradiation of the photosensitizer, \mathbf{MB}^+ , to the triplet excited state, generates the oxidizing agent in situ (Figure 2.14). This triplet excited state has a sufficient redox potential (0.97 V vs. SCE) to oxidize the redox appended azobenzene **11** (0.88 V vs. SCE), triggering the electron transfer cycle. The resulting \mathbf{MB}^* doublet state can then behave as a reducing agent, returning to the ground singlet state. Now, blue light is used to trigger $E \rightarrow Z$ switching of **11**, while red light will form $^3\mathbf{MB}^+$ triggering $Z \rightarrow E$ isomerization by the electron transfer cycle. Therefore, a combined solution of **ra**-azobenzene (**11**) and a catalytic amount of \mathbf{MB}^+ should allow for photo, photo-redox cycling, repeatedly toggling from $E \rightarrow Z \rightarrow E$, by alternating between red and blue-light sources.

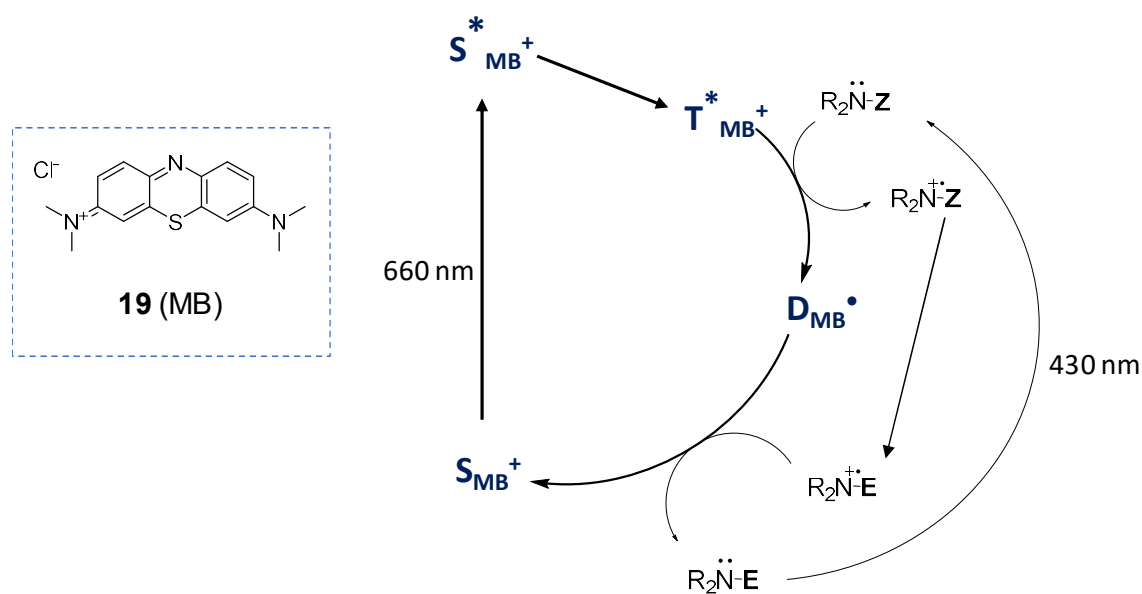
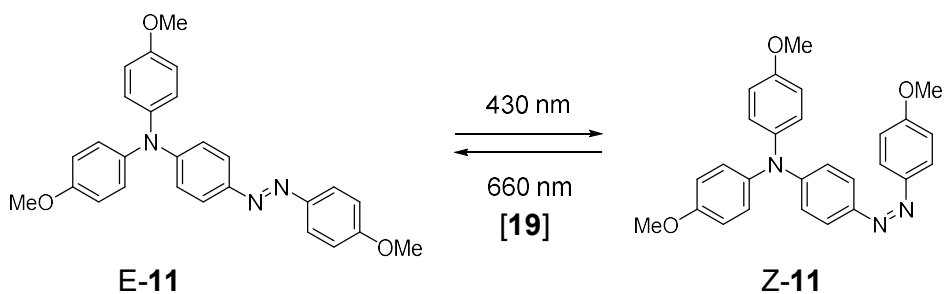


Figure 2.14. Proposed mechanism of electron transfer cycle upon excitation of MB^+ with red light to the singlet excited state ($S_{MB^+}^*$), which relaxes to the triplet excited state ($T_{MB^+}^*$) before oxidizing the redox amine. The resulting doublet excited state ($D_{MB\cdot}$) behaves as a reducing agent returning to the singlet ground state. The $E \rightarrow Z \rightarrow E$ cycle can then continue by irradiating the system with blue light for $E \rightarrow Z$ isomerization.

Since the mixture must be in solution, an appropriate solvent must be determined. MB^+ is soluble in water, acetic acid and alcohols, but only minimally soluble in tetrahydrofuran or acetone. It is not soluble in common organic solvents such as benzene, toluene, xylenes, mesitylene, anisole, ethyl acetate, or acetonitrile. The study cataloging organic photosensitizer excited state redox potentials and lifetimes used a mixture of nitromethane and acetonitrile.⁷⁶ MB^+ was found to be soluble in nitromethane.

The solvent chosen also must be compatible with the amino-azobenzene system. When in certain solutions the redox appended azobenzene systems are not stable at PSS. For example, chlorinated solvents (chloroform or dichloromethane) can form free radicals returning the *E* isomer even when kept under constant irradiation of the π - π^* band. When solvents acetonitrile and nitromethane were used with **11**, the system showed immediate signs of degradation or a large color change. The system **11** was stable in THF and acetone, but it was determined that **MB⁺** was not soluble enough. Giving up on finding a single solvent choice, a combination of toluene and methanol were decided upon. The azobenzene systems are stable in toluene and benzene solvents, while **MB⁺** is highly soluble in methanol. The two systems are individually prepared in the preferred solvent. Toluene is used to create a solution of **11** at UV-vis concentrations. Methanol is used to create a concentrated solution of **MB⁺**. A cuvette of **11** solution is prepared for UV-vis spectroscopy. Then a syringe is used to inject the solution of **MB⁺** into the toluene solution. A control experiment of injecting the **MB⁺**-methanol mixture (5-100 microliters) into toluene (3 mL) is used to determine if **MB⁺** will stay in solution or crash back out. The methanol-toluene solution was found to be miscible with no evidence of **MB⁺** crashing out of solution.

The solvent mixture is then taken through a few control experiments. A mixed solution of **11** (3.0 mL; 5.51×10^{-5} M) and **MB⁺** (5 mole %; 65.00 μ L; 1.28×10^{-4} M) in deaerated 2.1% methanol in toluene is measured by UV-vis spectroscopy. The absorbance bands of *E*-**11** and **MB⁺** remain unchanged compared to the individual optical spectra, indicating no interaction between the two systems (Figure 2.15). Blue light (430 nm) irradiation is used to trigger *E*→*Z* isomerization of **11**. Blue light irradiation was found to have no impact on the **MB⁺** absorbance

band (Figure 2.16), while red light exposure generates singlet oxidation, degrading the **MB**⁺ sensitizer as seen in the photodegradation over 10 minutes of constant exposure (Figure 2.16).

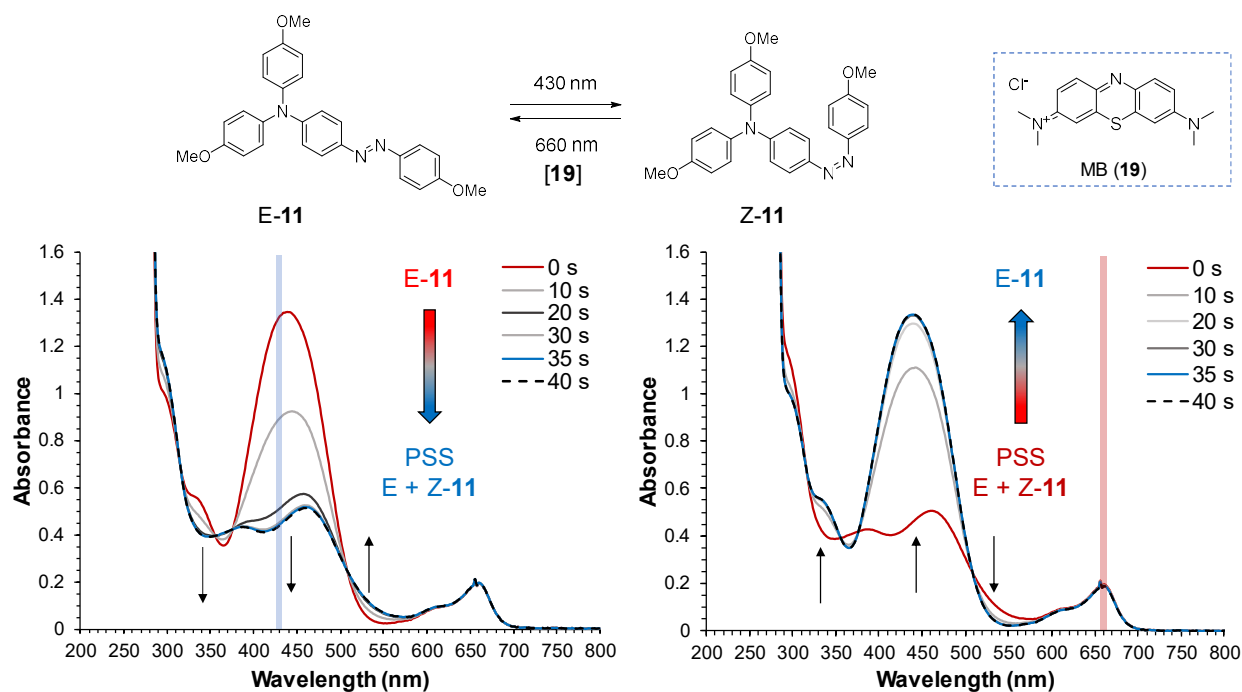


Figure 2.15. Optical spectra of **11** (3.0 mL; 5.51×10^{-5} M) and **MB**⁺ (**19**) (5 mole %; 65.00 μ L; 1.28×10^{-4} M) in deaerated 2.1% methanol:toluene in a 1.0 cm quartz cuvette at 25 °C. (left) Overlay of optical spectra of **11:MB**⁺ following *E*→*Z* isomerization under blue light irradiation to achieve PSS_{430 nm}. (right) Overlay of optical spectra of **11:MB**⁺ following *Z*→*E* isomerization under red light irradiation to excite **MB**⁺.

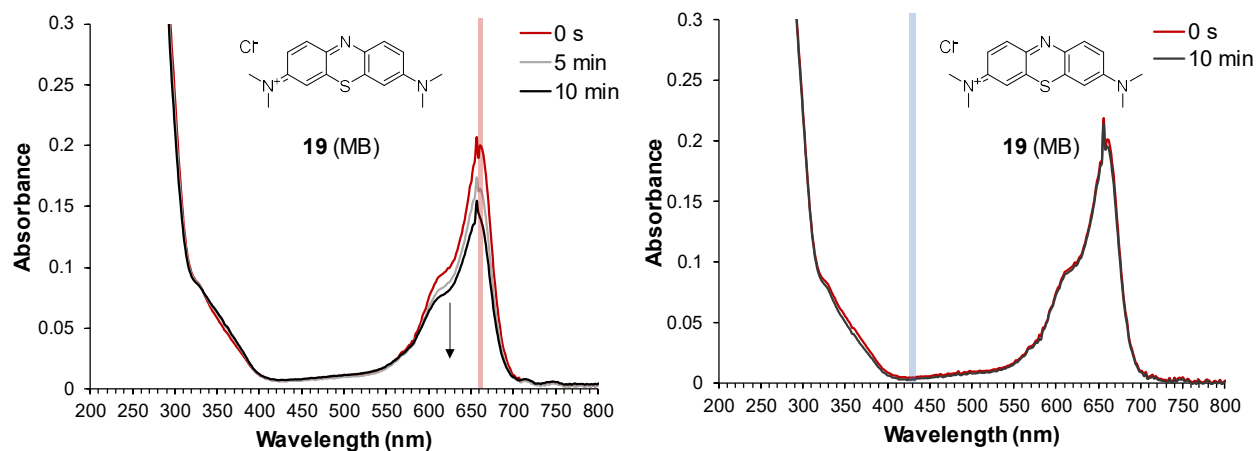


Figure 2.16. Optical spectra of MB^+ (**19**) (3.0 mL; 2.77×10^{-6} M) in deaerated 2.1% methanol:toluene in a 1.0 cm quartz cuvette at 25 °C. Optical overlays following for 10 minutes of red light irradiation (left) or blue light irradiation (right).

Red light (660 nm) is used to excite MB^+ to the triplet excited state. While the triplet excited state is too short lived to be observed on the UV-vis spectroscopy timescale, the evidence of its formation is observed by the change in absorbance at the $\pi\text{-}\pi^*$ band from acceleration of $Z \rightarrow E$ -**11**. The triplet excited state was able to successfully oxidize the amino center to a radical cation, prompting fast, complete $Z \rightarrow E$ isomerization. In comparison, while the control experiment of applying red-light to the **11** toluene-methanol solution (in absence of MB^+) did show that red-light does generate a new E -rich PSS state, it was at a significantly slower rate, taking 3600 s (1 hour), while not fully returning to an all E -state (Figure 2. 17). MB^+ does not prevent thermal $Z \rightarrow E$ isomerization. Thermal relaxation of $Z \rightarrow E$ -**11** is still observed in the presence of MB^+ when kept in the dark and followed by UV-vis spectroscopy for about 4 hours (Figure 2.18).

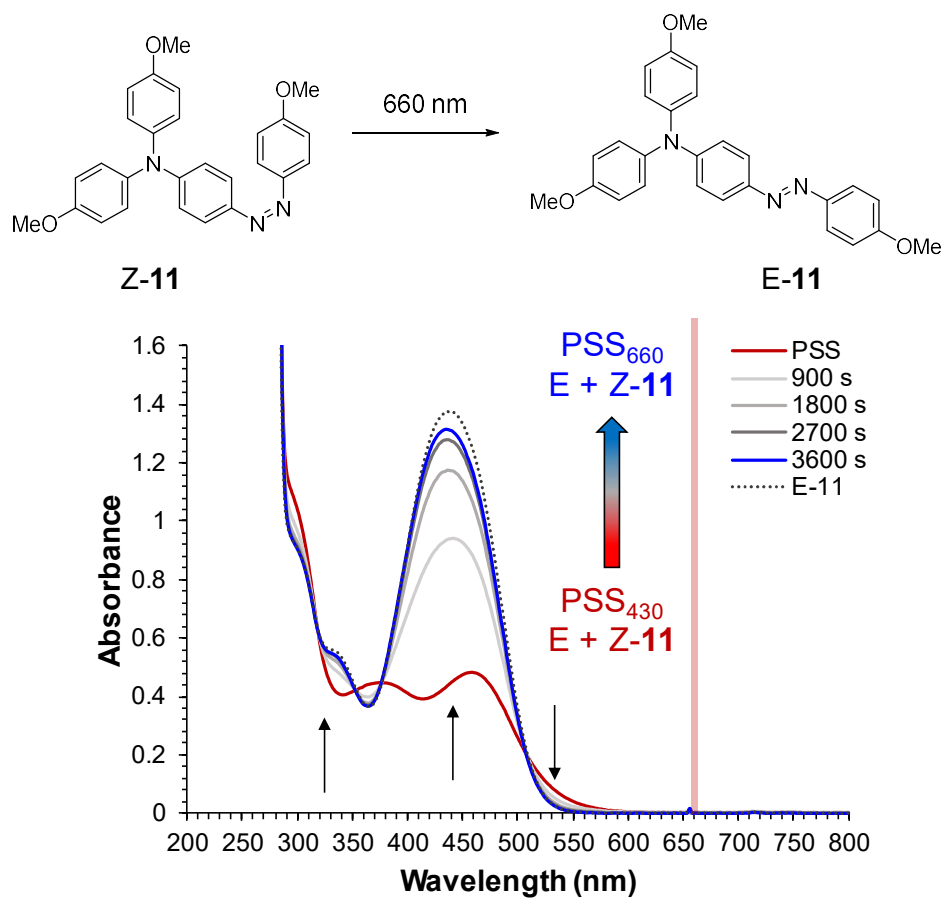


Figure 2. 17. Optical spectra of **11** (3.0 mL; 5.51×10^{-5} M) in deaerated 2.1% methanol:toluene in a 1.0 cm quartz cuvette at 25 °C. The spectra overlay is starting at PSS₄₃₀ nm and following the *Z*→*E* isomerization until PSS₆₆₀ nm is achieved after ~ 1 hour. The pre-irradiation spectra (dashed-grey) is included for comparison.

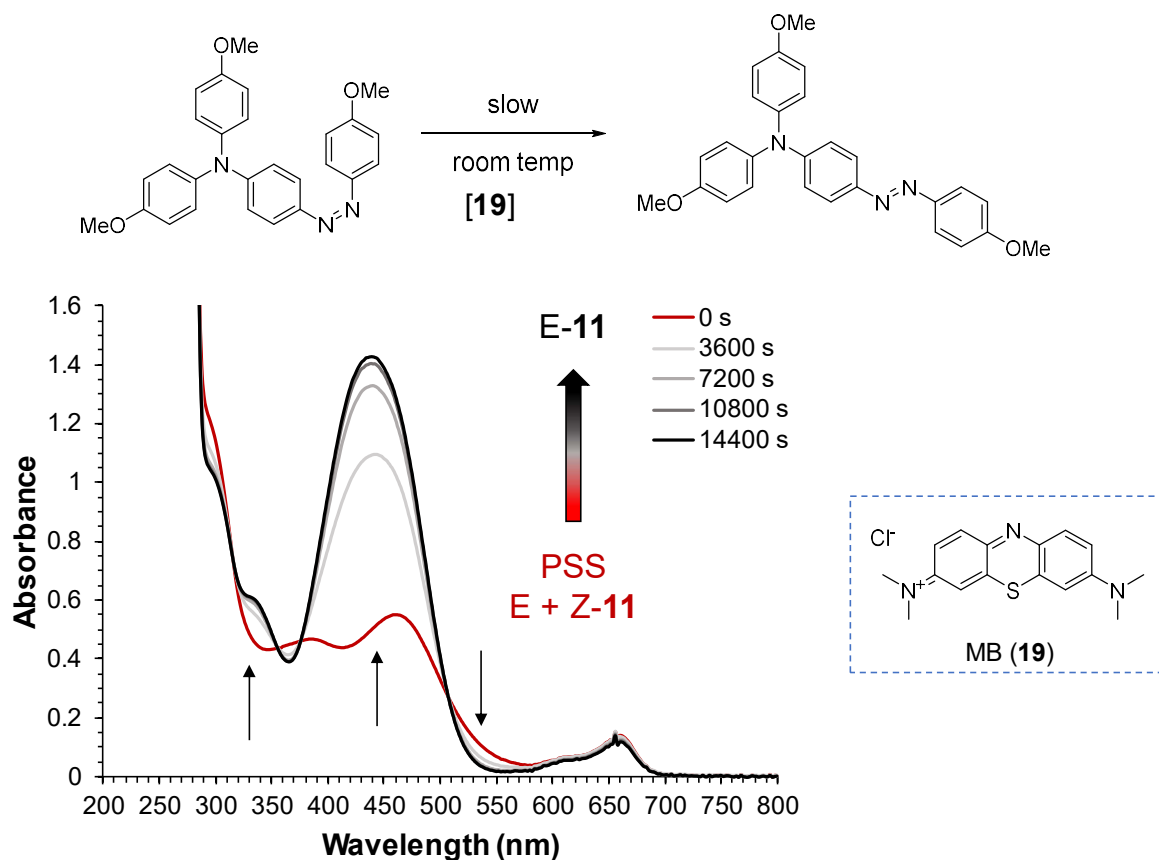


Figure 2.18. Optical spectra of **11** (3.0 mL; 5.51×10^{-5} M) and **MB⁺ (19)** (5 mole %; 65.00 μ L; 1.28×10^{-4} M) in deaerated 2.1% methanol:toluene in a 1.0 cm quartz cuvette at 25 °C. The spectra overlay is starting at PSS_{430 nm} and following the $Z \rightarrow E$ thermal isomerization after \sim 4 hours.

The **11/MB⁺** system is followed by UV-vis spectroscopy at 15 second intervals while switching between no light exposure, blue-light irradiation, and red-light irradiation at 1-minute intervals. The system cycled from $E \rightarrow Z$ under blue light and $Z \rightarrow E$ under red light exposure. Plotting the absorbance change at a specific wavelength versus time gives a clear picture of the cycling. Figure 2.19 plots $E \rightarrow Z \rightarrow E$ cycling for 10 repetitions. This shows that we can in fact cycle between PSS and E isomers using blue and red light when a photosensitizer is introduced to the solution.

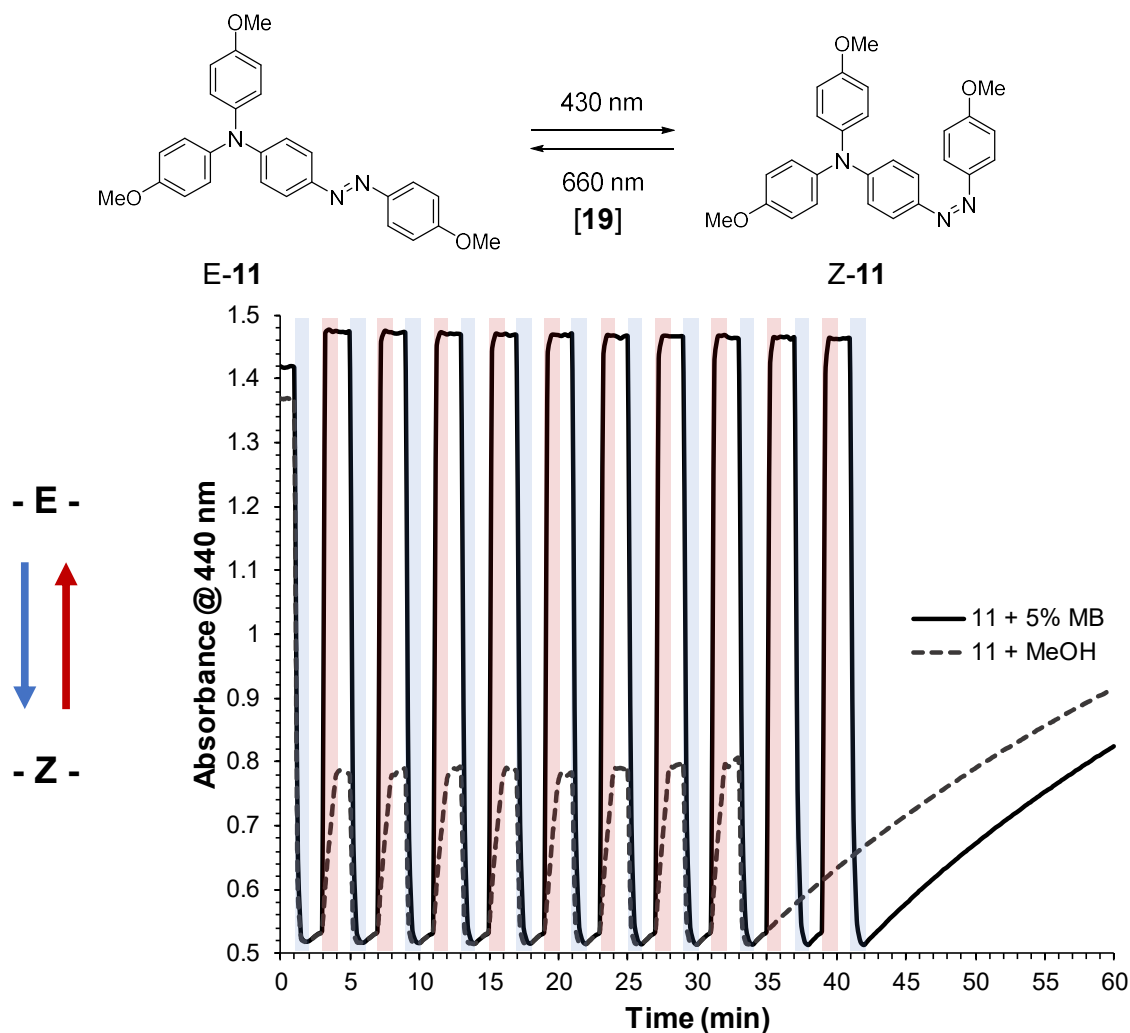


Figure 2.19. The *E*→*Z*→*E* cycling of **11** (5.51×10^{-5} M) and 5% **MB**⁺ (injection of 65.0 μ L of 1.28×10^{-4} M) in deaerated 2.1% methanol in toluene in a 1.0 cm quartz cuvette at 25 °C cycling from no light exposure, blue light exposure, no light exposure, and red light exposure to complete 10 cycles. The grey-dashed line shows the cycling of **11** in the absence of **MB**⁺ for 8 cycles. After toggling light sources, the solutions are followed while left in the dark until 60 minutes in total passed.

No fatigue of the redox appended system **11** (*E*/*Z*-isomer) was observed using methylene blue as the photo-electron transfer agent. Methylene blue survival was found to be limiting in this cycling set-up, because a generation of singlet oxygen from irradiation degrades the sensitizer. The *Z*→*E* acceleration was recently shown by Hecht and coworkers for the parent azobenzene **1**.⁷⁵ Comparing the two set-ups, the *Z*→*E* acceleration is greater for the ra-

azobenzene **11** at the same loading of 5% methylene blue and 660 nm light irradiation, taking 6.5 minutes for the parent azobenzene **1** and <1 minute for the **ra**-azobenzene **11** to return to the *E* isomeric state. We have also demonstrated that *E*→*Z*→*E* cycling for 10 cycles can be performed at 5% loading for the redox appended system **11** versus 100% loading used on the parent azobenzene **1** for 5 cycles.

2.5. Introduction and Synthesis Of AA-AB^{•+} (**11**^{•+})

The three oxidation methods from the previous sections produce the radical cation species during the electron transfer cycle. This radical cation species is the driving force behind the *Z*→*E* rate acceleration. Therefore, we are interested in generating a persistent radical cation system to characterize. A radical cation salt is expected to be persistent enough to obtain optical and spin distribution information for the system.

A stoichiometric amount of nitrosonium hexafluorophosphate (NOPF₆) and **11** is used in the synthesis towards the radical cation salt, **11**^{•+} PF₆⁻. The reaction is carried out in freshly distilled, deaerated dichloromethane under nitrogen atmosphere. The by-product of the reaction is nitric oxide gas, which is removed by sparging the system with nitrogen gas. The reaction generates a deep green-blue opaque solution immediately upon combination of NOPF₆ and azobenzene. The radical cation is persistent in solution, so characterization is carried out without isolation of the product from dichloromethane.

2.5.1. Optical absorption of AA-AB^{•+} (**11**^{•+})

The optical spectrum of **11**^{•+}PF₆⁻ in dichloromethane solution is given in Figure 2.20. The band at 418 nm belongs to the π - π^* band of **11**. The radical cation species is characterized by the red shifting of the n - π^* band and π - π^* , which is consistent with a reduction in energy. The π - π^* band has shifted to 586 nm, and the n - π^* band is at 758 nm. The n - π^* experiences a greater

energy impact allowing it to no longer be overlapped by the stronger absorbing π - π^* band. The optical spectrum shows the radical cation is produced, though not to completion.

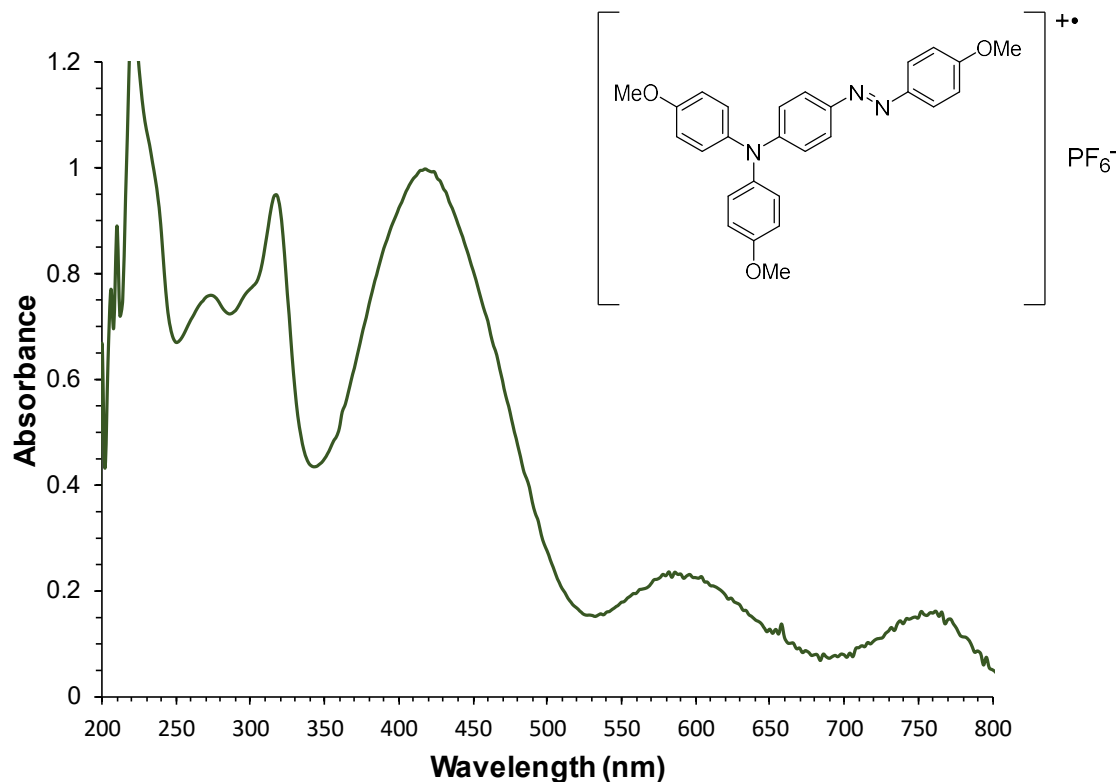


Figure 2.20. Optical spectra of $11^{+\bullet}\text{PF}_6^-$ (~ 1 mM) in deaerated dichloromethane in a 0.1 cm quartz cuvette at 25 °C.

2.5.2. Electron paramagnetic resonance (EPR) spectrum activity

The spin distribution for $11^{+\bullet}\text{PF}_6^-$ was determined by pulsed electron paramagnetic resonance (EPR) spectroscopy. The EPR spectrum of $11^{+\bullet}\text{PF}_6^-$ using distilled dichloromethane was recorded at room temperature. The EPR spectrum in Figure 2.21 has a triplet splitting pattern that is consistent with an unpaired electron being isolated on a single nitrogen, like the appended redox amine. Computer simulation of the spectrum has an isotropic g -value of 2.006, also expected of a radical coupled to one nitrogen, and a hyperfine coupling ($a(\text{N})$) of 8.2 G,

consistent with the tri-*p*-anisylamine radical cation $a(N)$ of 8.9 G.⁷⁷ The root mean square deviation (RMSD) for the fit is 0.019. No other hyperfine coupling is observed. The EPR results are consistent with the radical being centralized on the redox amine and not distributed throughout the azobenzene system, showing the electron is removed from the redox center.

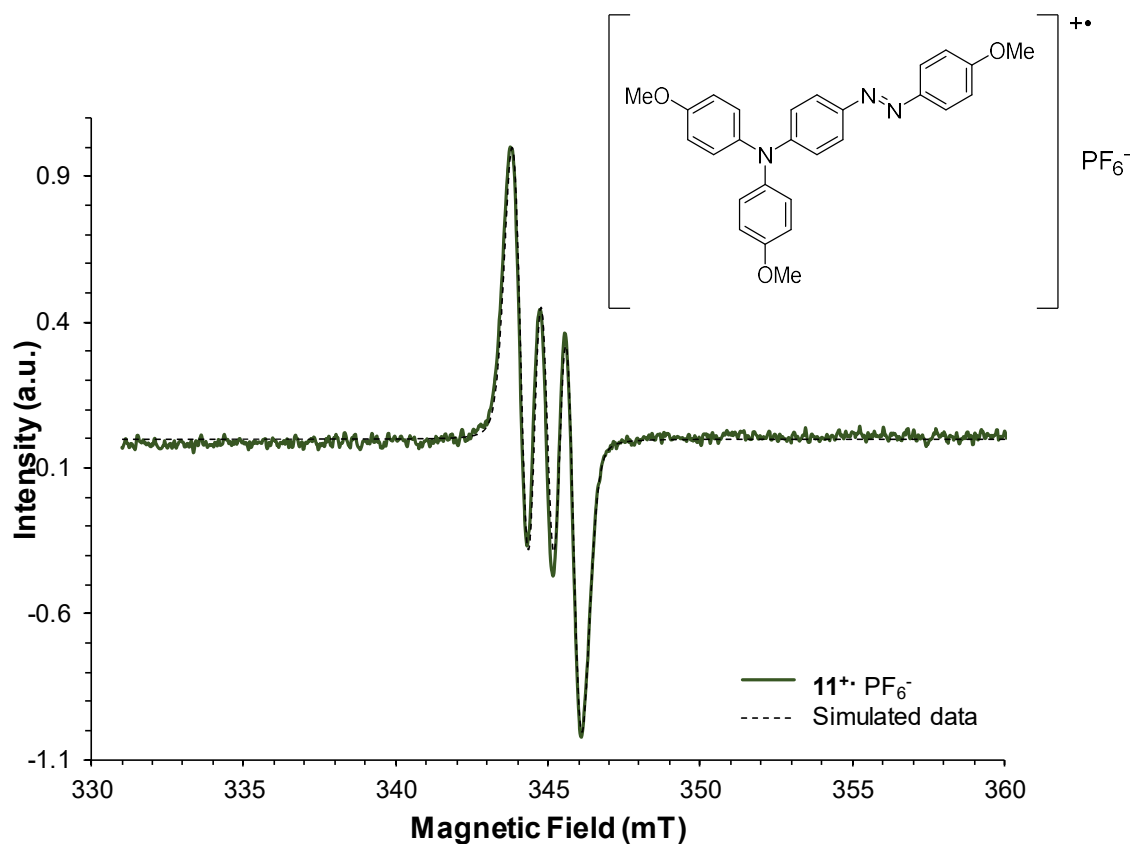


Figure 2.21 Pulsed EPR spectrum of $11^{+\bullet}PF_6^-$ (1 mM) in purified and distilled dichloromethane taken on a Bruker ELEXSYS E680 EPR spectrometer at 293 K.

2.6. Conclusion

Attaching a redox amine to azobenzene systems was explored for acceleration of $E \rightarrow Z$ isomerization rate. The redox center is attached to a bromine substituted azobenzene by Buchwald-Hartwig amination. The redox appended azobenzene **11** is red-shifted (436 nm) in

comparison to the parent **1** system and overlaps the $n\text{-}\pi^*$ band, which is commonly observed with substituted azobenzenes. Photoisomerization $E\rightarrow Z$ to the PSS_{430 nm} gave 77% *Z* isomer. The $Z\rightarrow E$ converted at a $2.6 \times 10^{-4} \pm 2.8 \times 10^{-6} \text{ s}^{-1}$ rate, which is 45-minute half-life when left in the dark at 25°C.

The redox group on **11** controls where the electron is removed. The resulting radical cation is stable, returning the azobenzene with no decomposition or configuration change. Characterization of the synthesized radical cation salt by EPR spectroscopy indicates the radical is located on a single nitrogen like the redox center and not the azo unit with an $a(\text{N})$ value consistent to an aryl amine radical cation.

The oxidation can be induced by a chemical oxidant, applied voltage, or excitation of a photosensitizer. In each case, oxidation induces the electron transfer catalytic cycle with rapid, complete, and catalytic $Z\rightarrow E$ conversion observed within seconds. Extrapolating to 100% oxidant found a minimum rate acceleration of 540,000x that of neutral $Z\rightarrow E$ isomerization. A cycling system was developed using photo, photo-electro cycling by alternating blue and red-light irradiation, toggling between $E\rightarrow Z\rightarrow E$ units. The photosensitizer has the advantage of the photo-electro effect remaining off until irradiated, preventing competition during $E\rightarrow Z$ photoisomerization. The radical cation effectively accelerates the $Z\rightarrow E$ isomerization for the attached azobenzene unit. A question now is: could additional azobenzenes be attached to the radical cation? Could it work equally well?

2.7. Experimental Section

Materials and general instrumentation

Starting materials and solvents were purchased from Aldrich Chemical Co., Alfa Aesar, Oakwood Chemical, Ark Pharm Inc., Chem-Impex International, Inc., and TCI America and used without further purification unless otherwise noted. Standard purity N₂ gas was purchased from Airgas. All Pd-catalyzed reactions were performed under a N₂ atmosphere. Pd(dba)₂ and Pd₂(dba)₃ were purchased from Ark Pharm Inc and used without further purification. P(*t*Bu)₃ and NaO*t*Bu were purchased from Alfa Aesar and used without further purification. Pd(dba)₂, Pd₂(dba)₃, P(*t*Bu)₃ and NaO*t*Bu were measured and stored in a N₂ dry box. A stock solution of P(*t*Bu)₃ in anhydrous toluene was prepared for easy dispensing via microliter syringe, and this solution was added to the reaction flask whenever P(*t*Bu)₃ was used. Activity III alumina was prepared from mixing DI H₂O (6 mL) and basic alumina (100 g) (Aldrich, activated Brockmann I, ~150 mesh). Celite[®] 545 (0.02-0.1 mm particle size) for use in filtration was purchased from EMD Millipore. Deuterated solvents for NMR spectroscopy were purchased from Cambridge Isotopes and used without further purification. Thin layer chromatography was performed using TLC Silica gel 60 F254 aluminum sheets from EMD Millipore. Column chromatography was performed using 60 Å, 32 - 63 micron standard grade silica gel from Sorbent Technologies.

Purification of solvents

Dichloromethane for use in UV-Vis spectroscopy, EPR spectroscopy and cyclic voltammetry was purified by stirring over sulfuric acid, washing with DI H₂O, washing with 5% aq. KOH, drying with CaCl₂ and distilling from CaH₂ under N₂ atmosphere.⁷⁸

Purification of TBABF₄ electrolyte

TBABF₄ solid was purchased from TCI America and purified by recrystallizing three times from a 1:1 solution of millipore H₂O:EtOH and then drying in a vacuum oven (110 °C, 0.1 Torr) for 48 h. ⁷⁸

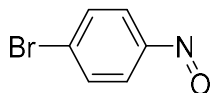
Apparatus

¹H NMR and ¹³C NMR spectra were recorded on Bruker AM-360 or AM-500 instruments using CDCl₃, acetone-*d*₆ or benzene-*d*₆ solvents with chemical shifts reported relative to the residual non-deuterated solvent signal. Melting points were recorded using either a Mel Temp apparatus from Laboratory Devices or a Thomas Hoover 6406 Uni-Melt Capillary Melting Point Apparatus and are uncorrected. UV-Vis optical spectra were recorded on a HP8452A diode array spectrophotometer using a 0.1 cm or 1.0 cm quartz cuvette. Optical measurements were acquired with overhead lights turned off to minimize azo photoisomerization by ambient light, unless otherwise specified. The cyclic voltammetry was measured by a PAR 273 electrochemical potentiostat (EG&G Instruments) using a saturated calomel reference electrode (SCE), a platinum wire counter electrode, and a platinum disc working electrode. The electrochemistry experiments were carried out under ambient conditions in distilled DCM solvent containing 0.1 M electrolyte (normally TBABF₄). Tetrabutylammonium hexafluorophosphate (Sigma-Aldrich) was also employed as an electrolyte. A 'blank' voltammogram of the solvent with electrolyte was measured before each electrochemical analysis. Ferrocene was used as a potential standard to calibrate the electrochemical voltage measured vs SCE for the CV measurements.

Excitation sources

The 430 and 457 nm light-emitting diode sources were purchased from Zhongshan LED Technology Co., Ltd. and are composed of 7x1 W Diamond Grow LEDs with an input voltage of AC 90-264 V having a spectral bandwidth of 426 ± 8 nm and 457 ± 7 nm. The 7x1 W LEDs are housed in a 3.70 in. x 3.86 in. Fins Slotted Aluminum casing. The 395-410 nm LED source was a single 7 W BLB7W bulb purchased from ADJ Products, LLC[®]. The 660 nm LED source was purchased from Abi (A Brighter Idea) and is composed of 12x1 W Grow LEDs. The excitation source band width is 660 ± 10 nm. Excitation spectra for these irradiation sources are given in Appendix B Figure B1.

1-bromo-4-nitrosobenzene (**13**)



13

4-Bromoaniline, **12**, (3.0980 g, 18.008 mmol) (Oakwood Chemical) was placed in a 500 mL round bottom flask (RBF) with DCM (90.0 mL) and stirred at rt to dissolve. OXONE[®] (22.1693 g, 36.0184 mmol) (Alpha Aesar) was dissolved in water (115.0 mL) and added all at once to the stirring **12**-DCM mixture. The reaction was complete after 6 h of vigorous stirring as determined by TLC analysis indicating the absence of starting material **12**. The green organic layer was collected, and the aqueous layer extracted with DCM (3x10 mL). The combined organic phases were then dried over anhydr Na₂SO₄, filtered, and solvent was removed in vacuo to provide the crude product **13** (3.14 g, 16.9 mmol, 94%) as a faint beige solid, which was used without further purification in a Mills condensation reaction.

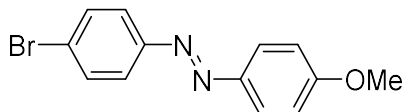
Rueck-Braun et al. previously reported the synthesis at 70% yield.⁶³

Crude Yield: 94%

MW = 186.01 g mol⁻¹

¹H-NMR (360 MHz, CDCl₃): δ 7.78 (s, 4H).

4-bromo-4'-methoxyazobenzene (**15**)



15

Product **13** (3.14 g, 16.9 mmol) was combined with glacial acetic acid (76.0 mL) and stirred in a 250 mL RBF, forming a colloidal mixture. Separately, *p*-anisidine **14** (1.9500 g, 15.834 mmol) (Acros Organics) was dissolved in ethanol (45.0 mL) in a beaker before being added slowly to the stirring **13**-acetic acid mixture. The reaction was stirred for 8 h at rt at which time TLC (1:1 DCM-Hexanes) indicated the absence of any starting material **13**. DCM (50 mL) was added to the RBF, and the organic phase extracted after adding brine (5 mL) as a separation aid. The aqueous layer was washed with DCM (3x50 mL) before extracting the combined DCM phase with saturated NaHCO₃ (aq) (20 mL) to neutralize any remaining acid. The organic phase was dried over anhydr MgSO₄, filtered, and solvent was removed in vacuo to yield crude **15** as a metallic brown powder. The crude product was dissolved in DCM (20 mL) and filtered through a plug of silica gel. After solvent removal in vacuo, the solid was recrystallized from 3:1 methanol/ethanol to produce a pale orange amorphous solid (4.28 g, 14.7 mmol, 93%).

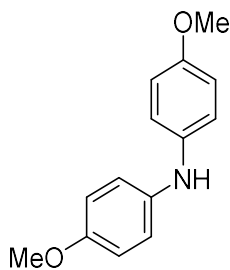
Feringa et al. previously reported the synthesis at 64% yield.⁷⁹

Yield: 93%

MW = 291.15 g mol⁻¹

¹H-NMR (360 MHz, CDCl₃): δ 7.91 (d, *J* = 9.1 Hz, 2H), 7.76 (d, *J* = 8.8 Hz, 2H), 7.62 (d, *J* = 8.8 Hz, 2H), 7.01 (d, *J* = 9.1 Hz, 2H), 3.90 (s, 3H).

N,N-di-*p*-anisylamine (**17**)



17

A 100 mL RBF was charged with *p*-anisidine **14** (4.93 g, 40.0 mmol) (Acros Organics) and 4-bromoanisole **16** (2.7 mL, 4.0 x 10¹ mmol) (Alpha Aesar) and transferred to a N₂ purged dry box, where Pd(dba)₂ (0.115 g, 0.200 mmol), a 0.100 M solution of P(*t*Bu)₃ in anhydr toluene (2.00 mL, 0.0405 g, 0.200 mmol), and NaO*t*Bu (5.77 g, 60.0 mmol). After adding 60 mL anhydr toluene, the mixture was stirred for ~1 min. The flask was capped with a rubber septum, removed from the dry box and placed under N₂. The reaction mixture was stirred for 1 h while heating in a silicone oil bath at 90 °C, allowed to cool, and then filtered through 5 g basic alumina III by vacuum filtration. The filter cake was washed with ethyl acetate (~ 200 mL), and the combined solvents were removed in vacuo to yield a grey-purple amorphous solid, which was recrystallized from hexanes to give pale pink crystals of pure **12** (8.71 g, 38.0 mmol, 95%).

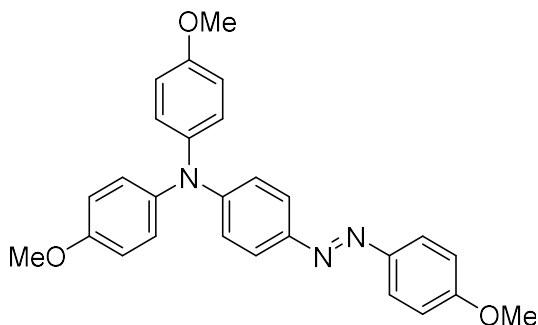
Endo et al. previously reported the synthesis using BHA condition with BINAP ligand at 67% yield.⁸⁰

Isolated Yield: 95%

MW = 229.28 g mol⁻¹

¹H-NMR (360 MHz, C₆D₆): δ 6.82 (d, *J* = 9.1 Hz, 4H), 6.77 (d, *J* = 9.2 Hz, 4H), 4.71 (s, 1H), 3.36 (s, 6H).

4-amino-(*N,N*-di-*p*-anisyl)-4'-methoxyazobenzene (**11**)



11

A flame-dried 2 dram vial was charged with **17** (0.1179 g, 0.5142 mmol), while a flame-dried 25 mL RBF was charged with 4-bromo-4'-methoxyazobenzene **15** (0.1503 g, 0.5162 mmol) and a stir bar. Transferring to a N₂ purged dry box, anhydr toluene (2 mL), Pd(dba)₂ (0.0056 g, 0.0097 mmol), and a

0.10 M solution of P(*t*Bu)₃ in anhydr toluene (1 μL, 0.0001 mmol) were added to the RBF. The vial of **17** was transferred to the RBF with toluene (6 mL) washings. Lastly, NaO*t*Bu (0.0754 g, 0.785 mmol) and toluene (2 mL) were added to the flask and stirred for ~1 min. The flask was capped with a rubber septum, removed from the dry box, and the mixture was stirred under N₂ in a silicone oil bath at 90 °C for ~24 h, allowed to cool, and then filtered through a layered bed of celite and 5 g basic alumina III by vacuum filtration. The filter cake was washed with THF (~ 100 mL), and the combined solvents were removed in vacuo to yield an orange-red amorphous solid, which was recrystallized from isopropanol to afford **11** (0.17 g, 0.39 mmol, 75%) as an amorphous orange solid.

Blackstock et al. previously reported the synthesis using BHA condition with at 89% yield (mp 100-104 °C).⁶⁰

Yield: 75%

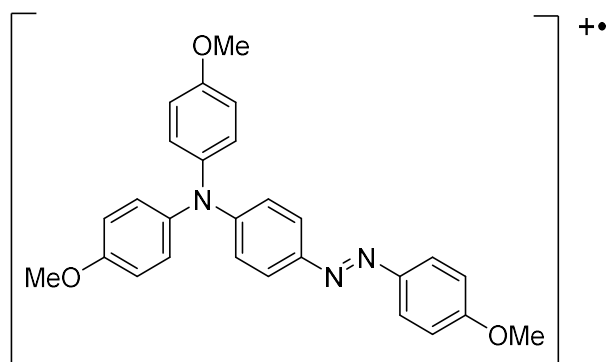
MW = 439.52 g mol⁻¹

¹H-NMR (500 MHz, CDCl₃): δ 7.85 (d, *J* = 9.0 Hz, 2H), 7.72 (d, *J* = 9.0 Hz, 2H), 7.12 (d, *J* = 9.0 Hz, 4H), 6.99 (d, *J* = 9.0 Hz, 2H), 6.96 (d, *J* = 9.0 Hz, 2H), 6.87 (d, *J* = 9.0 Hz, 4H), 3.88 (s, 3H), 3.82 (s, 6H).

^{13}C -NMR (125 MHz, CDCl_3): δ 161.4, 156.7, 151.0, 147.6, 146.4, 140.2, 127.5, 124.3, 124.0, 119.1, 115.0, 55.7, 55.6.

UV/Vis (benzene, λ_{max} , ϵ , concentration, path length): 440 nm, 19,000 $\text{M}^{-1}\text{cm}^{-1}$, 5.7×10^{-5} M, 1.0 cm (Figure 2.7).

$11^{+\bullet}\text{PF}_6^-$ salt



$11^{+\bullet}\text{PF}_6^-$

To a flame-dried 2 dram screw-capped vial equipped with a stir bar, **11** (0.0026 g, 0.0059 mmol), nitrosonium hexafluorophosphate (NOPF_6 , 0.0018 g, 0.010 mmol) and 3.0 mL purified⁷⁸ and freshly distilled DCM were added, and the vial was capped. The solution

immediately became an opaque deep blue-green color upon addition of DCM to the vial. The solution was stirred for 10 min at ambient temperature before sparging with N_2 for ~ 3 min to remove the nitric oxide gas by-product. Should purge with N_2 stream immediately on mixing. The $11^{+\bullet}\text{PF}_6^-$ product was not isolated from the DCM solution. An EPR spectrum was immediately measured on the resulting product solution.

Optical spectrum of $11^{+\bullet}\text{PF}_6^-$ salt (Figure 2.20)

A ~ 1 mM solution of $11^{+\bullet}\text{PF}_6^-$ in DCM was used directly from the $11^{+\bullet}\text{PF}_6^-$ synthesis. Then 300 μL of this solution was transferred to a 0.1 cm quartz cuvette and capped with a Teflon stopper. Absorbance was measured from 200 to 800 nm.

Figure 2.19 EPR spectrum of $11^+PF_6^-$ (Figure 2.19)

CWEPR spectrum of $11^+PF_6^-$ (~1 mM) at 293 K in purified and distilled DCM measured using a ELEXSYS E680 EPR spectrometer (Bruker-Biospin, Billerica, MA) equipped with a Bruker Flexline ER 4118 CF cryostat and an ER 4118X-MD4 ENDOR resonator.

Photochemical Experiments

Optical spectrum of **11 in benzene (Figure 2.7)**

A solution of 5.7×10^{-5} M **11** in deaerated benzene was prepared by dissolving 0.00025 g of **11** to 10.0 mL benzene solution via volumetric flask. Then 3.0 mL of this solution was transferred to a 1.0 cm quartz cuvette and capped with a Teflon stopper. Absorbance was measured from 200 to 800 nm.

Photochemical conversion of E-11 to PSS E/Z-11 mixture (Figure 2.8)

A solution of 5.7×10^{-5} M **11** in benzene was prepared as for Figure 2.6. Then 3.0 mL of this solution was transferred to a 1.0 cm quartz cuvette and capped with a Teflon stopper. The optical spectrum of the sample was recorded (200-800 nm) every 5 seconds under irradiation by a 430 nm 7 W LED source for 5 minutes to achieve the photostationary state of **11**.

1H -NMR spectra of E-11 and the E/Z-11 mixture at the PSS_{430 nm} (Figure 2.9)

A solution of 3.8×10^{-2} M **11** in benzene- d_6 was prepared by dissolving 0.0101g of **11** in 600.0 μ L benzene- d_6 and 2.0 μ L mesitylene in an NMR tube via gas-tight syringes. Benzene- d_6

was sparged with N₂ gas for ~ 5 min in a vial prior to use. A stream of N₂ gas was blown into the NMR tube for ~ 1 min prior to capping and sealing with a small strip of parafilm. The tube was kept covered until inserting into the NMR instrument to minimize light exposure to obtain an all *E* isomer spectrum. After the all *E* spectrum was measured the NMR tube was irradiated with a 430 nm light source to achieve PSS. The NMR tube was placed in a mirrored Dewar with ~100 mL of an ice-water slurry to prevent any sample heating from the light source placed on top. The sample was irradiated for ~ 30 min followed by additional ~15 min intervals until no change was detected in the ¹H-NMR spectrum.

Thermal Z→E conversion of 11 (Figure 2.10)

A solution of 6.4×10^{-4} M **11** in benzene-*d*₆ was prepared by first dissolving 0.0014 g of **11** in 1.0 mL benzene-*d*₆ to yield a 3.2×10^{-3} M stock solution of **11**, following with a dilution of 100 μL to 500 μL benzene-*d*₆. Prior to addition, benzene-*d*₆ was sparged with N₂ gas for ~5 min. The solution was sparged for ~1 min before transferring 300 μL to a 0.1 cm quartz cuvette via gas-tight syringe and capped with a Teflon stopper. The solution was irradiated with a 430 nm 7 W LED source to reach the PSS, as confirmed by the optical spectrum. The thermal Z→E conversion starting at PSS, was followed by measuring the absorbance (200-800 nm region) in the dark at 10 min intervals for 12 h.

Cyclic voltammogram of 11 (Figure 2.11)

To a 25 mL volumetric flask, TBABF₄ (0.8242 g, 2.503 mmol) and purified,⁷⁸ freshly distilled DCM (25.0 mL) was added. The 0.100 M electrolyte solution (8.0 mL) was transferred

to an electrochemical cell (4-neck flask). A blank cyclic voltammogram (0.0 V to 1.1 V vs. SCE, 50 mV/s) confirmed an absence of impurities before adding **11** (0.0034 g, 7.7×10^{-6} mol) to the flask with stirring to make the 0.96 mM solution. The potential was scanned from 0.0 V to 1.05 V vs. SCE at a rate of 50 mV/s.

Redox Z→E switching of **11 (Figure 2.12)**

A 6.4×10^{-4} M **11** solution in benzene-*d*₆ was prepared as for Figure 2.9. Separately, a 6.3×10^{-4} M solution of CRET was prepared from dissolving CRET (0.00038 g, 6.3×10^{-7} mmol) in freshly distilled DCM (1.0 mL). To a 0.1 cm quartz cuvette, 300.0 μL of **11** solution (1.9×10^{-7} mol) was added and capped with a Teflon stopper and irradiated to the PSS with a 430 nm LED source as followed by optical spectroscopy. The PSS mixture was then injected via syringe with 3 μL of the CRET solution (1.9×10^{-9} mol, 1.0%), capped, and shaken (~2 s) before measuring the absorbance (200-800 nm).

Photo, Photo-Electro E→Z and Z→E switching of **11 with MB⁺ (Figure 2.15) and Photo, Photo-Electro E→Z→E cycling of **11** with MB⁺ (Figure 2.19)**

A N₂-deaerated 5.51×10^{-5} M solution of **11** in toluene was prepared. To a 1.0 cm quartz cuvette was added 3.0 mL of **11** in toluene solution along with 65 μL of a N₂-deaerated 1.28×10^{-4} M solution of MB⁺ in methanol (5.0 mol% based on **11**). The resulting concentrations of **11** and MB⁺ in the cuvette were 5.38×10^{-5} M and 2.7×10^{-6} M, respectively. The cuvette was closed with a Teflon™ stopper. Two LED light sources (430 nm and 660 nm) were positioned to irradiate the cuvette at a distance of 4-5 inches. The lights were toggled on and off, alternating in sequence, at 1 min intervals while the optical spectrum of the sample was recorded (200-800 nm)

every 15 s. A total of ten 430/660 nm switching cycles were performed, after which sample monitoring by UV-vis spectroscopy was continued for an additional 20 min with no irradiation. A control experiment (eight 430/660 nm switching cycles) was performed analogously but in the absence of methylene blue (**MB**⁺) photooxidant. The results from the control experiment (black curve) are overlaid with the results from the photooxidant cycling experiment (dashed-grey curve).

Optical spectrum of **MB⁺ under blue or red light exposure (Figure 2.16)**

A 2.7×10^{-6} M **MB**⁺ solution in 2.1% methanol:toluene was prepared as for Figure 2.15. To a 1.0 cm quartz cuvette was added 3.0 mL of **MB**⁺ solution. Two LED light sources (430 nm and 660 nm) were positioned to irradiate the cuvette at a distance of 4-5 inches. While either under red light (left) or blue light (right) exposure, the optical spectrum of the sample was recorded (200-800 nm) every 2 seconds for 10 minutes.

Photochemical conversion of the PSS_{430nm}→PSS_{660nm} of **11 (Figure 2.17)**

A 5.38×10^{-5} M **11** solution in 2.1% methanol:toluene was prepared as for Figure 2.15. To a 1.0 cm quartz cuvette was added 3.0 mL of **11** solution. Two LED light sources (430 nm and 660 nm) were positioned to irradiate the cuvette at a distance of 4-5 inches. PSS was achieved as with Figure 2.8. Starting from PSS_{430nm}, the optical spectrum of the sample was recorded (200-800 nm) every 10 s under a 430 nm 7 W LED source for 60 min to achieve the new photostationary state of **11**.

Thermal Z→E conversion of 11/MB⁺ mixture (Figure 2.18)

A 5.38×10^{-5} M **11** and 2.7×10^{-6} M **MB⁺** solution in 2.1% methanol:toluene was prepared as for Figure 2.15. To a 1.0 cm quartz cuvette was added 3.0 mL of **11/MB⁺** solution. The solution was irradiated with a 430 nm 7 W LED source for a few minutes to reach the PSS, as confirmed by the optical spectrum. The thermal Z→E conversion starting at PSS, was followed by measuring the absorbance (200-800 nm region) in the dark at 1 min intervals for 4 h.

CHAPTER 3.

PHOTO-REDOX SWITCHING OF BIS(AZOBENZENE) DERIVATIVES

3.1. Introduction

The substitution of a redox group onto azobenzene was demonstrated in chapter 2 to greatly accelerate $Z \rightarrow E$ isomerization upon a single electron oxidation, gaining greater switching control between the Z or E isomer on command. The Blackstock group has shown this with single azobenzene moieties attached to a dianisylamine center,⁶⁰ and a double azobenzene case using a phenylenediamine (PD) center.⁸¹ The phenylenediamine group has also been shown to be an efficient redox auxiliary center, allowing for low catalytic loading as a result of extreme chemical stability, which arises from the radical cation charge delocalization over two nitrogen atoms in the PD unit.⁸¹

This project focuses on bis-systems linking two azobenzene units to a single *p*-anisylamine N-center as shown in target molecules **20** and **21**. With both bis-systems, we hypothesize the simultaneous switching of 2 azobenzene groups connected to a single **ra** unit from their Z isomer to their E isomer using a single electron oxidation at the **ra** amine. The photo-, thermal-, and electro-switching properties of bis(azobenzene)-*p*-anisidines **20** and **21** have been examined and are presented in this chapter. In the case of the bis(azo) molecules **20** and **21**, there are three possible isomeric states and molecular shapes: the Z,Z -, E,Z - and E,E -states, allowing for a much more extensive molecular shape change than in a mono(azo) structure. Target structure **21** is chosen for its anticipated extended Z -azobenzene isomer

lifetimes based on the known increased persistence and stability afforded to the *Z* isomer for tetra-*ortho*-fluoroazobenzenes, whose lifetimes can be up to 2 years.^{82, 83}

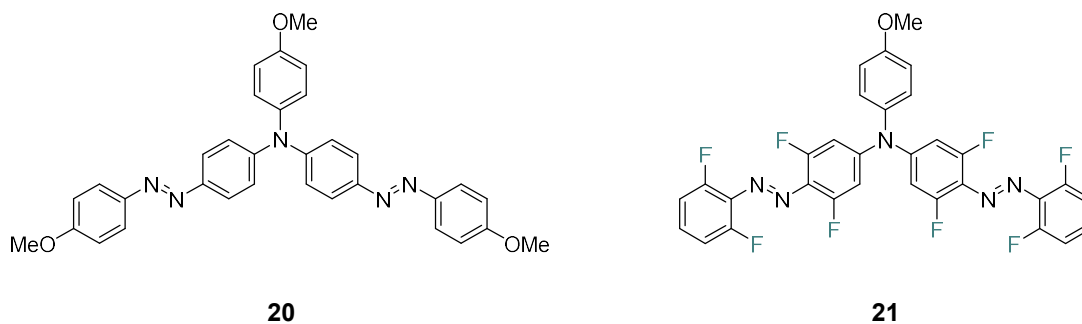
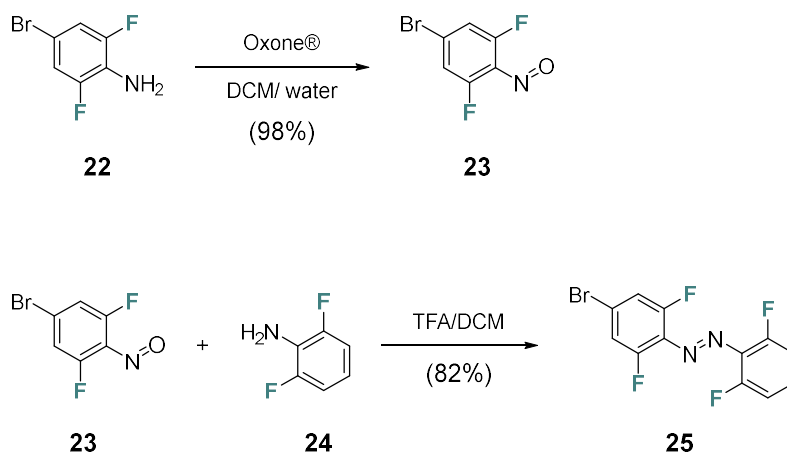


Figure 3.1. Target compounds **20** and **21**.

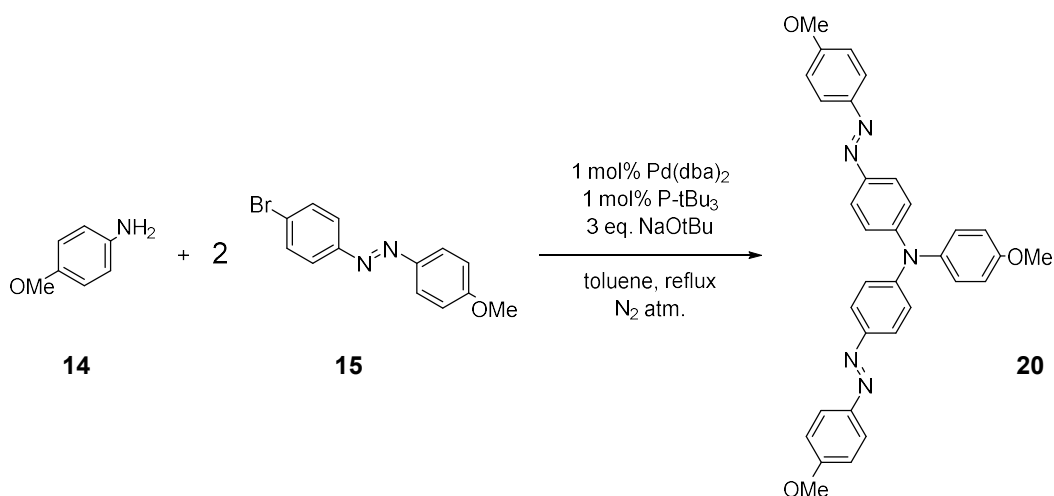
3.2. Synthesis of Redox Appended Bis(azobenzene)-*p*-anisidines **20** and **21**

The syntheses of bis(azobenzene)-*p*-anisidine derivatives **20** and **21** were achieved by Buchwald-Hartwig amination (BHA) reactions of the appropriate *p*-bromo-azobenzene with *p*-anisidine.⁶⁷⁻⁶⁹ The required bromo-azobenzene for BHA synthesis of **20** is 4-bromo-4'-methoxyazobenzene **15**, which was prepared and purified as discussed in Chapter 2 in 87% yield (Scheme 2.1). For BHA preparation of **21**, 4-bromo-2,2',6,6'-tetrafluoroazobenzene (**25**) is needed and has been similarly synthesized by the sequence shown in Scheme 3.1. OXONE[®] oxidation of 4-bromo-2,6-difluoroaniline (**22**) produces 5-bromo-1,3-difluoro-2-nitrosobenzene (**23**) as a green solution (brown solid) in 98% crude yield, followed by a Mills condensation reaction between **23** and 2,6-difluoroaniline (**24**) using catalytic trifluoroacetic acid (in place of the typical acetic acid medium),⁸⁴ yielding **25** as a red solid in 82% yield.



Scheme 3.1. Synthesis of nitrosobenzene **23** using OXONE oxidation in a biphasic solution of dichloromethane and water. The Mills condensation reaction using trifluoroacetic acid (TFA) and dichloromethane (DCM) to generate the unsymmetrical azobenzene **25**.

Scheme 3.1 illustrates the synthesis of **20** by BHA coupling of *p*-anisidine (**14**) and 4-bromo-4'-methoxyazobenzene (**15**) in a 1:2 molar ratio. The crude product was purified by crystallization from 1:3 benzene-isopropanol to yield the target **20** as a red powder in 70% yield.

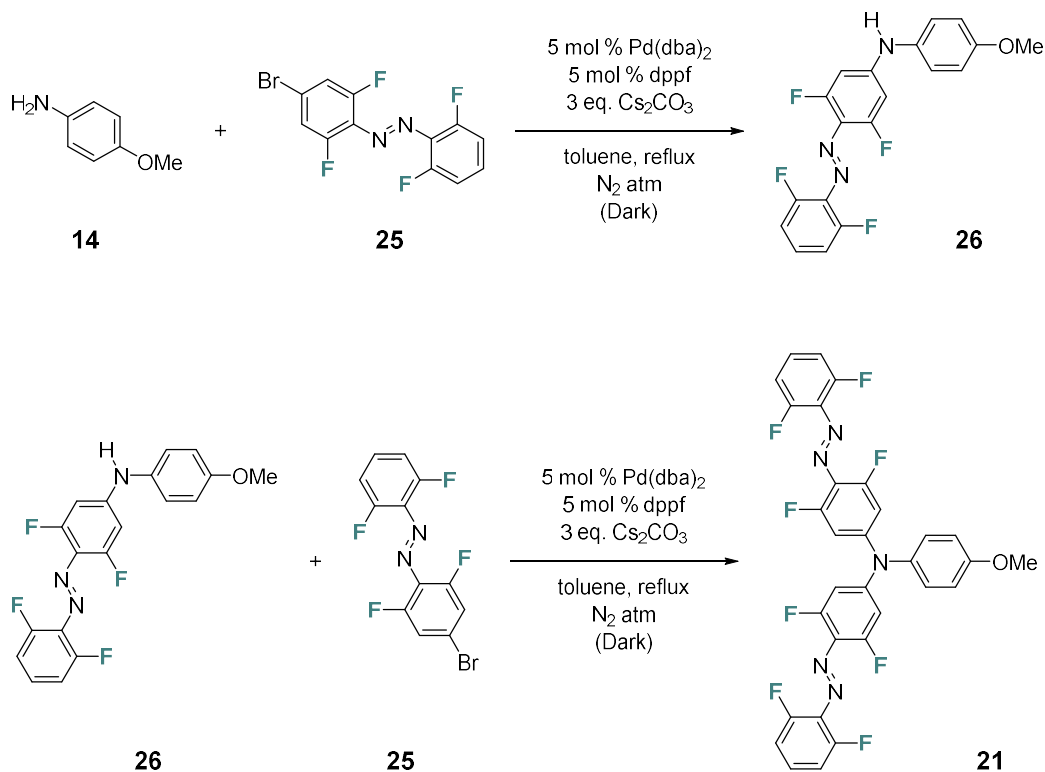


Scheme 3.2. Buchwald-Hartwig Coupling of **14** and **15** using bis(dibenzylideneacetone)palladium (0) (Pd(dba)₂), tri-*tert*-butylphosphine (P(*t*Bu)₃), and sodium *tert*-butoxide at 111 °C in an oil bath under N₂ atmosphere yielding **20**.

BHA coupling of aryl bromides and anilines using Pd(dba)₂ catalyst, P(*t*Bu)₃ ligand, and NaO*t*Bu base in toluene at 80-111 °C is commonly employed in the Blackstock group to afford *N*-amination products in good yield. However, this recipe for coupling of tetrafluoroazobenzene (**25**) to dianisylamine (**17**) produced only undesired products. It has been speculated that the fluorinated substrate **25** might be sensitive to the *t*-butoxide base. To remedy this issue, the milder base cesium carbonate (Cs₂CO₃) was used to limit possible base-substrate interactions.^{67, 85} The base exchange prevented the consumption of the reactants toward non-coupled products. The oxidative addition is favored with the electron-deficient bromoazobenzene **25**, and the electron-rich amine **17** favors the amine ligation step of the catalytic cycle, leaving reductive elimination to be optimized, which was best accomplished by changing to a bidentate ligand with a wider bite angle, 1,1'-bis(diphenylphosphino)ferrocene (dppf).^{86, 87} These 'alternative' BHA coupling conditions allowed for a successful C,N bond formation as shown in Scheme 3.3. Also as displayed in Scheme 3.3, sequential *N*-arylation reactions proved to give a better overall yield of **21** than running the reaction with 2 equivalents of bromoazobenzene.

First, BHA coupling of **25** and **14** affords, after crystallization from 1:100 toluene-hexane, monoazobenzene **26** as red needles in 79% yield. Next, a second BHA coupling of **25** and **26** affords, after crystallization from 1:10 benzene-isopropanol, the target bis-system **21** as a red powder in 68% yield. In general, all reactions involving tetrafluoroazobenzene moieties were kept in the dark to reduce the production of the long-lived *Z* isomers.

In summary, the two bis-systems (**20** and **21**) are synthesized in good to moderate yield as indicated above. The photochemical properties of **20** and **21** are next determined and compared.



Scheme 3.3. Buchwald-Hartwig coupling of **14** and **25** using bis(dibenzylideneacetone)-palladium(0) (Pd(dba)₂), 1,1'-bis(diphenylphosphino)-ferrocene (dppf), and cesium carbonate (Cs₂CO₃) at 111 °C in an oil bath under N₂ atmosphere yielding **26**. This is followed by a second coupling of **25** and **26** under the same conditions to yield the target, **21**.

3.3. The Optical Spectra and Photochemistry of Bis(azobenzene)-*p*-anisidines **20** and **21**

Figure 3.2 shows the optical spectrum of *E,E*-**20** in deaerated benzene. The spectrum contains a π - π^* band at 466 nm that overlaps its n - π^* band. The overlap of the π - π^* and n - π^* bands is a common consequence in *p*-amino-substituted azobenzenes as discussed in section 1.5. Red shifting of the π - π^* absorption is expected with the increased conjugation resulting from addition of a second azobenzene bonded to the amine N-atom in bis(azobenzene) **20**, whose λ_{\max} appears at 466 nm compared to the π - π^* band λ_{\max} for aminoazobenzene **11** at 436 nm and the parent azobenzene system (**1**) π - π^* band λ_{\max} at ~320 nm.

Irradiation at the π - π^* band triggers $E \rightarrow Z$ photoisomerization. The $E \rightarrow Z$ isomerization is followed by dynamic UV-vis spectroscopy until an equilibrium is achieved, which is termed the photostationary state (PSS). The isomer composition at the PSS is wavelength dependent.

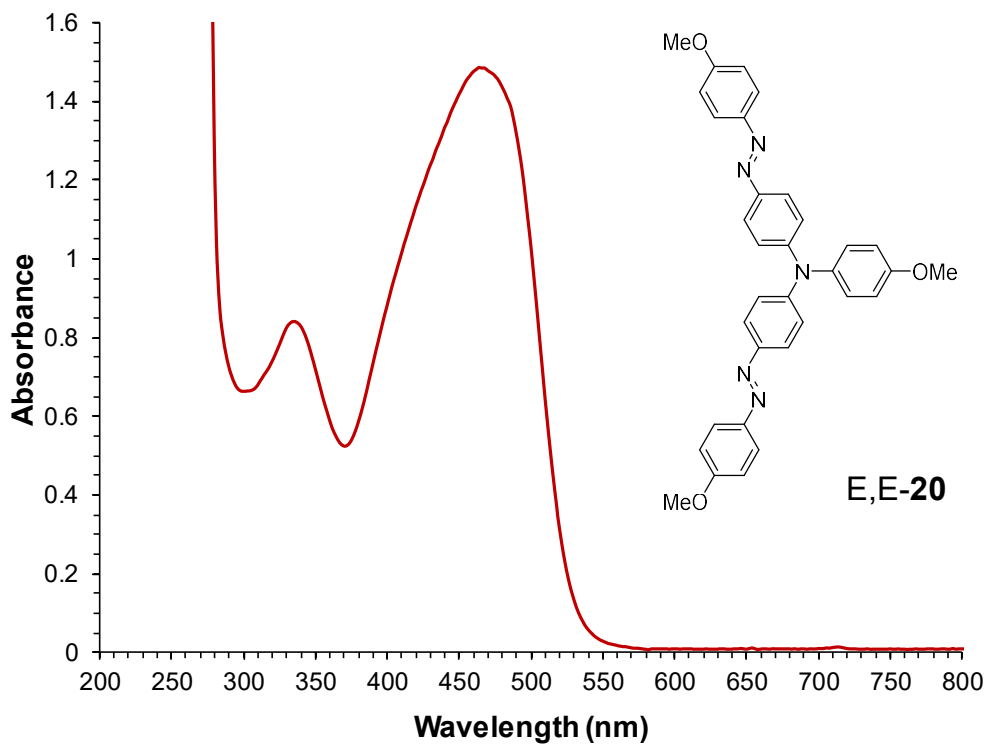


Figure 3.2. Optical spectrum of **20** in benzene (2.3×10^{-5} M) in a 1.0 quartz cuvette at room temperature.

A deaerated **20** benzene solution is irradiated using a 457 nm LED light. A decrease in the absorbance curve at most wavelengths is observed upon irradiation, with the increase in Z -isomer population, which has a weaker absorbance than the E isomer counterpart at 312 - 528 nm. Figure 3.3 shows the change in the absorbance curve over time until the $\text{PSS}_{457 \text{ nm}}$ is achieved. The optical spectra overlay of E,E -**20**, $\text{PSS}_{457 \text{ nm}}$, and intermediate spectra show two

isosbestic points at 312 nm and 528 nm. Isosbestic points occur when absorbance remains unchanged at a given wavelength for interconverting species. The points confirm the clean interchange of two or more isomer species in chemical equilibrium whose UV-vis spectra have identical absorptivity at these wavelengths.

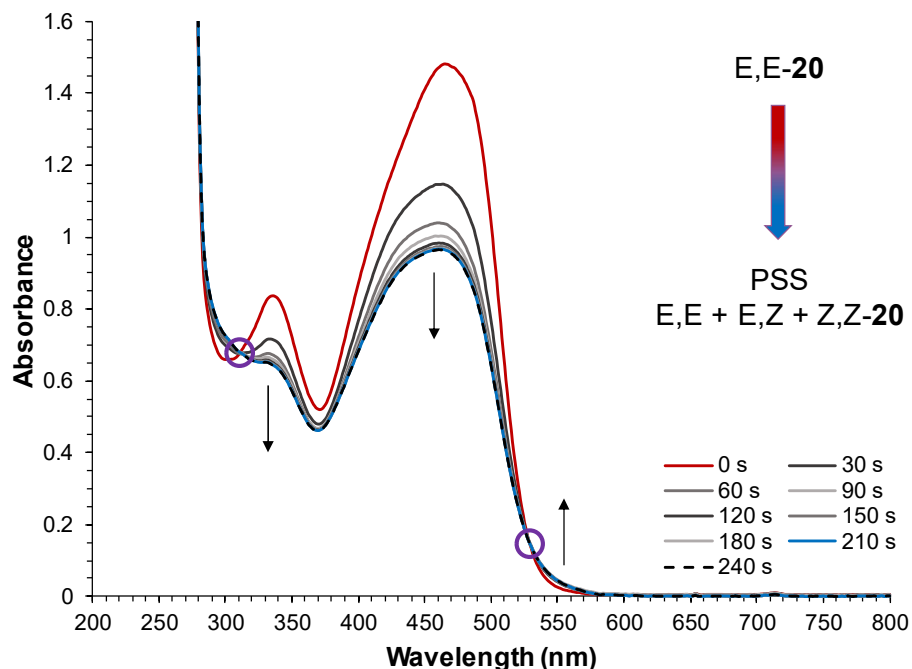
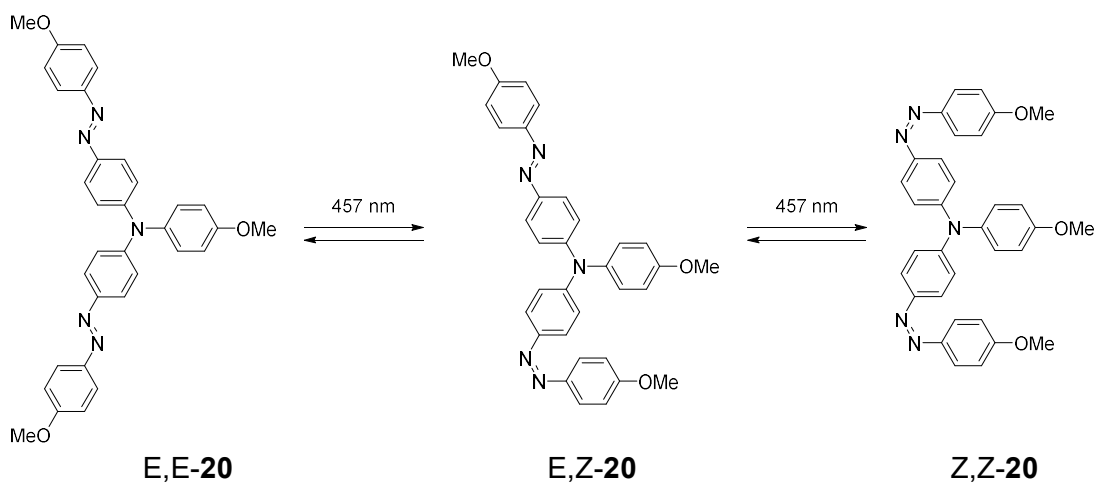


Figure 3.3. Optical spectra overlay of **20** (2.3×10^{-5} M in benzene) upon irradiation with 457 nm LED lamp in a 1.0 cm quartz cuvette at room temperature. Following from *E,E-20* to $PSS_{457\text{ nm}}$, with two isosbestic points observed at 312 and 528 nm.

The isomer composition at PSS_{457 nm} has been determined by ¹H-NMR spectroscopy. The spectrum for *E,E*-**20** is shown in Figure 3.4. The methoxy signals near 3-3.5 ppm are used as diagnostic peaks to identify and quantify the new *E,Z*- and *Z,Z*-isomer formed from irradiation. A ¹H-NMR spectrum expansion of the methoxy peak region pre- and post-irradiation to PSS_{457 nm} is shown in Figure 3.5. The anisyl methoxy peak appears near 3.3 ppm and is more deshielded than the azobenzene methoxy peak, which appears near 3.2 ppm for all isomers. The *E,E*-; *E,Z*-; and *Z,Z*-**20** methoxy signals are then identified in the post irradiation spectrum. Each additional *E*→*Z* azo moiety isomerization causes a slight shielding of the methoxy signals, owing to the decreased conjugation with the electron withdrawing azo moiety. The methoxy hydrogens on the *Z*-azobenzene have the largest ppm shift with *Z,Z*-**20** shifting to 3.13 ppm. The *E,E*-isomer peak positions remain unchanged from prior to irradiation, with a 1:2 integration ratio. The *E,Z*-isomer signals have a 1:1:1 integration ratio. Thus all **20** isomer methoxy ¹H-NMR signals can be identified and integrated to determine the PSS_{457 nm} composition, as depicted in Figure 3.5. The results give a PSS_{457 nm} composition of 38 % *E,E*-**20** (black), 47 % *E,Z*-**20** (red), and 15 % *Z,Z*-**20** (blue).

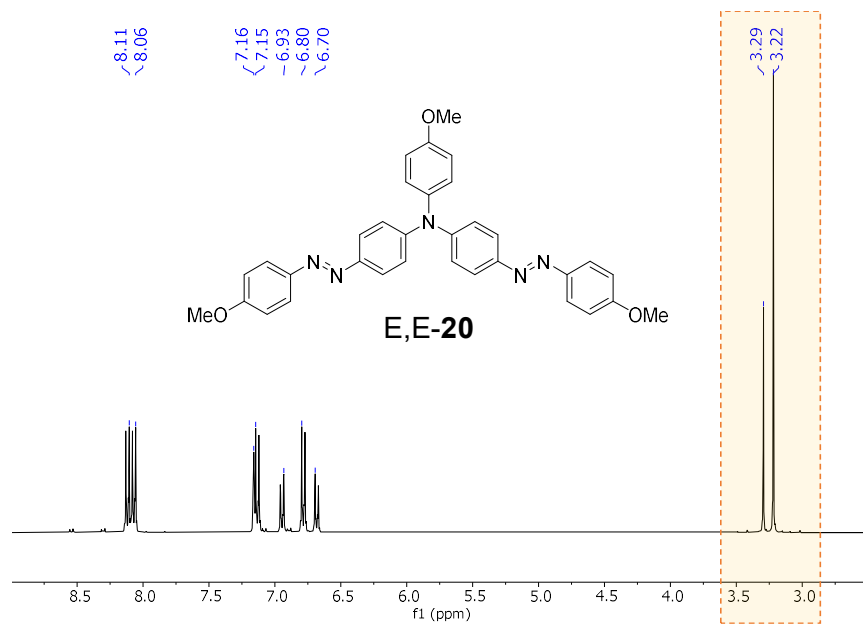


Figure 3.4. $^1\text{H-NMR}$ spectrum of **20** in benzene- d_6 .

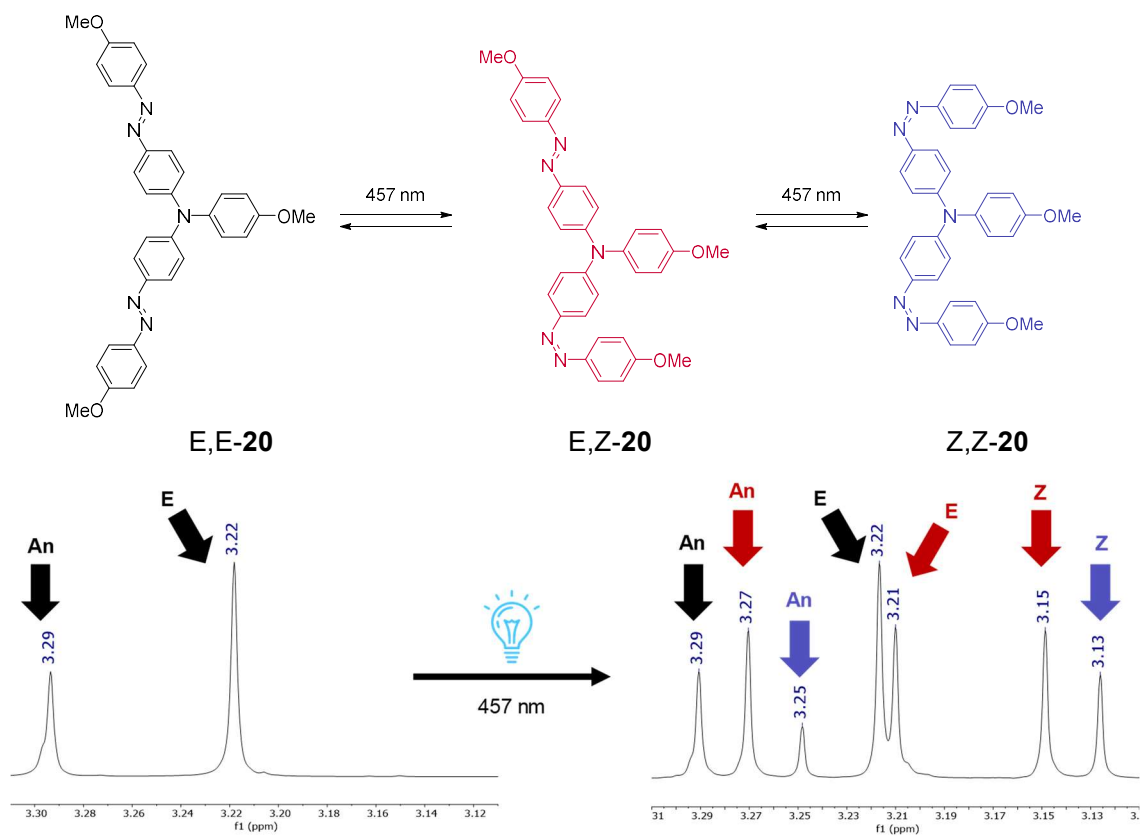


Figure 3.5. Methoxy region of the $^1\text{H-NMR}$ spectra of **20** in benzene- d_6 before and after irradiation to PSS $_{457\text{ nm}}$.

The optical spectrum of *E,E*-**21** in deaerated benzene contains a π - π^* band with $\lambda_{\text{max}} = 416$ nm (Figure 3.6). This absorption is red shifted in comparison the analogous bands in the optical spectra of similarly fluorinated systems **27** and **28** in Figure 3.7. Compound **27** has a π - π^* band with $\lambda_{\text{max}} = 305$ nm and a resolved n - π^* band at 458 nm in acetonitrile.³ While compound **28** has a π - π^* band with $\lambda_{\text{max}} = 406$ nm (overlapping the n - π^* band) in benzene.² When comparing the **21** π - π^* band (416 nm) to both those of **11** (436 nm) and **20** (466 nm), there is less red shifting occurring in comparison to **1** (320 nm). The electron-withdrawing effect of the *ortho*-fluoro groups is likely counteracting some of the red shifting effect expected upon the addition of the electron donating amine redox center and extended conjugation of the second azobenzene unit.

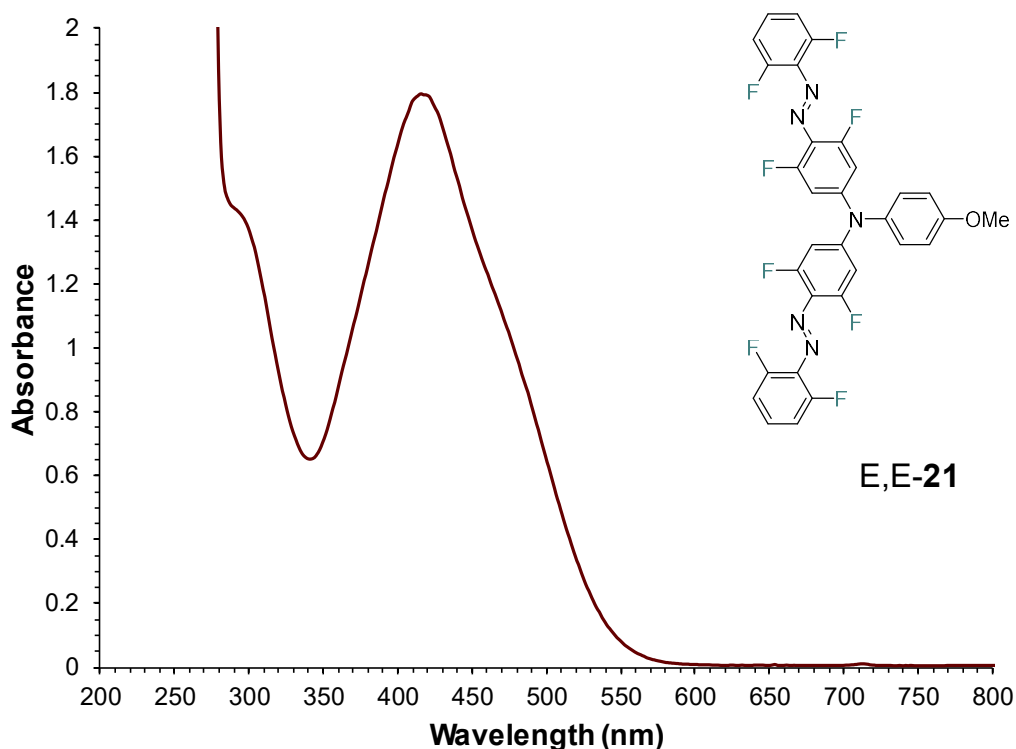


Figure 3.6. The optical spectrum of *E,E*-**21** in deaerated benzene (6.6×10^{-5} M) in a 1.0 cm quartz cuvette at room temperature.

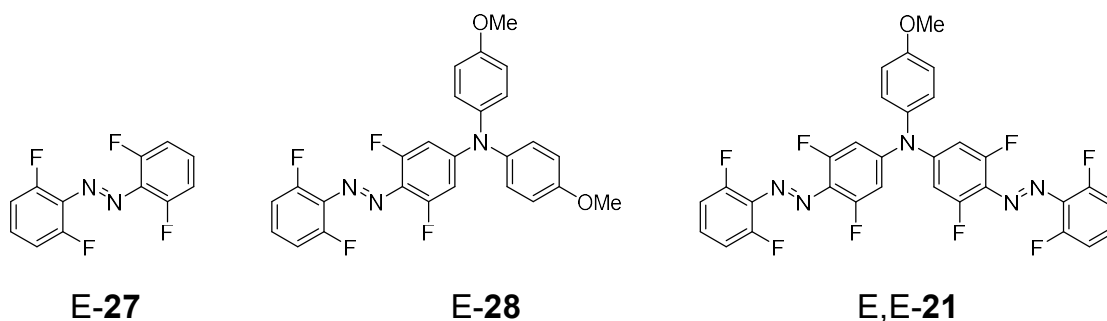


Figure 3.7. Structures of parent fluorinated azobenzene (**27**),³ redox appended fluorinated azobenzene (**28**),² and target bis-system (**21**).

The impact of irradiation with 457 nm is followed by UV-vis spectroscopy as displayed in Figure 3.8, which shows overlaid spectra during the $E \rightarrow Z$ photoconversion of E,E -**21** to $PSS_{457\text{ nm}}$ for **21**. The absorbance curve decreases with the increase of Z isomer concentration until the $PSS_{457\text{ nm}}$ is reached as observed for bis(azobenzene) **20**. However, in contrast to the photoisomerization of **20**, there are no clear isosbestic points observed upon photoisomerization of **21**. This can often occur when more than two isomeric states exist.

The $^1\text{H-NMR}$ spectrum for E,E -**21** is shown in Figure 3.9 with a single methoxy peak belonging to the anisyl group. This $^1\text{H-NMR}$ signal can be used to identify and quantify the isomer composition at PSS for **21** as the E,Z -**21** and Z,Z -**21** isomers form. The methoxy peak is shielded upon $E \rightarrow Z$ isomerization, as also observed in the photoisomerization of **20**. At the $PSS_{457\text{ nm}}$, there are 3 resolved methoxy signals, one belonging to each isomer (Figure 3.10), with the Z,Z -isomer having the most shielded signal. The assignment is again confirmed by observing the Z,Z -isomer signal disappears first thermally with time. These signal integrations are used to determine the isomer composition at the $PSS_{457\text{ nm}}$ as 29% E,E -, 45% E,Z -, and 26% Z,Z -**21**. This is a 9% decrease in E,E -**21**, a 2% decrease in E,Z -**21**, but an 11% increase in Z,Z -**21** in comparison to the isomer mixture for **20** at $PSS_{457\text{ nm}}$. Put another way, there is a 10% increase in

overall Z-isomer formation at the PSS_{457 nm} with **20** reaching 39% and **21** reaching 49%. The thermal stability of these Z isomers is next determined for both bis-systems **20** and **21**.

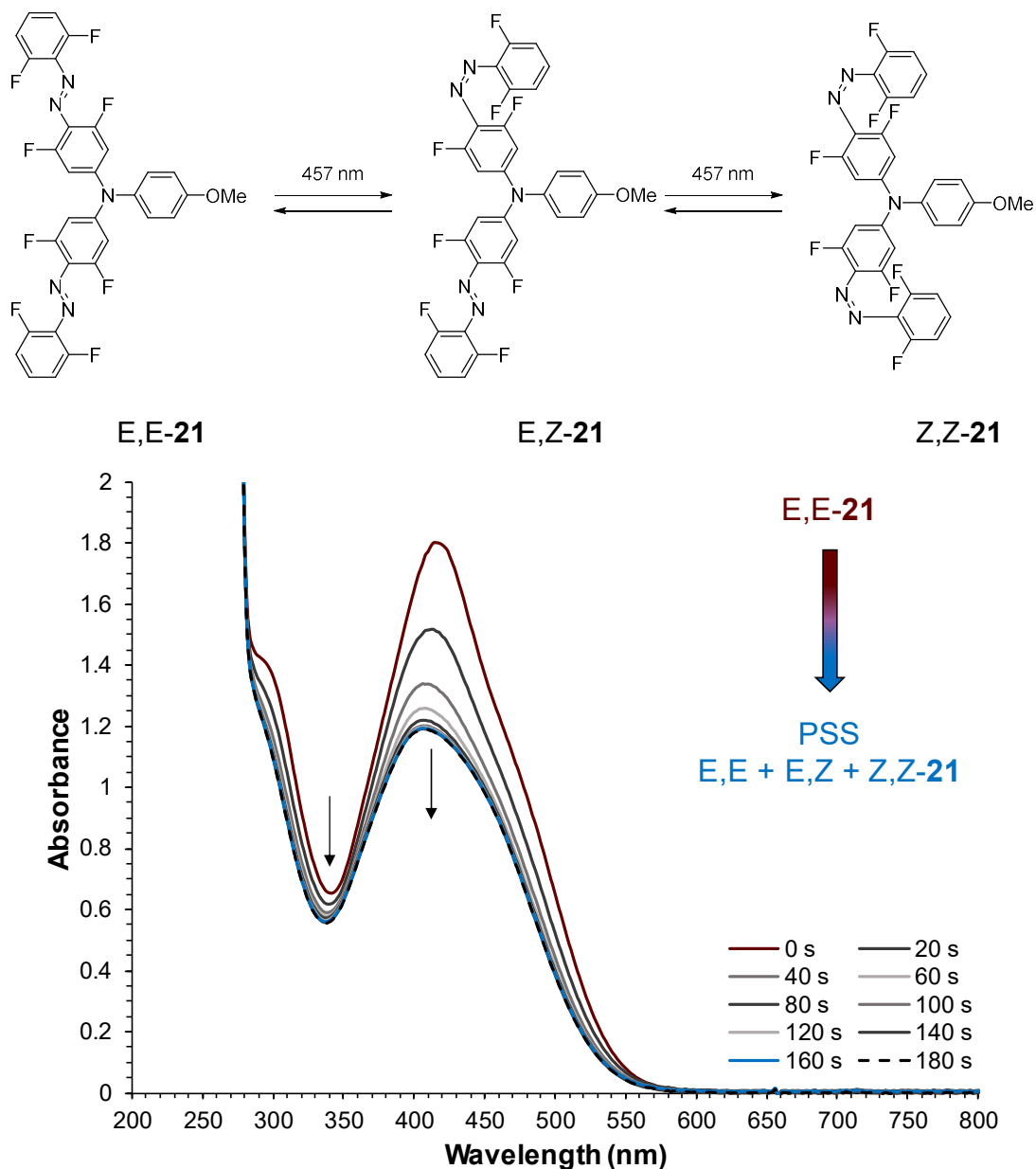


Figure 3.8. Optical spectra overlay following the irradiation of *E,E*-**21** (6.6×10^{-5} M) in deaerated benzene with 457 nm LED lamp showing conversion of *E,E*-**21** to PSS_{457 nm} composition in a 1.0 cm quartz cuvette at room temperature.

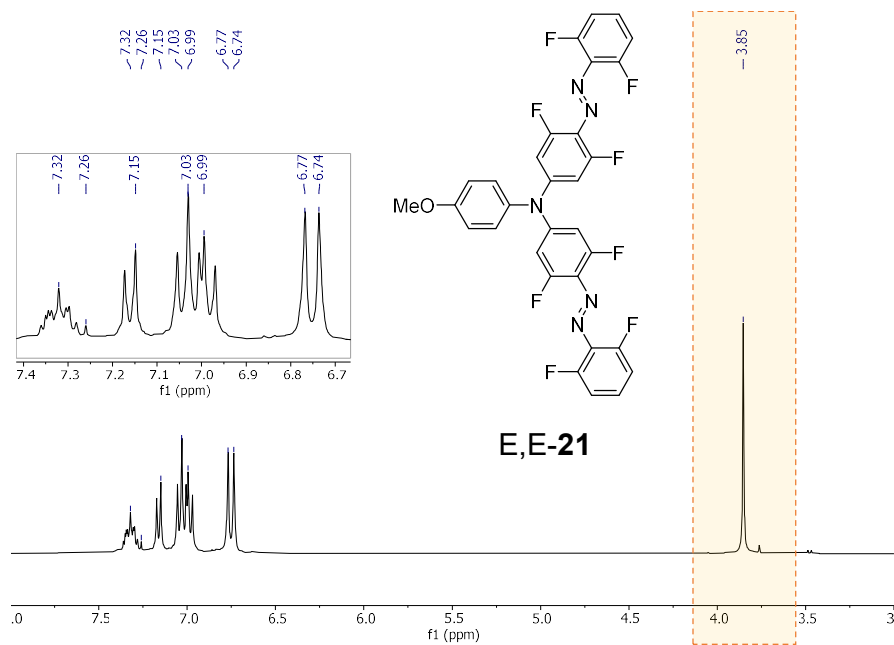


Figure 3.9. $^1\text{H-NMR}$ spectrum of **21** in chloroform- d_1 .

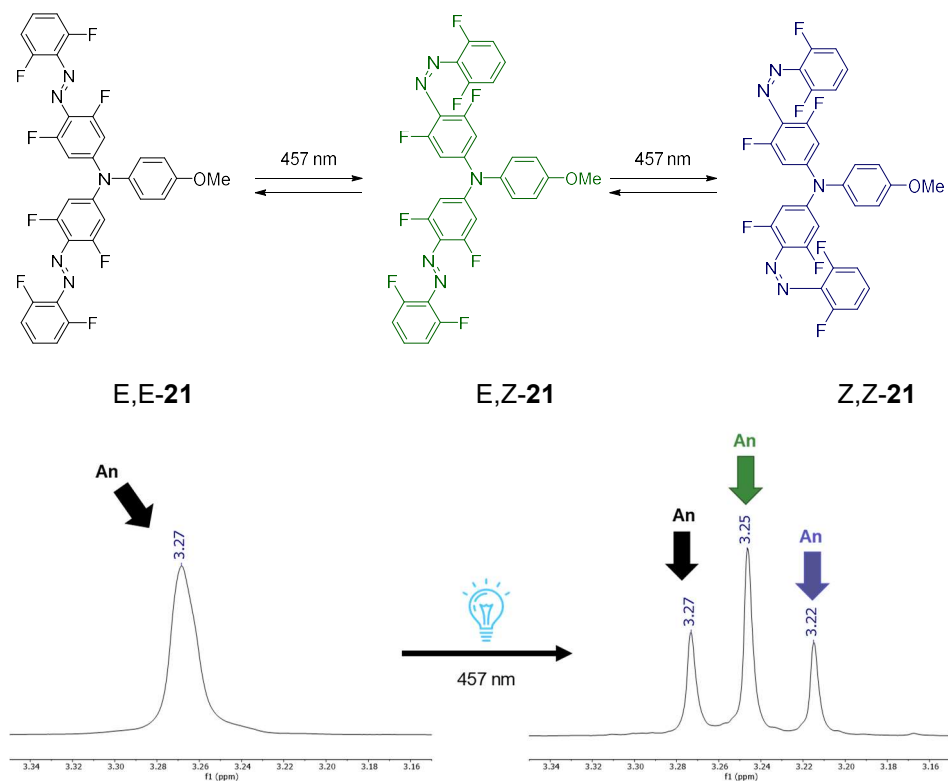


Figure 3.10. Methoxy region of the $^1\text{H-NMR}$ spectra of **21** in benzene- d_6 before and after irradiation to PSS $_{457\text{ nm}}$. The isomer peaks are identified: *E,E*- (black), *E,Z*- (green), and *Z,Z*- (purple).

3.4. Thermal $Z \rightarrow E$ Isomerization of Bis(azobenzene)-*p*-anisidines

The Z isomer stability is determined at a specific temperature, measuring the rate of thermal $Z \rightarrow E$ “expansion”. While dynamic UV-vis spectroscopy is used to give a qualitative picture, it cannot determine the rate when more than one azobenzene unit is present, giving rise to multiple isomeric states. $^1\text{H-NMR}$ spectroscopy is necessary to determine the multi-state composition. The isomer concentration is tracked over time by $^1\text{H-NMR}$ spectroscopy. Plotting isomer concentration versus time gives a similar exponential curve for each of the bis-systems, with thermal isomerization occurring step-wise from the $Z,Z \rightarrow E,Z \rightarrow E,E$ -isomer. The Z,Z isomer concentration is a simple exponential decay from $Z,Z \rightarrow E,Z$ formation. While E,Z isomer concentration is expressing both growth from $Z,Z \rightarrow E,Z$ formation (until Z,Z -isomer is depleted) and decay from $E,Z \rightarrow E,E$ isomerization. E,E -isomer concentration is a simple exponential growth. Modeling of these results accounts for the k_1 rate term when determining the k_2 rate. The system is modeled using the 2-step consecutive rate law below in equations (3.1-3.3).

$$[Z, Z] = [Z, Z]_0 e^{-k_1 t} \quad (3.1)$$

$$[E, Z] = [E, Z]_0 e^{-k_2 t} + \frac{k_1 [Z, Z]_0}{k_2 - k_1} (e^{-k_1 t} - e^{-k_2 t}) \quad (3.2)$$

$$[E, E] = [azo]_{total} - [Z, Z]_0 e^{-k_1 t} - [E, Z]_0 e^{-k_2 t} - \frac{k_1 [Z, Z]_0}{k_2 - k_1} (e^{-k_1 t} - e^{-k_2 t}) \quad (3.3)$$

Figure 3.11 shows the change in isomer concentration over time for **20**. The exponential curves are fit with the appropriate rate law equation above to determine the rate constants. The $Z,Z \rightarrow E,Z$ rate constant (k_1) at 298 K is $3.66 \times 10^{-4} \text{ s}^{-1}$, which is a half-life of 31.5 minutes. The $E,Z \rightarrow E,E$ rate constant (k_2) at 298 K is $1.87 \times 10^{-4} \text{ s}^{-1}$, which is a half-life of 61.9 minutes. The Gibbs free energy of activation ($\Delta G^\ddagger_{(298 \text{ K})}$) of **20** is 22.1 kcal/mol for $Z,Z \rightarrow E,Z$ isomerization and 22.5 kcal/mol for $E,Z \rightarrow E,E$ isomerization, found by applying the Eyring transition state

theory given in equation (2.4). The $\Delta G^\ddagger_{(298\text{ K})}$ for $E,Z \rightarrow E,E$ isomerization of **20** (22.5 kcal/mol) is similar to the $Z \rightarrow E$ isomerization of **11** (22.3 kcal/mol) while lower in energy than for parent **1** (25.8 kcal/mol).

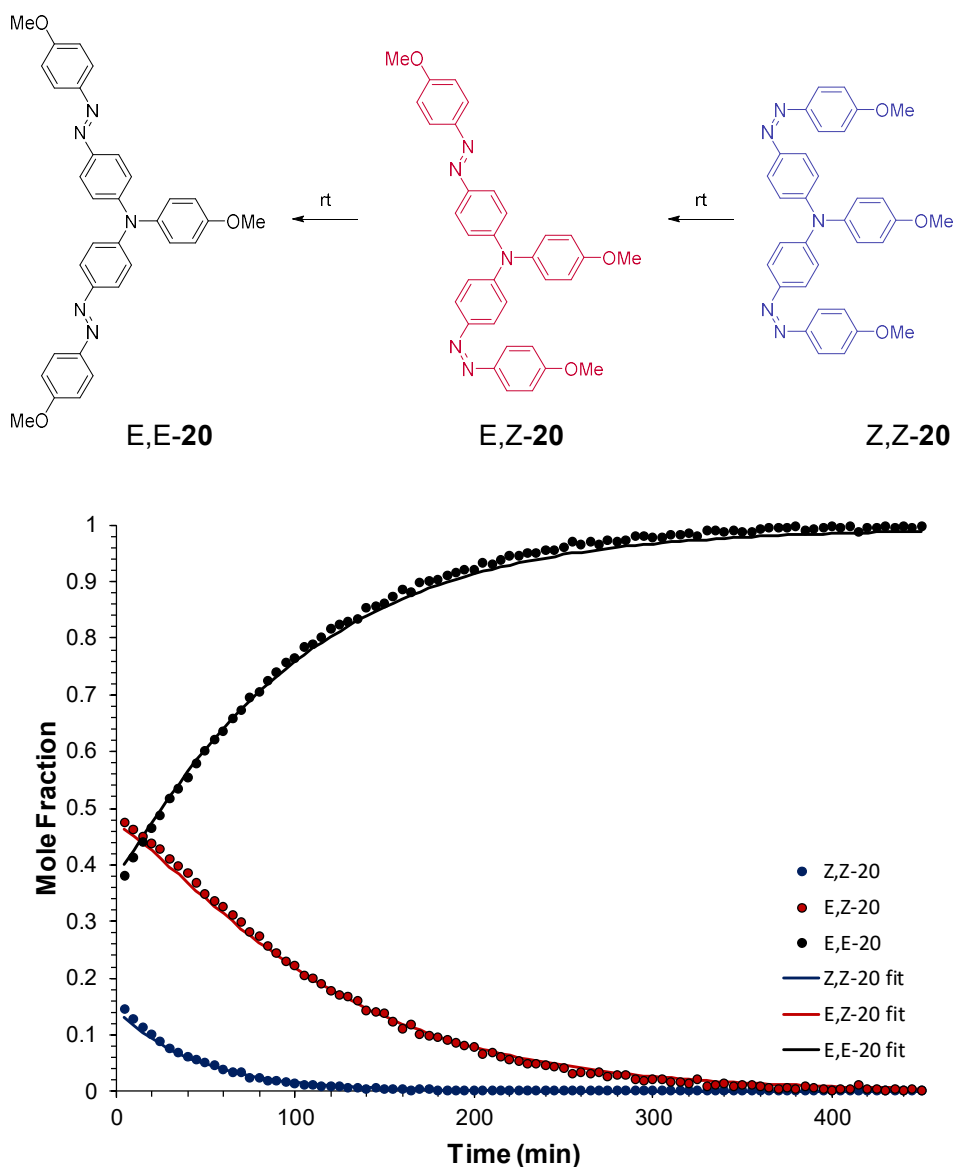


Figure 3.11. Isomer concentration versus time for **20** following from $\text{PSS}_{457\text{ nm}} \rightarrow E,E\text{-20}$ as determined using $^1\text{H-NMR}$ spectroscopy at room temperature. The data is modeled using a 2-step consecutive rate law. The isomers are identified as color coded: *E,E*- (black), *E,Z*- (red), and *Z,Z*- (blue).

The thermal expansion of $Z,Z\text{-}\mathbf{21} \rightarrow E,E\text{-}\mathbf{21}$ similarly follows a step-wise isomerization and is modeled using the same two-step consecutive rate laws in equations (3.1-3.3). In contrast to $\mathbf{20}$, the bis-system $\mathbf{21}$ is longer lived and is measured at elevated temperatures and extrapolated to room temperature. The isomer composition of $\mathbf{21}$ at PSS was monitored by ^1H -NMR spectroscopy over time while being kept in the dark, but the experiment was performed four separate times at four different temperatures (59, 71, 87, and 101 °C) using a hot oil bath to heat the NMR tube containing $\mathbf{21}$.

Figure 3.12 shows the change in isomer concentration of $\mathbf{21}$ over time at each temperature (59, 71, 87, and 101 °C). The exponential curves are fit with the appropriate rate law equation above to determine the rate constants.

The Eyring transition state theory given in equation (2.4) can be used to determine the ΔG^\ddagger at a given temperature. If the enthalpy of activation (ΔH^\ddagger) and entropy of activation (ΔS^\ddagger) are determined, then ΔG^\ddagger for any temperature (T) can be determined by applying equation (3.4). The ΔH^\ddagger and ΔS^\ddagger can be determined by applying equation (3.5) using the temperature dependence of the rate constant (k) and again assuming the transmission coefficient (κ) is 1.

$$\Delta G^\ddagger = \Delta H^\ddagger - T\Delta S^\ddagger \quad (3.4)$$

$$\ln\left(\frac{k}{T}\right) = -\frac{\Delta H^\ddagger}{RT} + \ln\left(\frac{k_B\kappa}{h}\right) + \frac{\Delta S^\ddagger}{R} \quad (3.5)$$

Plotting $\ln(k/T)$ versus $1/T$ gives a linear fit with a slope of $-\Delta H^\ddagger/R$ and a y-intercept of $\ln\left(\frac{k_B\kappa}{h}\right) + \frac{\Delta S^\ddagger}{R}$. In Figure 3.13, an Eyring plot using the $Z,Z\text{-}\mathbf{21} \rightarrow E,Z\text{-}\mathbf{21}$ and $E,Z\text{-}\mathbf{21} \rightarrow E,E\text{-}\mathbf{21}$ thermal rate constants determined at four different temperatures was used to determine the ΔH^\ddagger and ΔS^\ddagger from the linear fit. Then ΔH^\ddagger and ΔS^\ddagger were used in equation (3.4) to determine the ΔG^\ddagger at

room temperature. Equation (2.4) was then used to determine the rate constants at room temperature (Figure 3.13). The $Z,Z \rightarrow E,Z$ rate constant (k_1) at 298 K was $7.11 \times 10^{-7} \text{ s}^{-1}$, which was a half-life of 11.3 days. The $E,Z \rightarrow E,E$ rate constant (k_2) at 298 K was $2.86 \times 10^{-7} \text{ s}^{-1}$, which was a half-life of 28.0 days. The Gibbs free energy of activation (ΔG^\ddagger) of **21** at 298 K was 25.8 kcal/mol for $Z,Z \rightarrow E,Z$ isomerization and 26.3 kcal/mol for $E,Z \rightarrow E,E$ isomerization, found by applying the Eyring transition state theory given in equation (2.4). The $\Delta G^\ddagger_{(298 \text{ K})}$ for $E,Z \rightarrow E,E$ isomerization of **21** (26.3 kcal/mol) was similar in energy to the $\Delta G^\ddagger_{(298 \text{ K})}$ of **28** at 25.7 kcal/mol and greater than bis-system **20** (22.5 kcal/mol). There was a large difference in Z isomer persistence between the two bis-systems ranging from minutes to hours, which aligns with the difference in $\Delta G^\ddagger_{(298 \text{ K})}$ observed for two amino-azobenzene analogues **11** (22.0 kcal/mol) and **28** (25.7 kcal/mol).

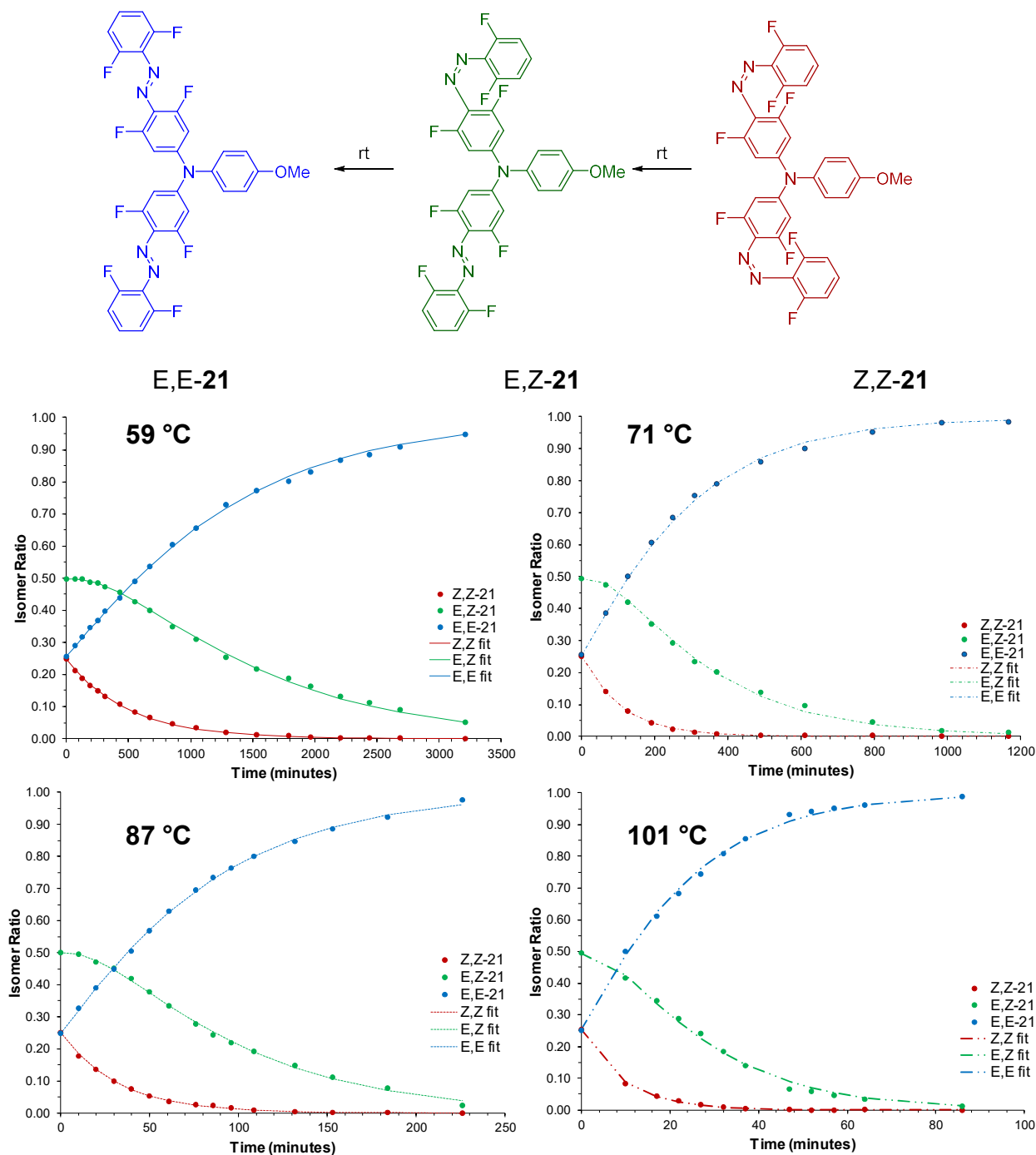


Figure 3.12. Isomer concentration versus time for **21** (9.61×10^{-3} M) in deaerated C₇D₈ following from PSS_{457 nm} → *E,E*-**21** (at 59, 71, 87, and 101 °C) as determined using ¹H-NMR spectroscopy. The data is modeled using a 2-step consecutive rate law. The isomers are identified as color coded: *E,E*- (blue), *E,Z*- (green), and *Z,Z*- (red).

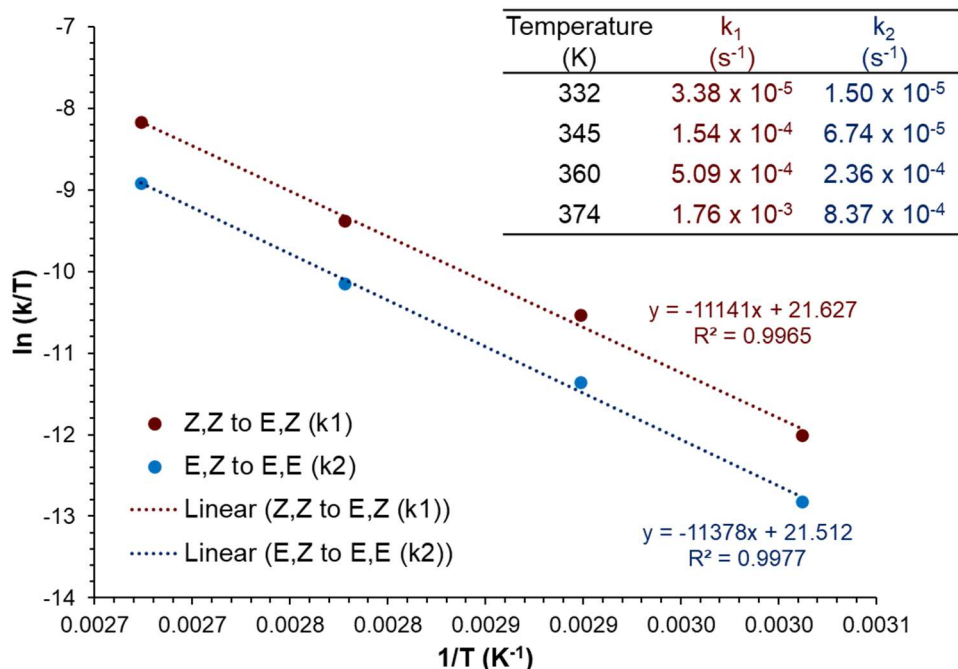


Figure 3.13. Eyring plot of $\ln(k/T)$ vs. $1/T$ for **21** (9.61×10^{-3} M) in deaerated C_7D_8 , where k_1 (red) is the rate constant for $Z,Z\text{-21} \rightarrow E,Z\text{-21}$ and k_2 (blue) is the rate constant for $E,Z\text{-21} \rightarrow E,E\text{-21}$ thermal isomerization at a given absolute temperature, T , in Kelvins. 1H -NMR spectroscopic measurements were taken in the dark using an NMR tube, and the temperature was controlled using a hot oil bath.

3.5. Redox Switching of Bis(azobenzene)-*p*-anisidines **20** and **21**

The electrochemical properties for **20** and **21** were determined by cyclic voltammetry (CV), and the spectrum (Figure 3.14) displays a reversible CV wave with an oxidation potential (E°) of 0.92 V (vs. SCE) for **20** and E° of 1.31 V (vs. SCE) for **21**. The reference electrode was a saturated calomel electrode (SCE). The electrolyte was tetrabutylammonium tetrafluoroborate (TBABF₄). The CV was calibrated against the standard ferrocene.⁷⁰ The chemical oxidant, CRET (Cation Radical Electron Transfer) has an E° measured to be 1.15 V (vs. SCE), and therefore is expected to efficiently oxidize and induce the redox catalysis cycle for **20**.⁷¹⁻⁷³

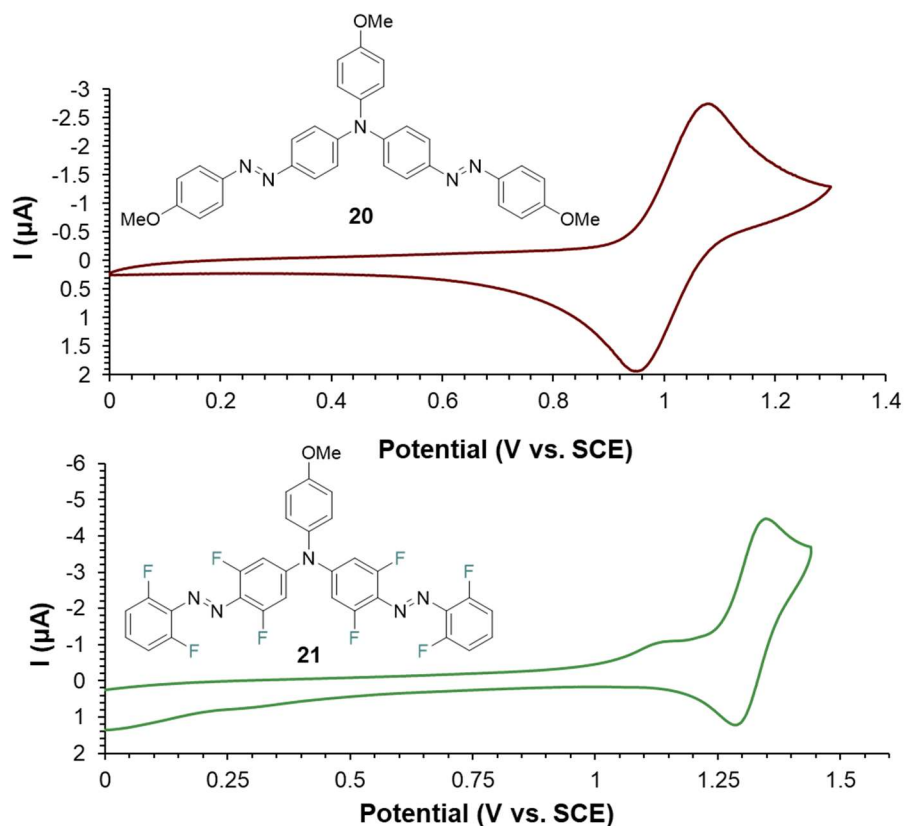


Figure 3.14. An overlay of the cyclic voltammograms of **20** (top) and **21** (bottom). Cyclic voltammogram of **20** at 1.0 mM in purified dichloromethane and 0.10 M TBABF₄ electrolyte gave an E° of 0.92 V vs. SCE. The scan rate was 25 mV/s. Cyclic voltammogram of **21** at 1.1 mM in acetonitrile (LC-MS grade) and 0.10 M TBABF₄ electrolyte gave an E° of 1.31 V vs. SCE. The scan rate was 50 mV/s. A platinum disc working electrode and platinum wire counter electrode were used.

The acceleration of electro-isomerization of **20** was tested next. A chemical oxidant is the first method of initiating the proposed catalytic radical cation mechanism. Oxidation of the single amino center will reduce the $Z \rightarrow E$ energy barrier to greatly accelerate the isomerization rate. We expect this single oxidation to accelerate $Z \rightarrow E$ isomerization for both attached azobenzene units. This can be followed by dynamic UV-vis spectroscopy. First, the **20** solution in benzene is irradiated to PSS_{457 nm}. The PSS solution is then injected with 1 mole percent of the CRET solution in methylene chloride. The PSS solution immediately isomerizes to E,E -**20** within

2 seconds at room temperature. The optical spectra overlay in Figure 3.15 shows the complete change from PSS back to *E,E*-**20** within seconds of adding CRET and taking the next scan. The results demonstrate that *Z*→*E* isomerization at room temperature can be greatly accelerated. A minimal acceleration can be calculated based on the assumption of at least a 0.5 second half-life. It took ~2 seconds to add the oxidant, shake the cuvette, and load it in the spectrophotometer. Given that complete conversion has occurred by this point, a half-life is conservatively estimated for less than 0.5 second based on four half-lives having already passed with less than 6.25% *Z* isomer remaining. Comparing the thermal half-life for the *E,Z*-isomer at 61.9 minutes (3,710 s) to the oxidized half-life of <0.5 second, there is a minimum *Z*→*E* rate acceleration of 7,400x upon a single electron oxidation. Extrapolating the oxidant loading from 1% to 100%, there is a minimum acceleration of 740,000x.

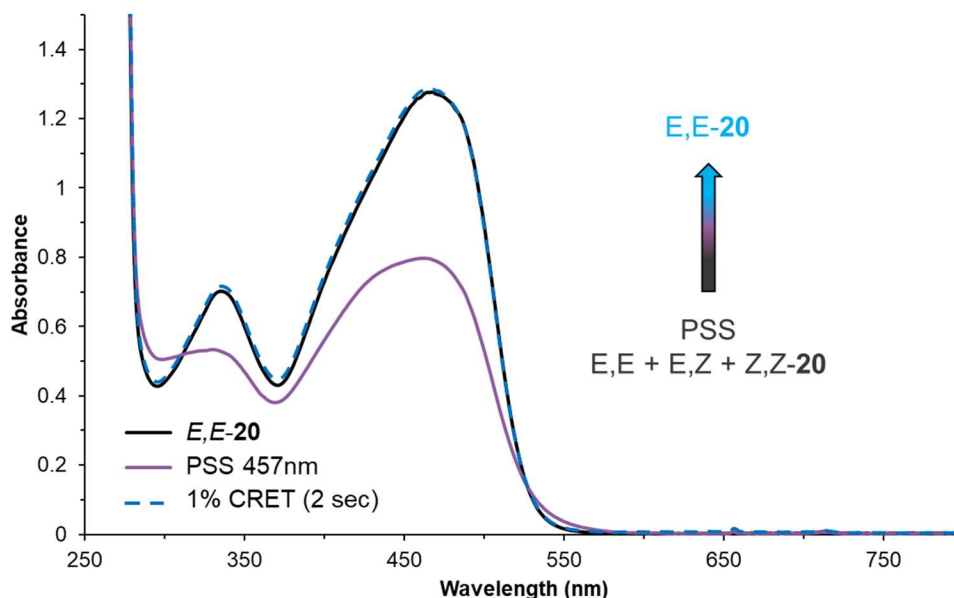


Figure 3.15. Optical spectra overlay of **20** at PSS_{457 nm} in benzene (3.00×10^{-5} M) taken prior to irradiation, after irradiation at the 457 nm PSS, and after the addition of 1.0 mol% oxidant CRET and shaking for 2 seconds in a 1.0 cm quartz cuvette at room temperature.

The same experiment is applied to system **21** to test for accelerated electro-switching using dynamic UV-vis spectroscopy. The **21** benzene solution is irradiated to PSS_{457 nm} and injected with a CRET-methylene chloride solution. It took a 15% CRET loading for complete $Z,Z \rightarrow E,E$ isomerization within 4 seconds at room temperature. The optical spectra in Figure 3.16 show the complete change from PSS back to E,E -**21** within seconds of adding CRET and taking the next scan. The results demonstrate that $Z \rightarrow E$ isomerization for this long-lived system can be greatly accelerated at room temperature. CRET initiated the electron transfer catalytic cycle for both bis-systems (**20** and **21**) demonstrating fast, complete, catalytic $Z \rightarrow E$ switching of two attached azobenzene moieties with a single electron transfer.

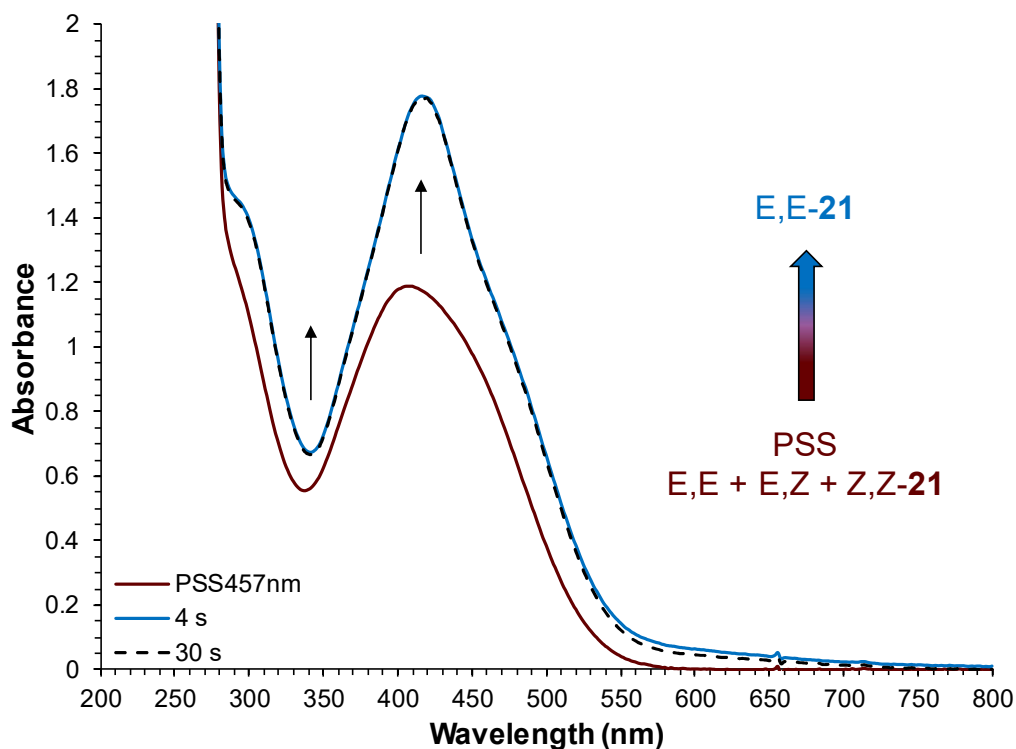


Figure 3.16. Optical spectra overlay of **21** at PSS_{457 nm} in benzene (6.6×10^{-5} M) followed by the addition of 15 % CRET to return the E,E -isomer in a 1.0 cm quartz cuvette at room temperature.

3.6. Photosensitizer for Photo-Electro Catalytic Switching of Bis(azobenzene)-*p*-anisidines

A cycling method developed using two wavelengths of light employs the oxidation abilities of an organic photosensitizer, methylene blue (MB^+). The triplet excited state of MB^+ has a redox potential of 0.97 V vs. SCE and a 32 μs lifetime. A mixed solution of **20** and 5% MB^+ in methanol-toluene (1:49) is measured by UV-vis spectroscopy. Blue light (457 nm) irradiation is used to trigger $E \rightarrow Z$ isomerization of **20**. Red light (660 nm) is used to excite MB^+ to the triplet excited state, which oxidizes the amino center to a radical cation, prompting fast, complete $Z \rightarrow E$ isomerization. Figure 3.17 plots $E \rightarrow Z \rightarrow E$ cycling for 15 repetitions, showing cycling between PSS and E, E -isomers using blue and red light when a photosensitizer is introduced to the solution. Photo, photo-electro cycling is possible for both the single azobenzene (**11**) and bis(azobenzene)-**20** redox appended systems. The same cycling setup was applied for **21**. However, MB^+ was unable to oxidize the redox center when irradiated. The redox potential of ${}^3\text{MB}^+/\text{MB}^{\bullet}$ is 0.97 V vs. SCE, potentially unable to oxidize the mismatched system **21** (1.31 V vs. SCE) to initiate the electron transfer cycle.

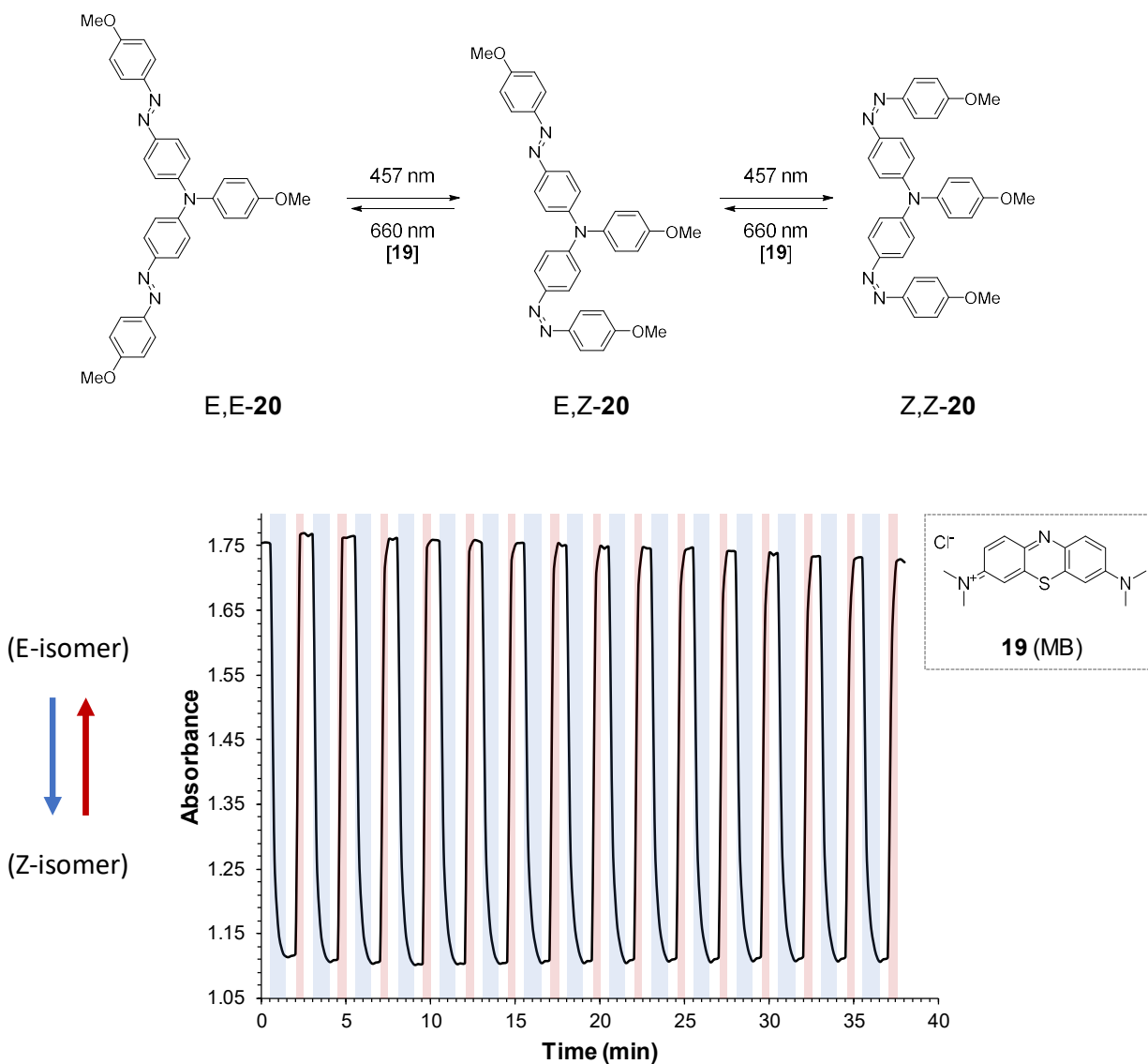


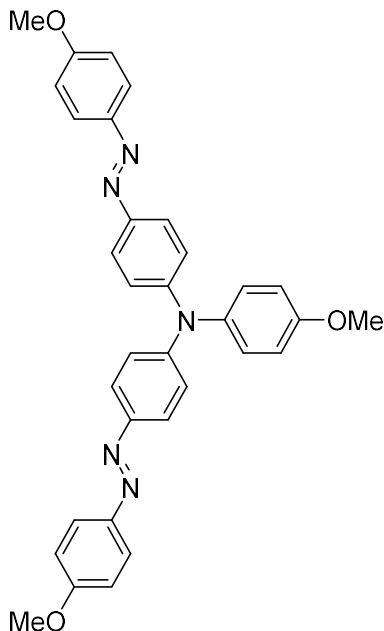
Figure 3.17. Photo, photo-electro cycling of **20** (3.58×10^{-5} M) and 5% **MB**⁺ (injection of 60.0 μL of 8.95×10^{-5} M) in deaerated 2% methanol in toluene in a 1.0 cm quartz cuvette at 25 °C, following alternating cycles of blue and red light irradiation to toggle between *E*→*Z*→*E* isomers with blue light exposure for 1 minute and red/no light exposure for 30 seconds for 15 cycles.

3.7. Conclusions

The bis(azobenzene)-*p*-anisidine systems, **20** and **21**, were successfully synthesized and characterized by UV-vis and NMR spectroscopy. The isomer composition at PSS_{457 nm} is 38% *E,E*-**20**, 47% *E,Z*-**20**, and 15% *Z,Z*-**20**. While **21** had a composition of 29% *E,E*-, 45% *E,Z*-, and 26% *Z,Z*-isomer at PSS_{457 nm}, reaching a 10% greater overall *Z* isomer formation. The thermal half-life for *Z,Z*-**20** is 1,700 seconds and 3,150 seconds for the *E,Z* isomer at room temperature. The *Z* isomeric states of **21** are more persistent as predicted. The thermal half-life at 57 °C for *Z,Z*-**21** is 9.7 hours and 18 hours for the *E,Z* isomer. Rapid and complete *Z*→*E* isomerization is successfully demonstrated upon oxidation of the single redox center. The electron transfer catalytic cycle is initiated for both systems with the chemical oxidant (CRET), though higher loading was needed for **21**. A minimum electro-stimulated half-life of <1 second for **20** and **21** was estimated. The Electro-stimulated minimum rate acceleration for **20** is 370,000x that of neutral *Z*→*E* isomerization when extrapolated to 100% CRET loading. While photo, photo-electro cycling was successful at toggling between *E*→*Z*→*E* **20**, it was not able to oxidize and promote *Z*→*E* isomerization with **21**.

3.8. Experimental Section

N,N-bis(azobenzene)-*p*-anisidine (**20**)



20

A flame-dried 2 dram vial was charged with *p*-anisidine **14** (0.1008 g, 0.8184 mmol) (Acros Organics), while a flame-dried 25 mL RBF was charged with 4-bromo-4'-methoxyazobenzene **15** (0.5004, 1.719 mmol) and a stir bar. Both the vial and RBF were transferred to a N₂ purged dry box, where anhydr toluene (2 mL), Pd(dba)₂ (0.0046 g, 0.0080 mmol), and a 0.10 M anhydr toluene solution of P(*t*Bu)₃ (85 μL, 0.0085 mmol) were added to the RBF. The reactant **14** was transferred to the RBF with toluene (6 mL) washings. Lastly, NaOtBu (0.2354 g, 2.450 mmol) and toluene (2 mL) were added to the flask and the mixture was stirred for ~1 min. The flask was capped with a rubber septum, removed from the dry box, and the mixture was stirred under N₂ with heating in a silicone oil bath at 111 °C for ~24 hours, allowed to cool, and then filtered through a layered bed of celite and 5 g basic alumina III by vacuum filtration. The filter cake was washed with toluene (~ 200 mL), and the combined solvents were removed in vacuo to yield a red glassy solid, which was recrystallized from 1:3 benzene-isopropanol to afford **20** (0.31 g, 0.57 mmol, 70%) as an amorphous red solid.

Yield: 70%

mp 172-174 °C

MW = 543.63 g mol⁻¹

¹H-NMR (360 MHz, CDCl₃): δ 7.89 (d, *J* = 8.9 Hz, 4H), 7.80 (d, *J* = 8.9 Hz, 4H), 7.20-7.15 (m, 6H), 7.01 (d, *J* = 9.0 Hz, 4H), 6.92 (d, *J* = 8.9 Hz, 2H), 3.89 (s, 6H), 3.84 (s, 3H).

^{13}C -NMR (125 MHz, CDCl_3): δ 161.8, 157.4, 149.5, 148.0, 147.4, 139.5, 128.3, 124.5, 124.0, 122.8, 115.3, 114.3, 55.70, 55.66.

UV-vis (benzene, λ_{max} , ϵ , concentration, path length): 336 and 466 nm, $37,000 \text{ M}^{-1}\text{cm}^{-1}$ and $65,000 \text{ M}^{-1}\text{cm}^{-1}$, $2.3 \times 10^{-5} \text{ M}$, 1.0 cm (Figure 3.2).

HRMS (EI/EBE) m/z : $[\text{M} + \text{H}]^+$ Calcd for $\text{C}_{33}\text{H}_{30}\text{N}_5\text{O}_3$ 544.2349; Found 544.2343.

5-bromo-1,3-difluoro-2-nitrosobenzene (**23**)



23

4-Bromo-2,6-difluoroaniline **22** (0.5031 g, 2.419 mmol) (Matrix Scientific) was dissolved in 20.0 mL DCM in a 100 mL RBF. OXONE[®] (2.7749 g, 4.5084 mmol) was dissolved in water (26.0 mL) and added all at once to the stirring **22**-DCM mixture. The reaction mixture was stirred vigorously for 3 days, when TLC analysis indicated the complete consumption of starting material **22**. The deep green DCM phase was collected, and the aqueous layer extracted with DCM (3x10 mL). The combined organic phases were then dried over anhydr Na_2SO_4 , filtered, and solvent was removed in vacuo to provide the crude product **23** (0.54 g, 2.4 mmol, 93%) as a beige solid, which was used without further purification in a subsequent Mills condensation reaction with aniline **22** (see below).

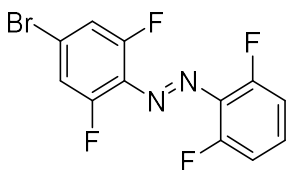
Shibasaki, et al. previously reported the synthesis at 87% yield.⁸⁸

Crude yield: 93%

MW = $221.99 \text{ g mol}^{-1}$

^1H -NMR (500 MHz, CDCl_3): δ 7.34 (d, $J = 8.1 \text{ Hz}$, 2H).

4-bromo-2,2',6,6'-tetrafluoroazobenzene (**25**)



25

Crude **23** (0.50 g, 2.3 mmol) was combined with 2,6-difluoroaniline **24** (245.0 μ L, 2.275 mmol) (Oakwood Chemical), DCM (10.0 mL) and trifluoroacetic acid (170.0 μ L, 2.220 mmol) in a 100 mL RBF. The RBF was completely wrapped in foil to shield it from ambient light exposure, and the reaction was stirred for 23 h at rt at which time TLC analysis indicated the absence of any starting material **23**. The reaction mixture was neutralized and dried with \sim 10-20 mg Na_2CO_3 , filtered, and solvent was removed in vacuo to give **25** as a red-black goop. The crude product **25** was dissolved in 100 mL 1:1 DCM:hexanes and filtered through a plug of silica gel, followed by solvent removal in vacuo to afford a deep orange amorphous solid (0.59 g, 1.8 mmol, 79%).

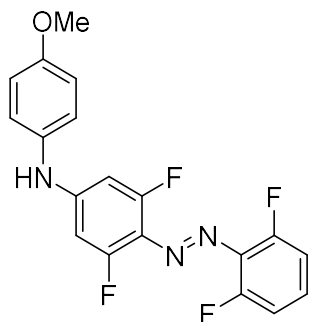
Hecht, et al. previously reported the synthesis of **25** in 93% yield.⁸⁹

Yield: 79%

MW = 333.08 g mol^{-1}

$^1\text{H-NMR}$ (360 MHz, CDCl_3): δ 7.39 (m, 1H), 7.28 (d, $J = 9.6$ Hz, 2H), 7.07 (t, $J = 8.8$ Hz, 2H).

N-(4-methoxyphenyl)-4-amino-2,6,2',6'-tetrafluoroazobenzene (**26**)



26

A flame-dried 2 dram vial was charged with *p*-anisidine **14** (0.3001 g, 2.437 mmol) (Acros Organics), while a flame-dried 250 mL RBF was charged with 4-bromo-2,2',6,6'-tetrafluoroazobenzene **25** (0.7703 g, 2.313 mmol) and a stir bar. Both the vial and RBF were transferred to a N_2 purged dry box, where anhydr toluene (10 mL), $\text{Pd}(\text{dba})_2$ (0.0705 g, 0.123 mmol), and bis(diphenylphosphino)ferrocene, dppf, (0.0675 g, 0.122 mmol) were added to the RBF. Amine **14** was transferred to the RBF with anhydr toluene (30 mL)

washings. Lastly, Cs₂CO₃ (1.2710 g, 3.9009 mmol) and toluene (10 mL) were added to the flask and the mixture was stirred for ~1 min. The flask was capped with a glass stopper, removed from the dry box, and the mixture was stirred under N₂ with heating in a silicone oil bath at 111 °C for ~24 h, allowed to cool, and then vacuum filtered through a layered bed of 5 g basic alumina III topped with 1 g celite. The filter cake was washed with toluene (~ 300 mL), and the combined solvents were removed in vacuo to yield a red tacky solid, which was recrystallized by dissolving in minimal amount toluene (~5 mL) diluting with hexanes (~150 mL) until a cloudy orange solution was achieved, which afforded **26** as thin red needles (0.69 g, 1.8 mmol, 79%) on cooling.

Note: The set-up and reaction were kept in the dark to minimize ambient light exposure.

Yield: 79%

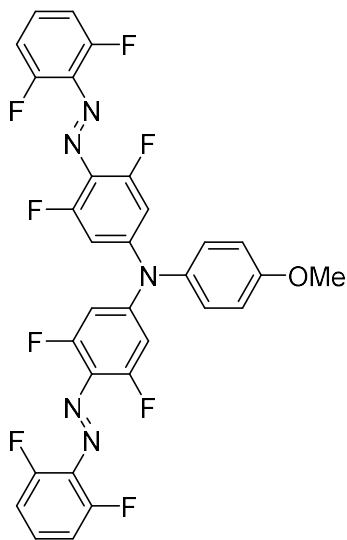
MW = 375.33 g mol⁻¹

¹H-NMR (500 MHz, CDCl₃): δ 7.25 (m, 1H), 7.16 (d, *J* = 8.7 Hz, 2H), 7.00 (t, *J* = 8.6 Hz, 2H), 6.95 (d, *J* = 8.8 Hz, 2H), 6.40 (d, *J* = 11.9 Hz, 2H), 6.06 (s, 1H), 3.84 (s, 3H).

¹³C-NMR (125 MHz, CDCl₃): δ 159.6 (d, *J* = 7.3 Hz), 157.8 (s), 157.5 (d, *J* = 7.4 Hz), 156.6 (d, *J* = 4.5 Hz), 154.6 (d, *J* = 4.5 Hz), 150.3 (t, *J* = 14.0 Hz), 131.6 (s), 129.5 (t, *J* = 10.3 Hz), 125.9 (s), 115.2 (s), 112.5 (dd, *J* = 4.6 Hz, *J* = 19.4 Hz), 97.3 (d, *J* = 26.8 Hz), 55.7 (s).

HRMS (EI/EBE) *m/z*: [M + H]⁺ Calcd for C₁₉H₁₄N₃OF₄ 376.1073; Found 376.1066.

***N,N*-bis(2,2',6,6'-tetrafluoroazobenzene)-*p*-anisidine (**21**)**



21

A flame-dried 2 dram vial was charged with **25** (0.2667 g, 0.8007 mmol), while a flame-dried 250 mL RBF was charged with **26** (0.33 g, 0.88 mmol), and a stir bar. Both the vial and RBF were transferred to a N₂ purged dry box, where anhydr toluene (10 mL), Pd(dba)₂ (0.0230 g, 0.0400 mmol), and dppf, (0.0220 g, 0.0397 mmol) were added to the RBF. From the vial, **25** was transferred to the RBF with anhydr toluene (30 mL) washings. Lastly, Cs₂CO₃ (0.4167 g, 1.279 mmol) and toluene (10 mL) were added to the flask and stirred for ~1 min. The flask was capped with a glass stopper, removed from the dry

box, and the mixture was stirred under N₂ with heating in a silicone oil bath at 111 °C for ~24 h, allowed to cool, and then vacuum filtered through a layered bed of 1 g celite above 5 g basic alumina III. The filter cake was washed with toluene (300 mL), and the combined solvents were removed in vacuo to yield a tacky red solid. The crude product **21** was dissolved in 1:1 toluene-hexanes (200 mL) and filtered through a plug of silica gel. The filter cake was then washed with DCM (100 mL), followed by solvent removal in vacuo to afford a red solid, which was recrystallized from 1:10 benzene-isopropanol to afford **21** as a red amorphous solid (0.34 g, 0.54 mmol, 68%).

Yield: 68%

MW = 627.50 g mol⁻¹

¹H-NMR (360 MHz, CDCl₃): δ 7.32 (m, 2H), 7.16 (d, *J* = 8.8 Hz, 2H), 7.03 (t, *J* = 8.8 Hz, 4H), 6.98 (d, *J* = 8.9 Hz, 2H), 6.76 (d, *J* = 11.0 Hz, 4H), 3.85 (s, 3H).

UV-vis (benzene, λ_{\max} , ϵ , concentration, path length): 416 nm, 12,000 M⁻¹cm⁻¹, 6.6 x 10⁻⁵ M, 1.0 cm (Figure 3.6).

HRMS (EI/EBE) m/z: [M + H]⁺ Calcd for C₃₁H₁₇N₅O_F₈ 627.1323; Found 627.1305.

Photochemical Experiments:

Optical spectrum of **20 in benzene (Figure 3.2)**

Benzene was sparged with N₂ gas for ~ 5 min in a vial prior to use. A stock solution of 3.1 x 10⁻⁵ M **20** in deaerated benzene was prepared by diluting 0.00017 g of **20** in benzene using a 10.0 mL volumetric flask. A dilution of 3.5 mL of the stock solution to a 5.0 mL solution with benzene yields the 2.3 x 10⁻⁵ M **20** solution, which was transferred to a 1.0 cm quartz cuvette and capped with a Teflon stopper. Absorbance was measured from 200 to 800 nm.

Photochemical conversion of *E*-20** to PSS *E/Z*-**20** mixture (Figure 3.3)**

A solution of 2.3 x 10⁻⁵ M **20** in benzene was prepared as for Figure 3.2. Then 3.0 mL of this solution was transferred to a 1.0 cm quartz cuvette and capped with a Teflon stopper. The optical spectrum of the sample was recorded (200-800 nm) every 5 s under irradiation by a 457 nm 7 W LED source for 4 min to achieve the PSS mixture of *E,E*-, *E,Z*-, and *Z,Z*-**20**.

¹H-NMR spectra of *E,E*-20** and the *E/Z*-**20** mixture at the PSS_{457 nm} (Figure 3.5) and
¹H-NMR spectra of *E,E*-**21** and the *E/Z*-**21** mixture at the PSS_{457 nm} (Figure 3.10)**

Benzene-*d*₆ was sparged with N₂ gas for ~ 5 min in a vial prior to use. A solution of 6.9 x 10⁻³ M **20** in benzene-*d*₆ was prepared by dissolving 0.0030 g of **20** in 800.0 μL benzene-*d*₆. A stream of N₂ gas was blown into the NMR tube for ~ 1 min prior to capping and sealing with a small strip of parafilm. The tube was kept covered until inserting into the NMR instrument to minimize light exposure to obtain an all *E* isomer spectrum. After the all *E* spectrum was measured, the NMR tube was irradiated with a 457 nm light source to achieve PSS. The NMR tube was placed in a mirrored Dewar with ~100 mL of an ice-water slurry to prevent any sample heating from the light source placed on top. The sample was irradiated for ~ 30 min followed by additional ~15 min intervals until no change was detected in the ¹H-NMR spectrum.

Using the same procedure, a solution of 4.28 x 10⁻² M **21** in benzene-*d*₆ was prepared by dissolving 0.02014 g of **21** in 750 μL benzene-*d*₆ and 1.0 μL mesitylene in an NMR tube via gas-tight syringes.

Optical spectrum of **21 in benzene (Figure 3.6)**

A solution of 6.6 x 10⁻⁵ M **21** in deaerated benzene was prepared by dissolving 0.00109 g of **21** in benzene using a 25.0 mL volumetric flask. The solution was transferred to a 1.0 cm quartz cuvette and capped with a Teflon stopper. Absorbance was measured from 200 to 800 nm.

Photochemical conversion of *E*-21 to PSS *E/Z*-21 mixture (Figure 3.8)

A solution of 6.6×10^{-5} M **21** in deaerated benzene was prepared as for Figure 3.6. Then 3.0 mL of this solution was transferred to a 1.0 cm quartz cuvette and capped with a Teflon stopper. The optical spectrum of the sample was recorded (200-800 nm) every 5 s under irradiation by a 457 nm 7 W LED source for 4 min to achieve the PSS mixture of **21**.

Thermal *Z*→*E* conversion of **20 evaluated by ¹H-NMR spectroscopy (Figure 3.11)**

A solution of 6.9×10^{-3} M **20** in deaerated benzene-*d*₆ was prepared and the PSS achieved as described above in Figure 3.5. Then a ¹H-NMR spectrum of the mixture was taken every 4 min 44 s for a total of 100 spectra using the Bruker AM-500 NMR spectrometer, whose cavity was capped to prevent ambient light exposure at 295 K.

Thermal *Z*→*E* conversion of **21 evaluated by ¹H-NMR spectroscopy (Figure 3.12)**

A solution of 9.61×10^{-3} M **21** in deaerated toluene-*d*₈ was prepared (with added mesitylene internal standard) and the PSS achieved as described above in Figure 3.10. The NMR sample was heated in a hot oil bath (59 °C). Then a ¹H-NMR spectrum of the mixture was taken periodically using the Bruker AM-500 NMR spectrometer at 295 K. The thermal conversion accounts for time spent in the oil bath. The time is suspended overnight by removing the sample from the oil bath and storing in a closed dewar filled with ice-water. The experiment was repeated a total of four times at four temperatures (59, 71, 87, 101 °C).

Cyclic voltammogram of **20** and **21** (Figure 3.14)

To a 25.0 mL volumetric flask, TBABF₄ (0.82 g, 2.5 mmol) and purified,⁷⁸ freshly distilled DCM were added. The 0.10 M electrolyte solution (8.0 mL) was transferred to an electrochemical cell (4-neck flask) equipped with a freshly polished platinum disc working electrode, platinum wire counter electrode and SCE reference electrode. A blank cyclic voltammogram (0.0 V to 1.3 V vs. SCE, 25 mV/s) confirmed the baseline current response of the cell and absence of impurities. Next, **20** (0.0044 g, 8.1 x 10⁻⁶ mol) was added to the cell with stirring to make the 1.0 mM solution. The potential was scanned from 0.0 V to 1.3 V vs. SCE at a rate of 25 mV/s. The parameters for **21** were the same except to exchange acetonitrile for the DCM solvent.

Redox *Z*→*E* switching of **20** (Figure 3.15)

A 2.3 x 10⁻⁵ M **20** solution in deaerated benzene was prepared as for Figure 3.3. Separately, a 4.4 x 10⁻⁴ M solution of CRET was prepared by dissolving CRET (0.00022 g, 1.3 x 10⁻⁶ mmol) in freshly distilled DCM (3.0 mL). To a 1.0 cm quartz cuvette, 3.0 mL of **20** solution was added and capped with a Teflon stopper and irradiated to the PSS with a 457 nm LED source as followed by optical spectroscopy. To the PSS mixture was then injected via syringe 1.6 μL of the CRET solution (6.9 x 10⁻¹⁰ mol, 1.0%), capped, and shaken (~4 s) before measuring the absorbance (200-800 nm).

Redox $Z \rightarrow E$ switching of **21** (Figure 3.16)

A 6.6×10^{-5} M **21** solution in deaerated benzene was prepared as for Figure 3.6. Separately, a 4.97×10^{-3} M solution of CRET was prepared from dissolving CRET (0.00601 g, 9.94×10^{-6} mol) in freshly distilled, deaerated DCM (2.0 mL). To a 1.0 cm quartz cuvette, 3.0 mL of **21** solution was added and capped with a Teflon stopper and irradiated to the PSS with a 457 nm LED source as determined by optical spectroscopy. To the PSS mixture was then injected via syringe 6.0 μ L of the CRET solution (3.0×10^{-8} mol, 15%), capped, and shaken (~ 4 s) before measuring the absorbance (200-800 nm).

Photo, Photo-Electro $E \rightarrow Z \rightarrow E$ cycling of **20** with MB^+ (Figure 3.17)

A N_2 -deaerated 3.58×10^{-5} M solution of **20** in toluene was prepared. To a 1.0 cm quartz cuvette was added 3.0 mL of **20** in toluene solution along with 60.0 μ L of a N_2 -deaerated 8.95×10^{-5} M solution of MB^+ in methanol (5.0 mol% based on **20**). The resulting concentrations of **20** and MB^+ in the cuvette were 3.51×10^{-5} M and 1.76×10^{-6} M, respectively. The cuvette was closed with a TeflonTM stopper. Two LED light sources (457 nm and 660 nm) were positioned to irradiate the cuvette at a distance of 4-5 inches. The lights were toggled on and off, alternating in sequence, at 30 s intervals (blue light 1 min) while the optical spectrum of the sample was recorded (200-800 nm) every 15 s. A total of fifteen 457/660 nm switching cycles were performed.

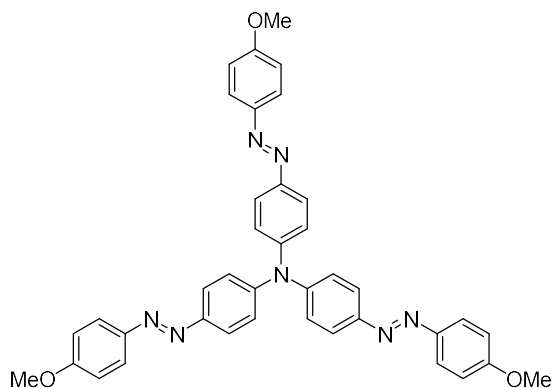
CHAPTER 4.

PHOTO-REDOX SWITCHING OF TRIS(AZOBENZENE)AMINE

4.1. Introduction

The addition of the redox aryl amine group has proven to greatly accelerate $Z \rightarrow E$ isomerization, giving greater control of Z or E isomer on command. This project focuses on linking three azobenzene units in a star-shaped arrangement about a single redox group to form an N,N,N -tris(azobenzene)amine (**29**) capable of multi-state formation. It is predicted that the amine center will switch all three attached units effectively with a single electron transfer.

Star-shaped azobenzene arrangements have been made using central aromatic, amine, carbon, or phosphine linkers. Chapter 1 presented a couple examples of these star-shaped systems. The rigid center of **8** gave rise to STM level imaging during photoisomerization.^{51, 52} The tetra(azobenzene) system (**10**) had high porosity that allowed for reversible gas adsorption and release upon photoisomerization.⁵⁸ While Blackstock and coworkers have presented four bis(azobenzene) systems, including **20** and **21**, this is the only tris(azobenzene) system using the redox center for accelerated $Z \rightarrow E$ isomerization. The photo-, thermal-, and electro-switching properties will be examined. The crystal arrangement and potential as a donor towards donor-acceptor co-crystallization will also be explored.



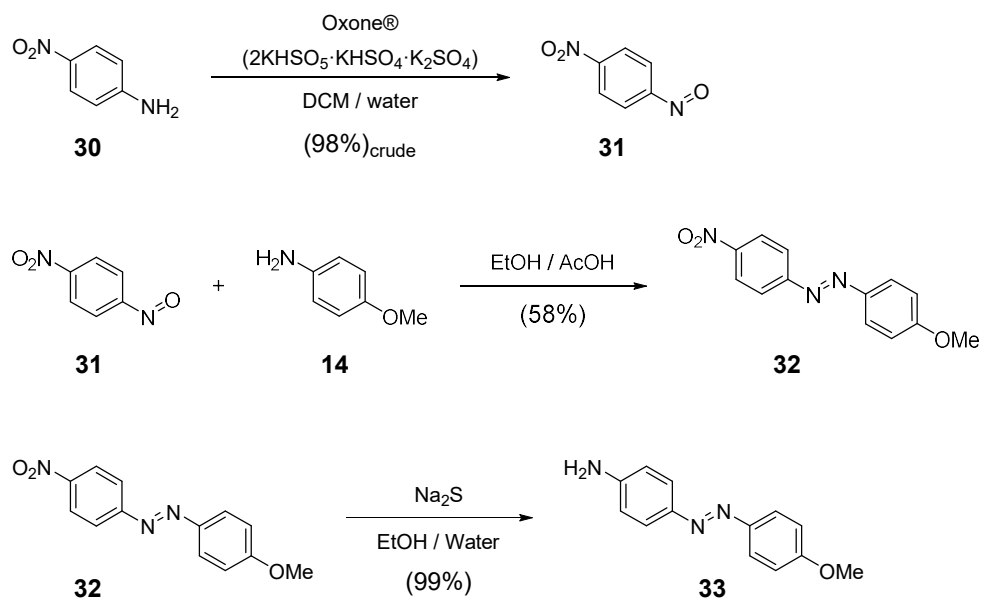
E,E,E-29

Figure 4.1. Target *N,N,N*-tris(azobenzene)amine compound **29** (TA).

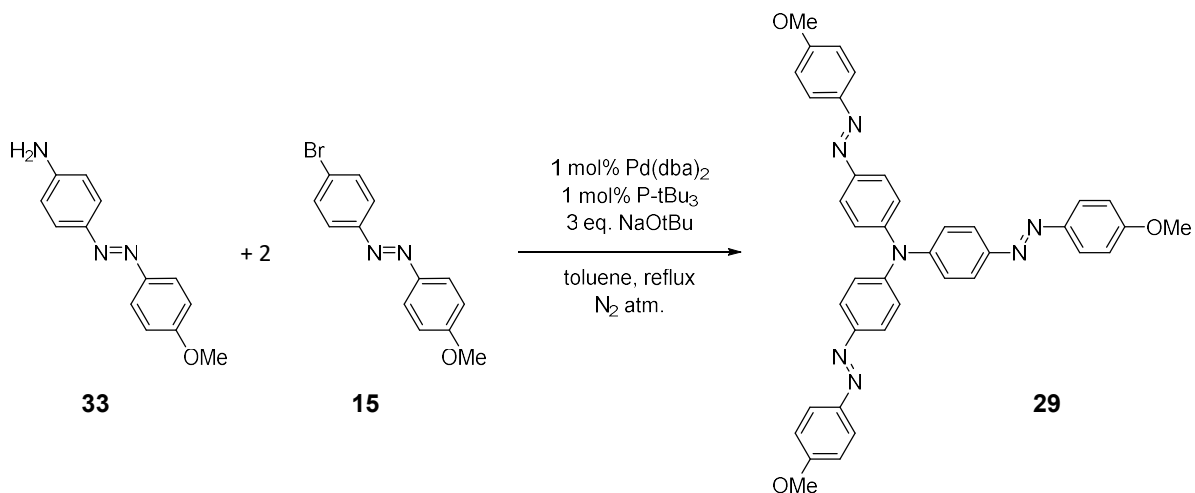
4.2. Synthesis of TA (**29**)

Scheme 4.1 and Scheme 4.2 outline the synthetic route taken to synthesize **29**. 4-Methoxy-4'-nitroazobenzene **32** was achieved via Mills condensation of *p*-anisidine **14** and *p*-nitro-nitrosobenzene **31**, the latter formed by OXONE oxidation of *p*-nitroaniline **30**. The isolated crude nitrosobenzene **31** product was a yellow solid (green solution) in 98 % crude yield and was used in the Mills condensation reaction without further purification as **31** proves difficult to purify, and the two minor byproducts present do not interfere with the subsequent step. The Mills condensation reaction gave **32**, after column chromatography, as an orange solid in 58% yield. Sodium sulfide was used to reduce the nitro group to an amine without cleaving the azo (-N=N-) group. The facile reduction of **32** with sodium sulfide gave 4-amino-4'-methoxyazobenzene (**33**) as an orange-brown solid in 99% yield. Alternately, the reduction of the crude **32** azobenzene product and subsequent purification gave **33** in a 98 % yield, avoiding the yield loss from purification of **32**. BHA coupling of **33** and 4-bromo-4'-methoxyazobenzene

(15) gave the target tris-system **29**, after crystallized from acetone, as red crystalline needles at 82% yield.



Scheme 4.1. Oxone oxidation of **30** to nitrosobenzene **31**, Mills condensation of **31** and **14** to yield the azobenzene **32**, followed by reduction to 4-amino-4'-methoxyazobenzene (**33**).



Scheme 4.2. BHA coupling of **33** and **15** to yield the target tris(azobenzene)-**29**.

4.2.1. Crystal Structure of TA (29)

Red-orange flakes of **29** were achieved via crystallization from a 1:2 dichloromethane-methanol solution at -20 °C overnight. The solution of **29** crystallizes in the monoclinic space group $P2_1/n$ with an R_1 of 0.0418, and a GooF of 1.087 as determined by single crystal X-ray diffraction (XRD) measured at 20 °C illustrated in Figure 4.2. The unit cell parameters are listed in Table 1. These crystals are a polymorph compared to the ether-benzene solution yielding crystals in the monoclinic $P2_1C$ space group with an R_1 of 0.0868 and GooF of 1.007 as determined by single crystal XRD measured at -100 °C.⁶⁰ The single crystal X-ray structure was collected and processed using SHELXL-97 and OLEX-2 programs.

Table 1. Unit Cell Parameters for the Crystal (29)

Unit cell	TA (29)
Identification code	SCB295
Temperature/K	293(2)
Crystal system	monoclinic
Space group	$P2_1/n$
$a/\text{Å}$	10.32804(8)
$b/\text{Å}$	11.18167(9)
$c/\text{Å}$	28.8284(2)
$\alpha/^\circ$	90
$\beta/^\circ$	96.5850(7)
$\gamma/^\circ$	90
Volume/ Å^3	3307.28(5)

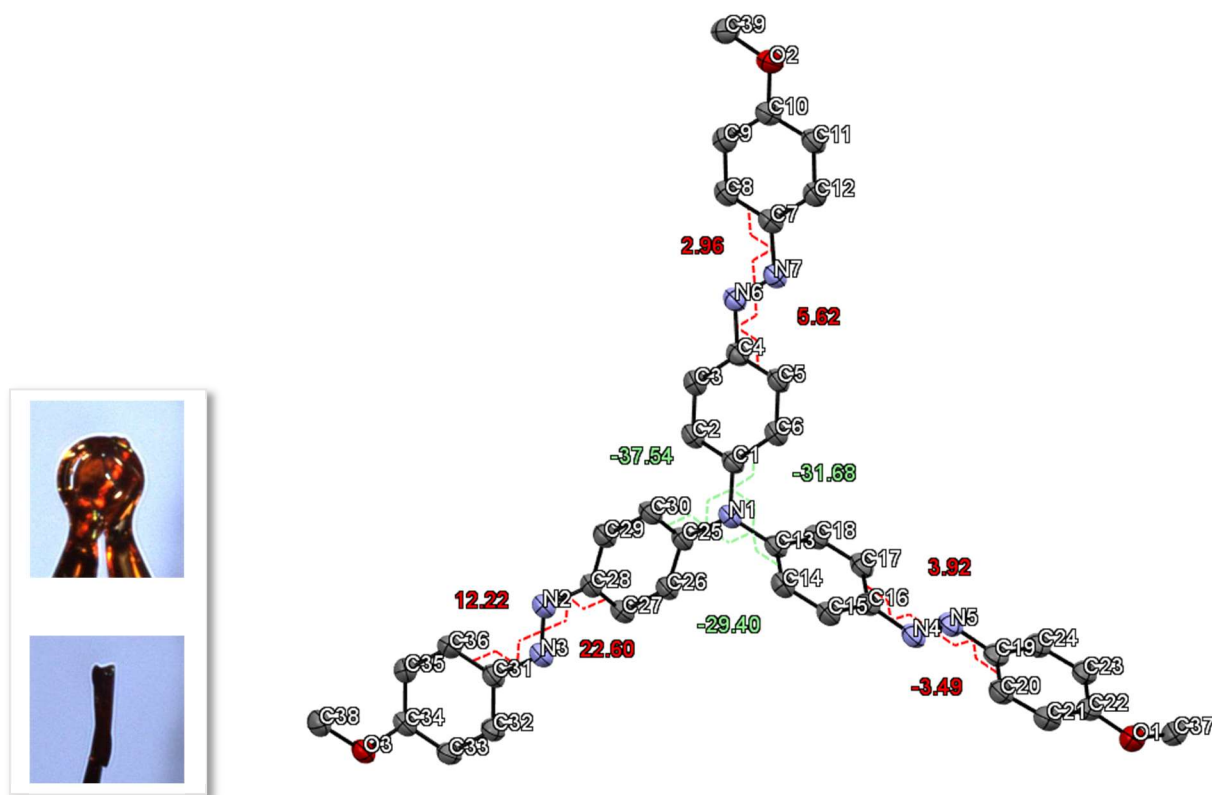


Figure 4.2. Mounted crystal and crystal structure of **29** illustrating the three-blade propeller shape of the azobenzene units around the amine center (green dihedral angles). Six twisting dihedral angles between the phenyl ring of each azobenzene moiety are listed in red.

The asymmetric unit consists of a single molecule of **29** (Figure 4.2). The phenyl rings of each azobenzene unit are twisted in a three-blade propeller form about the amine center with the nearly equal dihedral angles $\angle C6C1N1C13$ (-31.68°), $\angle C14C13N1C25$ (-29.40°), and $\angle C30C25N1C1$ (-37.54°) as labeled in green in Figure 4.2. The symmetric twisting is expected based on the symmetric three-blade propeller form in the triphenylamine structure. The increased twisting about the amine decreases the π overlap between the amine and azo units. The azobenzene units are expected to be planar to extend the π system throughout the unit. However, each azobenzene core is experiencing some twisting from planarity as shown in red labels in

Figure 4.2. Two units are experiencing a dihedral angle of $\sim 3-6^\circ$ between the two phenyl rings, while the third unit is twisted out of planarity with the dihedral angles $\angle N3N2C28C27$ (22.60°) and $\angle N2N3C31C36$ (12.22°) between the phenyl rings. The tight packing environment is likely the cause for the twisting azobenzene core. The crystal packing of **29** is also illustrated (Figure 4.3 left to right) viewing down the three axes (a, b, and c) of the unit cell. The structures are grouped by symmetry operation (identity, 2-fold screw axis, inversion center, glide plane) in Mercury to yield the four colored structures (grey, green, yellow, and pink), respectively.

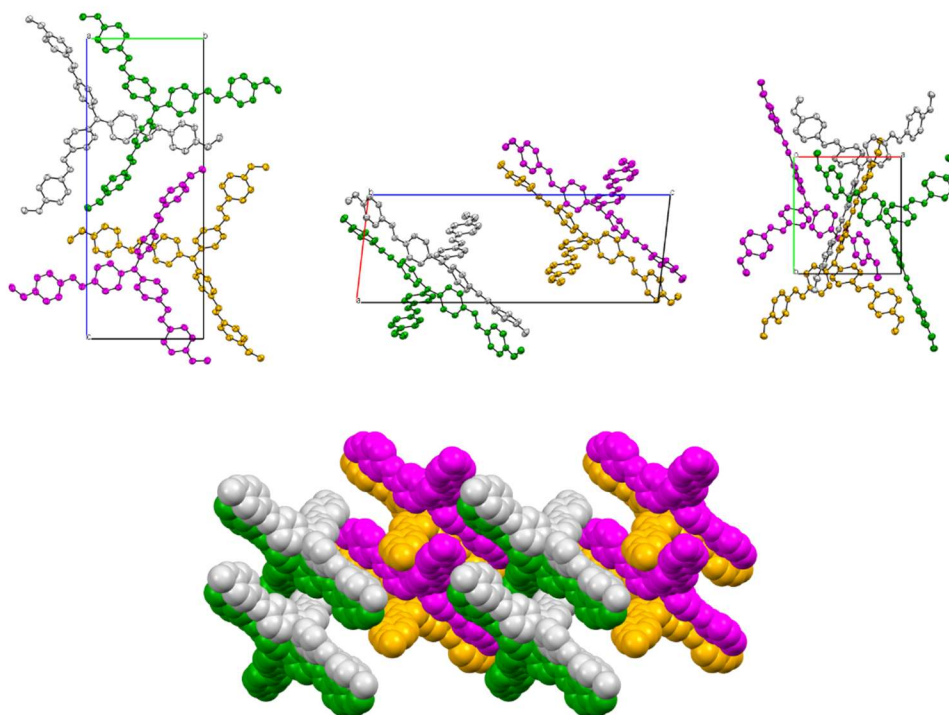


Figure 4.3. (Top) Crystal structure illustrating the packing at the unit cell viewing down the three axes (a,b, and c). (Bottom) Space-filling modeling the packing viewed down the b-axis.

4.3. Photochemistry and Optical Absorption of TA (**29**)

The UV-vis absorption spectrum of **29** in deaerated benzene (5.15×10^{-5} M) shows a π - π^* absorption band at 452 nm ($\epsilon = 2.89 \times 10^4$ M $^{-1}$ cm $^{-1}$) with an overlapped n- π^* band. The

addition of a third azobenzene moiety increases the conjugated π system. The tris-system **29** is red shifted compared to a single azobenzene system, like **1** (320 nm) and **11** (436 nm). However, increased twisting about the nitrogen center, decreasing the π system overlap, leaving the bis-system **20** (466 nm) with the longer wavelength π - π^* band. **29** is red shifted versus the bis-system **21** (416 nm) from the electron withdrawing fluorine substituents.

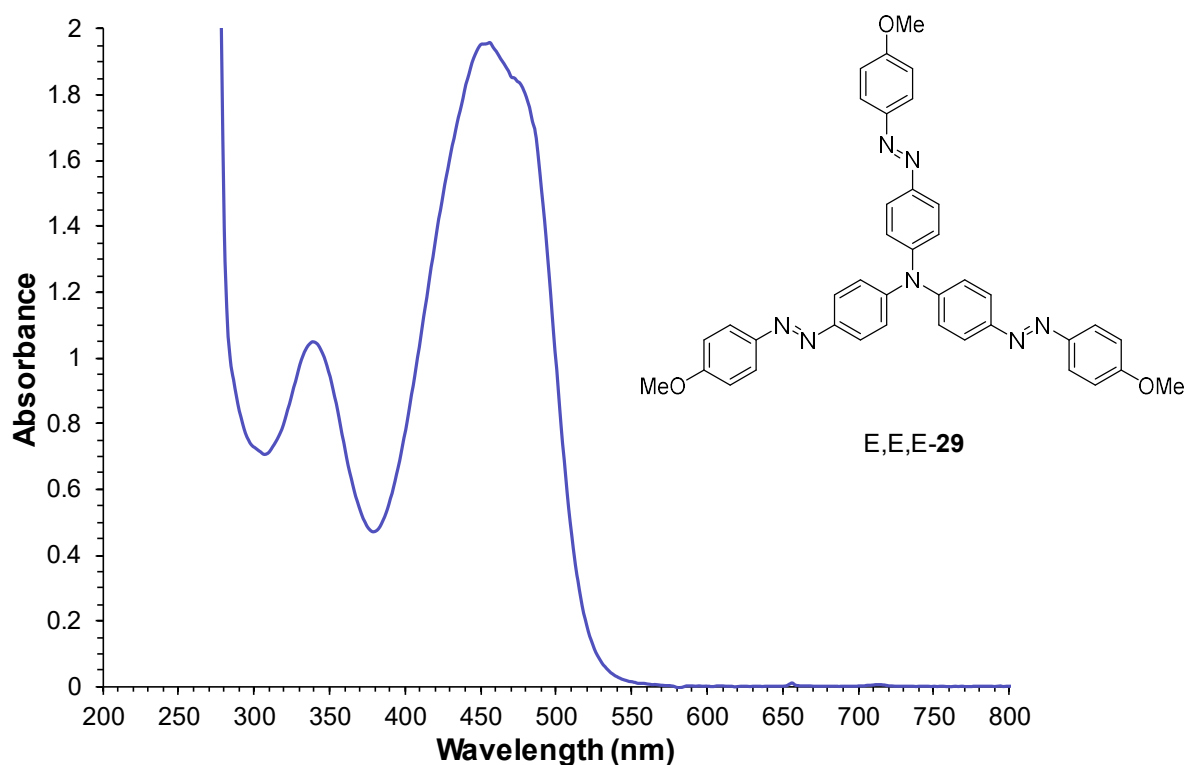


Figure 4.4. Optical spectrum of **29** in benzene (3.3×10^{-5} M) in a 1.0 quartz cuvette at room temperature.

Irradiation of the $\pi \rightarrow \pi^*$ band is used to induce $E \rightarrow Z$ switching. A light source will ideally be absorbed strongly by the $\pi \rightarrow \pi^*$ band of the E isomer and not by the Z isomer for greater conversion to the Z isomer. Irradiation of a solution of **29** in deaerated benzene with a 457 nm LED light source (7 watts) is monitored by dynamic UV-vis spectroscopy until the sample reached the photostationary state (PSS). The absorption decreases with increasing Z

isomer formation until PSS. The UV-vis spectra in Figure 4.5 shows three isosbestic points occurring at 310 nm, 374 nm, and 518 nm. An isosbestic point occurs when the absorption of a mixture remains constant at a wavelength while the mixture composition is changing. The presence of these points indicate that an interconversion of isomers in a chemical equilibrium.

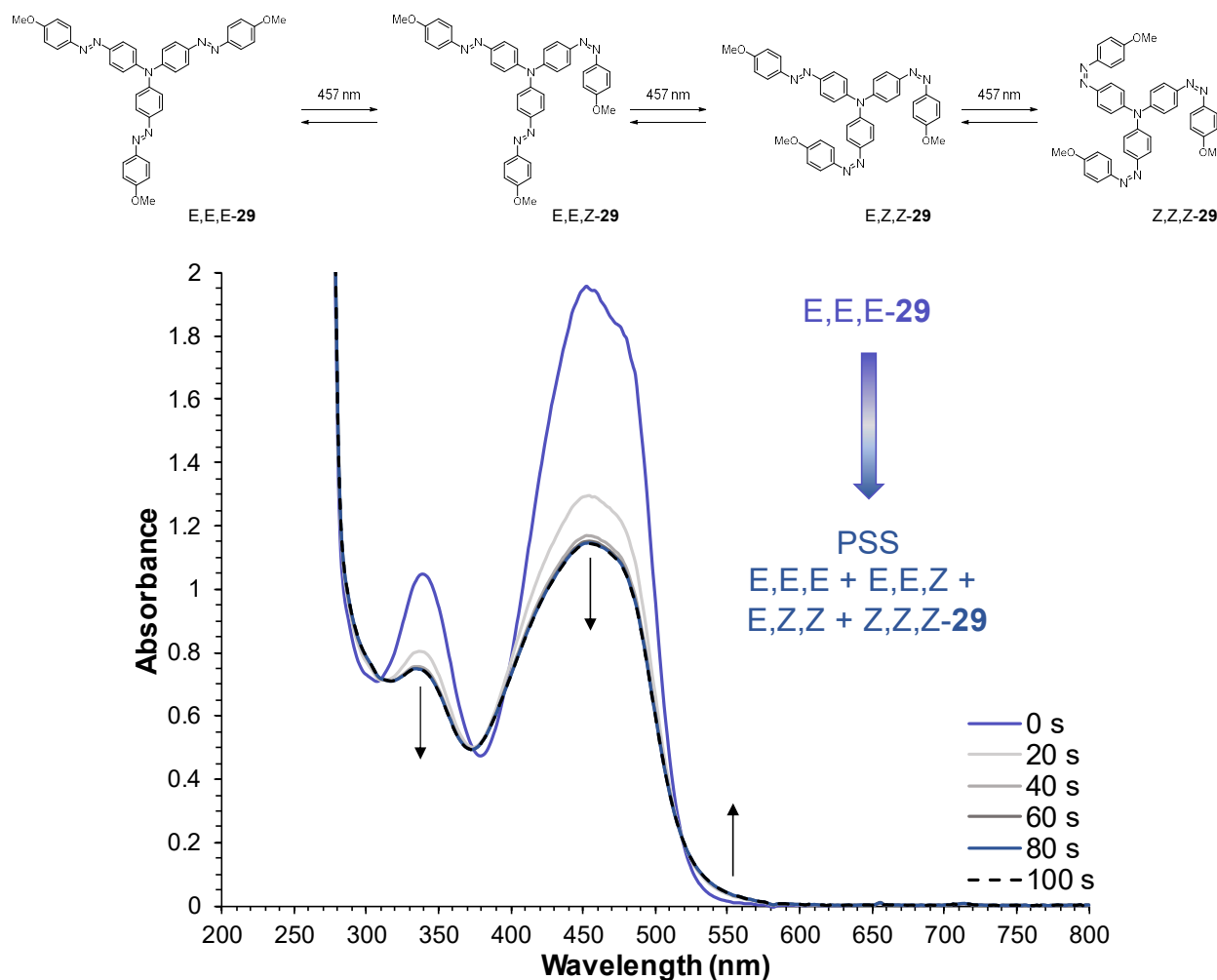


Figure 4.5. Optical spectra overlay of **29** (3.3×10^{-5} M in benzene) while irradiating with 457 nm light in a 1.0 quartz cuvette at room temperature. Following from E,E,E-**29** to PSS_{457 nm}, with three isosbestic points seen at 310, 374 and 518 nm.

E→*Z* photoisomerization of **29** can form up to three additional isomers. The UV-vis spectra gave a qualitative picture of the isomer system, leaving the identification and

quantification of the isomers present at PSS to be studied by $^1\text{H-NMR}$ spectroscopy. The full spectra of *E,E,E*-**29** is shown in Figure 4.6 in deaerated benzene- d_6 with a single methoxy singlet. The methoxy peaks are used to identify and determine the isomer composition at PSS.

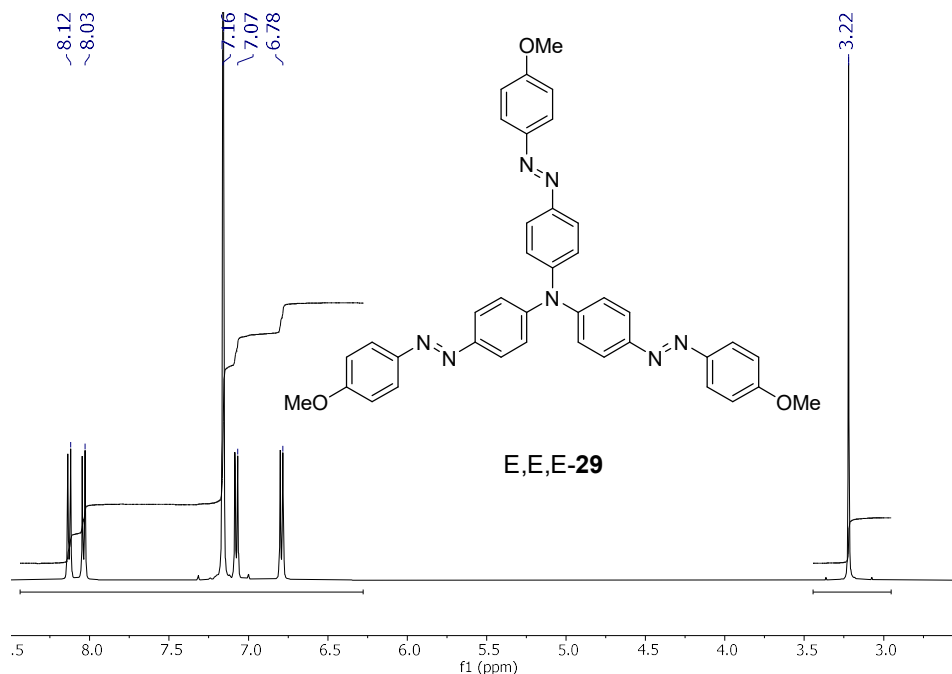


Figure 4.6. $^1\text{H-NMR}$ spectrum of *E,E,E*-**29** in benzene- d_6 .

Figure 4.7 shows a blow up of the spectra at the methoxy region pre- and post-irradiation of **29** with a 457 nm light. Five new peaks have formed, while some *E,E,E*-isomer (black) remains. The new peaks are identified as *E,E,Z*-**29** (red); *E,Z,Z*-**29** (purple); and *Z,Z,Z*-**29** (green). With *E,E,Z*-**29** having two singlets in a 2:1 (*E:Z*) isomer ratio and *E,Z,Z*-**29** having two peaks in a 1:2 (*E:Z*) isomer ratio, the *Z* isomer has a larger additive shielding effect on the methoxy peaks directly attached, which is consistent with the previous azobenzene systems discussed. These three *Z* isomer peaks are resolved and used to determine isomer composition at PSS_{547 nm}. The methoxy peaks on the non-switching *E* unit experience little shielding and poor peak resolution. The PSS_{457 nm} solution contains 30 % *E,E,E*-**29**; 38 % *E,E,Z*-**29**; 27 % *E,Z,Z*-**29**;

and 5 % *Z,Z,Z*-**29**. Overall *Z* isomer formation was 36% for **29** at PSS_{457 nm}, which is comparable to **20** at 39%. The overall *Z* isomer formation is less than **21** at 49% and **11** at 77% (PSS_{430 nm}).

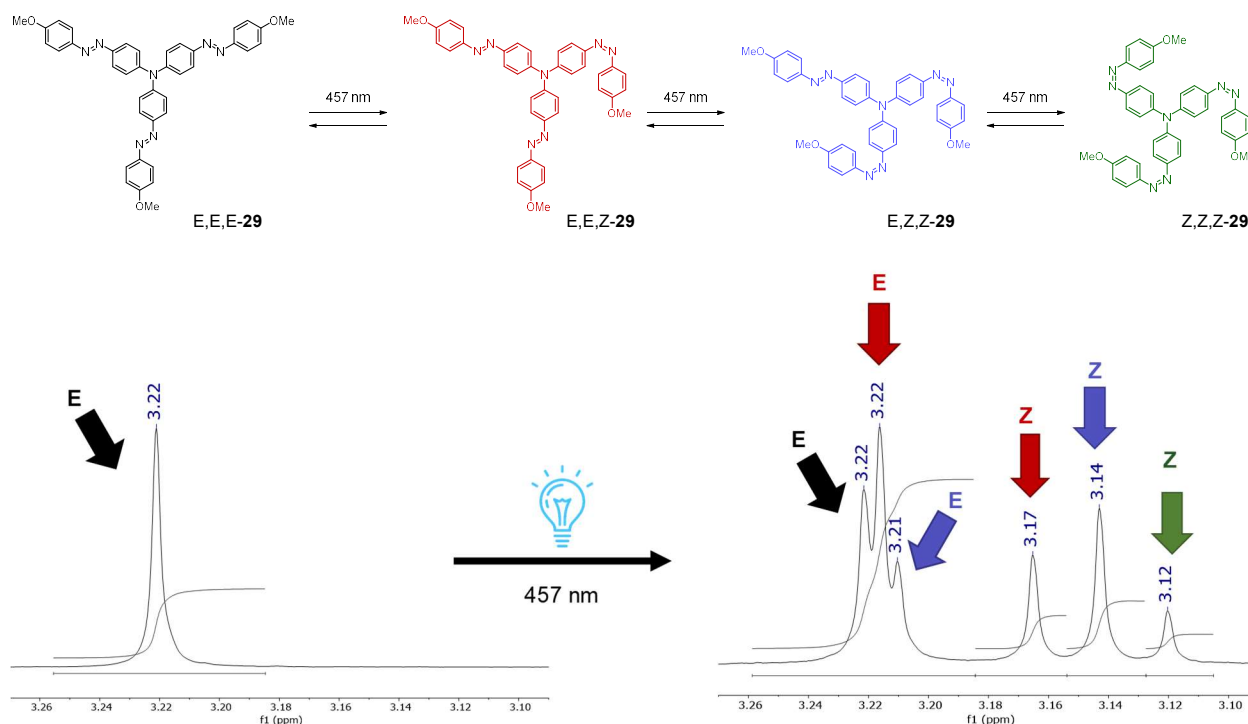


Figure 4.7. Methoxy region of the ¹H-NMR spectra of **29** in benzene-*d*₆ pre- and post-irradiation to PSS_{457 nm}.

4.4. Thermal *Z*→*E* isomerization of TA (**29**)

The *n*- π^* band of the optical spectrum at PSS_{457 nm} is overlapped by the stronger absorbing π - π^* band preventing the possibility of significant *Z*→*E* photoisomerization. However, *Z*→*E* isomerization will occur thermally over time as the system relaxes to the lower energy state. This can qualitatively be observed by dynamic UV-vis spectroscopy. The π - π^* absorption band was followed from the PSS_{457 nm} isomer mixture until only *E,E,E*-**29** remained, indicated by no further changes in the absorption spectrum in Figure 4.8. The isosbestic points were retained as the system returned to the all *E* isomer state. The thermal relaxation can also be followed by ¹H-NMR spectroscopy to gain the quantitative picture of how the isomer

composition changes over time, which is needed to determine the rate constant and thermal half-life for **29**.

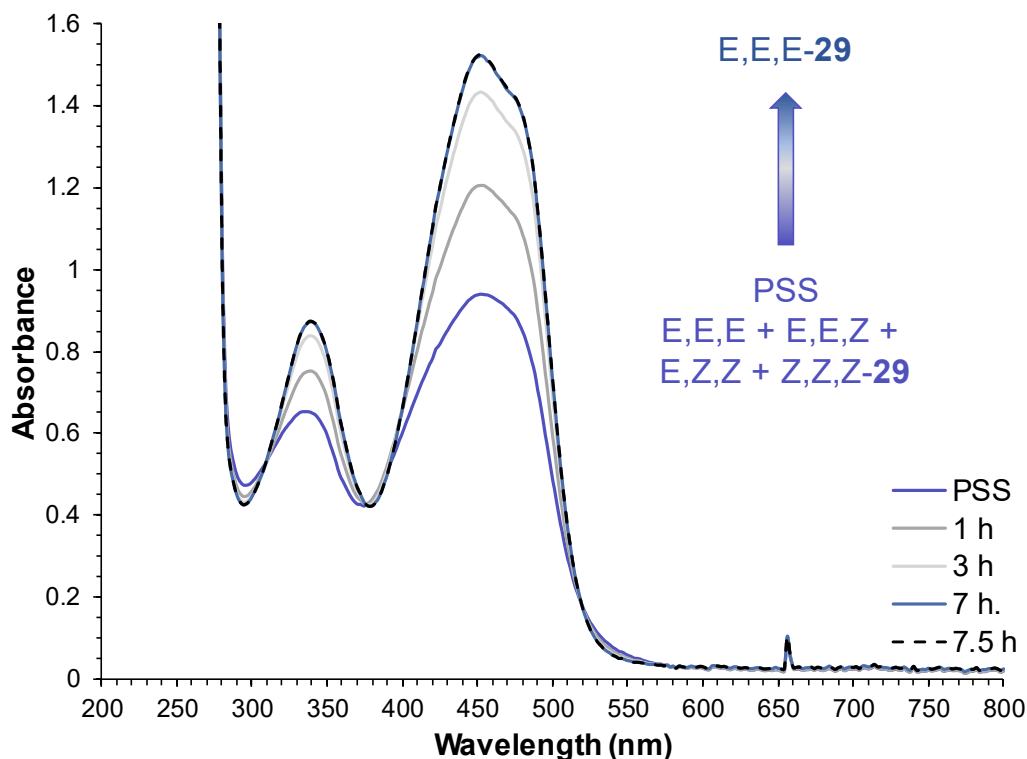


Figure 4.8. Optical spectrum of the thermal $Z \rightarrow E$ isomerization of **29** (5.15×10^{-5} M in benzene) at rt in the dark starting from $PSS_{457\text{ nm}}$ in a 1.0 cm quartz UV-vis cell.

A $^1\text{H-NMR}$ spectrum is evaluated over a set time interval to follow the **29** $PSS_{457\text{ nm}}$ solution until only the single $E,E,E\text{-29}$ peak remains. Plotting the concentration of the isomer versus time gives three thermal exponential decays and one growth in Figure 4.9. Each Z isomer arm will unwind until all arms have reached the E isomer in a three step consecutive fashion from $Z,Z,Z\text{-29} \rightarrow E,Z,Z\text{-29} \rightarrow E,E,Z\text{-29} \rightarrow E,E,E\text{-29}$. Because of this consecutive reaction, the first-order kinetics rate law for a 3 step consecutive reaction is applied. Equations 4.2 and 4.3 can account for the rate of formation simultaneously experienced when determining the rate of

decay for the isomers *E,Z,Z-29* and *E,E,Z-29*. The appropriate rate law equation (4.1-4.3) is applied to model the data and determine the rate constant (*k*). These rate constants are used to calculate the thermal half-life of each step ($t_{1/2}$) from the $\ln(2)/k$.

$$[Z, Z, Z] = [Z, Z, Z]_0 e^{-k_1 t} \quad (4.1)$$

$$[E, Z, Z] = [E, Z, Z]_0 e^{-k_2 t} + \frac{k_1 [Z, Z, Z]_0}{k_2 - k_1} (e^{-k_1 t} - e^{-k_2 t}) \quad (4.2)$$

$$[E, E, Z] = [E, E, Z]_0 e^{-k_3 t} + \frac{k_2 [E, Z, Z]_0}{k_3 - k_2} (e^{-k_2 t} - e^{-k_3 t}) + [Z, Z, Z]_0 e^{-k_1 t} \quad (4.3)$$

$$[E, E, E] = [azo]_{total} - [Z, Z, Z]_0 e^{-k_1 t} - [E, Z, Z]_0 e^{-k_2 t} - \frac{k_1 [Z, Z, Z]_0}{k_2 - k_1} (e^{-k_1 t} - e^{-k_2 t}) - [E, E, Z]_0 e^{-k_3 t} - \frac{k_1 [E, Z, Z]_0}{k_3 - k_2} (e^{-k_2 t} - e^{-k_3 t}) \quad (4.4)$$

The rate constants (*k*) at 298 K for *Z,Z,Z*→*E,Z,Z-29* is $4.54 \times 10^{-4} \text{ s}^{-1}$, for *E,Z,Z*→*E,E,Z-29* is $3.18 \times 10^{-4} \text{ s}^{-1}$, and for *E,E,Z*→*E,E,E-29* is $1.52 \times 10^{-4} \text{ s}^{-1}$, which translates to a thermal half-life ($t_{1/2}$) of 25 minutes, 36 minutes, and 76 minutes when left in the dark at 298 K. The methoxy functional groups are seen to decrease the stability of the *Z* isomer unit versus the unsubstituted tris-system analogue with a 170 minutes half-life (*E,E,Z* isomer).⁹⁰ The Gibbs free energy of activation (ΔG^\ddagger) is found by applying the Eyring transition state theory. A comparison of $\Delta G^\ddagger_{(298 \text{ K})}$ values for trisazo-**29** (25.4 kcal/mol) versus monoazo-**11** (22.3 kcal/mol) and bisazo-**20** (22.5 kcal/mol) shows a larger energy barrier for *Z*→*E* isomerization for **29** that is similar to that of parent azobenzene **1** (25.8 kcal/mol). As demonstrated in the previous two chapters, we are now looking to accelerate this *Z*→*E* rate by inducing the electron transfer cycle. The single amine center will ideally switch all three azobenzene arms. We will now discuss the impact of chemical and photo-electro oxidation on **29**.

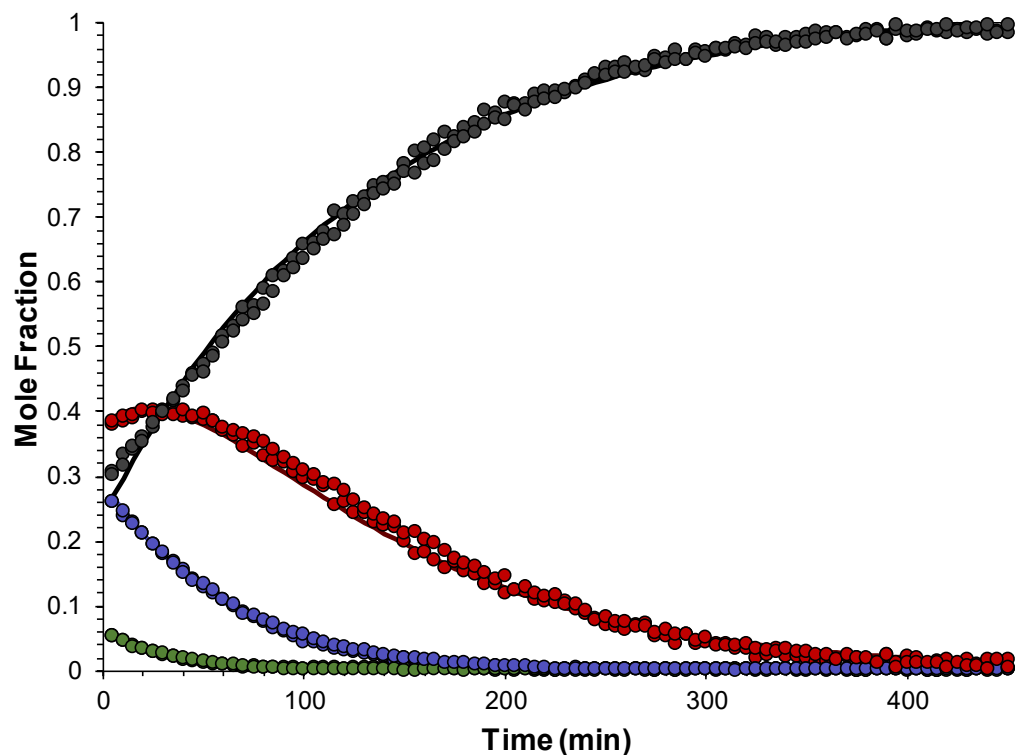
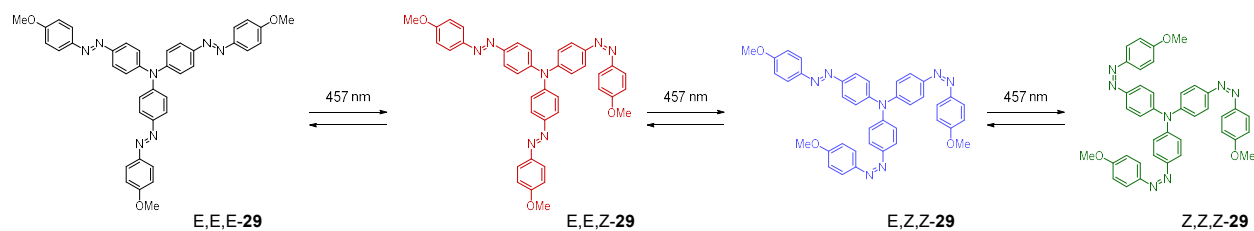


Figure 4.9. Isomer composition, determined by $^1\text{H-NMR}$ spectroscopy in benzene- d_6 , starting at $\text{PSS}_{457 \text{ nm}}$ to follow the thermal decay of $\text{Z,Z,Z} \rightarrow \text{E,Z,Z-29}$ (green); $\text{E,Z,Z} \rightarrow \text{E,E,Z-29}$ (purple); $\text{E,E,Z} \rightarrow \text{E,E,E-29}$ (red); and thermal growth of E,E,E-29 (black) over time.

4.5. Redox Switching of TA (29)

The electrochemical behavior from the redox active amino center of TA is measured by cyclic voltammetry (CV), which displays a single reversible CV wave (Figure 4.10). The oxidation potential (E°) of **29** is 1.04 V (vs SCE) with an E_{pp} of 90 mV. Each additional azobenzene attachment to the redox center is seen to increase the redox potential of the system with an E° of 0.92 V and 0.88 V vs SCE for **20** and **11**, respectively. The reference electrode is a

saturated calomel electrode (SCE), the electrolyte is tetrabutylammonium hexafluorophosphate (NBu₄PF₆), and the CV is calibrated by the standard ferrocene.⁷⁰ CRET (Cation Radical Electron Transfer) has an E° of 1.15 V (vs. SCE).⁷¹⁻⁷³ The oxidation of **29** is expected to lower the Z→E activation energy barrier to simultaneously convert all three units of Z isomers efficiently to *E,E,E*-**29**.

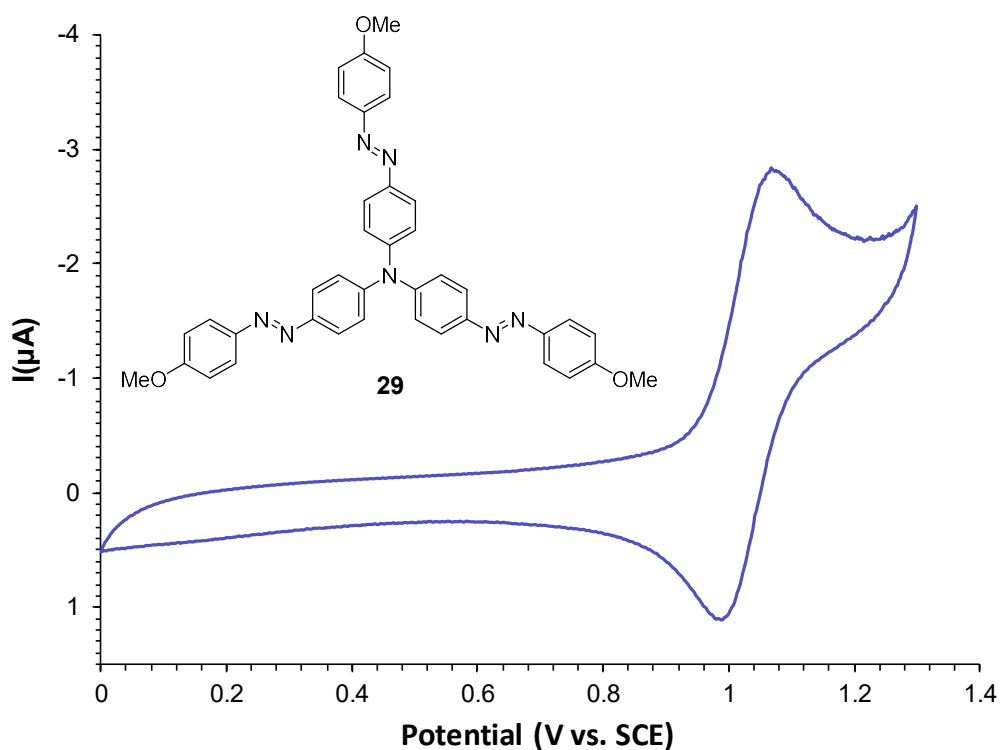


Figure 4.10. Cyclic voltammogram of **29** at 1.0 mM in purified dichloromethane and 0.10 M NBu₄PF₆ electrolyte gave a redox potential of 1.04 V vs. SCE. Scan rate was 20 mV/s with a 90 mV peak separation

To test this hypothesis, a solution of **29** in deaerated benzene is irradiated to the PSS_{457 nm} before adding 2 mole % of a CRET solution in DCM. The isomerization from PSS_{457 nm}→*E,E,E*-**29** is followed by UV-vis spectroscopy, occurring faster than the two seconds to record the

sample after injection. The results shown in Figure 4.11 show that a chemical oxidant induced a fast, complete, and catalytic conversion from $Z,Z,Z\text{-29} \rightarrow E,E,E\text{-29}$.

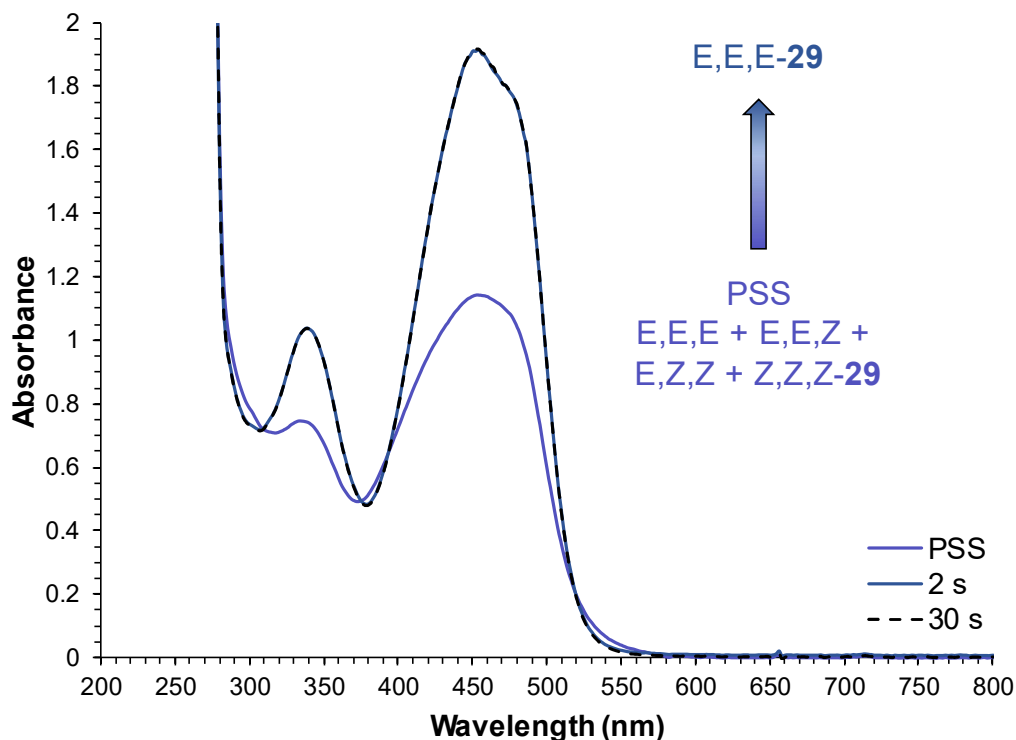


Figure 4.11. Optical spectra overlay of **29** at $PSS_{457\text{ nm}}$ in benzene ($3.3 \times 10^{-5}\text{ M}$) followed by the addition of 2.0 mole % CRET to return the E,E -isomer in a 1.0 cm quartz cuvette at rt.

Comparing the thermal half-life for the E,E,Z -isomer at 76 minutes (4,600 seconds) to the oxidized half-life of <0.5 second, there is a minimum $Z \rightarrow E$ rate acceleration of 9,100x upon a single electron oxidation. Extrapolating the oxidant loading from 2% to 100%, there is a minimum acceleration of 460,000x. The single electron oxidation of the amino center reduces the $Z \rightarrow E$ energy barrier versus the neutral case, demonstrating oxidation of one redox center converts all three azobenzene moieties effectively. The impact of photo-electro oxidation is next explored.

4.6. Photosensitizer for Photo, Photo-Electro catalytic switching of TA (29)

Photo-electro oxidation is carried out by introducing the photosensitizer, methylene blue (MB^+ -19) to the system, as introduced in chapter 2. A mixed solution of **29** and 5% MB^+ are combined in a methanol:toluene mixture. The UV-vis spectrum of the **29**/ MB^+ mixture shows a band at 452 nm belonging to the π - π^* band of **29** and at 660 nm belonging to MB^+ . Blue light (457 nm) irradiation is used to trigger $E \rightarrow Z$ isomerization of **29** without interference from MB^+ . Red light (660 nm) irradiation excites the MB^+ band to the triplet excited state ($^3\text{MB}^+$), which initiates the electron transfer mechanism. The resulting triplet excited state is observed to oxidize **29**, from the change in the π - π^* band indicating $Z \rightarrow E$ switching, returning to the E,E,E -**29** absorbance profile. These results indicate that the $^3\text{MB}^+$ triplet excited state successfully oxidizes the redox center of **29** to trigger the electron transfer cycle.

In the absence of an excitation source, the triplet excited state returns to the singlet ground state. Therefore, the oxidizing agent, MB^+ can be turned on and off in situ. Blue light can again trigger $E \rightarrow Z$ switching in the presence of the now “off” oxidizing agent. Therefore, a combined solution of **29** and MB^+ should allow for $E \rightarrow Z \rightarrow E$ toggling by interchanging between blue and red light irradiation to produce a photo, photo-electro catalytic switching cycle. The **29**/ MB^+ system is followed by dynamic UV-vis spectroscopy while toggling between blue and red light irradiation at 1 minute intervals with 30 seconds of no light exposure in between. The system reversibly displays $E \rightarrow Z$ switching under blue light exposure and $Z \rightarrow E$ switching under red light exposure. Plotting the absorbance at 454 nm versus time gives a clear picture of the $E \rightarrow Z \rightarrow E$ cycling (Figure 4.12) for 10 repetitions. The robust redox attachment is shown to go through the electron transfer cycle if a catalytic amount of the redox group is oxidized by chemical or photo-electro oxidation.

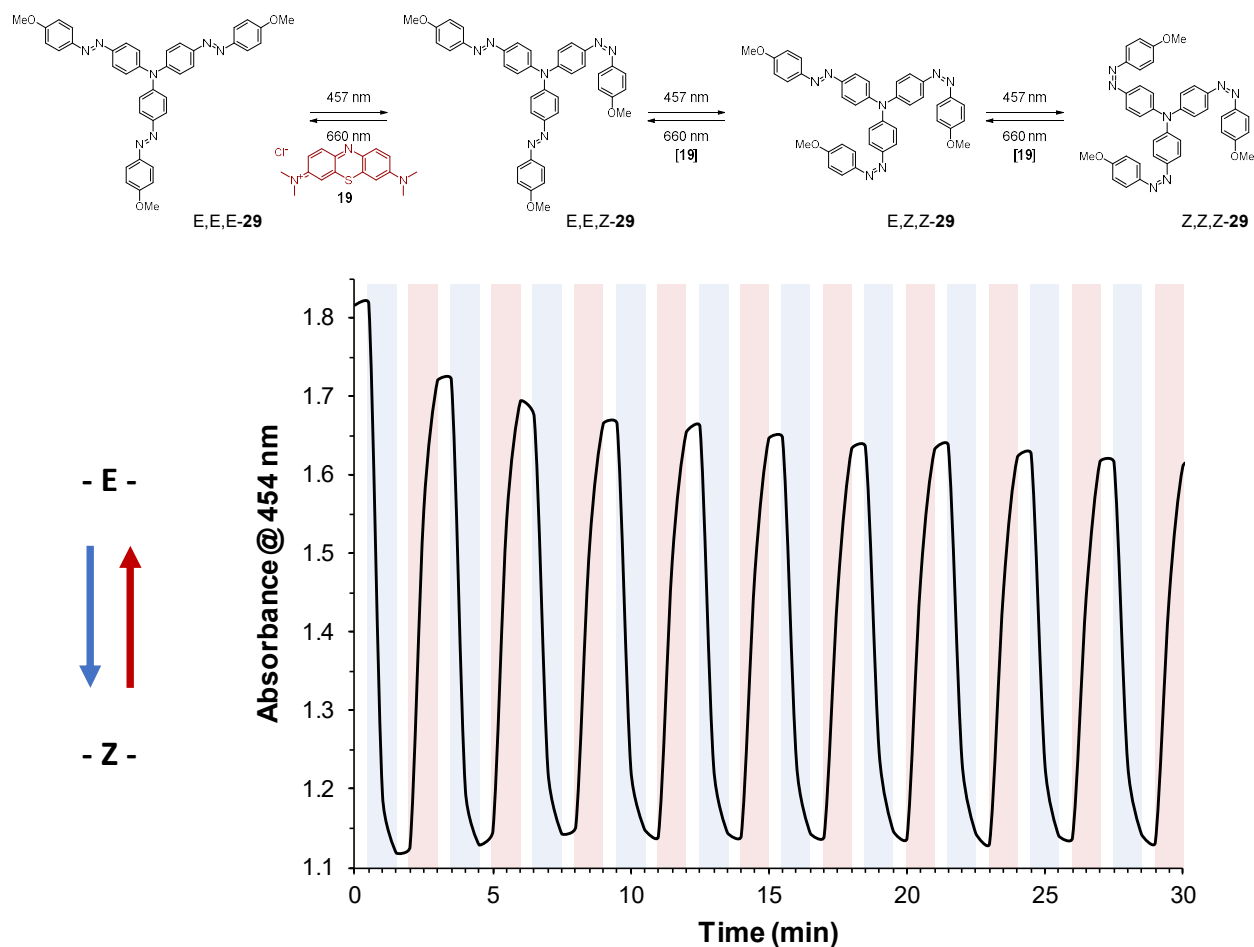


Figure 4.12. Photo, Photo-Electro cycling of **29** (2.9×10^{-5} M) and 9.9% **MB⁺** (injection of $100 \mu\text{L}$ of 8.91×10^{-5} M **MB⁺**) in deaerated 3% methanol in benzene in a 1.0 cm quartz cuvette at rt. The solution is irradiated with alternating cycles of blue then red light to toggle between E→Z→E isomers with blue/red light exposure for 1 min and no light exposure for 30 s for ten cycles.

A loss of effectiveness is observed in the photo redox cycling of compound **29** with **MB⁺** in comparison to the cycling of previous compounds **11** and **20** with **MB⁺**. The redox potential (E°) of **MB⁺** (0.97 V vs. SCE) is less than **29** (1.04 V vs. SCE) for this cycling system, while the E° of **MB⁺** is greater than compounds **11** (0.88 V vs. SCE) and **20** (0.92 V vs. SCE). The effectiveness of radical cation formation from the triplet excited state (${}^3\text{MB}^{++}$) decreases and may be more sensitive to trace impurities quenching the ${}^3\text{MB}^{++}$ or ${}^{29+}$. The system is also more

sensitive to the photodegradation of MB^+ under red light exposure. The $Z \rightarrow E$ isomerization also appears to be incomplete. The Z,Z,Z and E,Z,Z isomers of **29** are hypothesized to have a lower redox potential than the E,E,Z isomer, reducing radical cation accelerated $E,E,Z \rightarrow E,E,E$ isomerization

4.7. Co-crystallization of TA•DDQ

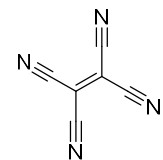
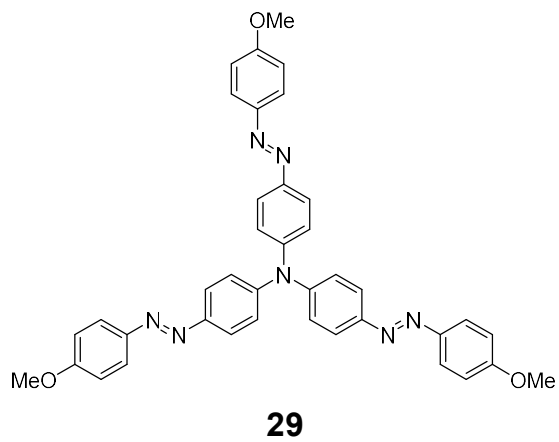
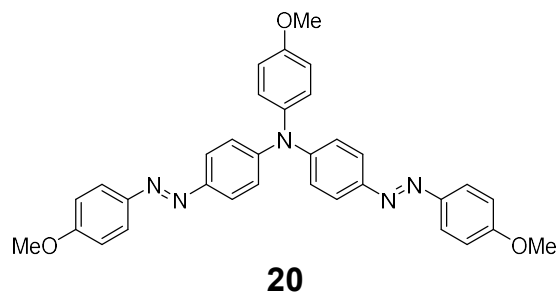
Recently, designing photomechanical crystals using multiple components including azobenzenes have been used towards designing actuators. Co-crystallization is a crystal engineering technique where a crystal consists of at least two different molecules. Cocrystals are obtained from tuning intermolecular interactions. In the case of electron donor-acceptor (DA) cocrystals, the key design requirement is to employ an electron-rich donor molecule and an electron-poor acceptor molecule designed for prospective DA intermolecular association.⁹¹ The **ra**-azobenzene systems should be a good donor competent, potentially forming photomechanical cocrystals with suitable acceptors.

These cocrystal non-covalent interactions are weak and reversible. Polymorphs, as well as solvates and hydrates, could occur by variances in condition during assembly, so forms are not always predictable. Polymorphs are of interest for the change in the cocrystal's bulk properties.⁹² Cocrystals typically require discrete supramolecular synthons, which are units formed or assembled by known or conceivable cohesive intermolecular interactions.⁹³ Cocrystal formation is contingent on favoring heteromeric assembly over the homomeric assembly observed in regular crystallization. Due to the inherent reversibility of non-covalent bonding, the formation and isolation of DA cocrystals can become challenging, and the co-crystallization conditions can play an important role in the successful formation and isolation of cocrystals.

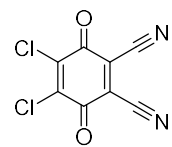
The tris-system **29** and bis-system **20** are electron rich donor groups that may form cocrystals when paired with a strong electron acceptor, establishing donor-acceptor (HOMO-LUMO) interactions in a set ratio of donor-acceptor stacking. The HOMO of the donor and LUMO of the acceptor are used to predict the interactions.⁹⁴ Ideally the donor group will have a high energy HOMO, while the LUMO energy is low. Phase matching between the orbitals then can form a donor-acceptor complex, whose structure may be elucidated by single-crystal XRD. Two common electron acceptors are 2,3-Dichloro-5,6-dicyano-1,4-benzoquinone (DDQ) and tetracyanoethylene (TCNE), which have been used successfully in the past to form donor-acceptor complexes with azobenzene and nitrosoamine donor molecules⁹⁵⁻⁹⁷.

4.7.1. Preparation of Cocrystals

Equal molar solutions of donor and acceptor are prepared individually in benzene. The donor solution is then transferred to the vial containing the acceptor solution. The donor components, tris-system **29** and bis-system **20** are orange in benzene (Figure 4.13). The acceptor components, DDQ and TCNE are pale yellow and colorless, respectively. The 1:1 mixture of **29:DDQ** immediately turns deep blue, while **29:TCNE** remains orange in color. Similarly, **20:DDQ** immediately turns deep blue, while **20:TCNE** experiences little in color change (Figure 4.13). A donor-acceptor interaction is expected to form a donor-acceptor complex as indicated by a color change (a new CT band of the DA complex). The **DDQ** acceptor appears to form a complex in solution with both **29** and **20**. The solution mixtures are cooled overnight (0°C) with no crystal or solid formation observed. Slow evaporation at rt forms crystals for the **29:DDQ** complex and an amorphous solid for the **20:DDQ** complex.



TCNE (35)



DDQ (34)

Scheme 4.3. Donor-acceptor co-crystallization building blocks. The donor components left (**20** and **29**) and the acceptor components (**TCNE** and **DDQ**).

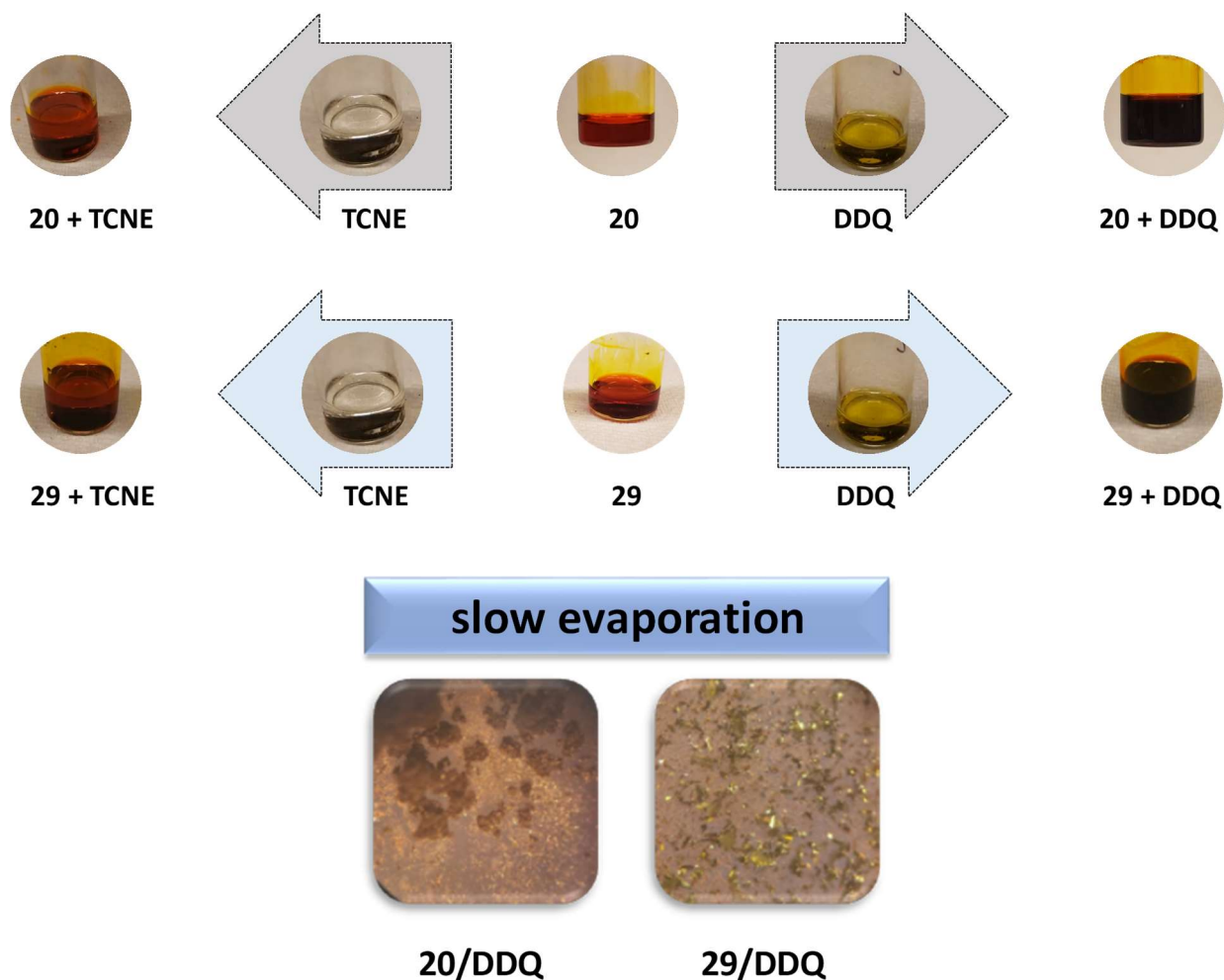


Figure 4.13. Benzene solutions of **20** (red-orange), **29** (red-orange), **TCNE** (colorless), and **DDQ** (yellow). The resulting mixed solutions of **20+TCNE** and **20+DDQ** (Top) or **29+TCNE** and **29+DDQ** (Middle) illustrate any solution color changes with mixing. (Bottom) Dark blue-green solid formed for **DDQ** combinations, with crystals forming by slow evaporation for **29/DDQ**.

4.7.2. Single-crystal XRD structure

The single-crystal XRD structure of the **29:DDQ** cocrystal is obtained. The solution of **29•DDQ** crystallizes in the triclinic space group P1 with an R_1 of 0.1465, and a GooF of 2.333 as determined by single crystal X-ray diffraction (XRD) measured at 20 °C illustrated in Figure 4.14. The unit cell parameters are listed in Table 2. The asymmetric unit cell contains a 2:2 ratio

of **29:DDQ**. Some short contacts (green dashes) are listed in Figure 4.14 between **29-DDQ** and **DDQ-DDQ**. Typically, **DDQ** crystal packing produces a singly stranded **DDQ** motif along the carbonyl groups,⁹⁸ which is not present in the **29**-complex.

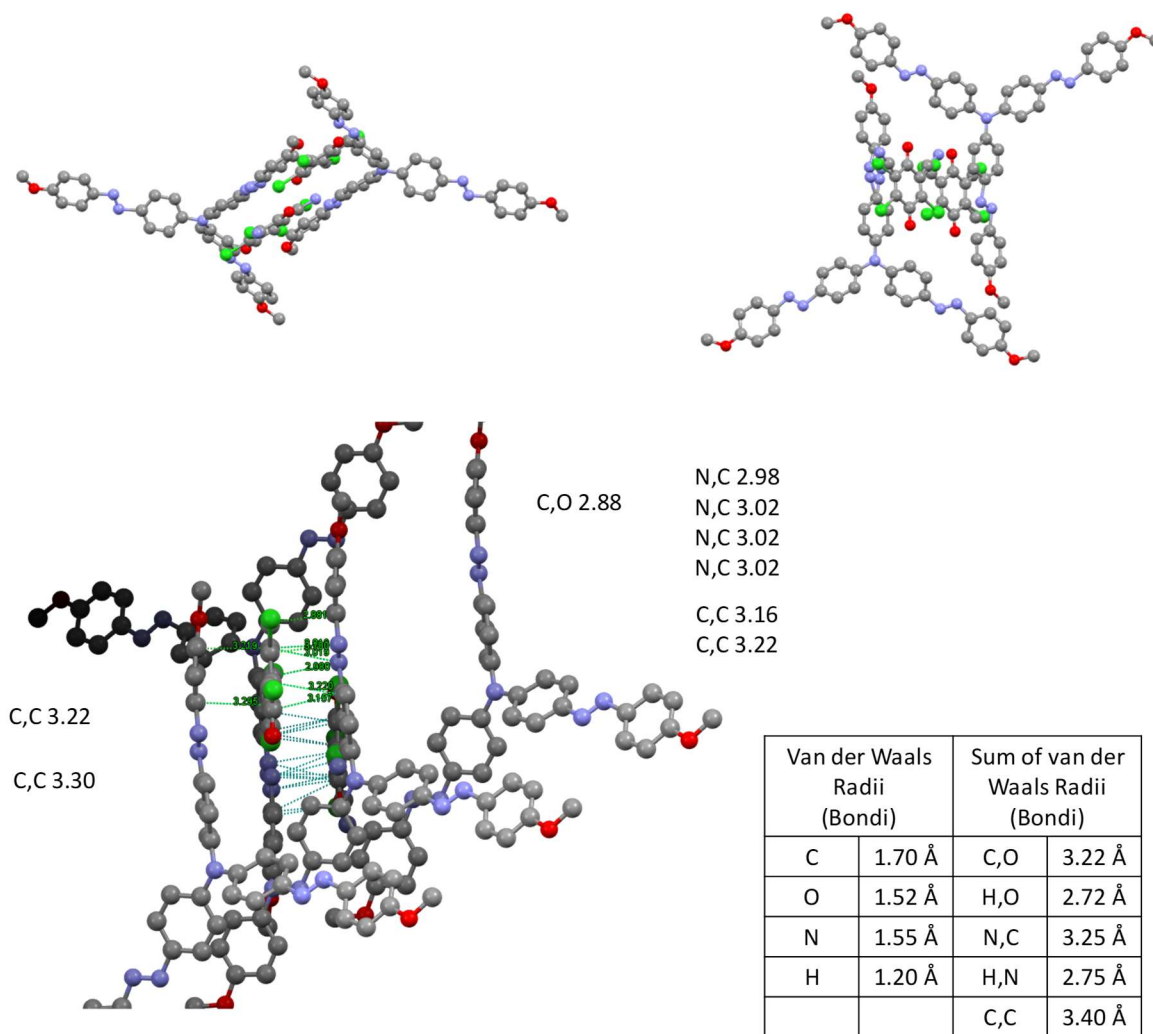


Figure 4.14. Crystal structure of the **29•DDQ** complex illustrating the packing of the asymmetric unit cell. (bottom) Short contacts interactions between the **29•DDQ** complex.

Table 2. Unit Cell Parameters for the Cocrystal (29•DDQ)

Unit cell	29•DDQ
Identification code	SCB296
Temperature/K	293(2)
Crystal system	triclinic
Space group	P1
a/Å	7.16022(12)
b/Å	15.7569(2)
c/Å	18.3717(3)
α /°	86.2966(11)
β /°	86.3981(13)
γ /°	81.6571(13)
Volume/Å ³	2043.53(5)

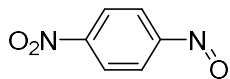
4.8. Conclusions

Tris(azobenzene)amine **29** is successfully synthesized and characterized by UV-vis and NMR spectroscopy. The isomer composition at PSS_{457 nm} is 30 % *E,E,E-29*; 38 % *E,E,Z-29*; 27 % *E,Z,Z-29*; and 5 % *Z,Z,Z-29*. Thermal relaxation from *Z,Z,Z-29*→*E,Z,Z-29*→*E,E,Z-29*→*E,E,E-29*, monitored by ¹H-NMR spectroscopy, was used to calculate the thermal half-life for *Z,Z,Z-29* as 25 minutes, *E,Z,Z-29* as 36 minutes, and *E,E,Z-29* as 76 minutes at room temperature. Rapid and complete *Z*→*E* isomerization is successfully demonstrated upon oxidation of the single redox center of **29**. The electron transfer catalytic cycle is initiated with the chemical oxidant (CRET), and a minimum electro-stimulated half-life of <0.5 second for **29**^{•+}

is estimated. The electro-stimulated minimum rate acceleration for **29**⁺ is 460,000x that of neutral **29** when *Z*→*E* isomerization is extrapolated to 100% CRET loading. Photo, photo-electro cycling was successful at toggling between *E*→*Z*→*E* **29**. Initial work towards donor-acceptor cocrystals yields a moderate quality cocrystal of **29** and **DDQ**. Further experiments are needed to generate higher quality single crystals. The combination of **20** and **DDQ** suggest a complexation occurs with the large color change, though no crystals were formed. Rapid, complete, catalytic *Z*→*E* isomerization of **29** is observed for all attached azobenzene units through the oxidation of the single redox center.

4.9. Experimental Section

1-nitro-4-nitrosobenzene (31)



31

4-Nitroaniline **30** (0.5538 g, 4.009 mmol) was placed in a 250 mL RBF with DCM (24.0 mL) and stirred until dissolved at rt to dissolve. Separately, OXONE® (4.9258 g, 8.003 mmol) was dissolved in DI water (20.0 mL) and added all at once to the stirring **30**-DCM mixture. The reaction was complete after 6 h of vigorous stirring as determined by TLC analysis indicating the absence of starting material **30**. The green organic layer was collected, and the aqueous layer extracted with DCM (2x10 mL) but are not combined. It was found that the washings mostly consist of the over oxidized *p*-dinitrobenzene product. The combined organic phases were then dried over anhydr Na₂SO₄, filtered, and solvent was removed in vacuo to provide the crude product **31** as a yellow solid (0.60 g, 3.9 mmol, 98% crude yield), which was used without further purification in a Mills condensation.

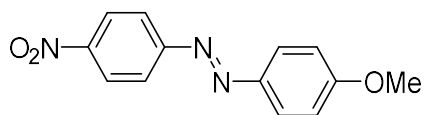
Penoni, et al. previously reported the synthesis at 71% yield.⁹⁹

Crude Yield: 98%

MW = 152.11 g mol⁻¹

¹H-NMR (360 MHz, CDCl₃): δ 8.52 (d, *J* = 9.0 Hz, 2H), 8.05 (d, *J* = 9.0 Hz, 2H).

4-methoxy-4'-nitroazobenzene (32)



32

Product **31** (0.6608 g, 4.344 mmol) was partially dissolved in glacial acetic acid (10.0 mL) and stirred in a 100 mL RBF forming a green colloidal slurry. Separately, *p*-anisidine **14** (0.5353 g, 4.347 mmol) was dissolved in ethanol (15.0 mL) in a beaker before being transferred slowly to the stirring **31**-

acetic acid mixture. The reaction was stirred for 24 h at rt at which time TLC indicated the absence of any starting material **31**. The reaction mixture was neutralized with NaOH aq before DCM (50 mL) was added to the RBF, and the deep red organic phase extracted after adding brine (5 mL) as a separation aid. The aqueous layer was washed with DCM (3x20 mL). The combined organic phase was dried over anhydr MgSO₄, filtered, and solvent was removed in vacuo to yield crude **32** as a grey-orange amorphous solid. Purification was achieved by silica gel column chromatography. The product **32** was dissolved in minimal 1:2 DCM-hexanes before loading the column and rinsing the product through the silica using 1:2 DCM-hexanes eluent. The solvent was removed in vacuo to yield **32** as an orange amorphous solid (0.65 g, 2.5 mmol, 58%).

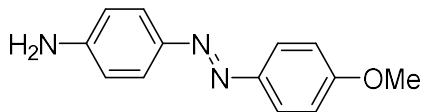
Ribagorda, et al. previously reported the synthesis at 66% yield.¹⁰⁰

Yield: 58%

MW = 257.25 g mol⁻¹

¹H-NMR (360 MHz, CDCl₃): δ 8.37 (d, *J* = 9.0 Hz, 2H), 7.99 (d, *J* = 9.0 Hz, 2H), 7.98 (d, *J* = 9.0 Hz, 2H), 7.03 (d, *J* = 9.1 Hz, 2H), 3.92 (s, 3H).

4-amino-4'-methoxyazobenzene (**33**)



33

Product **32** (1.57 g, 6.10 mmol) was dissolved in ethanol (250.0 mL) and stirred in a 500 mL RBF.

Sodium sulfide nonahydrate, Na₂S•9H₂O, (4.4229 g,

18.41 mmol) was dissolved in DI water (60.0 mL) and

added drop wise to the **32**-ethanol mixture over a period of 5 minutes. The solution was then set to reflux for 24 h in a silica oil bath, producing a deep red solution. DCM (50 mL) and brine (5 mL) were added to the RBF, and the organic phase collected. The aqueous layer was washed

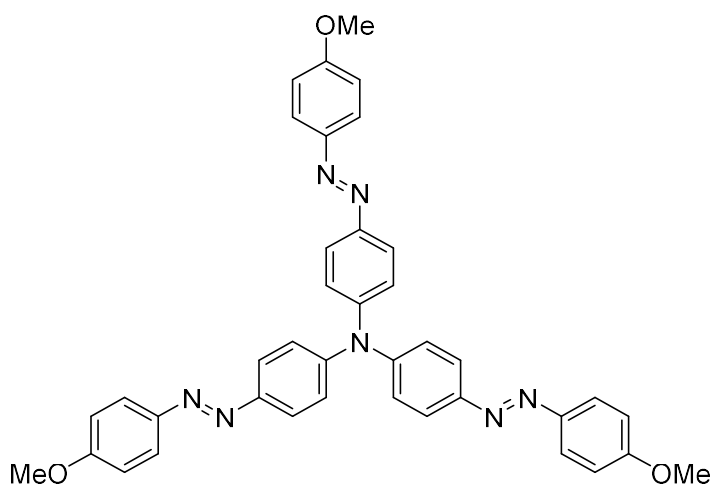
with DCM (3x 20mL). The combined organic phases were then dried over anhydr MgSO₄, filtered, and solvent was removed in vacuo to provide the crude product **33** as a red powder. The crude product was dissolved in DCM (100 mL) and filtered through a plug of silica gel, and the solvent was removed in vacuo to afford **33** as an orange powder (1.37 g, 6.03 mmol, 99% yield). Tripathy, et al. previously reported the synthesis at 40% yield.¹⁰¹

Yield: 99%

MW = 227.27 g mol⁻¹

¹H-NMR (360 MHz, CDCl₃): δ 7.85 (d, *J* = 9.0 Hz, 2H), 7.77 (d, *J* = 8.7 Hz, 2H), 6.99 (d, *J* = 9.0 Hz, 2H), 6.74 (d, *J* = 8.7 Hz, 2H), 3.99 (s, 2H), 3.88 (s, 3H).

N,N,N-tris(azobenzene)amine (TA) **29**



29

A flame-dried 2 dram vial was charged with **33** (0.1808 g, 07956 mmol), while a flame-dried 25 mL RBF was charged with 4-bromo-4'-methoxyazobenzene **15** (0.4900 g, 1.683 mmol) and a stir bar. Transferring to a N₂ purged dry box, anhydr toluene (9 mL), Pd(dba)₂ (0.0075 g, 0.013 mmol),

and a 0.10 M solution of P(*t*Bu)₃ in anhydr toluene (120 μL, 0.0120 mmol) were added to the RBF. The vial of **33** was transferred to the RBF with toluene (2 mL) washings. Lastly, NaO*t*Bu (0.25 g, 2.6 mmol) and toluene (1 mL) were added to the flask and stirred for ~1 min. The flask was capped with a rubber septum, removed from the dry box, and the mixture was stirred under

N₂ in a silicone oil bath at 90 °C for ~24 h, allowed to cool, and then filtered through a layered bed of celite and 5 g basic alumina III by vacuum filtration. The filter cake was washed with THF (100 mL), and the combined solvents were removed in vacuo to yield a red amorphous solid, which was recrystallized from acetone to afford **29** as a red needle solid (0.51 g, 0.79 mmol, 82%).

Yield: 82%

mp 211-213 °C

MW = 647.74 g mol⁻¹

¹H NMR-(500 MHz, C₆D₆): δ 8.13 (d, *J* = 8.9 Hz, 6H), 8.04 (d, *J* = 8.8 Hz, 6H), 7.08 (d, *J* = 8.8 Hz, 6H), 6.79 (d, *J* = 8.9 Hz, 6H), 3.22 (s, 9H).

¹³C-NMR (125 MHz, CDCl₃): δ 162.5, 151.6 147.0 132.4 125.0 124.7 124.2 114.4 55.7.

HRMS (EI/EBE) *m/z*: [M + H]⁺ Calcd for C₃₉H₃₄N₇O₃ 648.2723; Found 648.2746.

Photochemical Experiments

Optical spectrum of **29** in benzene (Figure 4.4)

Benzene was sparged with N₂ gas for ~ 5 min in a vial prior to use. A stock solution of 4.5 x 10⁻⁵ M **29** in deaerated benzene was prepared by diluting 0.00029 g of **29** in benzene using a 10.0 mL volumetric flask. A dilution of 2.2 mL stock solution to 3.0 mL yields **29** solution at 3.3 x 10⁻⁵ M, which was transferred to a 1.0 cm quartz cuvette and capped with a Teflon stopper. Absorbance was measured from 200 to 800 nm.

Photochemical conversion of *E,E,E*-**29** to PSS *E/Z*-**29** mixture (Figure 4.5)

A solution of 3.3×10^{-5} M **29** in benzene was prepared as for Figure 4.4. Then 3.0 mL of this solution was transferred to a 1.0 cm quartz cuvette and capped with a Teflon stopper. The optical spectrum of the sample was recorded (200-800 nm) every 4 s under irradiation by a 457 nm 7 W LED source for 6 min to achieve the PSS of **29**.

¹H-NMR spectra of *E,E,E*-**29** and the *E/Z*-**29** mixture at the PSS_{457 nm} (Figure 4.7)

Benzene-*d*₆ was sparged with N₂ gas for ~ 5 min in a vial prior to use. A solution of 6.2×10^{-3} M **29** in benzene-*d*₆ was prepared by dissolving 0.0040g of **29** in 1.0 mL benzene-*d*₆ in an NMR tube via gas-tight syringes. A stream of N₂ gas was blown into the NMR tube for ~ 1 min prior to capping and sealing with a small strip of parafilm. The tube was kept covered until inserting into the NMR instrument to minimize light exposure to obtain an all *E* isomer spectrum. After the all *E* spectrum was measured the NMR tube was irradiated with a 457 nm light source to achieve PSS. The NMR tube was placed in a mirrored Dewar with ~100 mL of an ice-water slurry to prevent any sample heating from the light source placed on top. The sample was irradiated for ~ 30 min followed by additional ~15 min intervals until no change was detected in the ¹H-NMR spectrum.

Thermal *Z*→*E* conversion of **29** in benzene (Figure 4.8)

Prior to addition, benzene was sparged with N₂ gas for ~ 5 min. A stock solution of 5.15×10^{-5} M **10** in benzene was prepared by first dissolving 0.0100 g of **29** in 30.0 mL benzene to

yield a 5.15×10^{-5} M stock solution of **29**. The solution was sparged for ~1 min before transferring 3.0 mL to a 1.0 cm quartz cuvette via 500 μ L gas-tight syringe. The cuvette was capped with a TeflonTM stopper. The solution was irradiated with a 457 nm 7 W LED source for a few minutes to reach the PSS, as confirmed by the optical spectrum. The thermal Z→E conversion starting at PSS, was followed by measuring the absorbance (200-800 nm region) in the dark at 15 min intervals for 12 h.

Thermal Z→E conversion of 29 followed by ¹H-NMR spectroscopy (Figure 4.9)

A solution of 6.2×10^{-3} M **29** in benzene-*d*₆ was prepared and the PSS achieved as described above in Figure 4.7. Then a ¹H-NMR spectrum of the mixture was taken every 4 min 44 s for a total of 100 spectra using the Bruker AM-500 NMR spectrometer, which was capped to prevent ambient light exposure at 295 K.

Cyclic voltammogram of 29 (Figure 4.10)

To a 25.0 mL volumetric flask, TBAPF₆ (0.97 g, 2.5 mmol) and purified,⁷⁸ freshly distilled DCM were added. The 0.1 M electrolyte solution (8.0 mL) was transferred to an electrochemical cell (4-neck flask). A blank cyclic voltammogram (0.0 V to 1.3 V vs. SCE, 20 mV/s) confirmed an absence of impurities before adding **29** (0.0052 g, 8.0×10^{-6} mol) to the flask with stirring to make the 1.0 mM solution. The potential was scanned from 0.0 V to 1.3 V vs. SCE at a rate of 20 mV/s.

Redox $Z \rightarrow E$ switching of **29** (Figure 4.11)

A 3.3×10^{-5} M **29** solution in benzene- d_6 was prepared as for Figure 4.4. Separately, a 4.35×10^{-4} M solution of CRET was prepared from dissolving CRET (0.00079 g, 1.3×10^{-6} mol) in freshly distilled DCM (3.0 mL). To a 1.0 cm quartz cuvette, 3.0 mL of **29** solution (9.9×10^{-8} mol) was added and capped with a Teflon stopper and irradiated to the PSS with a 457 nm LED source as followed by optical spectroscopy. The PSS mixture was then injected via syringe with 4.5 μ L of the CRET solution (2.0×10^{-9} mol, 2.0%), capped, and shaken (~ 2 s) before measuring the absorbance (200-800 nm).

Photo, Photo-Electro $E \rightarrow Z \rightarrow E$ cycling of **29** with MB^+ (Figure 4.12)

A N_2 -deaerated 3.00×10^{-5} M solution of **29** in toluene was prepared. To a 1.0 cm quartz cuvette was added 3.0 mL of **29** in toluene solution along with 100.0 μ L of a N_2 -deaerated 8.91×10^{-5} M solution of MB^+ in methanol (9.9 mol% based on **29**). The resulting concentrations of **29** and MB^+ in the cuvette were 2.9×10^{-5} M and 2.9×10^{-6} M, respectively. The cuvette was closed with a TeflonTM stopper. Two LED light sources (457 nm and 660 nm) were positioned to irradiate the cuvette at a distance of 4-5 inches. The lights were toggled on and off, alternating in sequence, at 1 min light on and 30 s light off intervals while the optical spectrum of the sample was recorded (200-800 nm) every 15 s. A total of ten 457/660 nm switching cycles were performed.

CHAPTER 5.

STILBENE BIS-SYSTEMS

5.1. Introduction to the Electro-, Photo-, and Thermal Properties of Stilbenes

This project introduces the long-lived photochromic moiety, stilbene, to the bis-flexor redox system. A stilbene consists of two phenyl rings linked by a C=C double bond in either the *Z* or *E* isomeric form. Stilbenes are chemically and thermally stable with tunable switching rates. Like azobenzenes, stilbenes can reversibly switch between these two isomeric states. *E*-stilbene (*E*-**36**) is near planar while *Z*-**36** is twisted out of the plane by 30-50° between the phenyl rings (Figure 5.1).^{102, 103} The optical spectrum of *E*-**36** has a π - π^* absorption band at ~320 nm, while *Z*-**36** has a π - π^* band at ~280 nm (Figure 5.2).^{104, 105} The *E* isomer is thermodynamically favored by 5 kcal/mol¹⁰⁶⁻¹⁰⁸ with an activation barrier of 46 kcal/mol for *Z*→*E* isomerization (Figure 5.2),¹⁰² which is nearly double that of the azobenzene *Z*→*E* barrier at 26 kcal/mol.^{26, 27} This barrier results in a thermal half-life of ~10¹² years (30 °C) for *Z*-**36**,^{109, 110} significantly longer than *Z*-azobenzene (**1**) at ~2 days. A disadvantage to the high energy barrier is that often high temperatures, greater than 210 °C, are needed for *Z*→*E* isomerization to occur on the hour timescale.^{109, 110}

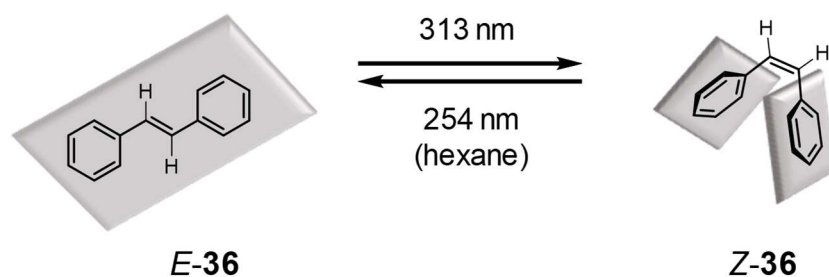


Figure 5.1. The *E* and *Z* isomer of stilbene (**36**) achieved photochemically.

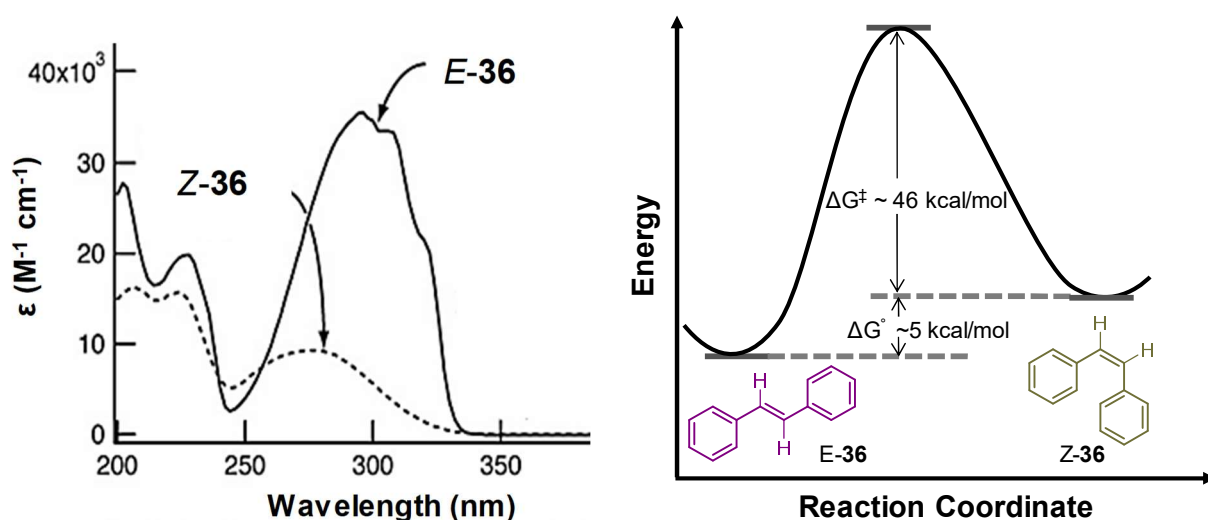


Figure 5.2. (Left) The electronic absorption spectra of *E*-**36** (solid line) and *Z*-**36** (dashed line). Figure reproduced from Ref. ¹⁰⁵. (Right) Stilbene (**36**) potential energy diagram for *E* and *Z* isomers with a *Z*→*E* activation energy barrier of 46 kcal mol⁻¹.

5.2. Photo-Electro-Transfer Catalysis of Redox Auxiliary-Mediated Stilbene (**37**)

Blackstock and coworkers proposed that the stilbene *Z*→*E* energy barrier would be greatly reduced by oxidizing an attached redox unit. Therefore, dianisylamine was attached to a series of stilbene moieties to demonstrate the impact that oxidizing the attached redox group has on the rate of stilbene *Z*→*E* isomerization. Oxidation of the **ra** unit for a *Z*-**ra**-stilbene to its

radical cation state quickly isomerizes the molecule to the more stabilized *E*-isomer.¹¹¹ The oxidized *E*-isomer can then electron transfer with another neutral *Z*-isomer to complete the catalytic electron transfer cycle. Blackstock and coworkers demonstrated that the single electron oxidation of the **ra**-stilbene was found to be catalytic while also producing *E*-stilbene at room temperature for a series of substituted amino-stilbene derivatives.¹¹¹ For the case of stilbene **37**, the photoconversion to the PSS_{430nm} consists of 60:40 *Z*:*E*-**37** (Figure 5.4). The thermal *Z*→*E* isomerization half-life was 135,000 h at 30 °C in DMSO. The oxidation potential (E°) of **37** was 0.58 V vs SCE in 1.0 mM DCM with 0.1 M NBu₄PF₆.¹¹¹ Upon oxidation with 2 mole % CRET the *Z*→*E* isomerization experienced a minimum rate acceleration of 2,000,000,000x at rt.¹¹¹ Chemical oxidation was successful in accelerating the *Z*→*E* isomerization at rt. The E° of **MB**⁺ triplet state (0.97 V vs. SCE) was greater than **37** (0.58 V vs. SCE) for this cycling system. **MB**⁺ was introduced to a solution of **37** to test for photo-electro *Z*→*E* isomerization using red light irradiation. However, red light irradiation to excite **MB**⁺ to the triplet excited state showed no evidence to support oxidation of the system (**37**). Figure 5.4 illustrates that a solution of **37/MB**⁺ at the PSS did not initiate *Z*→*E* isomerization upon red light (660 nm) irradiation for 3.5 min. Photo, photo-electro switching does not look promising for *E*→*Z*→*E* cycling of stilbene systems.

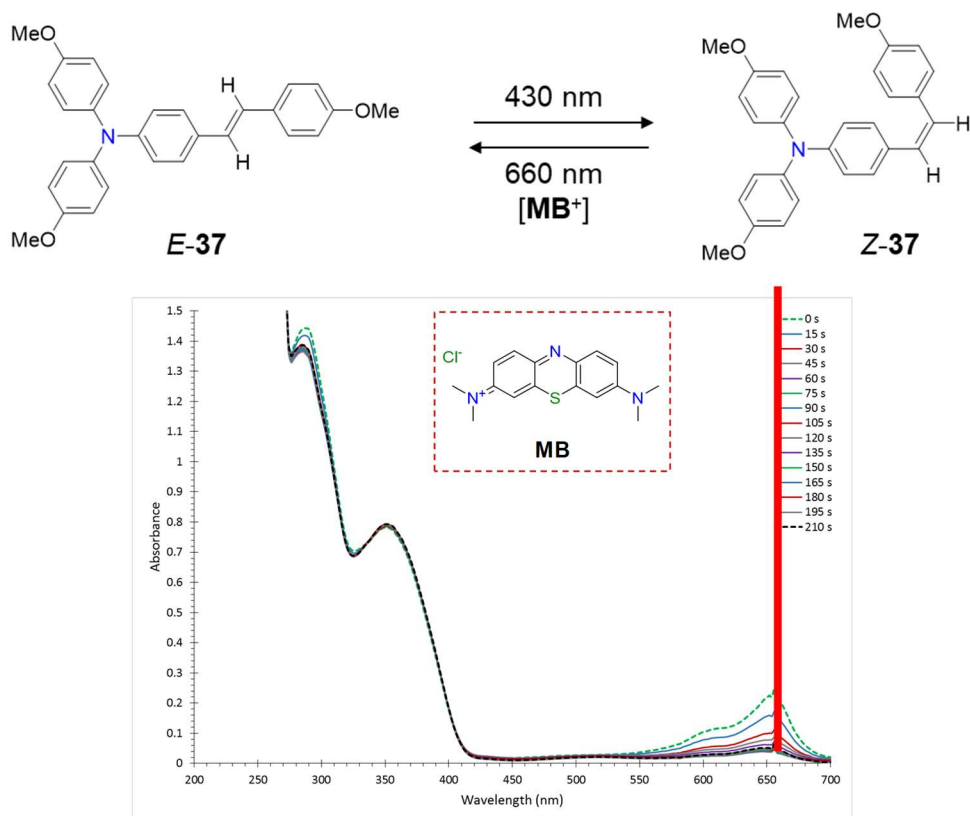


Figure 5.4. Optical spectra of **37** (5.4×10^{-5} M) and **MB⁺** (**19**) (5 mole %, 2.7×10^{-6} M) in deaerated 5% methanol:toluene in a 1.0 cm quartz cuvette at rt. Overlay of optical spectra of **37:MB⁺** starting at PSS_{430nm} under red light irradiation to excite **MB⁺**.

5.3. Photo-Redox Switching of Bis(stilbene)-*p*-anisidine

5.3.1. Introduction

The bis(stilbene)-*p*-anisidine (**38**) is synthesized and switching properties tested with light ($E \rightarrow Z$) and with electric stimulation ($Z \rightarrow E$). Incorporating two stilbene moieties across a single redox amine center would ideally increase the $Z \rightarrow E$ acceleration through a single electron oxidation as demonstrated for the azobenzene bis-systems in chapter 3. The stilbene bis-system (**38**) is expected to behave similarly (Figure 5.5). Both the E,E -**38** and Z,Z -**38** target isomers are synthetically proposed from BHA coupling. The ability to isolate the long-lived *Z*-bromostilbene (**43**) affords the opportunity for direct Z,Z -**38** synthesis using Pd-catalyzed *N*-arylation.

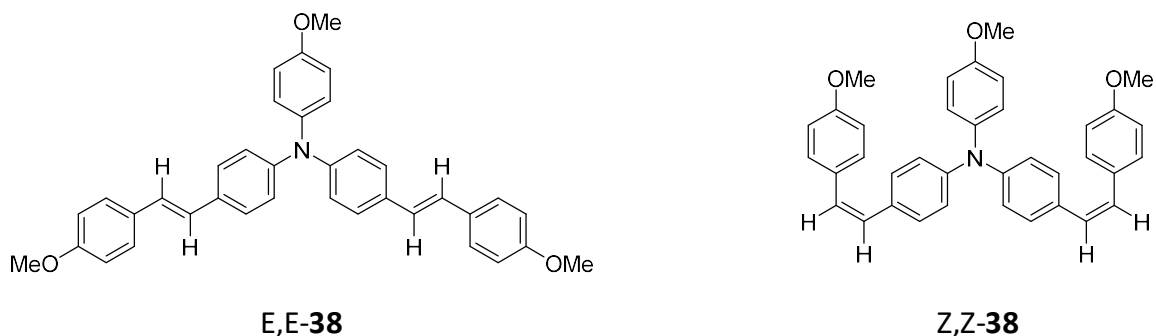
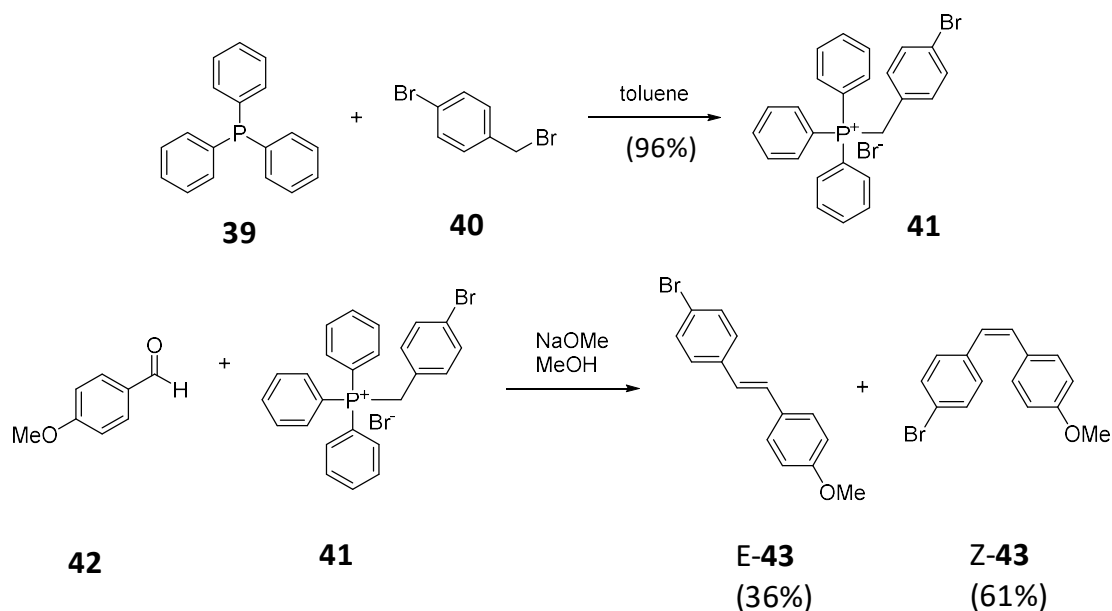


Figure 5.5 Target bis(stilbene) compounds *E,E*-**38** and *Z,Z*-**38**.

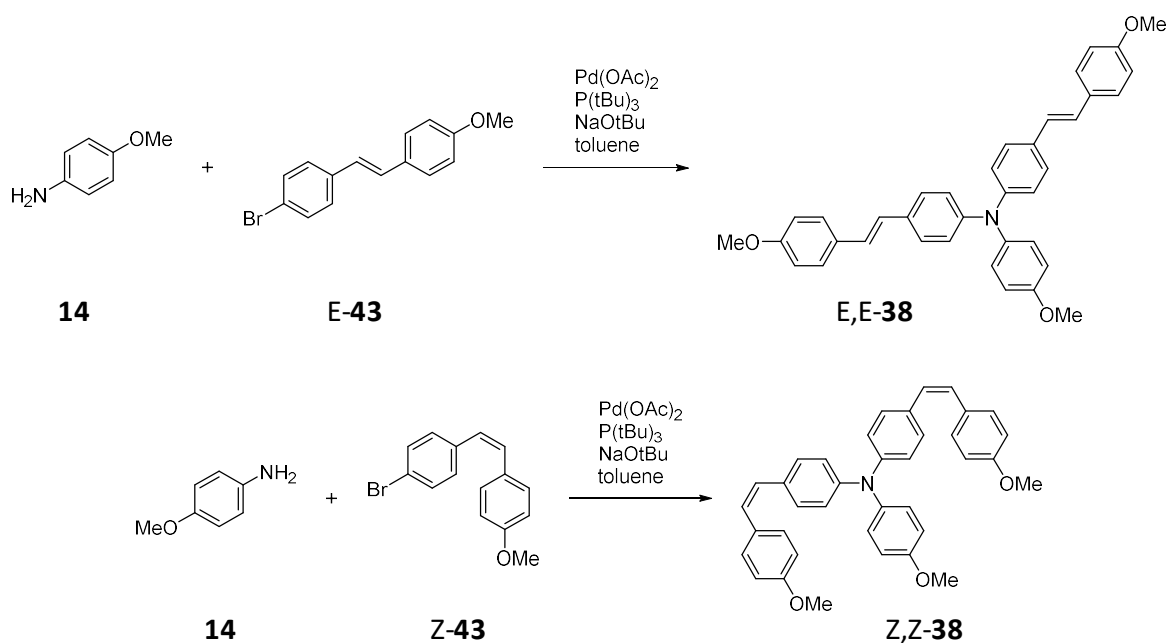
5.3.2. Synthesis of *E,E*- and *Z,Z*-(**38**)

The substitution reaction between triphenylphosphine (**39**) and 4-bromobenzylbromide (**40**) is achieved by refluxing in toluene to yield the phosphonium bromide salt (**41**) as a white powder at 96% yield (Scheme 5.1). A Wittig reaction between the phosphonium salt **41** and 4-methoxybenzaldehyde (**42**) yields a mixture of *E*-**43** and *Z*-**43** as a white powder and clear oil mixture. *Z*-**43** is isolated from a hexanes slurry, filtered, and filtrate solvent removed in vacuo to give a colorless oil (61%). The isolation of *E*-**43** from phosphonium oxide is achieved by filtering the crude mixture through a plug of silica gel using a DCM-hexanes mixture to yield *E*-**43** as a white powder in a 36% yield. The Wittig reaction gave a combined isolated product yield of 97% (Scheme 5.1).



Scheme 5.1. Substitution reaction between **39** and **40** to produce target phosphonium salt **41**. Wittig reaction conditions between **41** and **42** to yield stilbene target (*E/Z*)-**43**.

BHA coupling of *p*-anisidine (**14**) and *E*-**43** achieves the target bis-system *E,E*-**38** as a yellow powder in 88% yield (Scheme 5.2). Bis-system (*E,E*-**38**) is unstable in most organic solvents, so care is taken to only use toluene, benzene, or hexanes during the work-up. Similarly, synthesis of *Z,Z*-**38** is attempted from BHA coupling of **14** and *Z*-**43**, resulting in little success at yielding *Z,Z*-**38** without visible degradation during work-up (yellow → brown). A ¹H-NMR spectrum of the crude reaction mixture shows the formation of *Z,Z*-**38**, which is unstable and not isolated from the crude reaction mixture without degradation.



Scheme 5.2. BHA coupling conditions and synthetic route to produce target compound *E,E*-**38** and *Z,Z*-**38**.

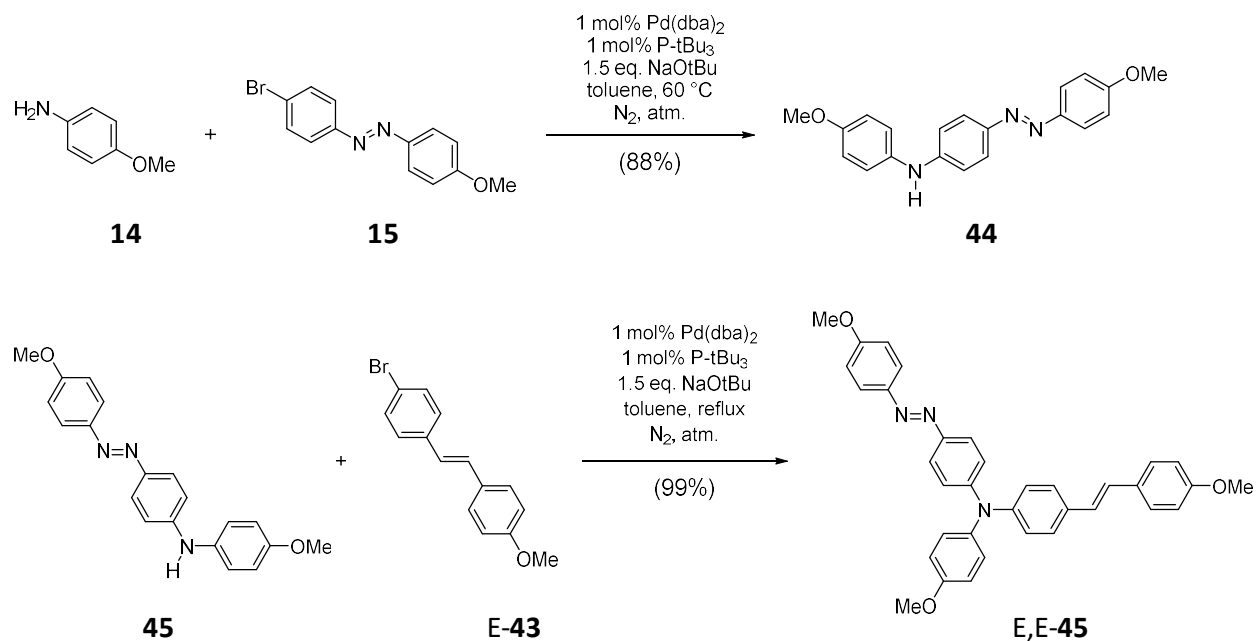
5.3.3. Photo-instability of *E,E* \rightarrow *Z,Z*-**38**

The photoisomerization for *E,E*-**38** is tested by irradiation with 430 nm LED light and monitoring by UV-vis spectroscopy. The optical spectra did not reach an equilibrium while monitoring up to 8 hours. A $^1\text{H-NMR}$ spectrum of *E,E*-**38** in benzene- d_6 is obtained pre-irradiation and post-irradiation with the 430 nm LED light periodically (1, 2, 5.5, and 10 h). After 1 hour the methoxy region has three new peaks that appear. As irradiation continued, all peaks in the spectrum began to disappear until only two peaks remained. It is unclear what degradation product would form with the loss of aromatic peaks from **38**. The experiment was repeated and monitored at shorter intervals (2, 4, 9, 14, 20, 30, 40, 50, and 60 min). The spectrum at 14 min exposure time has five methoxy peaks indicating that *E,Z*- and *Z,Z* isomer

may form. The PSS is never achieved as the peaks appear to decrease indicating that the *Z* isomeric state is unstable under these irradiation conditions for this system (**38**).

5.4. Photo-Redox *Z*→*E* Switching of Dual Component Bis-system **45**

A dual component flexor is next investigated to achieve a dual flexor of different timescales. It is expected to independently test the *Z*→*E* switching using a single electro-moiety to switch both components. The BHA coupling of *p*-anisidine (**14**) and 4-bromo-4'-methoxyazobenzene (**15**) to achieve the target system **44** as an orange solid in 75% yield. (Scheme 5.2). The BHA coupling of **44** and *E*-**43** gave the target system *E,E*-**45** as a red-orange solid in 99% yield.



Scheme 5.3. BHA coupling conditions and synthetic route to produce target compound **44** and target compound *E,E*-**45**.

5.4.1. Photochemistry and Optical Absorption of 45

UV-vis spectroscopy is used to determine the optical properties of the mixed azobenzene/stilbene chromophore, *E,E*-**45**. The optical spectrum of **45** in a deaerated benzene solution (Figure 5.6, black trace) shows two π - π^* bands at 352 and 448 nm. The two bands are predicted from the individual azobenzene and stilbene components. An overlay of the optical spectrum of **45** with parent amino-azobenzene **11** (red trace) at 436 nm and parent amino-stilbene **37** (green trace) at 364 nm demonstrate that the two π - π^* bands are consistent with the parent structures and are resolved for independent photoswitching of the two flexor units.

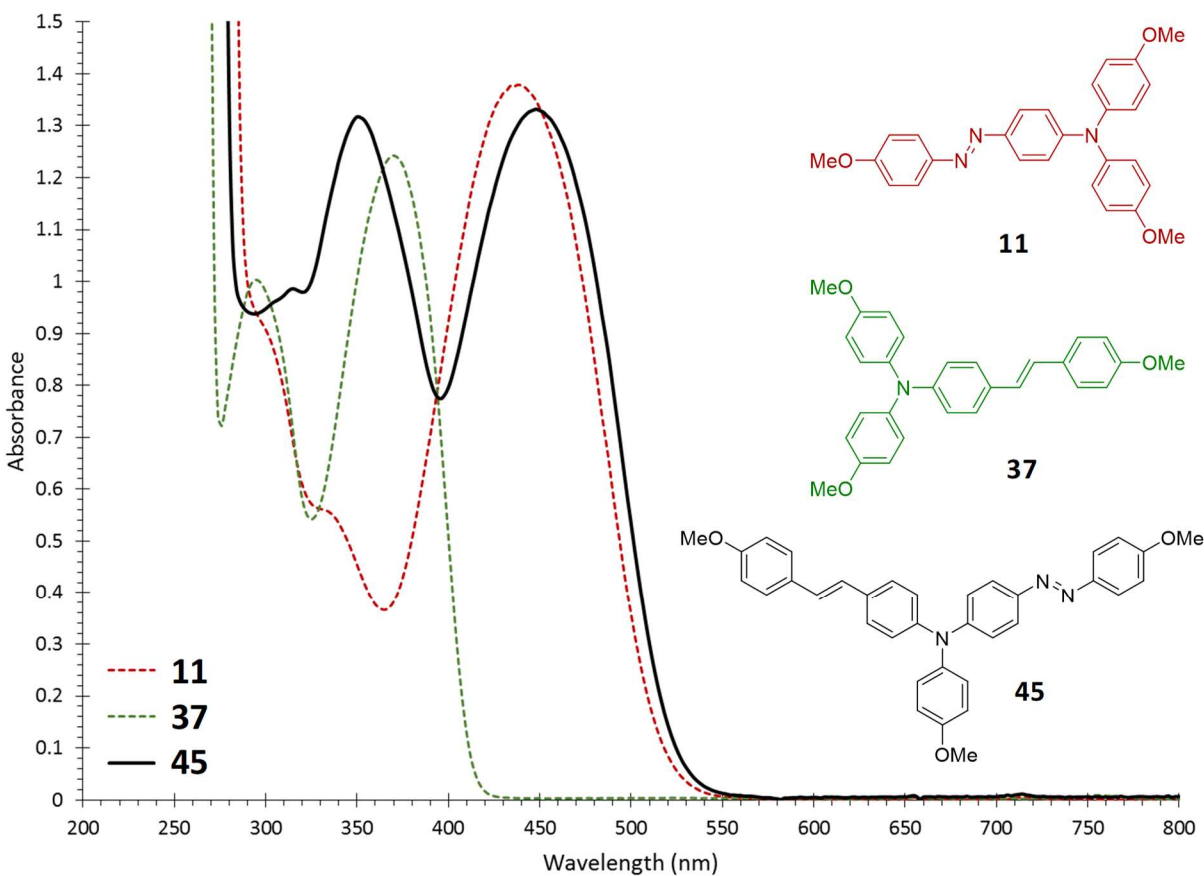


Figure 5.6. Optical spectra overlay of **45** (5.2×10^{-5} M), **11** (5.5×10^{-5} M), and **37** (5.7×10^{-5} M) each in deaerated benzene in a 1.0 cm quartz cuvette at rt.

A 457 nm LED light source is used to irradiate the 448 nm π - π^* band to photoisomerize $E \rightarrow Z$ **45**. The UV-vis spectra in Figure 5.7 show the change in optical properties indicating a change in species present. The spectra overlay shows the decrease in absorbance until the PSS is reached within 28 seconds in a benzene solution. The Z isomer is characterized by decreased molar absorptivity relative to the E isomer counterpart. Four isosbestic points are observed in the spectra overlay at 314, 364, 400, and 522 nm. At this point, $E \rightarrow Z$ isomerization is demonstrated in a qualitative manner to achieve PSS_{457 nm}. The actual $Z:E$ ratio at PSS_{457 nm} is determined by ¹H-NMR spectroscopy.

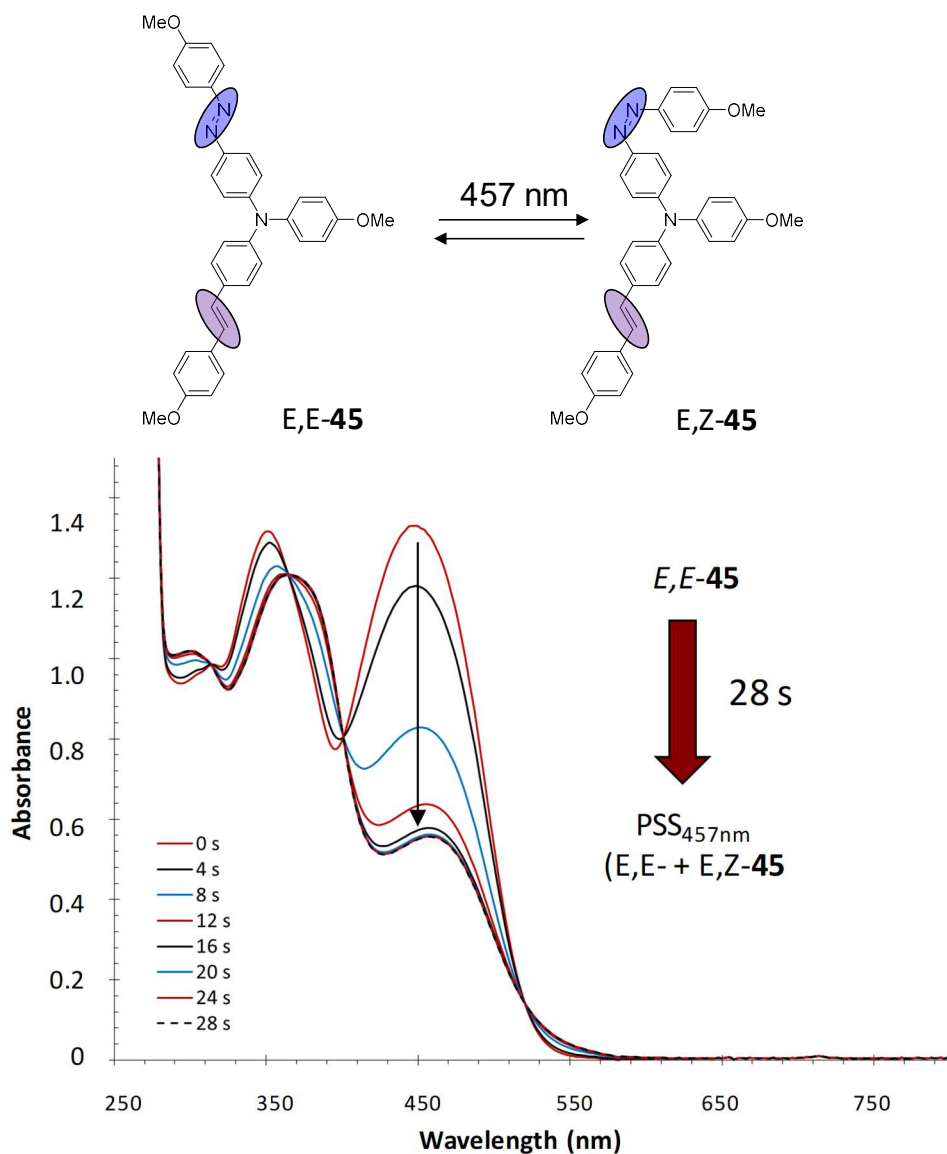


Figure 5.7. Optical spectra of *E,E*-**45** (5.2×10^{-5} M) in deaerated benzene in a 1.0 cm quartz cuvette shown before irradiation (red) and following under 457 nm LED light irradiation until $PSS_{457\text{ nm}}$ (black) was achieved.

The $^1\text{H-NMR}$ spectrum of *E,E*-**45** in benzene- d_6 shows three methoxy peaks in a 1:1:1 ratio. The methoxy singlets at 3.33, 3.30, and 3.22 ppm belong to the methoxy substituents on *p*-anisyl, stilbene, and azobenzene, respectively. The spectrum of **45** at $PSS_{457\text{ nm}}$ contains both *E* and *Z* isomers. The *E* isomer peaks remain the same as the pre-irradiation spectrum, while the

three new peaks belong to the *E,Z* isomeric state from *E*→*Z* isomerization of the azobenzene moiety only. All *Z* isomer peaks are shielded, though to a greater extent for the methoxy attached to the switching azobenzene moiety. Figure 5.8 shows the ¹H-NMR spectra between 3 and 4 ppm before and after irradiation to PSS_{430 nm}. The post-irradiation spectrum still has resolved methoxy peaks from the azobenzene moiety, which are integrated to determine the ratio of *E,Z*_{azo}-**45** to *E,E*-**45** as 68:32. The spectrum only contains *E,Z*_{azo}-**45** or *E,E*-**45**, with no sign of decomposition after irradiation. No *E*→*Z* isomerization of the stilbene moiety is observed. Only the azobenzene unit switched from irradiation with 360, 430, or 457 nm light sources. The results were unexpected as 360 and 430 nm irradiation achieved *E*→*Z* isomerization for the amino-stilbene system (**37**).¹¹¹ The mixed bis-system **45** appears to transfer any energy input at the stilbene moiety to the conjugated azobenzene moiety.

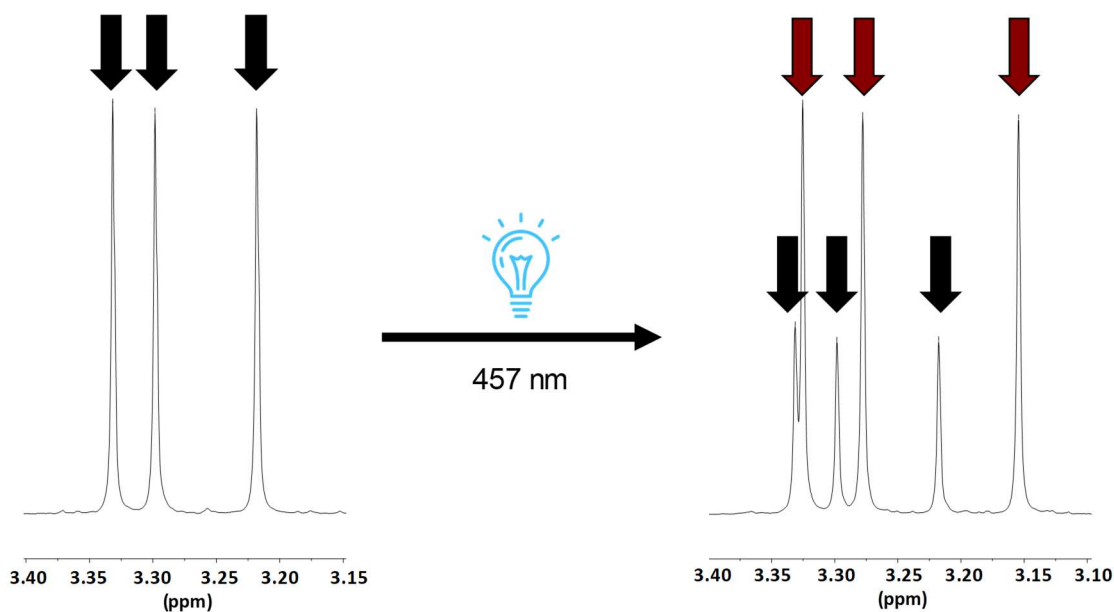


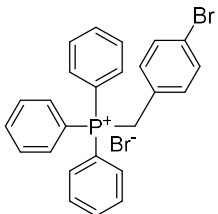
Figure 5.8. ¹H-NMR spectroscopy of **45** showing the methoxy peaks between 3-3.5 ppm. Left shows the spectrum sample pre-irradiation. Right shows the spectrum of the sample at PSS_{457 nm} with a *E,Z*_{azo}-**45** to *E,E*-**45** of 68:32.

5.5. Conclusions

The bis(stilbene)-*p*-anisidine system, *E,E*-**38** is successfully synthesized. Initial characterization by UV-vis and NMR spectroscopy determined the system is unstable during irradiation and in certain solvents. The synthesis of *Z,Z*-**38** is attempted with poor results. The product is unstable and degrades during the reaction mixture work-up. Alternatively, a mixed azobenzene-stilbene bis-system (**45**) is synthesized for the dual flexor potential. Unexpectedly, the coupled dual component flexors are found to interact with each other. The azobenzene flexor inhibits the switching of the linked stilbene flexor. The azobenzene flexor has shown *E*→*Z* photoisomerization, and the isomer composition at PSS_{457 nm} is 32 % *E,E*-**45** and 68 % *E,Z*_{azobenzene}-**45** (0 % *E,Z*_{stilbene}-**45**; and 0 % *Z,Z*-**45**). Only the azobenzene unit photoswitches from irradiation with 360, 430, or 457 nm light sources. The inability to photoswitch the stilbene flexor is unexpected considering the stability of the amino-stilbene (**37**) studied by Blackstock and coworkers, which reaches a *Z*-rich state upon 360 nm or 430 nm irradiation. The stilbene unit of the dual flexor **45** is stable, unlike what is observed for **38**. Coupling with a *Z*-stilbene versus *E*-stilbene would potentially produce the dual flexor *E,Z*_{stilbene}-**45**. Then *E*→*Z* photoisomerization of the azobenzene flexor would then achieve *Z,Z*-**45**, which would be able to *E*→*Z*→*E* cycle at the azobenzene flexor.

5.6. Experimental Section

(4-bromobenzyl)triphenylphosphonium bromide (**41**)



41

A 100 mL RBF was charged with triphenylphosphine, **39**, (1.2640 g, 4.8191 mmol), 4-bromobenzylbromide, **40**, (1.0073 g, 4.0303 mmol), and anhydr toluene (10 mL). The reaction mixture was stirred for 24 h under reflux in a silicone oil bath with the product crashing out as a white powder, allowed to cool, and filtered through a frit funnel to collect the solid. The white powder was washed with toluene (2 mL)

and solvent removed in vacuo to afford **41** (1.9815 g, 3.8685 mmol, 95.98%).

Kabachnik, et al. previously reported the synthesis at 94% yield (mp 276-277.5 °C).¹¹²

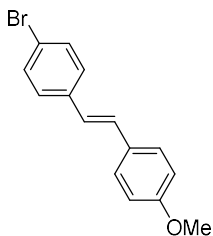
Yield: 95.98%

mp 274-275°C

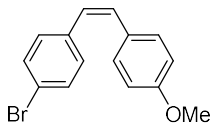
MW = 512.22 g mol⁻¹

¹H-NMR (360 MHz, CDCl₃): δ 7.72-7.66 (m, 9H), 7.56-7.51 (m, 6H), 7.09 (d, *J* = 8.2 Hz, H), 7.01-6.99 (m, H), 5.46 (d, *J* = 14.8 Hz, 2H).

(E/Z)-4-bromo-4'-methoxystilbene (E/Z-43)



E-43



Z-43

The Wittig reaction was adapted from a reported procedure by Bedekar et al.¹¹³ Product **41** (0.60 g, 1.2 mmol) was combined with *p*-anisaldehyde, **42**, (118.0 μ L, 0.9707 mmol) and methanol (3 mL) in a 100 mL RBF. To the stirring colloidal mixture under N₂ at rt, NaOMe (500.0 μ L, 2.7 mmol, 5.4 M NaOMe in MeOH) was added dropwise. The reaction stirred for 3.5 h at rt at which time TLC (1:4 EtOAc-Hexanes) analysis indicated the absence of starting material **42**. EtOAc (50 mL) and DI water (30 mL) were added to the reaction mixture, and the organic phase was collected. The aqueous phase was washed with EtOAc (3 x 10 mL). The combined organic phase was washed with saturated NaHCO₃ aq (1 x 10 mL) and DI water (1 x 10 mL), dried over anhydr MgSO₄, filtered, and solvent removed in vacuo to yield a crude product mixture of E/Z-**43** and triphenylphosphine oxide as a white solid. Triphenylphosphine oxide was removed by filtering the crude reaction mixture through a bed of silica gel (20 g) by vacuum filtration. The filter cake was washed with 1:1 DCM-Hexane (100 mL), and the combined solvents were removed in vacuo to yield a white solid containing E/Z-**43**. Warm hexane (20 mL) was added to the E/Z-**43** mixture creating a slurry before cooling (-20 °C) for 20 min. The E-**43** formed a white solid, while Z-**43** remained dissolved in hexane. The two phases were separated via vacuum filtration and solvent removed in vacuo affording E-**43** as a white powder (0.10g, 0.35 mmol, 36%) and Z-**43** as a yellow oil. Z-**43** was recrystallized in hexanes (20 mL), filtered, and solvent removed in vacuo to achieve Z-**43** as a colorless oil (0.17 g, 0.59 mmol 61%) for a combined yield of 97%.

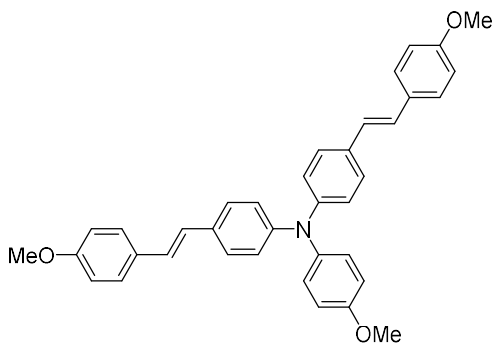
E-43 was previously reported as a white solid (80% yield, mp 202-204 °C),¹¹⁴ and **Z-43** was previously reported as a colorless oil (51.0% yield, 95:5 *Z:E*).¹¹⁵

Yield: 97% (36% **E-43**/ 61% **Z-43**) mp 199-200 °C (**E-43**) MW = 289.17 g mol⁻¹

E-43: ¹H-NMR (500 MHz, CDCl₃): δ 7.46 (d, *J* = 8.4 Hz, 2H), 7.45 (d, *J* = 8.7 Hz, 2H), 7.35 (d, *J* = 8.6 Hz, 2H), 7.05 (d, *J* = 16.3 Hz, 1H) 6.92-6.88 (m, 3H), 3.83 (s, 3H).

Z-43: ¹H-NMR (360 MHz, CDCl₃): δ 7.35 (d, *J* = 8.4 Hz, 2H), 7.17 (d, *J* = 8.8 Hz, 2H), 7.14 (d, *J* = 8.5 Hz, 2H), 6.77 (d, *J* = 8.7 Hz, 2H), 6.57 (d, *J* = 12.2 Hz, 1H), 6.42 (d, *J* = 12.1 Hz, 1H), 3.80 (s, 3H).

***E,E*-bis(stilbene)-*p*-anisidine (*E,E*-38)**



***E,E*-38**

A flame-dried 2 dram vial was charged with product **44** (0.0208 g; 0.169 mmol), while a flame-dried 50 mL RBF was charged with **E-43** (0.0971 g, 0.336 mmol) and a stir bar. Both the vial and RBF were transferred to a N₂ purged dry box, where anhydr xylenes (3 mL), Pd(OAc)₂ (0.0008 g, 0.004 mmol), and a 0.10 M solution of P(*t*Bu)₃

(190 μL, 0.0190 mmol) in anhydr toluene were added to the RBF. The vial of **44** was transferred to the RBF with toluene (4 mL) washings. Lastly, NaOtBu (0.0688 g, 0.716 mmol) and toluene (3 mL) were added to the flask and stirred for ~1min. The flask was capped with a glass stopper, removed from the dry box, and the mixture was stirred under N₂ in a silicone oil bath at 139°C for 3 h, allowed to cool, and then filtered through a layered bed of Celite on top of 5g basic

alumina III by vacuum filtration. The filter cake was washed with toluene (~200mL), and the combined solvents were removed in vacuo. The crude product was then filtered through a bed of silica gel (30 g) and washed with 1:2 toluene-hexane (200 mL) followed by DCM (50 mL). The solvent is removed from the DCM fraction yielding E,E-**45** as a yellow powder (0.08 g, 0.1 mmol, 89%).

Yield: 89%

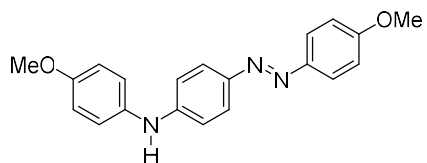
mp 215-220 °C (decomposed)

MW = 539.68 g mol⁻¹

¹H-NMR (360 MHz, CDCl₃): δ 7.43 (d, *J* = 8.8 Hz, 4H), 7.35 (d, *J* = 8.7 Hz, 4H), 7.10 (d, *J* = 8.9 Hz, 2H), 7.03 (d, *J* = 8.6 Hz, 4H), 6.94-6.85 (m, 10H), 3.83 (s, 6H), 3.82 (s, 3H).

HRMS (EI/EBE) *m/z*: [M + H]⁺ Calcd for C₃₇H₃₃NO₃ 539.2460; Found 539.2480.

N-p-anisyl-4-amino-4'-methoxyazobenzene (**44**)



44

A flame-dried 2 dram vial was charged with **15** (0.5005 g, 1.719 mmol), while a flame-dried 50 mL RBF was charged with **14** (0.2363, 1.919 mmol) and a stir bar. Both the vial and RBF were transferred to a N₂ purged dry box, where anhydr toluene (3 mL), Pd(dba)₂ (0.0200g, 0.03478 mmol), and a 0.10 M solution of P(*t*Bu)₃ in anhydr toluene (195 μL, 0.0195 mmol) were added to the RBF. **15** was transferred to the RBF with toluene (4 mL) washings. Lastly, NaO*t*Bu (0.2795 g, 2.908 mmol) and toluene (6 mL) were added to the flask and stirred for ~1min. The flask was capped with a glass stopper, removed from the dry box, and the mixture was stirred under N₂ in a silicone oil bath at 60°C for 1 h, allowed to cool, and then filtered through a layered bed of celite and 5g basic alumina III by vacuum filtration. The filter cake was washed with toluene (~300 mL), and the combined

solvents were removed in vacuo to yield an orange solid, which was recrystallized from 1:3 toluene-hexanes (40 mL) to afford **44** as an orange amorphous solid (0.50 g, 1.5 mmol, 88%).

Yield: 88%

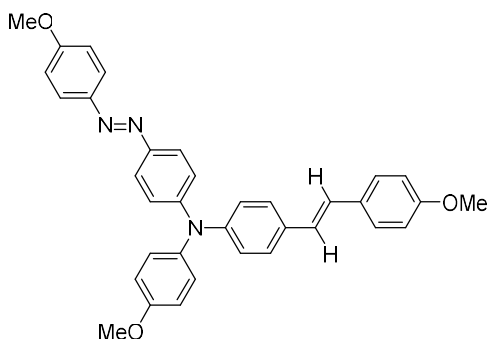
mp 135-137 °C

MW = 333.39 g mol⁻¹

¹H-NMR (360 MHz, CDCl₃): δ 7.85 (d, *J* = 9.0 Hz, 2H), 7.80 (d, *J* = 8.8 Hz, 2H), 7.16 (d, *J* = 8.9 Hz, 2H), 6.99 (d, *J* = 9.0 Hz, 2H), 6.92 (t, *J* = 8.6 Hz, 4H), 5.83 (s, 1H), 3.88 (s, 3H), 3.83 (s, 3H).

HRMS (ESI/Q-TOF) *m/z*: [M + H]⁺ Calcd for C₂₀H₂₀N₃O₂ 334.1556; Found: 334.1543.

(*E,E*)-*N*-*p*-anisyl-4-(4'-methoxy)azobenzene-4-amino-(4'-methoxy)stilbene (45**)**



E,E-**45**

A flame-dried 2 dram vial was charged with *E*-**43** (0.0461 g, 0.1383 mmol), while a flame-dried 50 mL RBF was charged with **44** (0.0465 g, 0.161 mmol) and a stir bar. Both the vial and RBF were transferred to a N₂ purged dry box, where anhydr toluene (9 mL), Pd(*dba*)₂ (0.0013 g, 0.0023 mmol), and a 0.10 M solution of P(*t*Bu)₃ in anhydr

toluene (15 μL, 0.0015 mmol) were added to the RBF. *E*-**43** was transferred to the RBF with toluene (2 mL) washings. Lastly, NaO*t*Bu (0.0383 g, 0.399 mmol) and toluene (1 mL) were added to the flask and stirred for ~1min. The flask was capped with a rubber septum, removed from the dry box, and the mixture was stirred under N₂ in a silicone oil bath at 111°C for 24 h, allowed to cool, and then filtered through a layered bed of celite and 5 g basic alumina III by vacuum filtration. The filter cake was washed with toluene (~300 mL), and the combined

solvents were removed in vacuo to yield **45** as a red solid, which was recrystallized from acetone to afford **45** as a red glassy solid (0.08 g, 0.1 mmol, 99%).

Yield: 99%

mp 213-215 °C

MW = 541.65 g mol⁻¹

¹H-NMR (500 MHz, C₆D₆): δ 8.12 (d, *J* = 8.9 Hz, 4H), 7.31 (t, *J* = 9.0 Hz, 4H), 7.20-7.13 (m, 4H), 7.05-6.93 (m, 4H), 6.81 (d, *J* = 8.7 Hz, 2H), 6.79 (d, *J* = 9.0 Hz, 2H), 6.72 (d, *J* = 8.9 Hz, 2H), 3.33 (s, 3H), 3.30 (s, 3H), 3.22 (s, 3H).

¹³C-NMR (125 MHz, C₆D₆): δ 162.0, 159.9, 157.5, 150.6, 148.1, 148.0, 146.8, 140.2, 133.4, 130.8, 126.5, 124.9, 124.7, 124.6, 121.7, 115.4, 114.58, 114.56, 55.1, 55.0, 54.9.

HRMS (EI/EBE) *m/z*: [M + H]⁺ Calcd for C₃₅H₃₂N₃O₃ 542.2444; Found 542.2435.

SUMMARY AND FUTURE DIRECTIONS

In summary, we have addressed two primary questions: can multiple azobenzenes be attached to a single **ra** (redox auxiliary) unit, and, if so, can they all be *Z*-to-*E* 'switched' by removal of a single electron as efficiently as in the case of monoazobenzene **ra**-azo **11**? We have demonstrated (1) that up to three photochromic flexors (azobenzene and/or stilbene units) can be covalently linked to a single redox-active arylamino **ra** group and (2) that the multiple azobenzene flexors undergo rapid, complete, and catalytic *Z*→*E* isomerization upon single electron loss from the **ra** unit for compounds **11**, **20**, **21**, **29**, and **45**. Extending the number of **ra**-linked azobenzene flexors creates a more complex and extensive geometry change for the molecule upon switching between isomeric states. These multi-flexor systems can be switched between 'on' and 'off' states, potentially acting as a host for capture and release of guests. Three alternate modes to achieve accelerated *Z*→*E* switching for **ra**-linked flexors through oxidation of the **ra** unit have recently been introduced by Blackstock and coworkers.

The **ra**-azo **11** *Z*→*E* isomerization was demonstrated using chemical oxidation (redox switching) by Carl Saint-Louis, electrochemical oxidation (electro switching) by Melody Kelley, and newly developed photochemical oxidation (photoredox switching) in the present work. Photoredox switching was found to be a simple way to cycle the system between flexor isomeric states. The **ra**-azo structures **11**, **20**, **21**, and **29** were reversibly *E*→*Z*→*E* cycled by sequential photo (*E*→*Z*) and photo-redox (*Z*→*E*) stimulation. The *Z*→*E* acceleration upon one-electron

oxidation was found to be at least 540,000x for **ra**-azo **11**, 740,000x for **ra**-azo **20**, 6,500,000x for **ra**-azo **21**, and 460,000x for **ra**-azo **29**.

This work presents the first isolation and EPR characterization of the ‘active’ catalytic state, **11**⁺, for the **ra**-azobenzene system **11**. Synthesis and characterization of the **ra**⁺-azo **11** salt by EPR spectroscopy supports the hypothesis that the odd electron density is localized at the **ra** unit, hence imparting great persistence to this chain propagating intermediate, allowing for both dramatic *Z*-to-*E* reaction acceleration as well as high turnover numbers for the ET chain reaction catalytic cycle.

Photoredox switching was demonstrated for **11**, **20**, and **29** using a catalytic amount of photooxidant **MB**⁺ to enable rapid and complete *Z*→*E* conversion by irradiating at a wavelength absorbed by **MB**⁺ and minimally by the **ra**-azobenzene. Under these conditions, multiple *E*→*Z*→*E* cycling was performed by irradiating in tandem with two different wavelengths, one wavelength triggering *E*→*Z* photoisomerization and the other exciting the photooxidant **MB**⁺ to trigger rapid *Z*→*E* switching via electron transfer (ET) catalysis. In summary, multiple means of using single electron oxidation were demonstrated to rapidly and completely induce *Z*→*E* switching of a group of **ra**-azobenzenes, with little to no degradation of **ra**-azobenzene structure for up to three covalently linked azobenzene units.

One area of future work involves developing a working photoredox switching process for the **ra**-tetrafluoroazobenzene bis-system **21**, which appears to have too high of an oxidation potential to work well with the **MB**⁺ photo-oxidant. The photoredox switching for amino-tetrafluoroazobenzene **28** ($E^\circ = 1.12$ V vs SCE) can be tested for cycling using **MB**⁺, before troubleshooting the switching in the more complex bis-system **21** ($E^\circ = 1.31$ V vs SCE). The photoredox cycle might be further optimized by employing a new photooxidant with a higher

redox potential to oxidize the fluorinated azobenzenes **28** and **21** and initiate the $Z \rightarrow E$ acceleration. New methylene blue and methylene green (Figure 6.1) are potential photooxidant alternatives with higher excited state oxidation potentials that could be tried. However, their chromophores are not as fully separated from the azobenzene absorbance bands, which could pose some challenge in keeping the two photoisomerization processes distinct from each other. New Methylene Blue N (**NMB⁺**) is a photosensitizer with a $\lambda_{\text{max}} = 622$ nm. Irradiation of the **NMB⁺** band at 622 nm generates a triplet excited state. The triplet excited state has a redox potential of 1.34 V vs. SCE (${}^3\text{NMB}^{+\bullet}/\text{NMB}^{\bullet}$) and a thermal lifetime of 11 μs in acetonitrile solution. Methylene Green (**MG⁺**) with a $\lambda_{\text{max}} = 654$ nm. Irradiation of the **MG⁺** band at 654 nm generates a triplet excited state. The triplet excited state, ${}^3\text{MG}^{+\bullet}/\text{MG}^{\bullet}$, has a redox potential of 1.28 V vs. SCE and a thermal lifetime of 14 μs in acetonitrile solution.⁷⁶

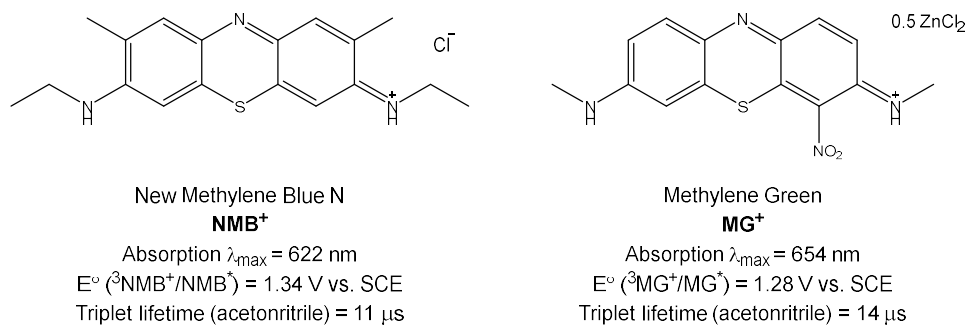


Figure 6.1. The chemical structure of alternate photooxidants New Methylene Blue N and Methylene Green.

Another area of future work involves developing a dynamic host-guest system using a multi-flexor system. Working with extended, more dynamic shape changes of the bis-systems introduces an electron-rich pocket in the case of the Z,Z isomeric state. The two flexors in the Z state have two phenyl units which can arrange to host a small electron-poor guest. A project of

interest is exploring the possible binding of small molecule cations in the anticipated electron-rich pocket in the *Z,Z* state, which could be released upon switching to the *E,E* isomeric state.

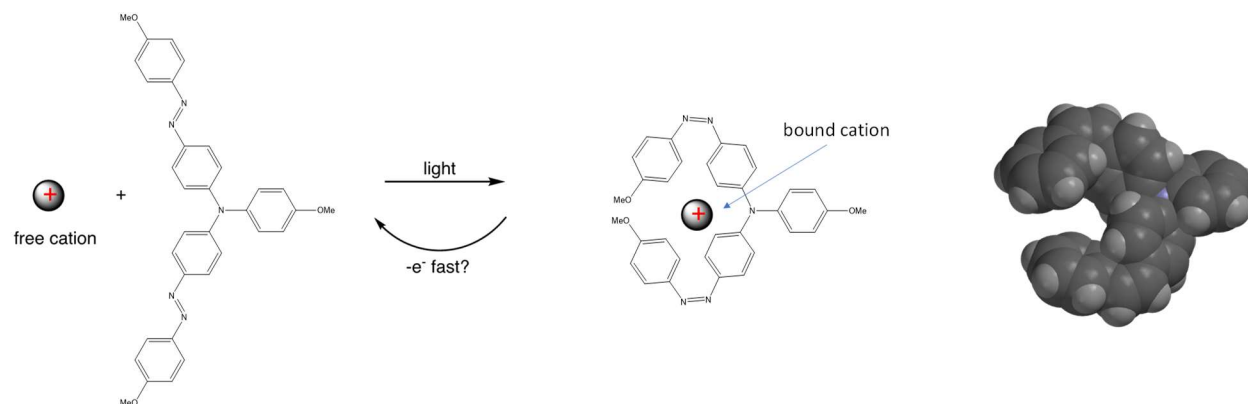


Figure 6.2. The envisioned model for host guest interactions using a bis-system such as **21**. A space-filling model of the *Z,Z*-isomeric state is shown to the right to highlight the electron rich cavity that can form.

Finally, further studies are needed to fully characterize and to potentially operationalize the isomer switching for mixed azobenzene-stilbene system **45**, which was unable to undergo $E \rightarrow Z$ photoisomerization of the stilbene unit. The bis-system **45** was demonstrated to undergo $E \rightarrow Z$ photoisomerization of the azobenzene unit while the stilbene unit remains in its *E* isomeric state. Since *Z,Z*-**45** cannot be prepared by $E \rightarrow Z$ photoisomerization of the stilbene flexor, the synthesis of the bis-system using the *Z*-stilbene **43** starting material would be one route to create a bis-flexor **45** having a *Z*-stilbene component (Figure 6.3). The azobenzene unit is expected to then be selectively $E \rightarrow Z \rightarrow E$ cycled using the photo- and photoredox switching mechanisms, since \mathbf{MB}^+ is unable to initiate the catalytic redox switching in the monostilbene system *Z*-**37**.

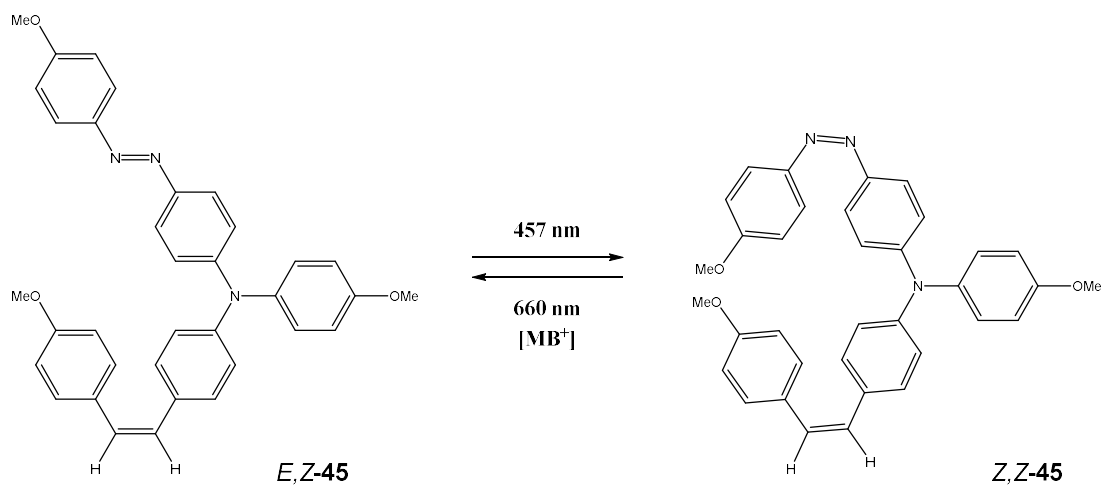


Figure 6.3. The envisioned photoredox $E \rightarrow Z \rightarrow E$ cycling of **45** with the stilbene flexor held in the Z isomeric state.

REFERENCES

1. Baroncini, M.; Bergamini, G., Azobenzene: A Photoactive Building Block for Supramolecular Architectures. *The Chemical Record* **2017**, *17*, 700-712.
2. Tylkowski, B.; Trojanowska, A.; Marturano, V.; Nowak, M.; Marciniak, L.; Giamberini, M.; Ambrogi, V.; Cerruti, P., Power of light – Functional complexes based on azobenzene molecules. *Coordination Chemistry Reviews* **2017**, *351*, 205-217.
3. Huang, S.-L.; Hor, T. S. A.; Jin, G.-X., Photodriven single-crystal-to-single-crystal transformation. *Coordination Chemistry Reviews* **2017**, *346*, 112-122.
4. Weis, P.; Wu, S., Light-Switchable Azobenzene-Containing Macromolecules: From UV to Near Infrared. *Macromolecular Rapid Communications* **2018**, *39*, 1700220.
5. Mitscherlich, E., Ueber das Stickstoffbenzid. *Annalen der Physik* **1834**, *108*, 225-227.
6. Hartley, G. S., The *Cis*-form of Azobenzene. *Nature* **1937**, *140*, 281.
7. Bandara, H. M. D.; Burdette, S. C., Photoisomerization in different classes of azobenzene. *Chem. Soc. Rev.* **2012**, *41*, 1809-1825.
8. Merino, E., Synthesis of azobenzenes: the coloured pieces of molecular materials. *Chem. Soc. Rev.* **2011**, *40*, 3835-3853.
9. Merino, E.; Ribagorda, M., Control over molecular motion using the *cis*–*trans* photoisomerization of the azo group. *Beilstein Journal of Organic Chemistry* **2012**, *8*, 1071-1090.
10. Garcia-Amoros, J.; Velasco, D. In *Light-triggered azobenzenes: from molecular architecture to functional materials*; 2014 John Wiley & Sons, Inc.; pp 27-58.
11. Leonard, E.; Mangin, F.; Villette, C.; Billamboz, M.; Len, C., Azobenzenes and catalysis. *Catal. Sci. Technol.* **2016**, *6*, 379-398.
12. Nguyen, T. H. L.; Gigant, N.; Joseph, D., Advances in Direct Metal-Catalyzed Functionalization of Azobenzenes. *ACS Catalysis* **2018**, *8*, 1546-1579.

13. Mahimwalla, Z.; Yager, K. G.; Mamiya, J.-I.; Shishido, A.; Priimagi, A.; Barrett, C. J., Azobenzene photomechanics: prospects and potential applications. *Polymer Bulletin* **2012**, *69*, 967-1006.
14. Pang, X.; Lv, J.-a.; Zhu, C.; Qin, L.; Yu, Y., Photodeformable Azobenzene-Containing Liquid Crystal Polymers and Soft Actuators. *Advanced Materials* **2019**, *31*, 1904224.
15. Warner, D. J.; Keane, K. S.; Saint-Louis, C. J.; Blackstock, S. C., Bridged Azobenzenes and Their Biological Applications. In *PATAI'S Chemistry of Functional Groups*; 2019 John Wiley & Sons; pp 1-35.
16. Bouwstra, J. A.; Schouten, A.; Kroon, J., Structural studies of the system trans-azobenzene/trans-stilbene. I. A reinvestigation of the disorder in the crystal structure of trans-azobenzene, C₁₂H₁₀N₂. *Acta Crystallographica Section C* **1983**, *39*, 1121-1123.
17. Adamson, A. W.; Vogler, A.; Kunkely, H.; Wachter, R., Photocalorimetry. Enthalpies of photolysis of trans-azobenzene, ferrioxalate and cobaltioxalate ions, chromium hexacarbonyl, and dirhenium decarbonyl. *J. Am. Chem. Soc.* **1978**, *100*, 1298-1300.
18. Cole, L. G.; Gilbert, E. C., The Heats of Combustion of Some Nitrogen Compounds and the Apparent Energy of the N-N Bond. *J. Am. Chem. Soc.* **1951**, *73*, 5423-5427.
19. Dias, A. R.; Minas Da Piedade, M. E.; Martinho Simões, J. A.; Simoni, J. A.; Teixeira, C.; Diogo, H. P.; Meng-Yan, Y.; Pilcher, G., Enthalpies of formation of *cis*-azobenzene and *trans*-azobenzene. *The Journal of Chemical Thermodynamics* **1992**, *24*, 439-447.
20. Schulze, F. W.; Petrick, H. J.; Cammenga, H. K.; Klinge, H., Thermodynamic Properties of the Structural Analogues Benzo[c]cinnoline, *Trans*-azobenzene, and *Cis*-azobenzene. In *Zeitschrift für Physikalische Chemie*, **1977**; Vol. 107, p 1.
21. Yager, K. G.; Barrett, C. J., Novel photo-switching using azobenzene functional materials. *Journal of Photochemistry and Photobiology A: Chemistry* **2006**, *182*, 250-261.
22. Mostad, A.; Roemming, C., Refinement of the crystal structure of *cis*-azobenzene. *Acta Chem. Scand.* **1971**, *25*, 3561-8.
23. Warner, D. J.; Keane, K. S.; Blackstock, S. C., Bridged Azobenzenes and Their Chemical Applications. In *PATAI'S Chemistry of Functional Groups*; pp 1-49.
24. Bahrenburg, J.; Sievers, C. M.; Schonborn, J. B.; Hartke, B.; Renth, F.; Temps, F.; Nather, C.; Sonnichsen, F. D., Photochemical properties of multi-azobenzene compounds. *Photochemical & Photobiological Sciences* **2013**, *12*, 511-518.
25. Fischer, E., Temperature Dependence of Photoisomerization Equilibria. Part I. Azobenzene and the Azonaphthalenes. *J. Am. Chem. Soc.* **1960**, *82*, 3249-3252.

26. Blevins, A. A.; Blanchard, G. J., Effect of Positional Substitution on the Optical Response of Symmetrically Disubstituted Azobenzene Derivatives. *The Journal of Physical Chemistry B* **2004**, *108*, 4962-4968.
27. Tamai, N.; Miyasaka, H., Ultrafast Dynamics of Photochromic Systems. *Chemical Reviews* **2000**, *100*, 1875-1890.
28. Crecca, C. R.; Roitberg, A. E., Theoretical Study of the Isomerization Mechanism of Azobenzene and Disubstituted Azobenzene Derivatives. *The Journal of Physical Chemistry A* **2006**, *110*, 8188-8203.
29. Dokic, J.; Gothe, M.; Wirth, J.; Peters, M. V.; Schwarz, J.; Hecht, S.; Saalfrank, P., Quantum Chemical Investigation of Thermal *Cis*-to-*Trans* Isomerization of Azobenzene Derivatives: Substituent Effects, Solvent Effects, and Comparison to Experimental Data. *J. Phys. Chem. A* **2009**, *113*, 6763-6773.
30. Garcia-Amorós, J.; Díaz-Lobo, M.; Nonell, S.; Velasco, D., Fastest Thermal Isomerization of an Azobenzene for Nanosecond Photoswitching Applications under Physiological Conditions. *Angewandte Chemie* **2012**, *124*, 12992-12995.
31. Nagamani, S. A.; Norikane, Y.; Tamaoki, N., Photoinduced Hinge-Like Molecular Motion: Studies on Xanthene-Based Cyclic Azobenzene Dimers. *The Journal of Organic Chemistry* **2005**, *70*, 9304-9313.
32. Woolley, G. A., An open and shut cage. *Nature Nanotechnology* **2013**, *8*, 892.
33. Hoersch, D.; Roh, S.-H.; Chiu, W.; Kortemme, T., Reprogramming an ATP-driven protein machine into a light-gated nanocage. *Nature Nanotechnology* **2013**, *8*, 928.
34. Subhas, S.; Chuanguang, Q.; J., L. A.; Andrew, W. G., Bidirectional Photocontrol of Peptide Conformation with a Bridged Azobenzene Derivative. *Angewandte Chemie*, **2012**, *51*, 6452-6455.
35. Lucia, G.; S., S. O.; J., W. C.; C., B. D.; Andrew, W. G.; K., A. R., Photochemical Regulation of DNA-Binding Specificity of MyoD. *Angewandte Chemie* **2005**, *117*, 7956-7960.
36. Mart, R. J.; Allemann, R. K., Azobenzene photocontrol of peptides and proteins. *Chemical Communications* **2016**, *52*, 12262-12277.
37. Madsen, A. S.; Olsen, C. A., An acetylation photoswitch. *Nature Chemical Biology* **2016**, *12*, 306.
38. Tian, T.; Song, Y.; Wang, J.; Fu, B.; He, Z.; Xu, X.; Li, A.; Zhou, X.; Wang, S.; Zhou, X., Small-Molecule-Triggered and Light-Controlled Reversible Regulation of Enzymatic Activity. *J. Am. Chem. Soc.* **2016**, *138*, 955-961.

39. Hien, L. T.; Zatsepin, T. S.; Schierling, B.; Volkov, E. M.; Wende, W.; Pingoud, A.; Kubareva, E. A.; Oretskaya, T. S., Restriction Endonuclease SsoII with Photoregulated Activity—a “Molecular Gate” Approach. *Bioconjugate Chemistry* **2011**, *22*, 1366-1373.
40. Wang, D.; Wu, S., Red-Light-Responsive Supramolecular Valves for Photocontrolled Drug Release from Mesoporous Nanoparticles. *Langmuir* **2016**, *32*, 632-636.
41. Croissant, J.; Maynadier, M.; Gallud, A.; Peindy N'Dongo, H.; Nyalosaso, J. L.; Derrien, G.; Charnay, C.; Durand, J.-O.; Raehm, L.; Serein-Spirau, F.; Cheminet, N.; Jarrosson, T.; Mongin, O.; Blanchard-Desce, M.; Gary-Bobo, M.; Garcia, M.; Lu, J.; Tamanoi, F.; Tarn, D.; Guardado-Alvarez, T. M.; and Zink, J. I., Two-Photon-Triggered Drug Delivery in Cancer Cells Using Nanoimpellers, *Angewandte Chemie*, **2013**, *125*, 14058-14062.
42. Angelos, S.; Choi, E.; Vögtle, F.; De Cola, L.; Zink, J. I., Photo-Driven Expulsion of Molecules from Mesostructured Silica Nanoparticles. *The Journal of Physical Chemistry C* **2007**, *111*, 6589-6592.
43. Jog, P. V.; Gin, M. S., A Light-Gated Synthetic Ion Channel. *Organic Letters* **2008**, *10*, 3693-3696.
44. Liu, T.; Bao, C.; Wang, H.; Lin, Y.; Jia, H.; Zhu, L., Light-controlled ion channels formed by amphiphilic small molecules regulate ion conduction via *cis-trans* photoisomerization. *Chemical Communications* **2013**, *49*, 10311-10313.
45. Mourot, A.; Kienzler, M. A.; Banghart, M. R.; Fehrentz, T.; Huber, F. M. E.; Stein, M.; Kramer, R. H.; Trauner, D., Tuning Photochromic Ion Channel Blockers. *ACS Chemical Neuroscience* **2011**, *2*, 536-543.
46. Volgraf, M.; Gorostiza, P.; Szobota, S.; Helix, M. R.; Isacoff, E. Y.; Trauner, D., Reversibly Caged Glutamate: A Photochromic Agonist of Ionotropic Glutamate Receptors. *J. Am. Chem. Soc.* **2007**, *129*, 260-261.
47. Dong, M.; Babalhavaeji, A.; Samanta, S.; Beharry, A. A.; Woolley, G. A., Red-Shifting Azobenzene Photoswitches for in Vivo Use. *Accounts of Chemical Research* **2015**, *48*, 2662-2670.
48. Rau, H., *Photoisomerization and Photo-orientation of Azobenzenes*. Academic Press: USA, 2002; pp 560.
49. Knie, C.; Utecht, M.; Zhao, F.; Kulla, H.; Kovalenko, S.; Brouwer, A. M.; Saalfrank, P.; Hecht, S.; Bléger, D., ortho-Fluoroazobenzenes: Visible Light Switches with Very Long-Lived Z Isomers. *Chemistry – A European Journal* **2014**, *20*, 16492-16501.
50. Heindl, A. H.; Becker, J.; Wegner, H. A., Selective switching of multiple azobenzenes. *Chemical Science* **2019**, *10*, 7418-7425.

51. Galanti, A.; Diez-Cabanes, V.; Santoro, J.; Valášek, M.; Minoia, A.; Mayor, M.; Cornil, J.; Samori, P., Electronic decoupling in C₃-symmetrical light-responsive tris (azobenzene) scaffolds: self-assembly and multiphotochromism. *J. Am. Chem. Soc.* **2018**, *140*, 16062-16070.
52. Galanti, A.; Santoro, J.; Mannancherry, R.; Duez, Q.; Diez-Cabanes, V.; Valášek, M.; De Winter, J.; Cornil, J.; Gerbaux, P.; Mayor, M., A new class of rigid multi (azobenzene) switches featuring electronic decoupling: Unravelling the isomerization in individual photochromes. *J. Am. Chem. Soc.* **2019**, *141*, 9273-9283.
53. Léonard, E.; Mangin, F.; Villette, C.; Billamboz, M.; Len, C., Azobenzenes and catalysis. *Catalysis Science & Technology* **2016**, *6*, 379-398.
54. Stoll, R. S.; Peters, M. V.; Kuhn, A.; Heiles, S.; Goddard, R.; Bühl, M.; Thiele, C. M.; Hecht, S., Photoswitchable Catalysts: Correlating Structure and Conformational Dynamics with Reactivity by a Combined Experimental and Computational Approach. *J. Am. Chem. Soc.* **2009**, *131*, 357-367.
55. Kaler, S.; McKeown, P.; Ward, B. D.; Jones, M. D., Aluminium(III) and zinc(II) complexes of azobenzene-containing ligands for ring-opening polymerisation of ϵ -caprolactone and rac-lactide. *Inorganic Chemistry Frontiers* 2021.
56. Fu, W.; Pi, Y.; Gao, M.; Wang, W.; Li, C.; Tan, R.; Yin, D., Light-controlled cooperative catalysis of asymmetric sulfoxidation based on azobenzene-bridged chiral salen Ti IV catalysts. *Chemical Communications* **2020**, *56*, 5993-5996.
57. Roy, S.; Pramanik, S.; Ghorui, T.; Pramanik, K., Insight into luminescent bisazoaromatic CNN pincer palladacycle: synthesis, structure, electrochemistry and some catalytic applications in C-C coupling. *RSC Adv.* **2015**, *5*, 22544-22559.
58. Baroncini, M.; d'Agostino, S.; Bergamini, G.; Ceroni, P.; Comotti, A.; Sozzani, P.; Bassanetti, I.; Grepioni, F.; Hernandez, T. M.; Silvi, S.; Venturi, M.; Credi, A., Photoinduced reversible switching of porosity in molecular crystals based on star-shaped azobenzene tetramers. *Nature Chemistry* **2015**, *7*, 634-640.
59. Blackstock, S. C.; Gray, L.; Kelley, M.; Saint-Louis, C. Redox Auxiliary Catalysis. US Patent 9,469,602 B2, October 18, 2016.
60. Saint-Louis, C. J. *Control of Molecular Geometries Using New Photo-electro-switchable Azobenzenes*. Ph.D. Dissertation, The University of Alabama, Tuscaloosa, AL, 2015.
61. Goulet-Hanssens, A.; Utecht, M.; Mutruc, D.; Titov, E.; Schwarz, J.; Grubert, L.; Bleger, D.; Saalfrank, P.; Hecht, S., Electrocatalytic *Z* \rightarrow *E* Isomerization of Azobenzenes. *J. Am. Chem. Soc.* **2017**, *139*, 335-341.
62. Kusumoto, M.; Moriwaki, K.; Nakano, H.; Shiota, Y., Photochromism of Dimethylaminoazobenzene in a Molecular Glass of 4, 4', 4''-Tri (N-carbazolyl) triphenylamine. *Journal of Photopolymer Science and Technology* **1998**, *11*, 29-31.

63. Priewisch, B.; Rück-Braun, K., Efficient Preparation of Nitrosoarenes for the **Synthesis** of Azobenzenes. *The Journal of Organic Chemistry* **2005**, *70*, 2350-2352.
64. Suresh, S.; Joseph, R.; Jayachandran, B.; Pol, A.; Vinod, M.; Sudalai, A.; Sonawane, H.; Ravindranathan, T., Catalytic selective oxidation of amines with hydroperoxides over molecular sieves: Investigations into the reaction of alkylamines, arylamines, allylamines and benzylamines with H₂O₂ and TBHP over TS-1 and CrS-2 as the new catalyst. *Tetrahedron* **1995**, *51*, 11305-11318.
65. Chang, C.-F.; Liu, S.-T., Catalytic oxidation of anilines into azoxybenzenes on mesoporous silicas containing cobalt oxide. *Journal of Molecular Catalysis A: Chemical* **2009**, *299*, 121-126.
66. Martin, J.; Dailey, B., Proton NMR spectra of disubstituted benzenes. *The Journal of Chemical Physics* **1962**, *37*, 2594-2602.
67. Surry, D. S.; Buchwald, S. L., Dialkylbiaryl phosphines in Pd-catalyzed amination: a user's guide. *Chemical Science* **2011**, *2*, 27-50.
68. Hartwig, J. F.; Shaughnessy, K. H.; Shekhar, S.; Green, R. A., Palladium-catalyzed amination of aryl halides. *Org. React.* **2019**, *100*, 853-943.
69. Hartwig, J. F.; Kawatsura, M.; Hauck, S. I.; Shaughnessy, K. H.; Alcazar-Roman, L. M., Room-Temperature Palladium-Catalyzed Amination of Aryl Bromides and Chlorides and Extended Scope of Aromatic C-N Bond Formation with a Commercial Ligand. *J. Org. Chem.* **1999**, *64*, 5575-5580.
70. Bao, D.; Millare, B.; Xia, W.; Steyer, B. G.; Gerasimenko, A. A.; Ferreira, A.; Contreras, A.; Vullev, V. I., Electrochemical Oxidation of Ferrocene: A Strong Dependence on the Concentration of the Supporting Electrolyte for Nonpolar Solvents. *J. Phys. Chem. A* **2009**, *113*, 1259-1267.
71. Connelly, N. G.; Geiger, W. E., Chemical Redox Agents for Organometallic Chemistry. *Chemical Reviews* **1996**, *96*, 877-910.
72. Rathore, R.; Burns, C. L.; Deselnicu, M. I.; Denmark, S. E.; Bui, T., Preparation of 1,4:5,8-Dimethano-1,2,3,4,5,6,7,8-Octahydro-9,10-Dimethoxyanthracenium Hexachloroantimonate (4⁺SbCl₆⁻): A Highly Robust Radical-Cation Salt. In *Organic Syntheses*, 2005.
73. Rathore, R.; Kochi, J. K., Isolation of Novel Radical Cations from Hydroquinone Ethers. Conformational Transition of the Methoxy Group upon Electron Transfer. *J. Org. Chem.* **1995**, *60*, 4399-411.
74. Kelley, M. D. Electrochromic and photoelectrochromic switching devices based on aryl amine redox chemistry. Ph.D. Dissertation, The University of Alabama, Tuscaloosa, AL, 2014.

75. Goulet-Hanssens, A.; Rietze, C.; Titov, E.; Abdullahu, L.; Grubert, L.; Saalfrank, P.; Hecht, S., Hole Catalysis as a General Mechanism for Efficient and Wavelength-Independent $Z \rightarrow E$ Azobenzene Isomerization. *Chem* **2018**, *4*, 1740-1755.
76. Pitre, S. P.; McTiernan, C. D.; Scaiano, J. C., Library of Cationic Organic Dyes for Visible-Light-Driven Photoredox Transformations. *ACS Omega* **2016**, *1*, 66-76.
77. Walter, R. I., Substituent effects on the properties of stable aromatic free radicals. The criterion for non-hammett behavior¹. *J. Am. Chem. Soc.* **1966**, *88*, 1923-1930.
78. Perrin, D. D.; Armarego, W. L. F., *Purification of Laboratory Chemicals*. Third ed.; Pergamon Press Inc.: Elmsford, New York 10523, 1988; p 391.
79. Wegener, M.; Hansen, M. J.; Driessen, A. J.; Szymanski, W.; Feringa, B. L., Photocontrol of antibacterial activity: shifting from UV to red light activation. *J. Am. Chem. Soc.* **2017**, *139*, 17979-17986.
80. Ohta, K.; Chiba, Y.; Kaise, A.; Endo, Y., Structure–activity relationship study of diphenylamine-based estrogen receptor (ER) antagonists. *Bioorganic & medicinal chemistry* **2015**, *23*, 861-867.
81. Warner, D. J. *Enhancing Thermal Isomerization Rates of Redox Auxiliary Appended Azobenzenes via Redox Auxiliary Catalysis*. Ph.D. Dissertation, The University of Alabama, Tuscaloosa, AL, 2020.
82. Bléger, D.; Schwarz, J.; Brouwer, A. M.; Hecht, S., o-Fluoroazobenzenes as readily synthesized photoswitches offering nearly quantitative two-way isomerization with visible light. *J. Am. Chem. Soc.* **2012**, *134*, 20597-20600.
83. Beharry, A. A.; Sadovski, O.; Woolley, G. A., Azobenzene photoswitching without ultraviolet light. *J. Am. Chem. Soc.* **2011**, *133*, 19684-19687.
84. Moreno, J.; Gerecke, M.; Grubert, L.; Kovalenko, S. A.; Hecht, S., Sensitized Two-NIR-Photon $Z \rightarrow E$ Isomerization of a Visible-Light-Addressable Bistable Azobenzene Derivative. *Angewandte Chemie*, **2016**, *55*, 1544-1547.
85. Meyers, C.; Maes, B. U.; Loones, K. T.; Bal, G.; Lemièrre, G. L.; Dommissse, R. A., Study of a new rate increasing “base effect” in the palladium-catalyzed amination of aryl iodides. *The Journal of organic chemistry* **2004**, *69*, 6010-6017.
86. Dierkes, P.; van Leeuwen, P. W., The bite angle makes the difference: a practical ligand parameter for diphosphine ligands. *Journal of the Chemical Society, Dalton Transactions* **1999**, 1519-1530.
87. Driver, M. S.; Hartwig, J. F., A second-generation catalyst for aryl halide amination: Mixed secondary amines from aryl halides and primary amines catalyzed by (DPPF) PdCl₂. *J. Am. Chem. Soc.* **1996**, *118*, 7217-7218.

88. Opie, C. R.; Kumagai, N.; Shibasaki, M., Reversible stereoselective folding/unfolding fueled by the interplay of photoisomerism and hydrogen bonding. *Angewandte Chemie* **2017**, *129*, 3397-3401.
89. Moreno, J.; Gerecke, M.; Grubert, L.; Kovalenko, S. A.; Hecht, S., Sensitized Two-NIR-Photon $Z \rightarrow E$ Isomerization of a Visible-Light-Addressable Bistable Azobenzene Derivative. *Angewandte Chemie*, **2016**, *55*, 1544-1547.
90. Bahrenburg, J.; Sievers, C. M.; Schoenborn, J. B.; Hartke, B.; Renth, F.; Temps, F.; Naether, C.; Soennichsen, F. D., Photochemical properties of multi-azobenzene compounds. *Photochem. Photobiol. Sci.* **2013**, *12*, 511-518.
91. Taniguchi, T.; Asahi, T.; Koshima, H., Photomechanical Azobenzene Crystals. *Crystals* **2019**, *9*, 437.
92. Aitipamula, S.; Chow, P. S.; Tan, R. B. H., Polymorphism in cocrystals: a review and assessment of its significance. *CrystEngComm* **2014**, *16*, 3451-3465.
93. Aakeröy, C. B.; Sinha, A. S., Chapter 1 Co-crystals: Introduction and Scope. In *Co-crystals: Preparation, Characterization and Applications*, The Royal Society of Chemistry 2018; pp 1-32.
94. Mulliken, R. S.; Person, W. B., *Molecular complexes : a lecture and reprint volume*. Wiley-Interscience: New York; London, 1969.
95. Greer, M. L.; Blackstock, S. C., Nitrosamine/2,3-Dichloro-5,6-dicyano-1,4-benzoquinone (DDQ) Complexes and the Formation of Donor-Appended DDQ Chains in the Solid State. *J. Am. Chem. Soc.* **1997**, *119*, 11343-11344.
96. Greer, M. L.; Blackstock, S. C., Azoalkane-DDQ arrays in the solid state. New donor-acceptor interactions for crystal engineering. *Mol. Cryst. Liq. Cryst. Sci. Technol., Sect. A* **1998**, *313*, 55-64.
97. Greer, M. L.; Duncan, J. R.; Duff, J. L.; Blackstock, S. C., Solid-state complexes of quinoxaline- and phenazine-N,N'-dioxide donors with tetracyanoethylene. Crystal engineering via donor-acceptor interactions. *Tetrahedron Lett.* **1997**, *38*, 7665-7668.
98. Zanotti, G.; Bardi, R.; Del Pra, A., Structure of 2,3-dichloro-5,6-dicyano-p-benzoquinone (DDQ). *Acta Crystallographica Section B* **1980**, *36*, 168-171.
99. Tibiletti, F.; Simonetti, M.; Nicholas, K. M.; Palmisano, G.; Parravicini, M.; Imbesi, F.; Tollari, S.; Penoni, A., One-pot synthesis of meridianins and meridianin analogues via indolization of nitrosoarenes. *Tetrahedron* **2010**, *66*, 1280-1288.
100. Carreno, M. C.; Mudarra, G. F.; Merino, E.; Ribagorda, M., Synthesis of azobenzenes from quinone acetals and arylhydrazines. *The Journal of organic chemistry* **2004**, *69*, 3413-3416.

101. Yang, S.; Li, L.; Cholli, A. L.; Kumar, J.; Tripathy, S. K., Azobenzene-modified poly (L-glutamic acid)(AZOPLGA): Its conformational and photodynamic properties. *Biomacromolecules* **2003**, *4*, 366-371.
102. Han, W. G.; Lovell, T.; Liu, T.; Noodleman, L., Density Functional Studies of the Ground-and Excited-State Potential-Energy Curves of Stilbene *cis-trans* Isomerization. *ChemPhysChem* **2002**, *3*, 167-178.
103. Bromberg, A.; Muszkat, K., The geometry of hindered stilbenes in their ground and excited states. *Tetrahedron* **1972**, *28*, 1265-1274.
104. Suzuki, H., Relations between Electronic Absorption Spectra and Spatial Configurations of Conjugated Systems. V. Stilbene. *Bulletin of the Chemical Society of Japan* **1960**, *33*, 379-388.
105. Cox, M. J.; Crim, F. F., Vibrational energy flow rates for *cis*-and *trans*-stilbene isomers in solution. *The Journal of Physical Chemistry A* **2005**, *109*, 11673-11678.
106. Troe, J.; Weitzel, K. M., MNDO calculations of stilbene potential energy properties relevant for the photoisomerization dynamics. *The Journal of chemical physics* **1988**, *88*, 7030-7039.
107. Saltiel, J.; Ganapathy, S.; Werking, C., The ΔH for thermal *trans/cis*-stilbene isomerization: do S_0 and T_1 potential energy curves cross? *Journal of Physical Chemistry* **1987**, *91*, 2755-2758.
108. Williams, R. B., Heats of catalytic hydrogenation in solution. I. Apparatus, technique, and the heats of hydrogenation of certain pairs of stereoisomers. *J. Am. Chem. Soc.* **1942**, *64*, 1395-1404.
109. Davies, M.; Evans, F., The kinetics of some *cis-trans* isomerization reactions in solutions. *Transactions of the Faraday Society* **1955**, *51*, 1506-1517.
110. Calvin, M.; Alter, H. W., Substituted stilbenes. ii. thermal isomerization. *The Journal of Chemical Physics* **1951**, *19*, 768-770.
111. Nwankwoala, C. I. Redox Auxiliary Mediated Catalysis of Organic Thermal Reactions. Stilbene Isomerization and Aza-Claisen Rearrangement. Ph.D. Dissertation, University of Alabama, Tuscaloosa, AL, 2018.
112. Lobanov, D.; Tsvetkov, E.; Saltanova, E.; Yakovleva, E.; Shatenshtein, A.; Kabachnik, M., Synthesis of some deuterated tertiary arylphosphines and their oxides. *Bulletin of the Academy of Sciences of the USSR, Division of chemical science* **1968**, *17*, 1949-1954.
113. Talele, H. R.; Chaudhary, A. R.; Patel, P. R.; Bedekar, A. V., Expedient synthesis of helicenes using an improved protocol of photocyclodehydrogenation of stilbenes. *Arkivoc* **2011**, *9*, 15-37.

114. Gigante, B.; Esteves, M. A.; Pires, N.; Davies, M. L.; Douglas, P.; Fonseca, S. M.; Burrows, H. D.; Castro, R. A.; Pina, J.; de Melo, J. S., Synthesis, spectroscopy, photophysics and thermal behaviour of stilbene-based triarylaminines with dehydroabiestic acid methyl ester moieties. *New Journal of Chemistry* **2009**, *33*, 877-885.
115. Giraud, A.; Provot, O.; Hamzé, A.; Brion, J.-D.; Alami, M., One-pot hydrosilylation–protodesilylation of functionalized diarylalkynes: a highly selective access to Z-stilbenes. Application to the synthesis of combretastatin A-4. *Tetrahedron Letters* **2008**, *49*, 1107-1110.

APPENDIX A – NMR SPECTRA

LIST OF NMR SPECTRA

Figure A1. ^1H -NMR spectrum (360 MHz) of crude compound 13 in CDCl_3	163
Figure A2. ^1H -NMR spectrum (360 MHz) of purified compound 15 in CDCl_3	164
Figure A3. ^1H -NMR spectrum (360 MHz) of purified compound 17 in C_6D_6	165
Figure A4. ^1H -NMR spectrum (500 MHz) of purified compound 11 in CDCl_3	166
Figure A5. ^{13}C -NMR spectrum (125 MHz) of purified compound 11 in CDCl_3	167
Figure A6. ^1H -NMR spectrum of (360 MHz) in CDCl_3 of purified compound 20 via column chromatography.	168
Figure A7. ^1H -NMR spectrum of (360 MHz) in CDCl_3 of purified compound 20 via recrystallization.....	169
Figure A8. ^{13}C -NMR spectrum of (125 MHz) of purified compound 20 in CDCl_3	170
Figure A9. ^1H -NMR spectrum (500 MHz) of purified compound 22 in CDCl_3	171
Figure A10. ^1H -NMR spectrum (360 MHz) of purified compound 25 in CDCl_3	172
Figure A11. ^1H -NMR spectrum (500 MHz) of compound 26 in CDCl_3	173
Figure A12. ^{13}C -NMR spectrum (125 MHz) of compound 26 in CDCl_3	174
Figure A13. ^1H -NMR spectrum (360 MHz) of compound 21 in CDCl_3	175
Figure A14. ^{13}C -NMR spectrum (125 MHz) of compound 21 in CDCl_3	176
Figure A15. ^1H -NMR spectrum (500 MHz) of 31 in CDCl_3	177
Figure A16. ^1H -NMR spectrum (360 MHz) of 32 in CDCl_3	178
Figure A17. ^1H -NMR spectrum (360 MHz) of pure 33 in CDCl_3	179

Figure A18. ^1H -NMR spectrum (500 MHz) of purified compound 29 in C_6D_6	180
Figure A19. ^{13}C -NMR spectrum (125 MHz) of compound 29 in C_6D_6	181
Figure A20. ^1H -NMR spectrum (360 MHz) of compound 41 in CDCl_3	182
Figure A21. ^1H -NMR spectrum (500 MHz) of compound <i>E</i> - 43 in CDCl_3	183
Figure A22. ^1H -NMR spectrum (360 MHz) of compound <i>Z</i> - 43 in CDCl_3	184
Figure A23. ^1H -NMR spectrum (360 MHz) of compound <i>E,E</i> - 38 in CDCl_3	185
Figure A24. ^1H -NMR spectrum (360 MHz) of compound 44 in CDCl_3	186
Figure A25. ^1H -NMR spectrum (500 MHz) of compound 45 in C_6D_6	187
Figure A26. ^{13}C -NMR spectrum (125 MHz) of compound 45 in C_6D_6	188

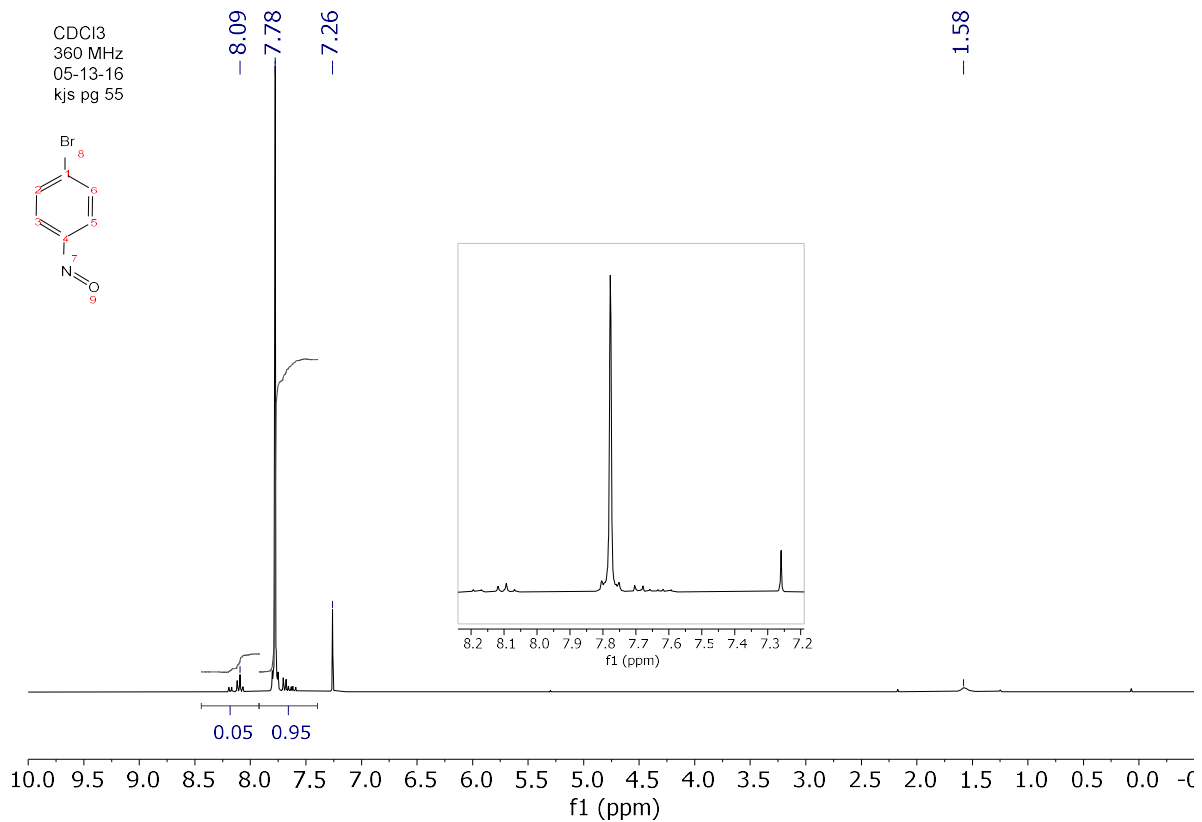


Figure A1. ¹H-NMR spectrum (360 MHz) of crude compound **13** in CDCl₃.

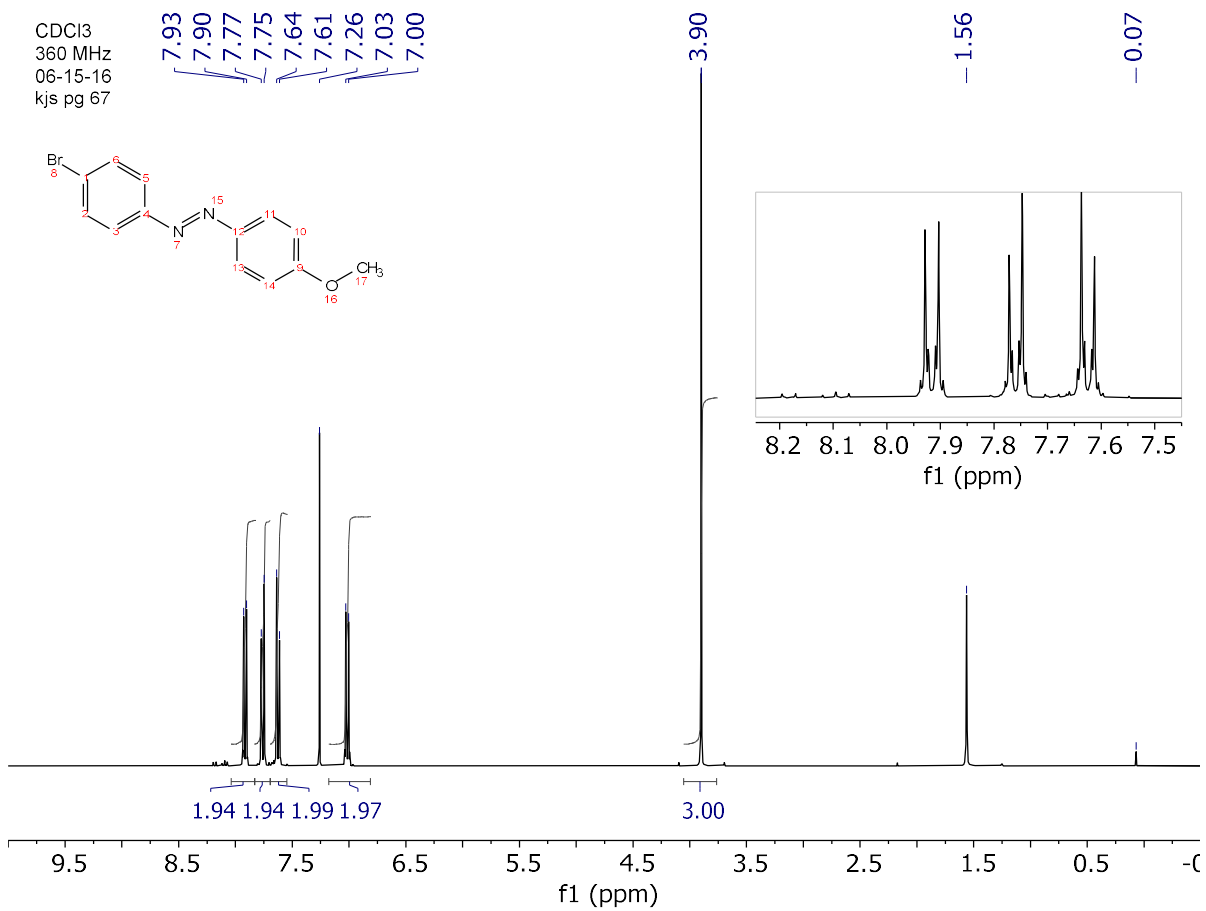


Figure A2. ¹H-NMR spectrum (360 MHz) of purified compound **15** in CDCl₃.

benzene-d6
360 MHz
NS=32
kjs 082019 4 1
recryst. dianasylamine

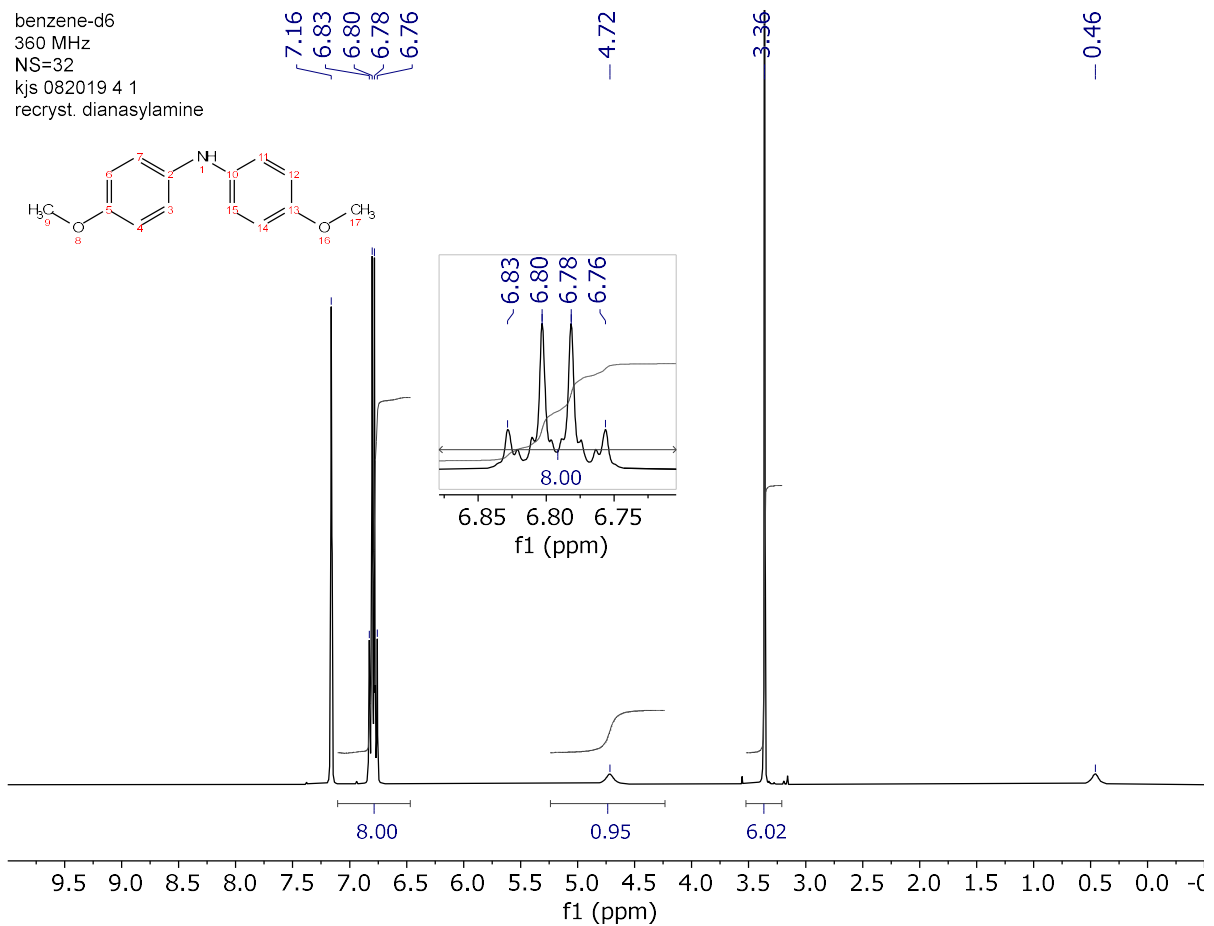


Figure A3. $^1\text{H-NMR}$ spectrum (360 MHz) of purified compound 17 in C_6D_6 .

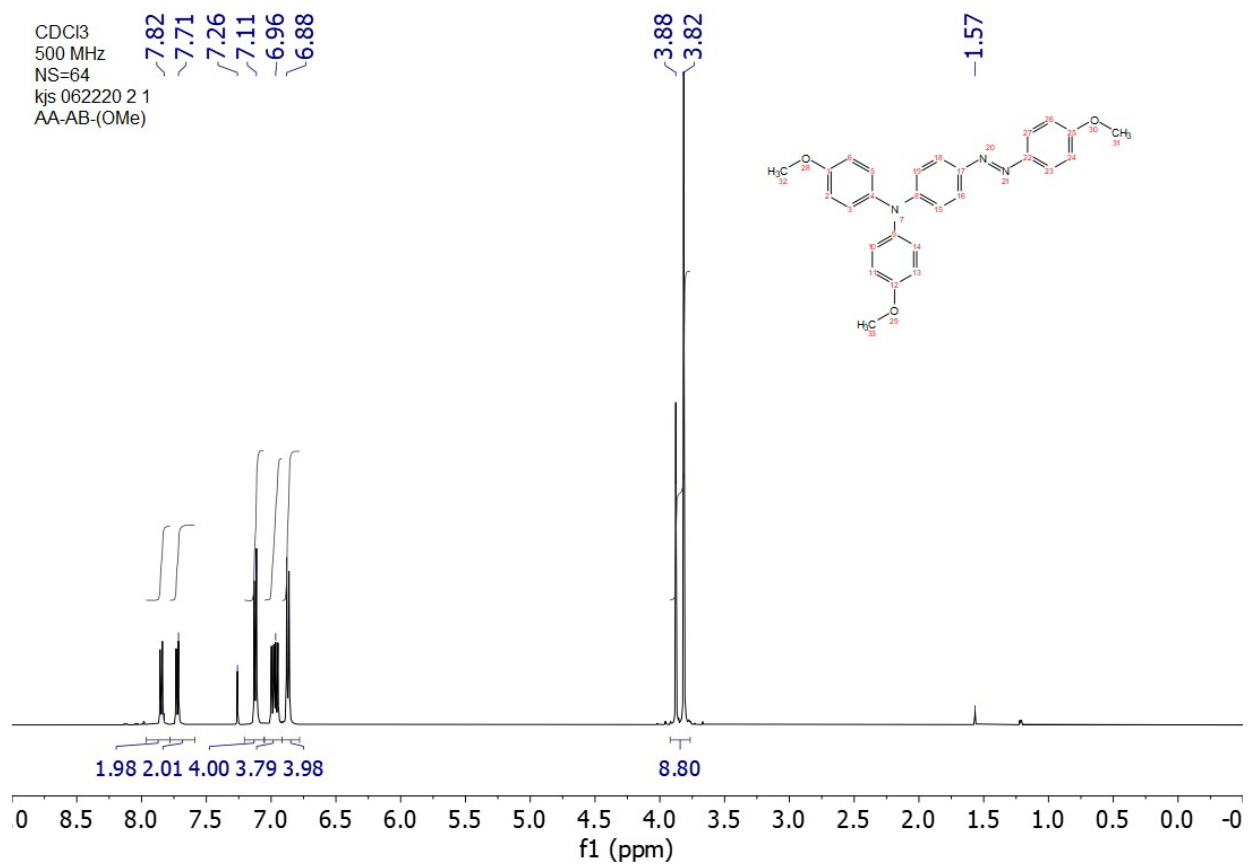


Figure A4. ¹H-NMR spectrum (500 MHz) of purified compound **11** in CDCl₃.

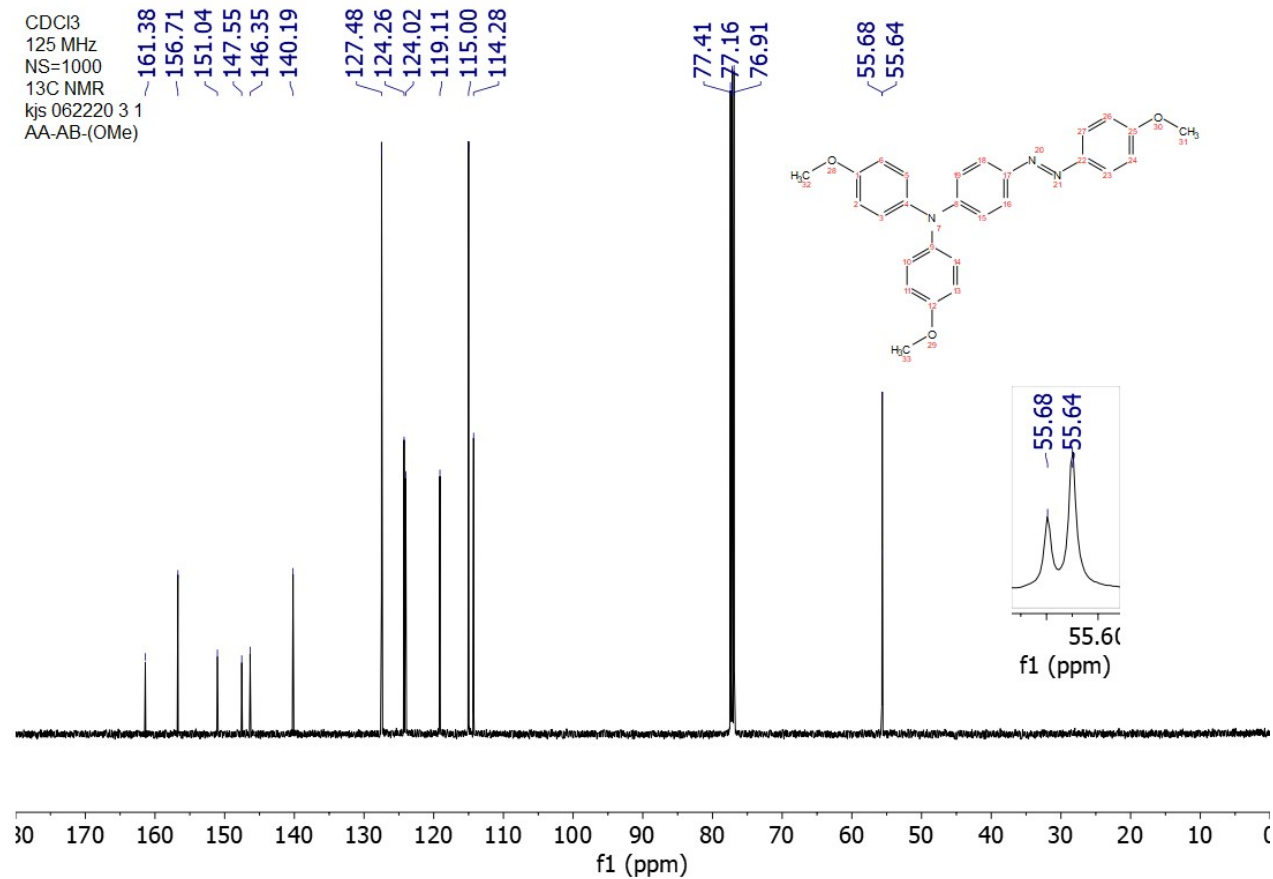


Figure A5. ¹³C-NMR spectrum (125 MHz) of purified compound **11** in CDCl₃.

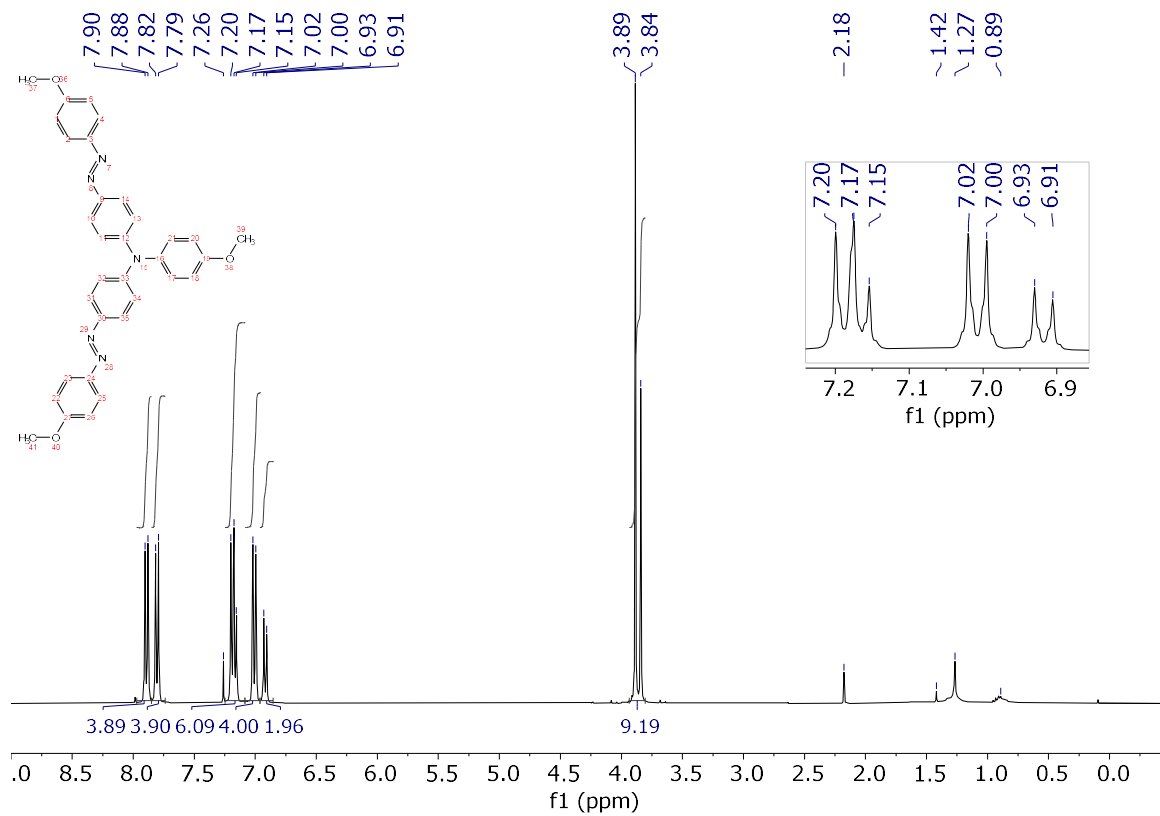


Figure A6. ¹H-NMR spectrum of (360 MHz) in CDCl₃ of purified compound **20** via column chromatography.

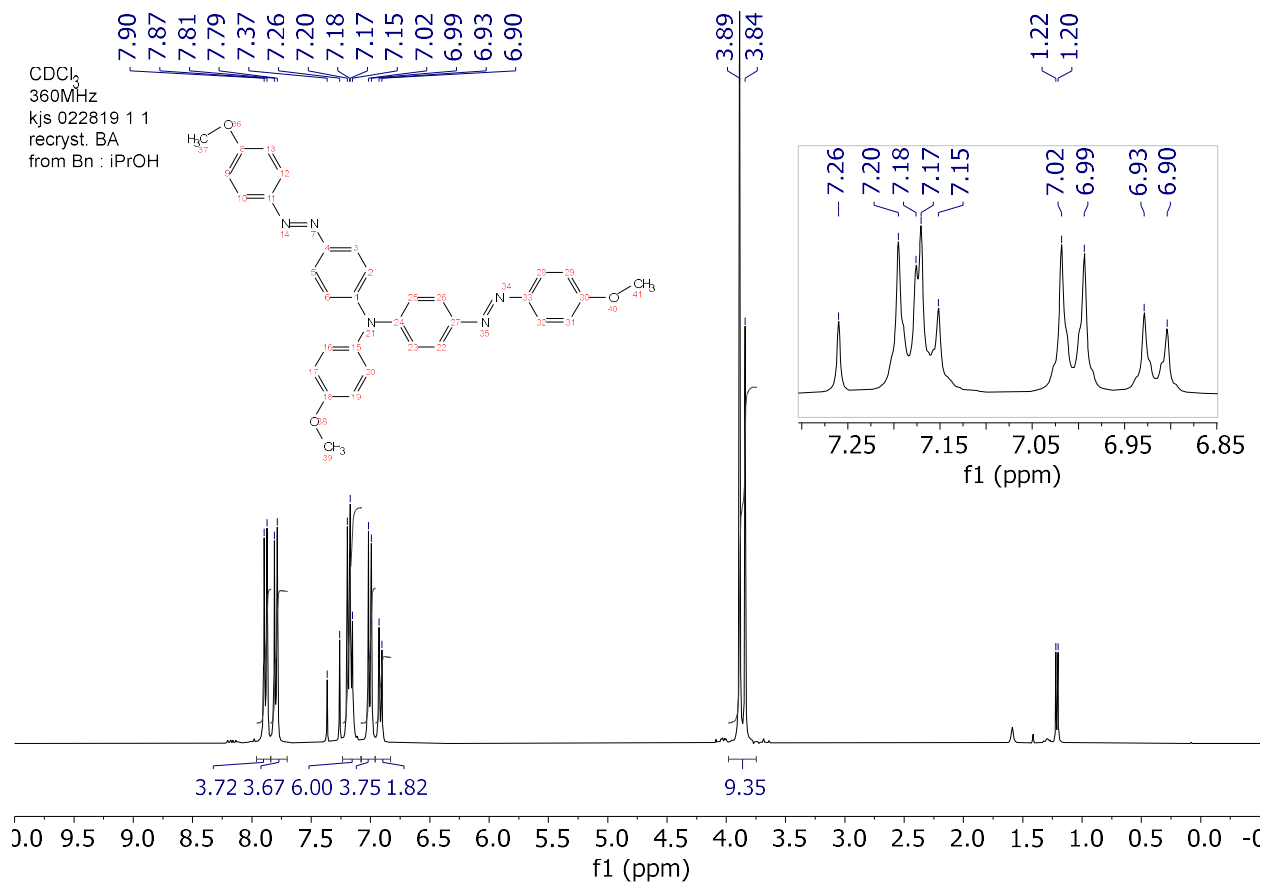


Figure A7. ^1H -NMR spectrum of (360 MHz) in CDCl_3 of purified compound **20** via recrystallization.

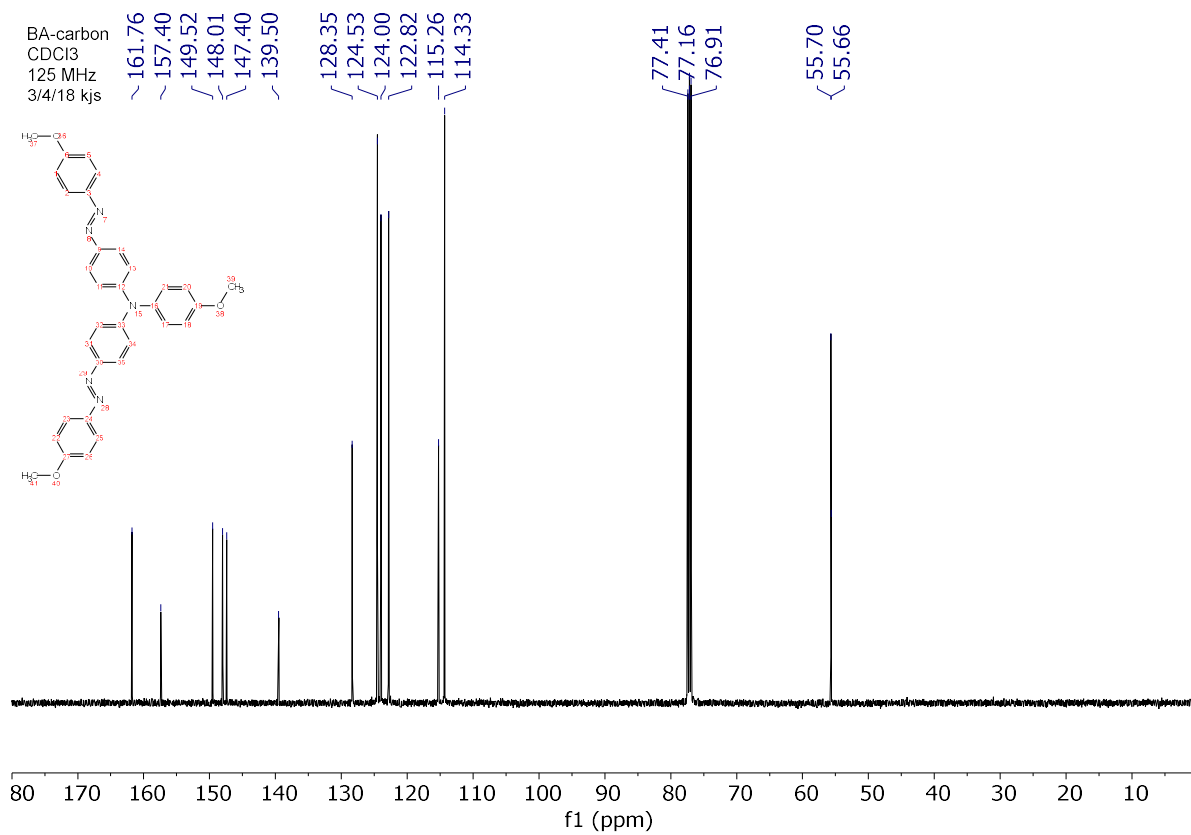


Figure A8. ¹³C-NMR spectrum of (125 MHz) of purified compound **20** in CDCl₃.

CDCl₃
500 MHz
NS=32
kjs 081319 2 1
5-bromo-1,3-difluoro-2-nitrosobenzene

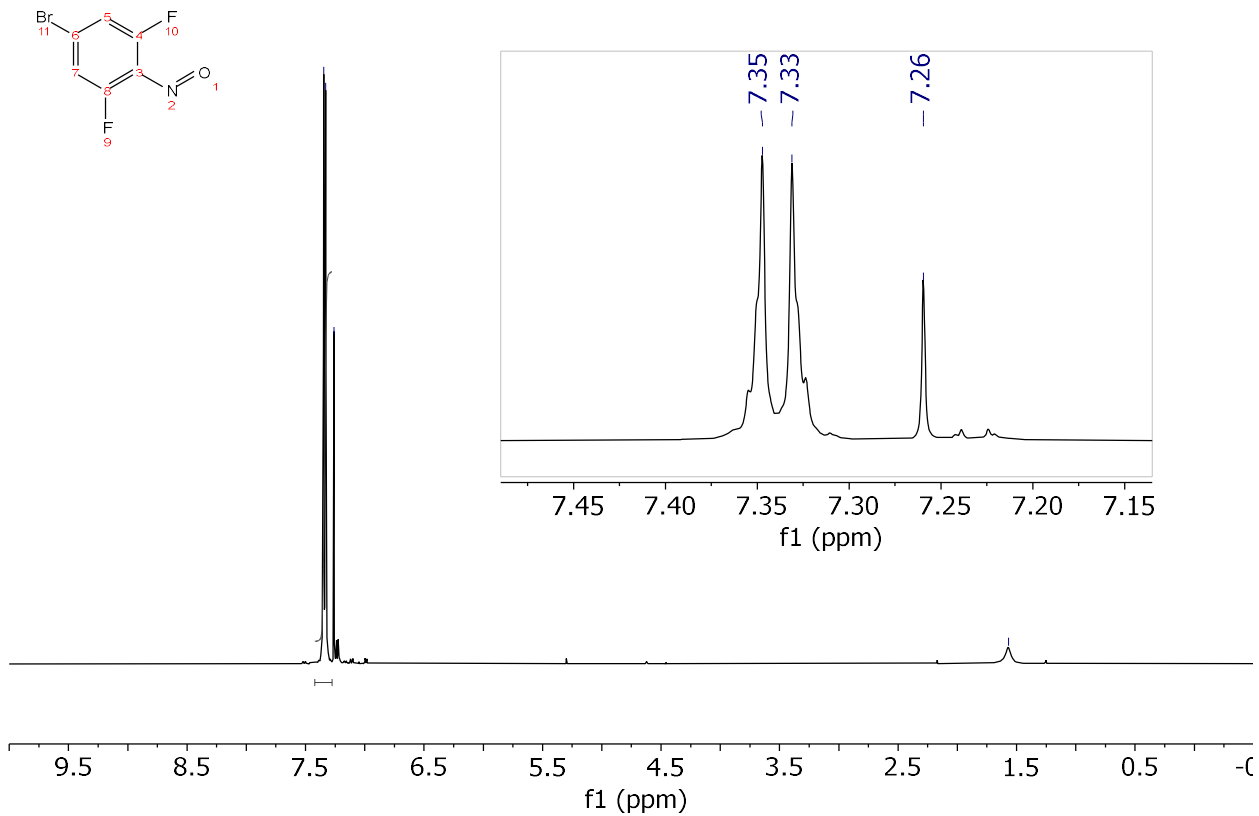


Figure A9. ¹H-NMR spectrum (500 MHz) of purified compound **22** in CDCl₃.

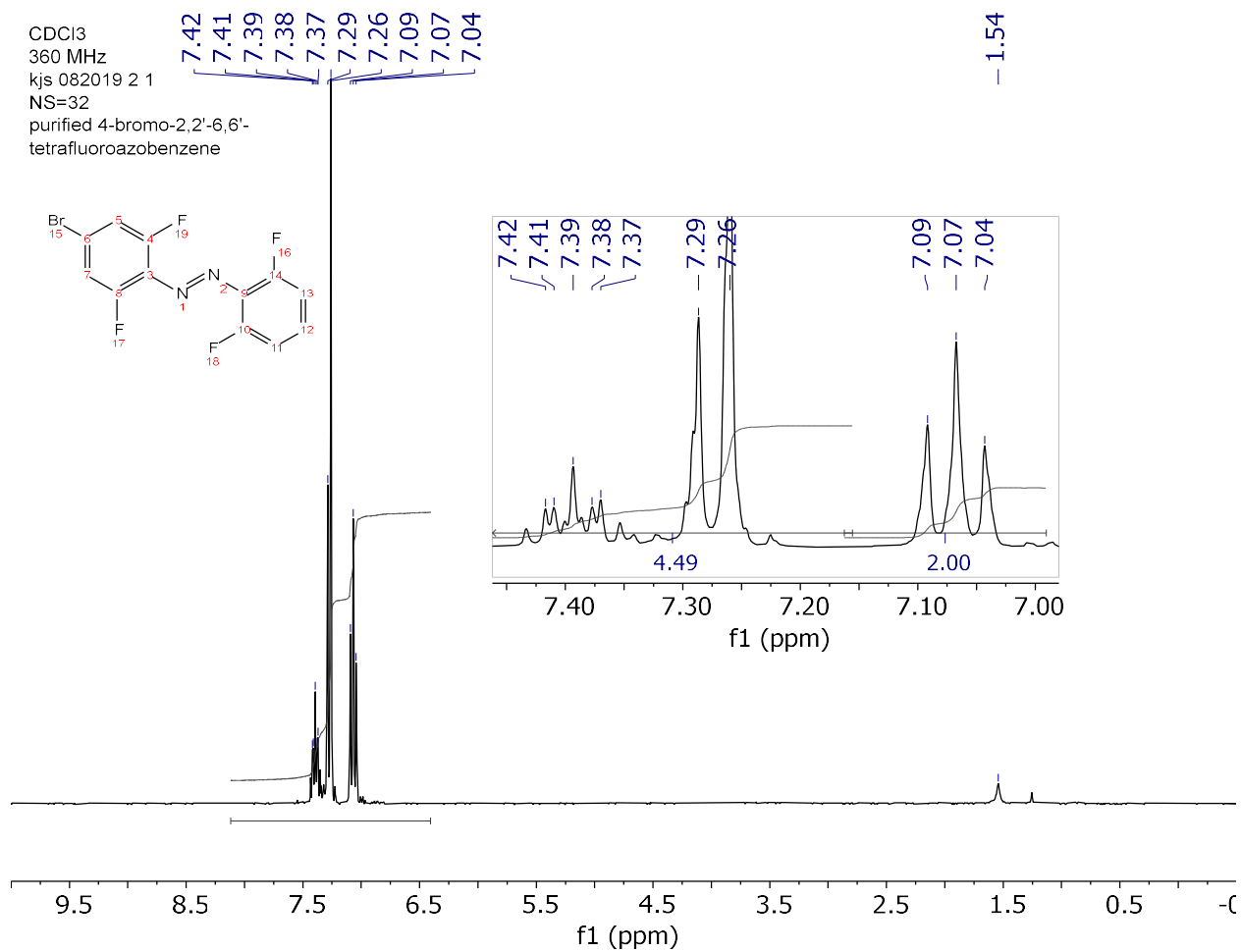


Figure A10. ¹H-NMR spectrum (360 MHz) of purified compound **25** in CDCl₃.

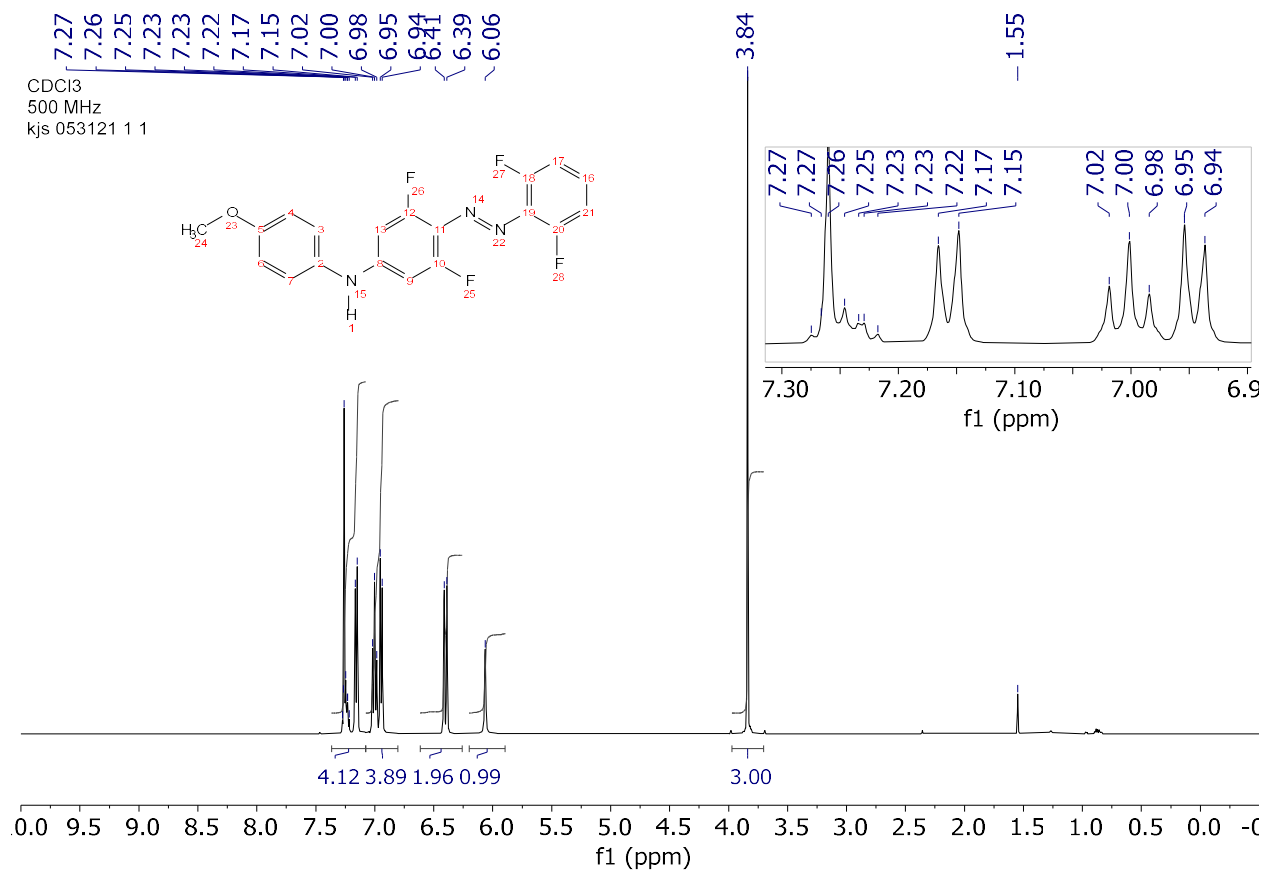


Figure A11. ¹H-NMR spectrum (500 MHz) of compound **26** in CDCl₃.

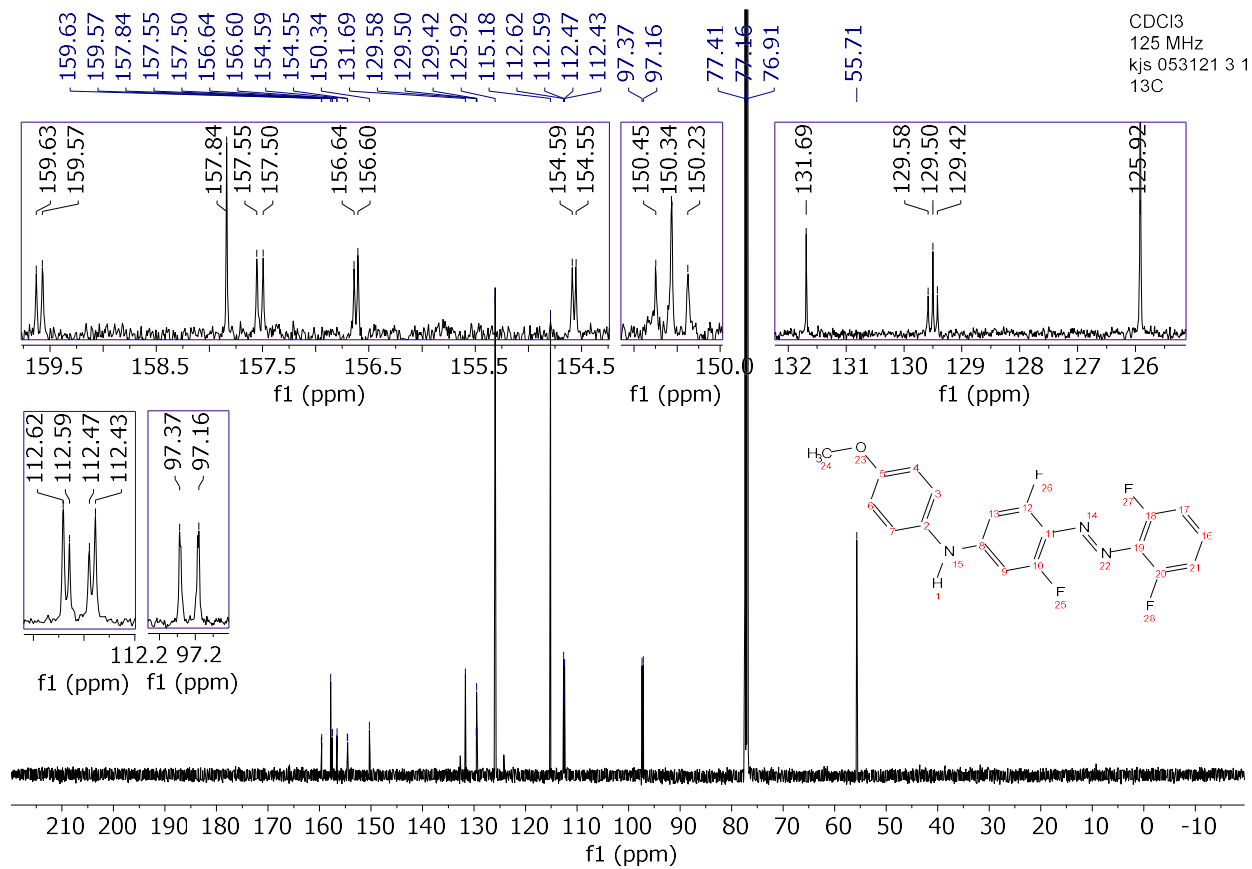


Figure A12. ¹³C-NMR spectrum (125 MHz) of compound **26** in CDCl₃.

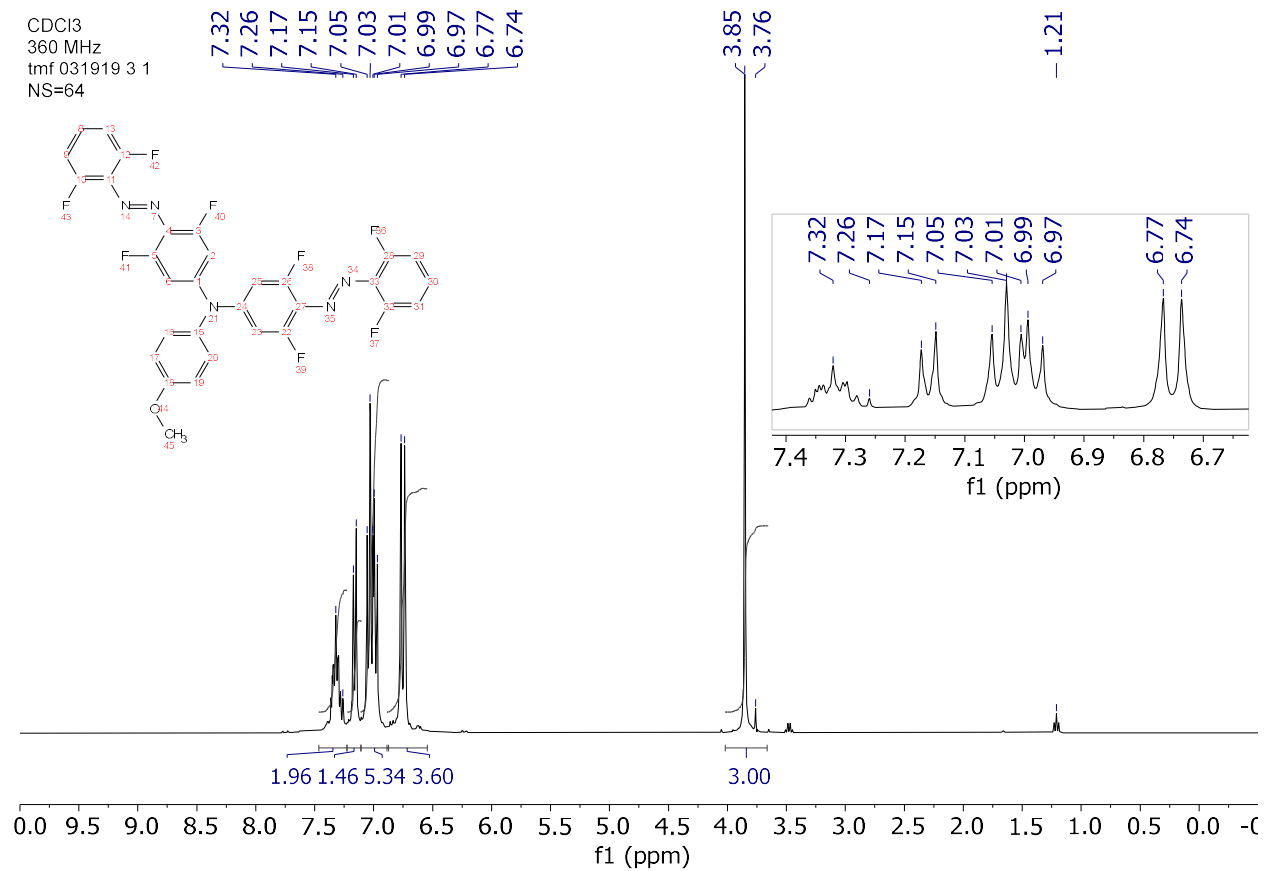


Figure A13. ¹H-NMR spectrum (360 MHz) of compound **21** in CDCl₃.

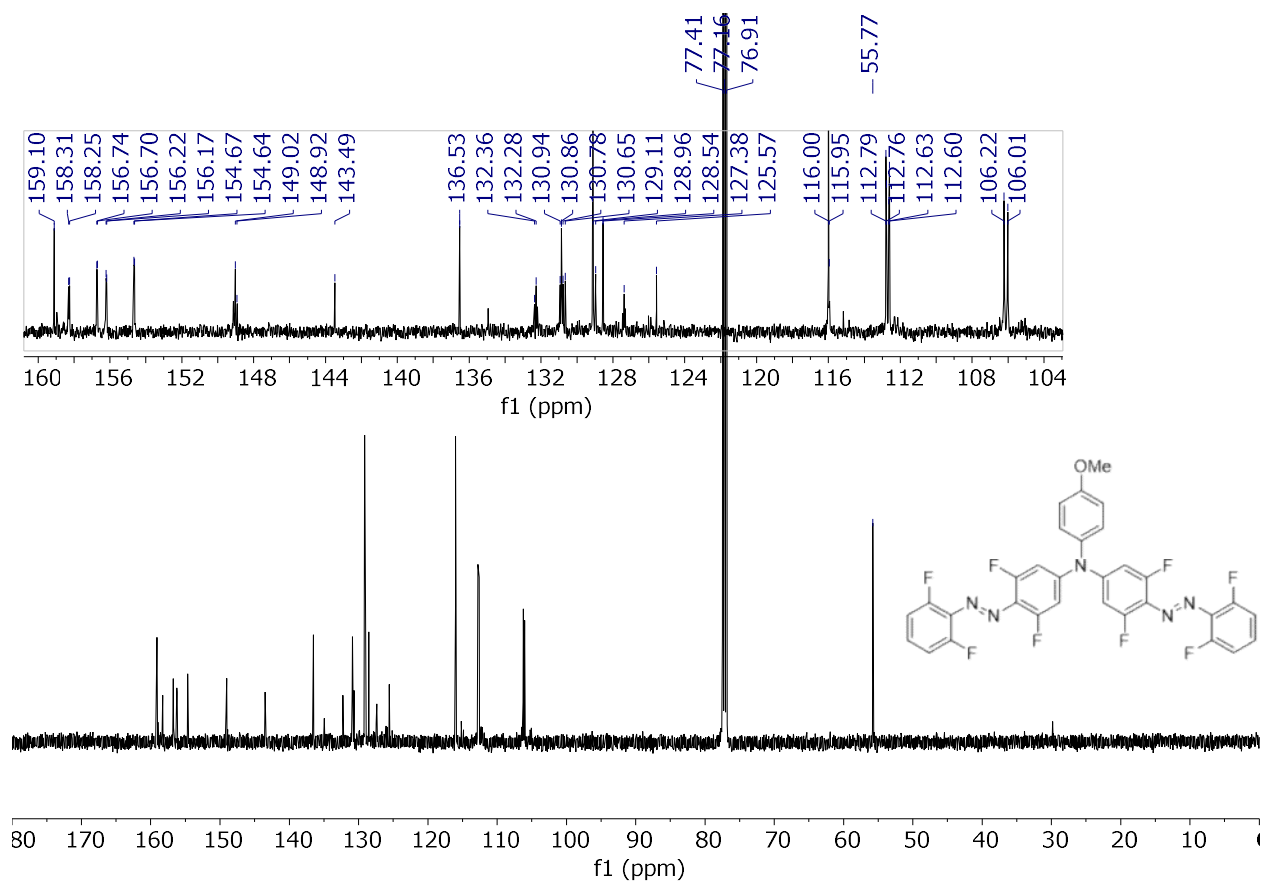


Figure A14. ^{13}C -NMR spectrum (125 MHz) of compound **21** in CDCl_3 .

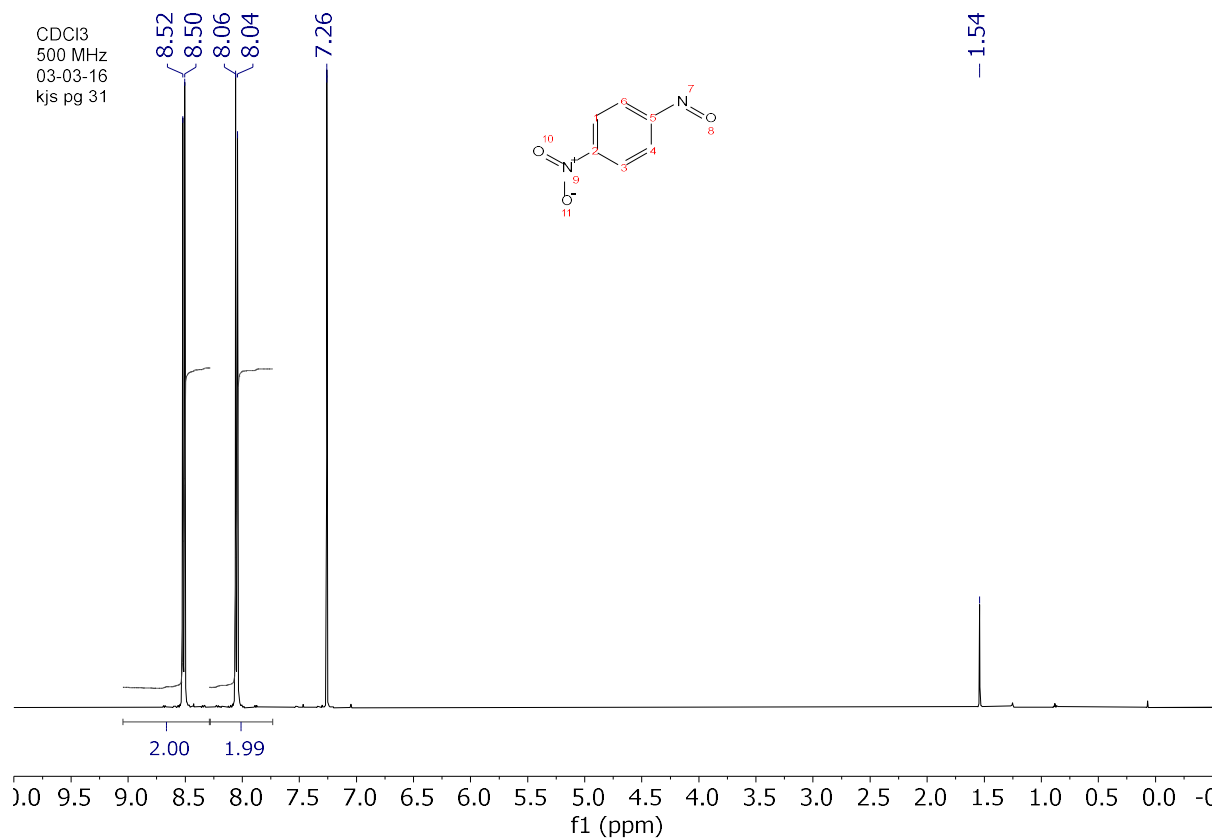


Figure A15. ¹H-NMR spectrum (500 MHz) of **31** in CDCl₃.

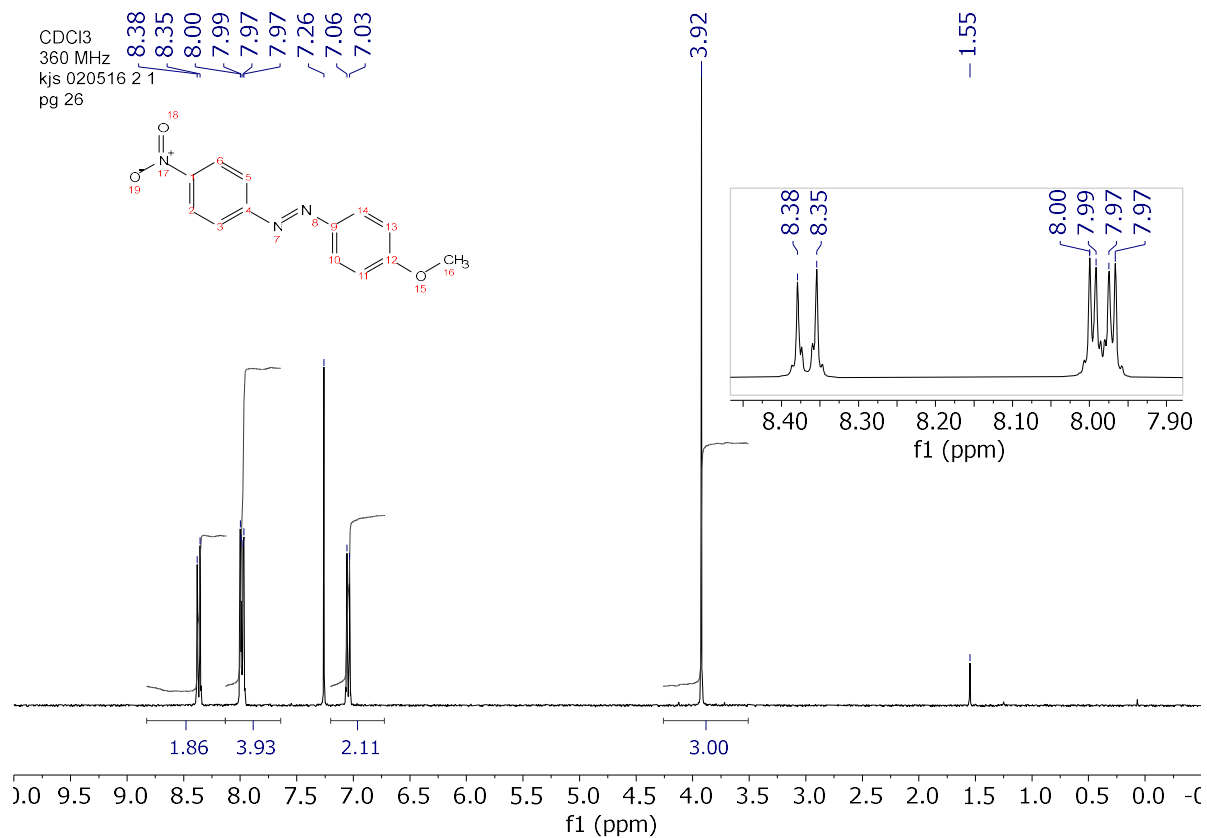


Figure A16. $^1\text{H-NMR}$ spectrum (360 MHz) of **32** in CDCl_3 .

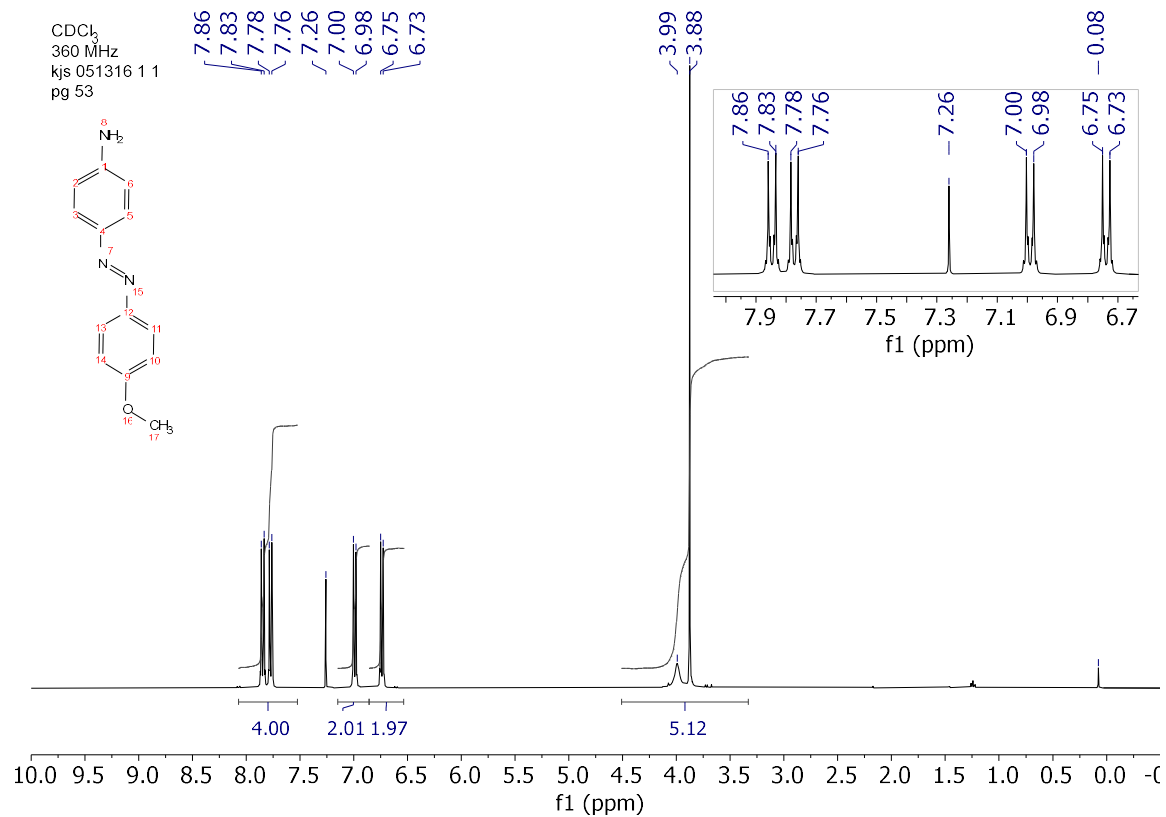


Figure A17. ¹H-NMR spectrum (360 MHz) of pure **33** in CDCl₃.

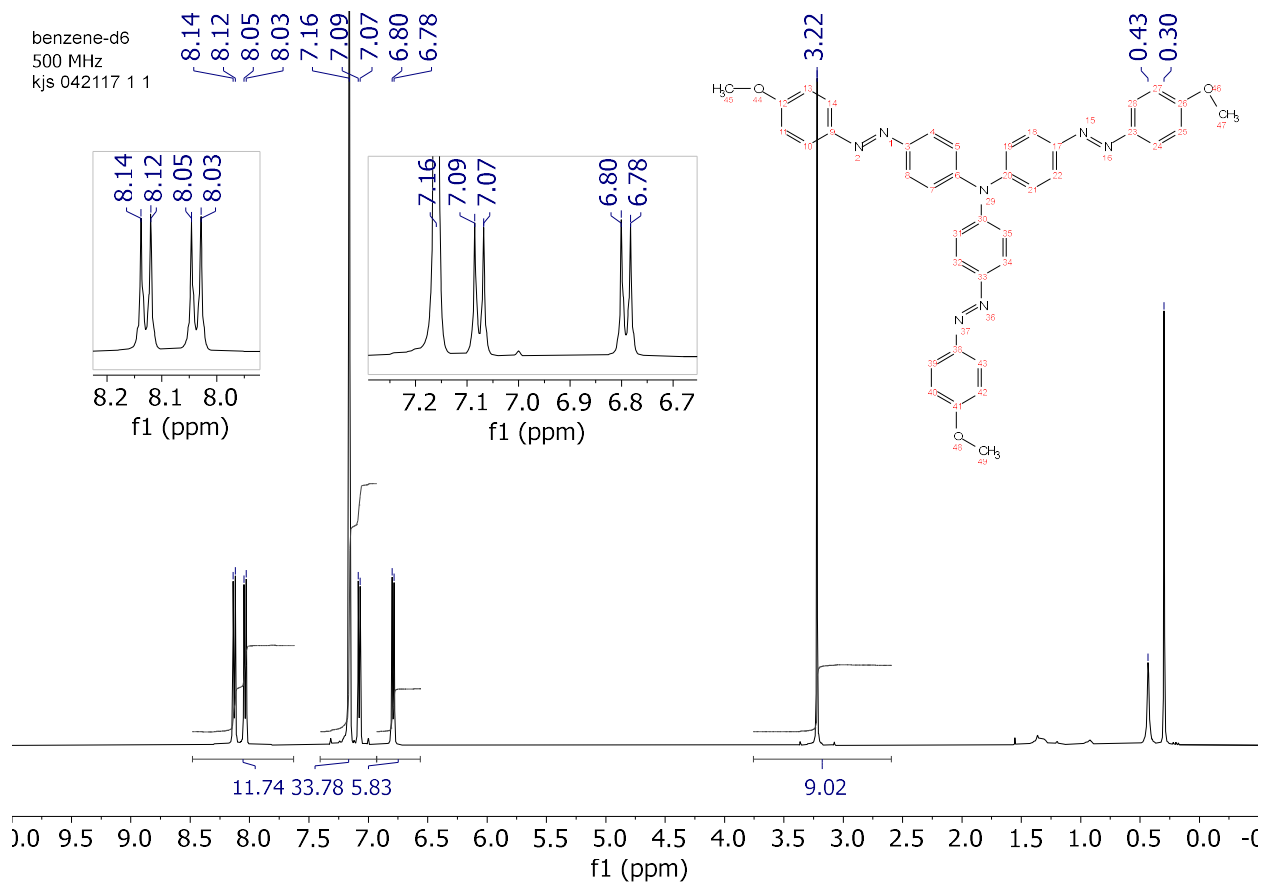


Figure A18. $^1\text{H-NMR}$ spectrum (500 MHz) of purified compound **29** in C_6D_6 .

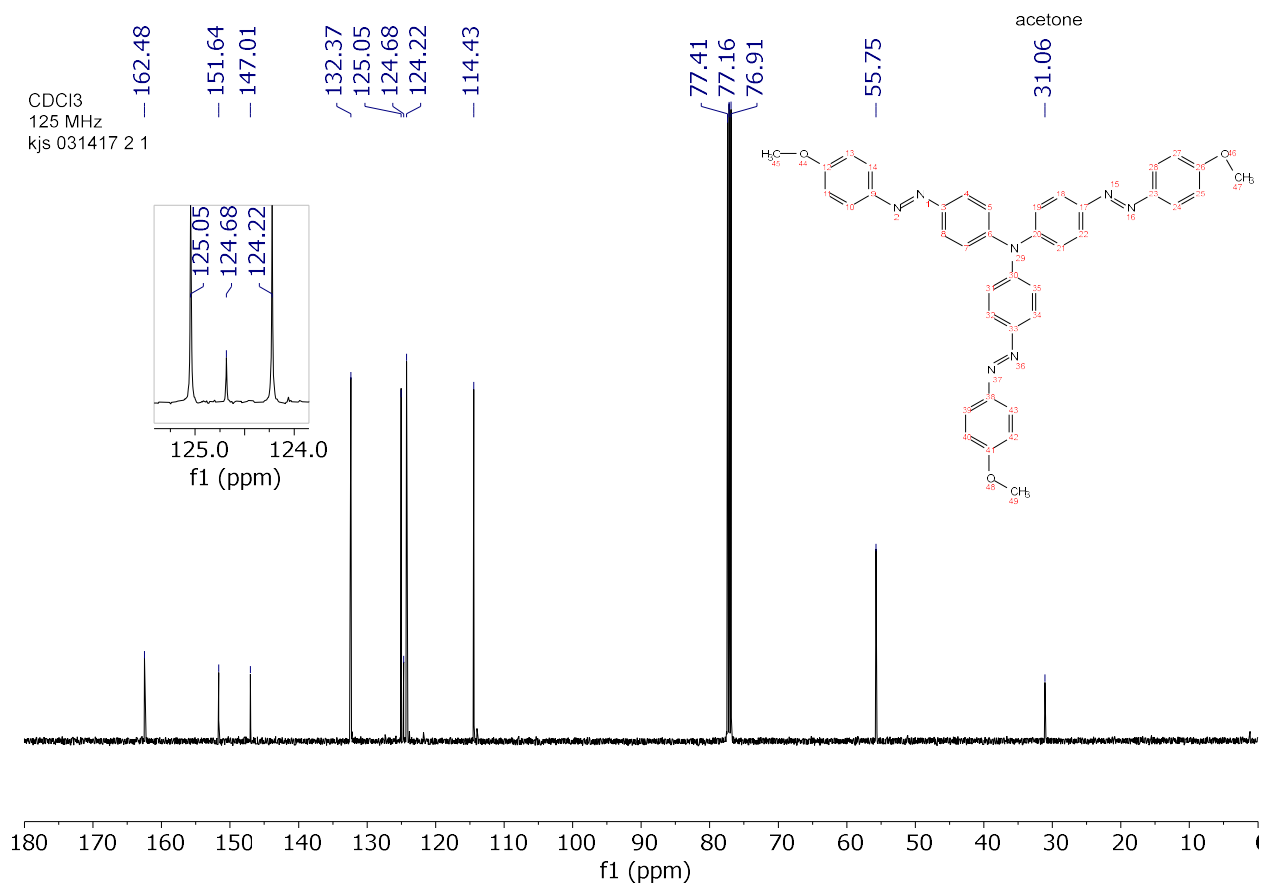


Figure A19. ¹³C-NMR spectrum (125 MHz) of compound **29** in C₆D₆.

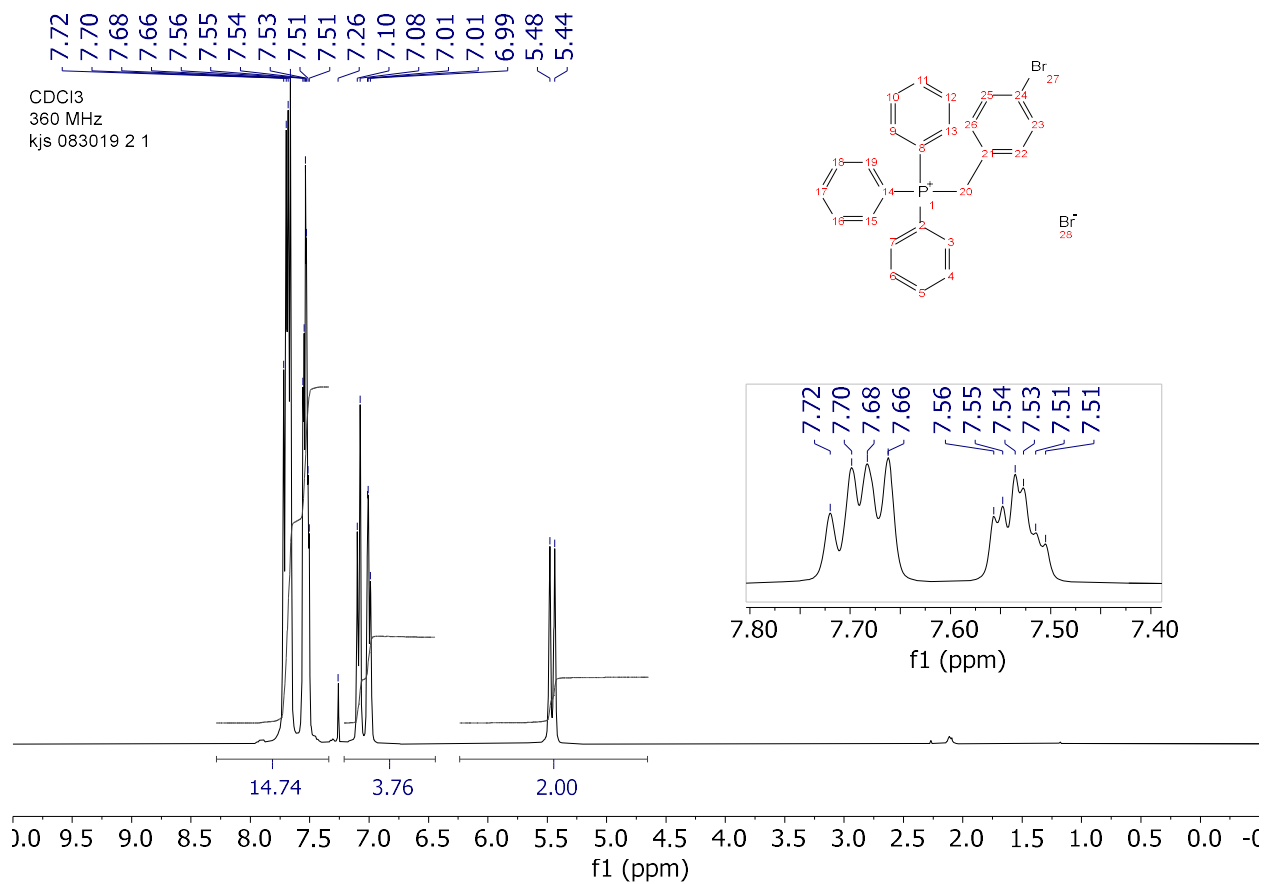


Figure A20. $^1\text{H-NMR}$ spectrum (360 MHz) of compound **41** in CDCl_3 .

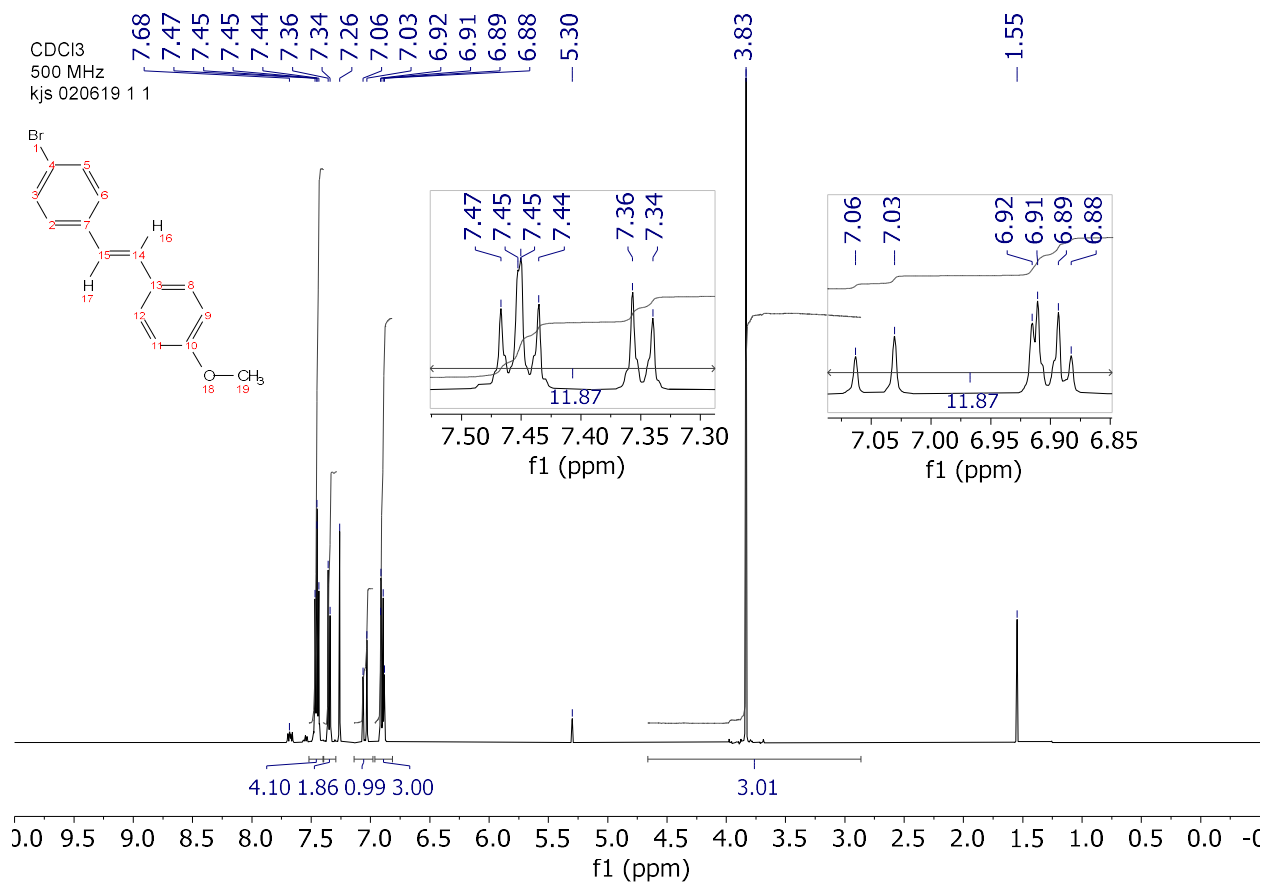


Figure A21. ¹H-NMR spectrum (500 MHz) of compound *E-43* in CDCl₃.

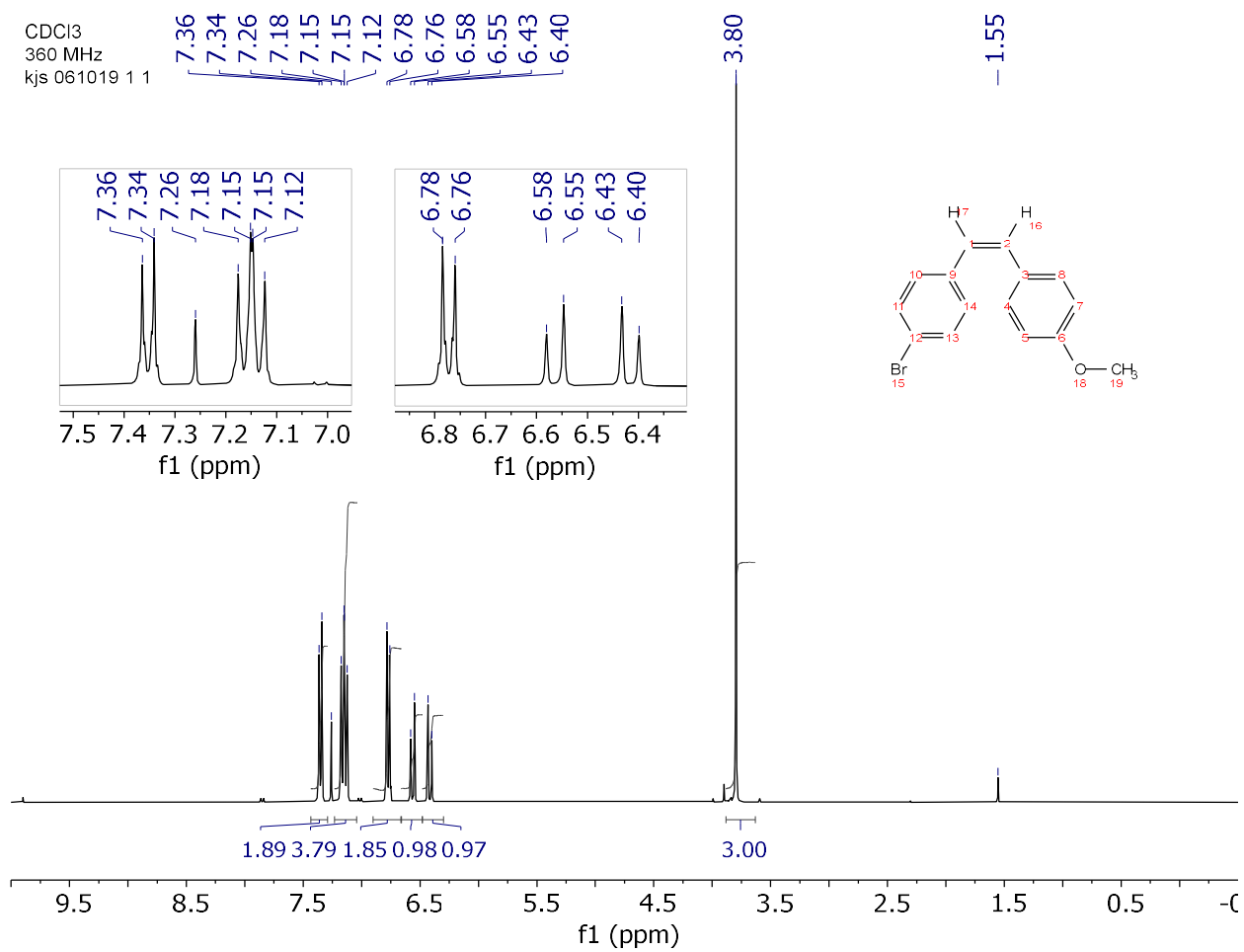


Figure A22. ¹H-NMR spectrum (360 MHz) of compound Z-43 in CDCl₃.

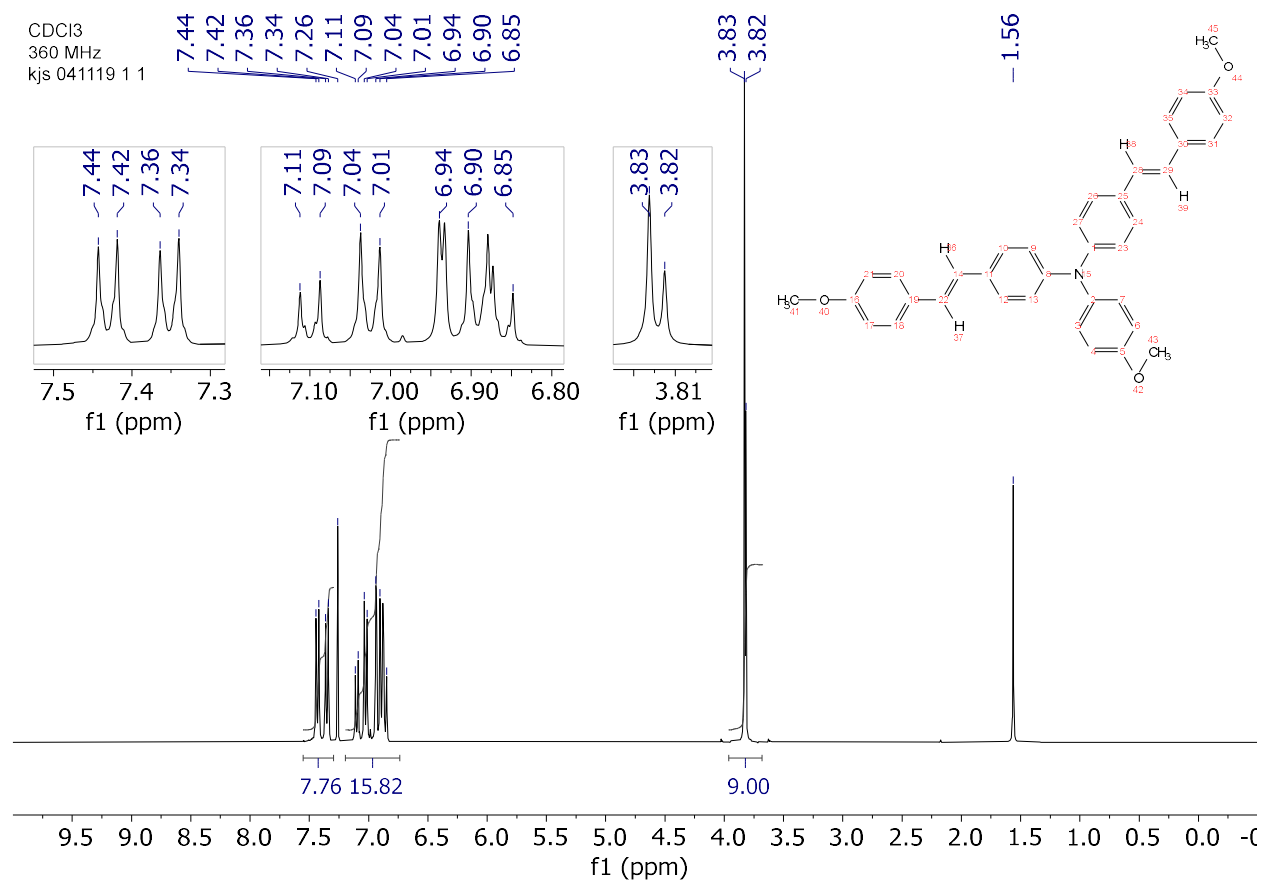


Figure A23. ¹H-NMR spectrum (360 MHz) of compound *E,E*-38 in CDCl₃.

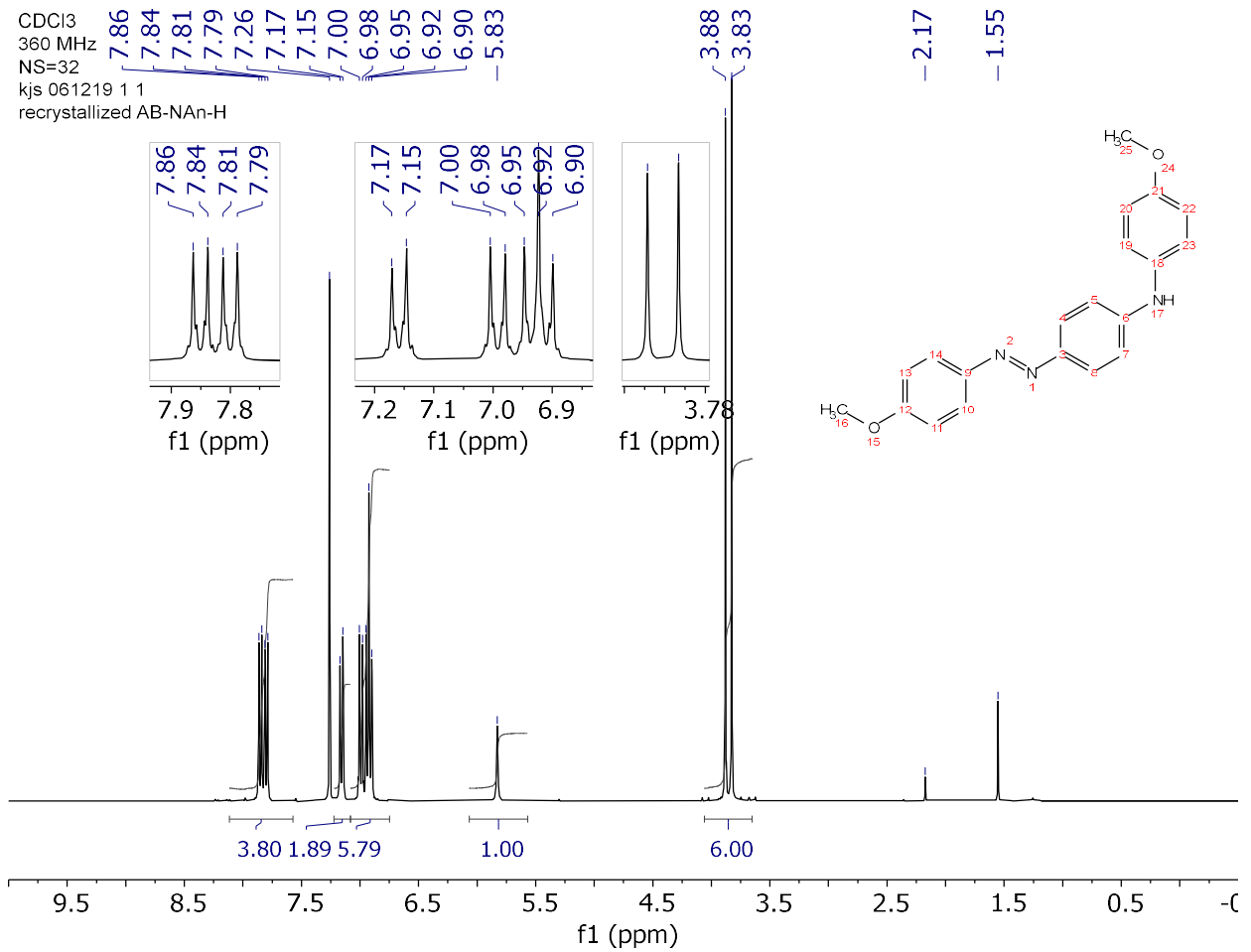


Figure A24. $^1\text{H-NMR}$ spectrum (360 MHz) of compound **44** in CDCl_3 .

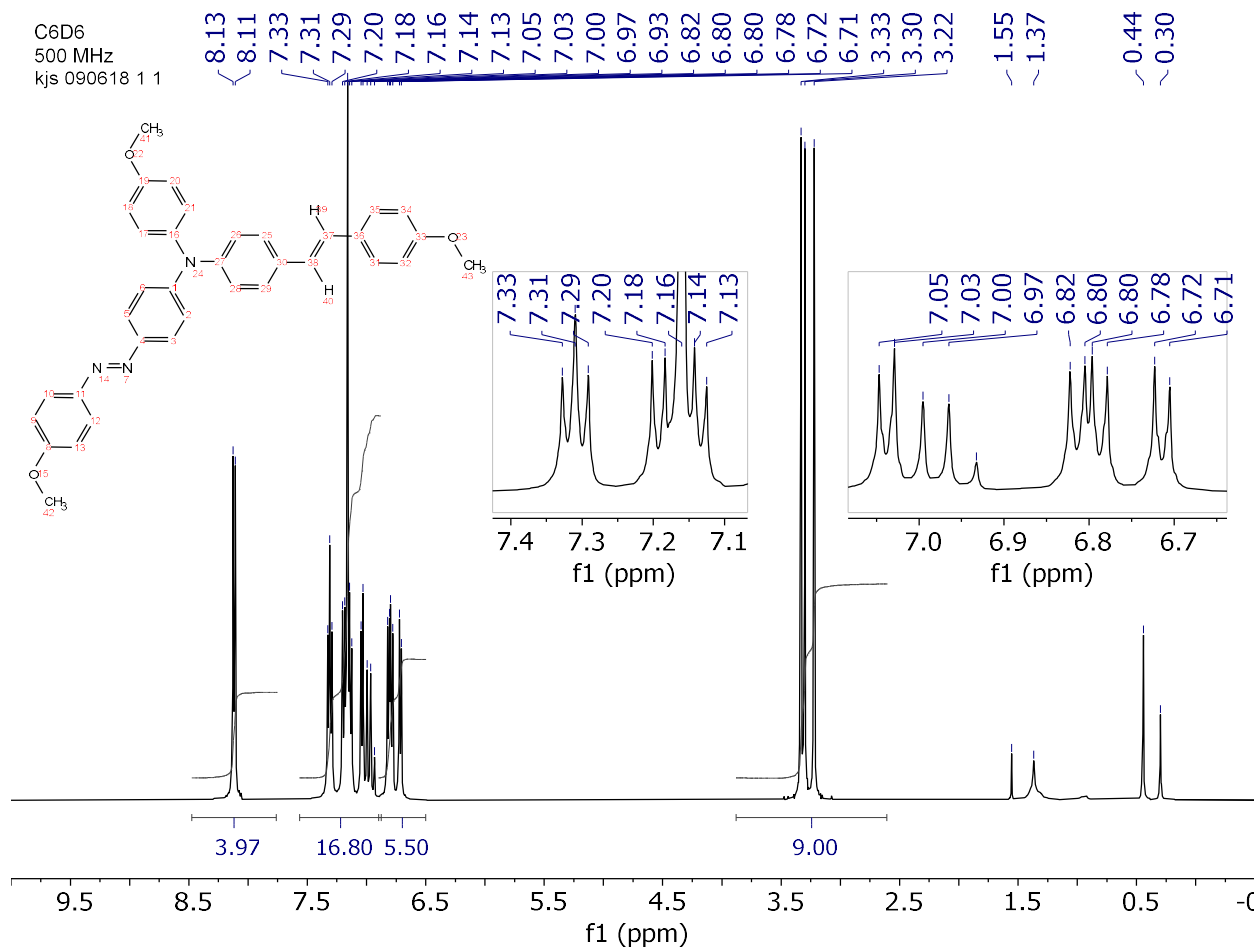


Figure A25. ¹H-NMR spectrum (500 MHz) of compound **45** in C₆D₆.

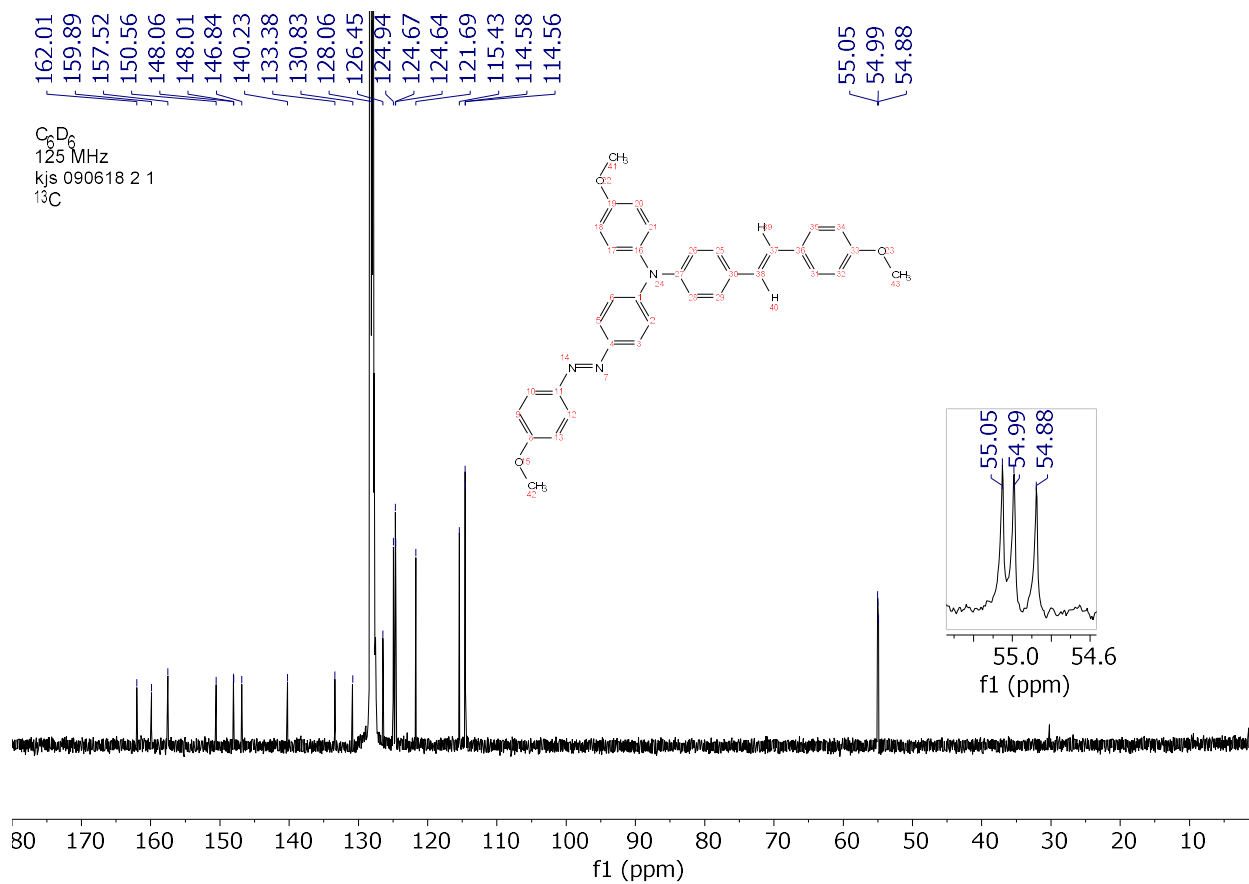


Figure A26. ^{13}C -NMR spectrum (125 MHz) of compound **45** in C_6D_6 .

APPENDIX B – LED LIGHT SOURCES

LIST OF LED LIGHT SPECTRA

Figure B1. Excitation Spectra overlay of LED light sources 430 nm (blue), 457 nm (black), and 660 nm (red)..... 190

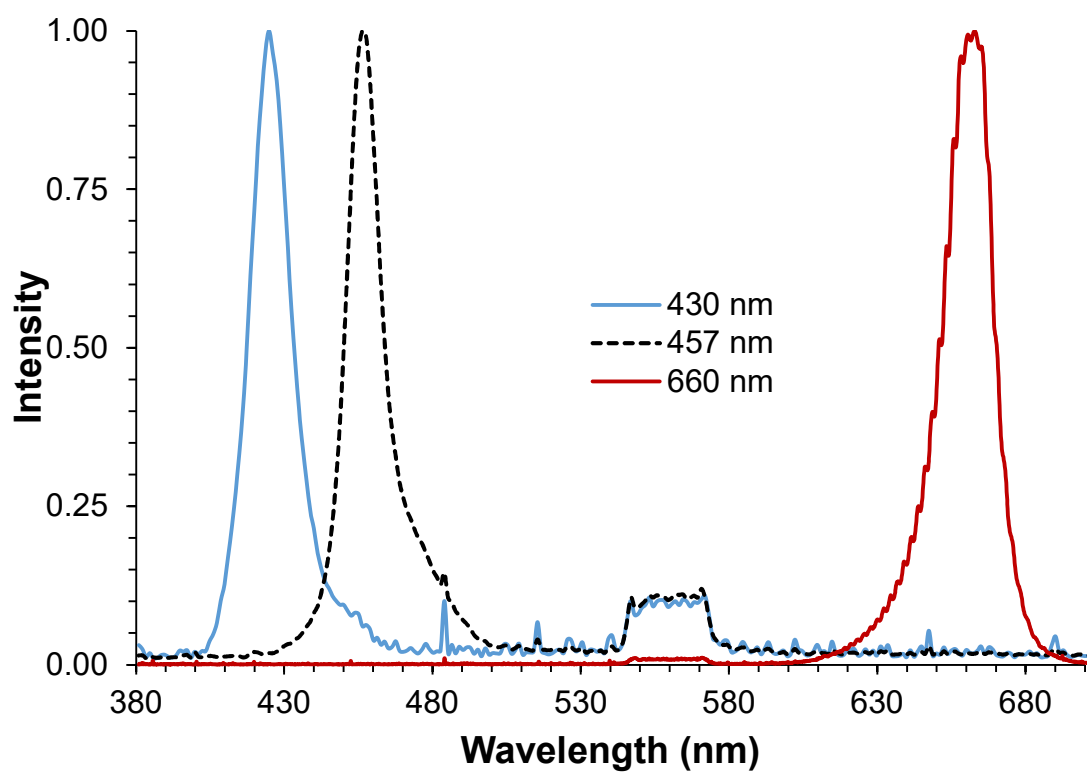


Figure B1. Excitation Spectra overlay of LED light sources 430 nm (blue), 457 nm (black), and 660 nm (red).